Design of new catalysts for chemical CO2 utilization

Katarzyna Swirk

Sorbonne Université

École doctorale SMAER (ED 391), Sciences Mécaniques Acoustique Électronique Robotique,

programme doctoral Génie des Procédés, *Institut Jean Le Rond d'Alembert*

AGH University of Science and Technology

Faculty of Energy and Fuels, *Department of Fuel Technology*

Design of new catalysts for chemical CO_2 utilization

Développement de catalyseurs innovants pour la valorisation chimique du CO_2

Projektowanie nowych katalizatorów do chemicznej utylizacji CO_2

By mgr inż. Katarzyna Świrk

Doctoral thesis in Chemical Engineering - Chemical Technology

Supervised by Prof. Patrick Da Costa and Prof. dr hab. Teresa Grzybek

Presented in public on 12 April 2019

The scientific committee :

Mrs. Ioana Fechete, Associate Professor, Université de Troyes, **Reviewer**

Mr. Jacek Grams, dr hab. inż., Prof. PŁ, Łódź University of Technology, **Reviewer**

Mr. Simeon Cavadias, Full Professor, Sorbonne Université, Examinator

Mr. Stanisław Dźwigaj, dr hab. Chargé de Recherche, Sorbonne Université, Examinator

Mrs. Monika Motak, dr hab., Prof. AGH, AGH University of Science and Technology, Co-supervisor

Mr. Wojciech Suwała, Prof. dr hab. inż., AGH University of Science and Technology, Examinator

Mrs. Teresa Grzybek, Prof. dr hab., AGH University of Science and Technology, Supervisor

Mr. Patrick Da Costa, Full Professor, Sorbonne Université, Supervisor

Moim rodzicom

Oświadczam, świadoma odpowiedzialności karnej za poświadczenie nieprawdy, że niniejszą pracę doktorską wykonałam osobiście i samodzielnie oraz iż nie korzystałam ze źródeł innych niż wymienione w pracy.

Katarzyna Świrk

The research presented in this doctoral thesis was carried out within the cotutelle agreement between Sorbonne Université and AGH University of Science and Technology

Liberté • Égalité • Fraternité
RÉPUBLIQUE FRANÇAISE
AMBASSADE DE FRANCE
EN POLOGNE

I would like to express my gratitude to the French Embassy in Poland for awarding me

BGF Doctorat Cotutelle scholarship for PhD studies between Sorbonne Université

and AGH University of Science and Technology

eit InnoEnergy
Knowledge Innovation Community

I would like to acknowledge InnoEnergy PhD school for the financial support

Erasmus+

I would like to also thank Erasmus + program for my internships

at Norwegian University of Science and Technology in the Chemical Engineering Department

(the KinCat Catalysis Group)

Acknowledgements

First of all, I would like to thank my PhD supervisors Prof. Patrick Da Costa, Prof. dr hab. Teresa Grzybek and dr hab. Monika Motak for their tremendous support, valuable research guidance and dedication. Without their knowledge, encouragement and positivism (acz) I would probably not have started. I would like to also express my gratitude to Prof. Magnus Rønning, from Norwegian University of Science and Technology, for inspiring supervision, whether it was experimental work, result analysis or writing.

I would like to acknowledge the technical staff from the Department of Fuel Technology (AGH), the Institut Jean Le Rond d'Alembert (SU), and the KinCat Catalysis Group (NTNU), who greatly contributed to the realization of this thesis.

I would like to also thank my colleagues from Poland, France and Norway for their friendship and support during my PhD journey.

Foremost, I would like to thank my parents and family who love me unconditionally and support my every decision. I value their opinion more than anything in my life. This would not have been possible without them.

Table of contents

Introduction

With the development of science and technology and the growing of people's awareness of environmental protection around the world, the issues of global warming and air pollution have been given more attention. Decreasing of carbon dioxide emissions was recognized as necessary, as CO_2 is one of the most important greenhouse gases. Two types of technologies are proposed to solve the problem - CCU (Carbon Capture and Utilization) and CCS (Carbon Capture and Storage). The former aims at utilization of carbon dioxide, among others treating it as a feedstock for chemical reactions. In this way CO_2 may play an important role in the sustainable development towards carbon-free economy. One of the possibilities of obtaining added-value is the production of synthesis gas which is currently used as feedstock in several chemical processes, among them liquid fuels production via Fischer-Tropsch or methanol synthesis.

Reforming of methane processes can be classified as the CCU methods. Nowadays, syngas is obtained mainly through steam methane reforming (SRM). Still, SRM yields a syngas with a far too high H_2/CO ratio and needs to be pre-treated before further use in liquid fuel synthesis. The other well-established technologies are autothermal reforming and partial oxidation of methane. Dry reforming of methane (called also CO_2 reforming) could lead to useful utilization of this greenhouse gas but until now was not introduced on a large industrial scale because of the lack of an appropriate catalyst, as well as high endothermicity of the process. The main problem connected with catalysts lies in their inadequate stability which is caused by the formation of carbon deposits and active metal sintering resulting from high temperature of the reaction. Noble metals were found to be fairly resistant to the formation of catalytic coke, but their high price and low availability make them difficult to be accepted by industry. Materials containing nickel have been proposed as promising alternative to noble metal-based ones, as Ni is available and low cost, and it is characterized by good catalytic performance. Moreover, the role of the support is crucial as strong interactions between support and active phase can decrease sintering and thus improve stability. Adding an appropriate promoter can also influence

both activity and stability. Double-layered hydroxides were reported to show good performance in the processes of reforming of methane. These materials show flexibility in composition, as divalent and trivalent cations may be introduced into the structure, allowing to determine their physico-chemical properties. Moreover, the thermal treatment allows to form the homogenous nano-oxides. Some added promoters, such as e.g. Zr or Ce were reported to have a positive influence. However, still improvements concerning stability are required. Thus, a **design of new catalysts for chemical CO_2 utilization** is an important aspect for future development of the reforming processes. Moreover, combining dry reforming of methane with other oxidative reactions could significantly help in oxidizing the formed carbon deposits. Partial oxidation of methane combined with dry reforming, which is under research, is an interesting alternative suggested in literature. The most promising, however, seems to be tri-reforming of methane (TRM). This process proposes the application of gases, such as CH_4, CO_2, H_2O and O_2 in order to obtain a mixture of H_2 and CO with the ratio of 1.5-2.0. TRM could be also used as an effective way for chemical CO_2 utilization without the separation of carbon dioxide from flue gases from natural gas fuel-fired power stations. The process was found to be thermodynamically feasible but until now there is very little experimental research on this subject.

Though double-layered hydroxides have gained more and more interest lately, there are still a lot of unsolved problems. The first group of them is connected with the search for new more effective promoters, or the use of co-promoters. In that respect yttrium is an interesting choice, as it was found to be effective both as a support in DRM, and as promoter in other catalytic reactions. Having chosen a promoter, it is of importance to determine the most effective way of introducing it into a catalyst, and here co-precipitation, impregnation or co-impregnation (in case of using two promoters) may be considered. The second group of not fully solved problems is connected with the addition of oxygen, or oxygen and water, to the reaction mixture, i.e., moving from DRM to CRPOM or TRM, which should improve the catalyst stability where carbon deposition is concerned.

Goals of doctoral thesis

The thesis focuses on the design of new catalysts for chemical CO_2 utilization processes, such as dry reforming of methane (DRM), CO_2 reforming combined with partial oxidation of methane (CRPOM) and tri-reforming of methane (TRM). Ni-containing Mg/Al double-layered hydroxide catalysts were prepared by co-precipitation method, and were further promoted with Y and Zr, or Ce by co-precipitation, co-impregnation or incipient wetness impregnation methods. The physico-chemical properties of the synthesized materials were evaluated by means of different techniques, in order to study the influence of the different textural, structural and chemical parameters on the activity, stability and selectivity. The main goals of the thesis are:

1. Improvement of the activity and/or stability in the DRM process of hydrotalcite catalysts containing Ni through:
    - Introducing a new promoter (Y) or co-promoting with Y and Zr or Y and Ce, and
    - Testing the effectiveness of various promotion methods.
2. Characterization of physico-chemical properties of so-promoted catalysts and determination of the relation between these properties and the activity and stability in DRM.
3. Determination of the effect of the addition of oxygen, or oxygen and water, on the effectiveness of selected hydrotalcite catalysts, and thus the determination of the possibilities of their application in processes of partial oxidation of methane combined with CO_2 reforming and tri-reforming.

The realization of these goals allowed to confirm the hypothesis that the modification of double-layered hydroxides (application of promoters-Y and Zr or Ce) allows to tailor catalytic properties of DLHs catalysts, which will further lead to the optimization of the catalyst activity and stability in methane reforming reactions.

Abbreviations

ATR – Autothermal Reforming

BET – Brunauer-Emmett-Teller

BJH – Barrett-Joyner-Halenda

CCS – Carbon Capture and Storage

CCU – Carbon Capture and Utilization

coP – Co-precipitation

COP – Conference of Parties

CRPOM – Combined CO_2 reforming with Partial Oxidation of Methane

CRR – Combustion and Reforming Reactions mechanism

DLH – Double-Layered Hydroxide

DMD – Direct Methane Decomposition

DME – Dimethyl Ether

DPO – Direct partial Oxidation mechanism

DRM – Dry Reforming of Methane

ECBM – Enhanced Coalbed Methane Recovery

EGR – Enhanced Gas Recovery

EOR – Enhanced Oil Recovery

ER – Eley-Rideal

EU – European Union

FT – Fischer-Tropsch

GHG – Greenhouse Gas

GHSV – Gas Hourly Space Velocity

HRTEM – High-Resolution Transmission Electron Microscopy

HT – Hydrotalcite

Imp – Impregnation

IPCC – Intergovernmental Panel on Climate Change

IWI – Incipient Wetness Impregnation

LFL – Lower Flammability Limit

LH – Langmuir-Hinshelwood

MTG – Methanol To Gasoline

POM – Partial Oxidation of Methane

RWGS – Reverse Water-Gas Shift

SCR – Selective Catalytic Reduction

SRM – Steam Reforming of Methane

TEM – Transmission Electron Microscopy

TGA – Thermogravimetric Analysis

TGA/MS – Thermogravimetric Analysis coupled with Mass Spectroscopy

TOM – Total Oxidation of Methane

TOS – Time On Stream

TPD – Temperature-Programmed Desorption

TPR – Temperature-Programmed Reduction

TPSR – Temperature-Programmed Surface Reaction

TRM – Tri-Reforming of Methane

UNFCCC – United Nations Framework Convention on Climate Change

UPL – Upper Flammability Limits

WGS – Water-Gas Shift

XRD – X-ray Diffraction

XRF – X-ray Fluorescence

Chapter 1 – Current status and literature review on CO_2 utilization

Chapter 1 – Current status and literature review on CO_2 utilization

1.1. CO_2 and climate

Growing awareness of environmental problems have triggered global efforts to reduce the levels of gases recognized as harmful. Greenhouse gases (GHGs) are believed to have the effect of trapping the sun's heat, and further result in the global warming and climate change [1].

Carbon dioxide (CO_2) is a gaseous compound which is considered to be one of the main causes of greenhouse effect, and according to the Intergovernmental Panel on Climate Change (IPCC) its rising concentration in the atmosphere mainly originates from fossil fuel combustion, petrochemical, chemical and cement industry [2]. In 2017, among the total anthropogenic GHGs emissions, two thirds belonged to energy sector, and 80% were assigned to the CO_2 presence. The estimations performed by the statistical office of the European Union (Eurostat) showed that CO_2 emissions significantly increased in 2017. Compared with the previous year the change 2017/2016 was at level +1.8% [3]. This is almost five times more than the registered in 2016, when the change was ca. +0.4%, and also higher than in 2015 when the CO_2 emissions increased by +0.7% [4,5]. The emissions growths recorded in years 2015-2017 are in contrast to the declines which were observed from 2011 to 2014, with the total decrease of CO_2 emissions of ca. -2.1%, -2.5% and -5.0%, respectively in 2011/12, 2012/13 and 2013/14 [6–8].

Other statistical source (BP Statistical Review of World Energy) shows that the global CO_2 emissions arising from oil, gas and coal consumption reached 33.4 Gt in 2017, and increased in comparison to the 30.1 Gt reported in 2007 [9]. The released CO_2 by country or region, depends on the geopolitical situation and economy. Asian-Pacific countries, including China, India, Japan were recognized as the biggest producers of CO_2 (Fig. 1.1). It is important to mention, however, that other nations are being in the rest of 51.17% of global emissions. In this worldwide classification Europe stands on the third place with Germany showing the significant production of carbon dioxide. On the other hand, Germany showed a negative growth rate as compared to last year. Comparing selected European countries –

Poland, France and Italy showed similar trends in 2017, with CO_2 release of ca. 300 Mt and the annual growth rate lower than +2.0%.

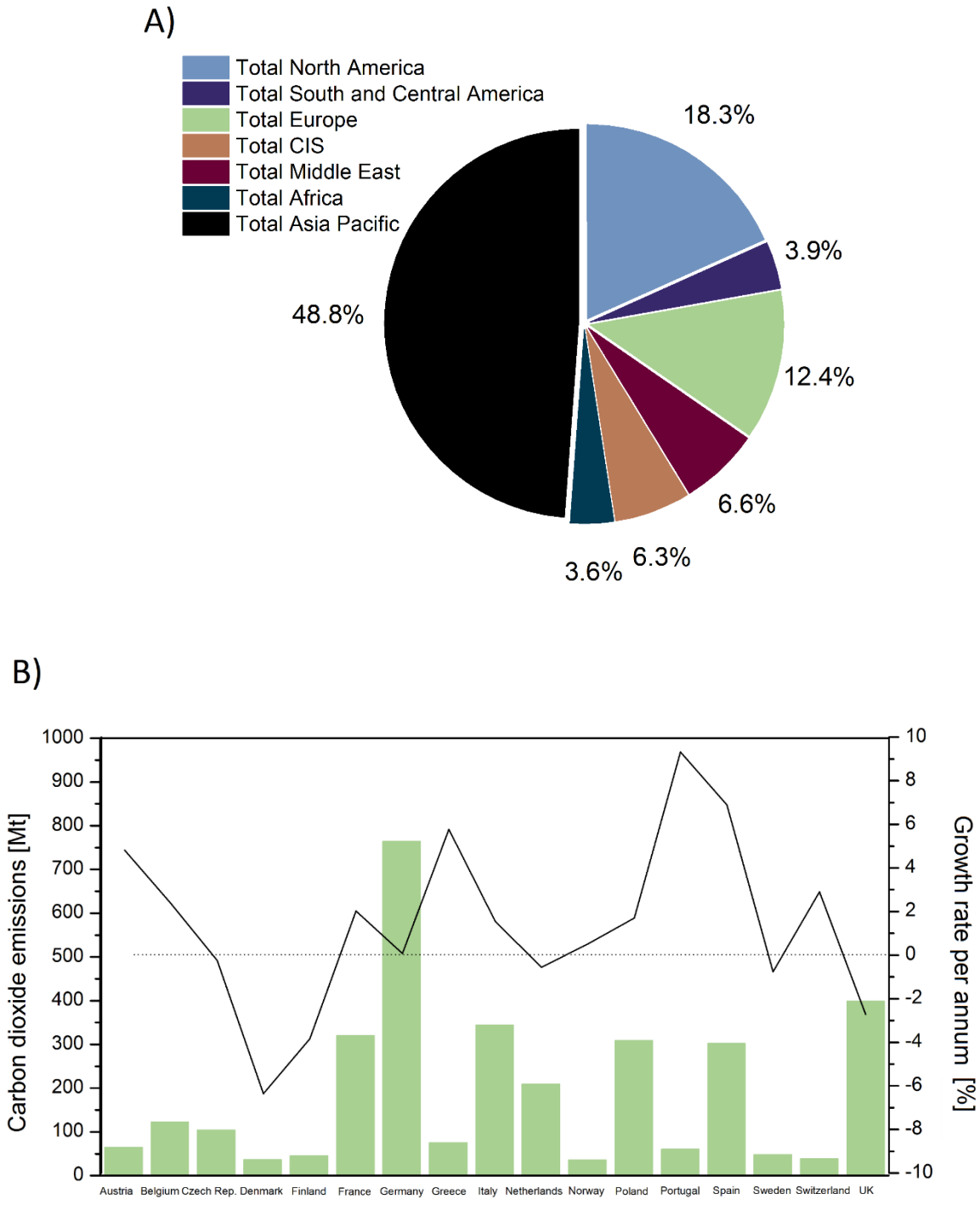

Fig. 1.1 The CO_2 emissions through consumption of oil, gas and coal for combustion related activates: (A) by region recorded in 2017, (B) by chosen European countries in 2017 [9].

The "carbon footprint", defined as the production of CO_2 per person can be controlled at a personal level through, e.g. choosing a way of transportation, recycling, consumption of less energy, etc. [10]. The most effective way of the reduction of anthropogenic CO_2 emission would be a decrease of the energy use, the energy efficiency improvement and application of alternative energy sources instead of fossil fuels. To fully address the threat of global warming, governments delegate measurements to limit levels of CO_2 and other greenhouse gases.

1.2. Reduction of CO_2 emissions – solutions and technologies

Many efforts have been undertaken to establish regulations which may lead to the decrease of concentrations of greenhouse gases in the atmosphere.

Kyoto Protocol was the first international agreement to reduce GHGs emissions (CO_2, CH_4, N_2O, HFCs, PFCs, SF_6) in the developed countries. It was signed in 1997 and entered into force in 2005 [11]. The global scale target was to decrease the emissions by 5.2% during the years 2008-2012, as compared to the level from 1990, with the individual reduction levels for each country considering its economy and political situation. The second commitment period (2013-2020) assumed reduction of at least 18% of emissions compared with the levels from 1990 [11,12].

During recent years the United Nations Framework Convention on Climate Change (UNFCCC) organized a number of conferences dedicated to the controlling of the CO_2 emissions. In 2009, the Copenhagen accord decided to continue with the Kyoto Protocol and the world-wide community agreed that climate change is the main concern, which can impact people living around the world. The Paris Climate Agreement, also known as Conference of Parties (COP21), gathered policy experts, scientists, and climate economists from 118 countries, who decided to combat the climate change, with the ultimate goal of keeping the global temperature increase below 2 °C (with the respect to 1990 levels). In 2016, COP22 took place in Marrakech (Morocco), where the roadmap for the development of Paris agreement was announced, and aimed at an intensive work to reach its fundamental decisions by 2018 [13]. During the COP23 in Bonn (Germany), the work program for the developing a roadmap

to 2020 was established [14]. 24th Conference of Parties (COP24) took place in Katowice (Poland) in December 2018, where the participating countries agreed to use "a rulebook" of the 2015 Paris Agreement, entering into force in 2020. It defines how the member nations will measure the carbon-emissions and report their emissions-cutting efforts [15].

European Union (EU) regulates the concentration of GHGs emissions in the atmosphere via long-time approaches. This includes 20/20/20 strategy in the *2020 climate & energy package*, which assumes: (i) 20% cut of GHGs emissions (from 1990 levels), (ii) 20% share of renewables, and (iii) 20% improvement in energy efficiency. In 2014, EU adopted a new *2030 climate & energy framework*, settings three following targets: (i) 40% lower emissions of GHGs in respect to 1990 levels, (ii) at least 27% share of renewables in the energy sector, and (iii) at least 27% improvement in energy efficiency. Afterwards, the European Commission proposed *2050 low-carbon economy* with the roadmap that suggests: (i) GHGs cut to 80% in comparison to 1990 levels, (ii) 40% lower emissions by 2030 and 60% by 2040, and (iii) a contribution of all sectors, i.e., transport, building, industry and agriculture [16]. Moreover, the EU issued a CO_2 Storage Directive (Directive 2009/31/EC), also known as "CCS Directive", to encourage all members to prepare appropriate regulations for CO_2 storage, accompanied by other provisions on the capture and transport components of CCS.

Imposing taxes on CO_2 emitted, or increasing taxes on gasoline, are other solutions to solve the problem of rising greenhouse gases emissions. A number of governments attempted to implement a widespread set of climate solutions that includes the development of renewable energy usage, building clean energy economy with the aid of fundamental science and translational technology, higher vehicle efficiency, limiting carbon emissions by introducing a carbon tax, diminishing tropical deforestation, etc. [10]. Although these large- and/or small-scale efforts can help in decreasing pollution, they are not satisfactory enough to solve the CO_2 problem.

To facilitate decreasing CO_2 emissions related to energy production and use, the following methods/technologies are proposed: an improvement of energy efficiency, carbon capture and

storage processes (CCS), carbon capture and utilization processes (CCU), and/or the application of renewable energy sources.

1.2.1. *Carbon dioxide capture and storage (CCS)*

Carbon dioxide capture and storage (CCS) is considered a crucial method for meeting CO_2 emission reduction targets. It covers broad types of technologies which aim at transporting carbon dioxide (from fossil fuels) via pipelines to safe underground storage, such as deep saline formations, coalbeds, mature and depleted oil and gas fields etc. [17]. Despite many CCS projects realized in Europe, Americas, Middle East and Asia Pacific, the technology has not yet been launched on an appropriate scale [18]. CO_2 capture systems involve the following types of capture: (i) post-combustion, (ii) pre-combustion, and (iii) oxyfuel combustion as schematically presented in Fig. 1.2.

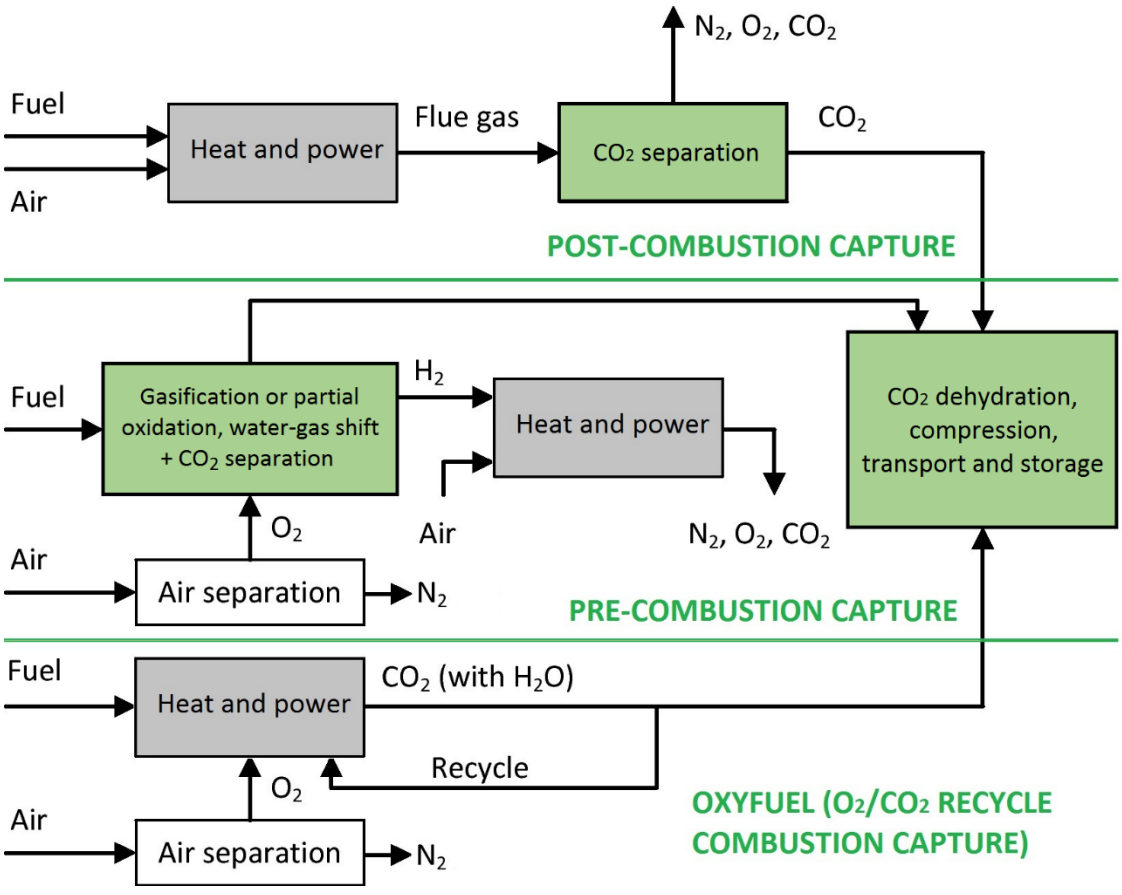

Fig. 1.2 Technological concepts of carbon dioxide capture (adapted from [19,20])

Post-combustion assumes the removal of carbon dioxide from the products of fuel combustion with air. Carbon dioxide is captured in the separation unit, and the rest gases (N_2, O_2, and remaining CO_2) are vented to atmosphere [21]. Wet scrubbing with different aqueous amine solutions is the most commercially advanced method used for CO_2 separation [19]. CO_2 is usually removed from the post-reaction solvent, by heating to around 120 °C, before being cooled and recycled continuously. This method found application in enhanced oil recovery, urea production and in food/beverage industry [20]. The CO_2 removed from the solvent in the regeneration process is dried, compressed and transported to safe geological storage [19].

Pre-combustion engages gasification or partial oxidation with sub-stoichiometric amounts of oxygen separated from the air, to subsequently give a mixture of synthesis gas (H_2 and CO). The formed hydrogen may be used in e.g. gas turbines, engines, furnaces or fuel cells [22]. Hydrogen content is increased and carbon monoxide removed via the water-gas shift reaction: $CO + H_2O = CO_2 + H_2$. The separation of CO_2 can be carried out by absorption, adsorption or membranes [23]. The pre-combustion can be used in power plants which employ integrated gasification combined cycle (IGGC) technology.

Oxyfuel combustion is performed with pure oxygen, which may be obtained by cryogenic air separation. After combustion, a part of the flue gas is recycled to the burner, in order to moderate the temperature of combustion [23,24]. The remaining flue gas is cooled to remove water, compressed, and separation of O_2 and N_2 from CO_2 takes place [25].

The captured carbon dioxide can be either stored or treated as a carbon source for the chemical supply chain. Thus, it may become an alternative feedstock for fuels production, replacing oil and gas in many applications. The processes, which deal with CO_2 utilization technologies are called Carbon Capture and Utilization (CCU).

1.2.2. *Current and emerging carbon dioxide utilization technologies*

Carbon capture and utilization (CCU) processes assume that CO_2 is used as feedstock in syntheses of desirable chemicals. Thus, carbon dioxide is treated as a valuable resource, with almost zero costs of production [8]. CCU shares the same initial steps as CCS, but instead of storing CO_2 underground, the gas is either directly utilized or converted into commercial products (Fig. 1.3). After capture and separation of CO_2, purification, and compression take place based on the type of transportation and the required purity of the receiver. The fifth step is the CO_2 transportation to the receiver. The type of transportation is determined by the stream characteristics (i.e., flowrate, purity), and the distance between source and sink. The final step is utilization with CO_2 delivered to the receiver at the required purity and flowrate, and converted to the final product [17].

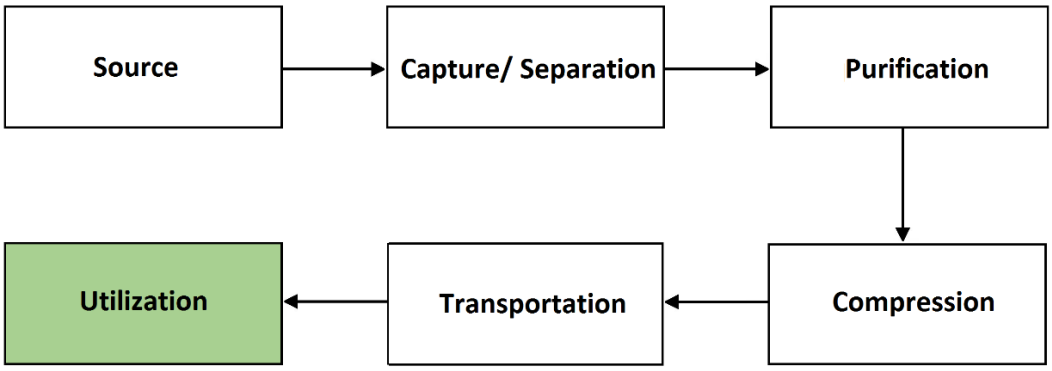

Fig. 1.3 Chain steps of carbon capture and utilization (CCU) (adapted from [17]).

Both Carbon Capture and Storage (CCS) and Carbon Capture and Utilization (CCU) processes aim at the application of non-converted carbon dioxide. CO_2 as non-converted molecule, may be used in the technologies, such an enhanced oil recovery (EOR), enhanced gas recovery (EGR) and enhanced coal bed methane recovery (ECBM) (Fig. 1.4). Most anthropogenic CO_2 currently being geologically stored is associated with CO_2-EOR. However, to be considered as CCS, the CO_2-EOR must demonstrate that the injected CO_2 is stored permanently. Regulations and policy are required to transition from CO_2-

EOR to CCS [26]. Table 1.1. and 1.4 illustrate the pathways for converted or unconverted CO_2 applications.

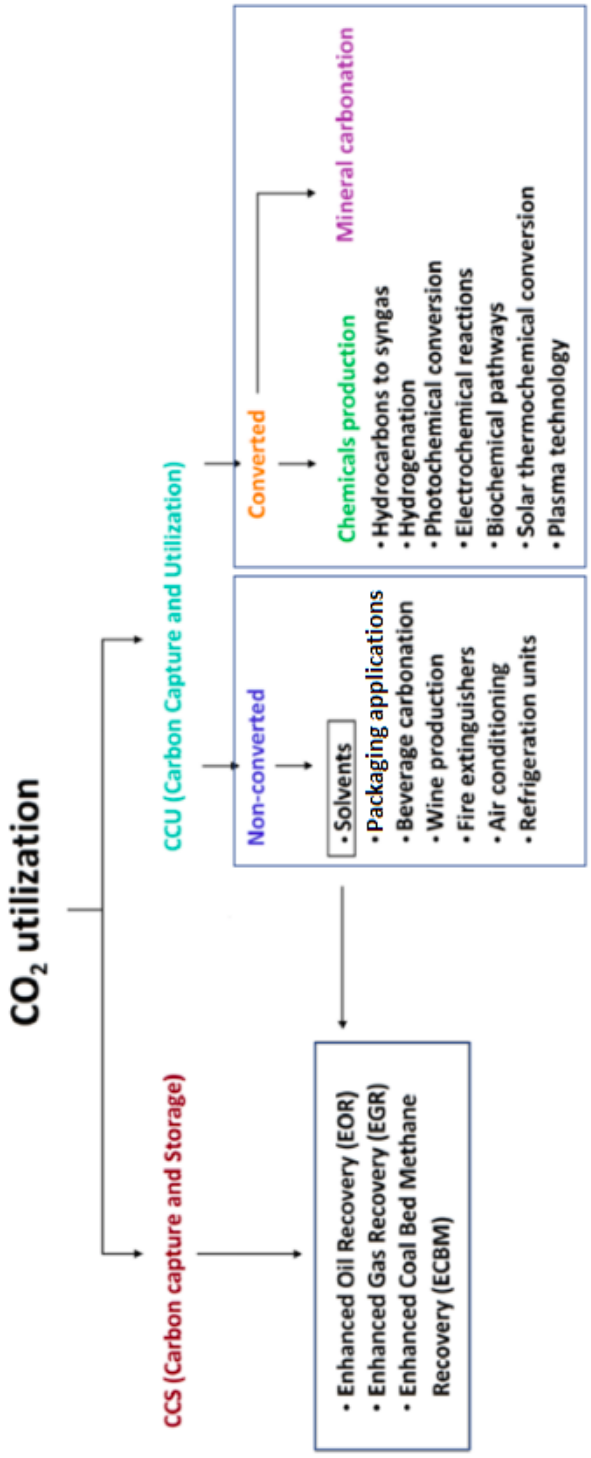

Fig. 1.4 Pathways of carbon dioxide reduction in which CO_2 is converted and non-converted.

Table 1.1 CCU technologies based in which CO_2 is non-converted.

Technology	Summary	Ref.
Enhanced oil recovery (EOR)	CO_2 is injected into an oil reservoir and acts as a solvent which helps to expand oil more easily to production wells	[27–29]
Enhanced gas recovery (EGR)	CO_2 injection into gas field in order to recover e.g. methane	[29,30]
Enhanced coal bed methane recovery (ECBM)	CO_2 is injected into a coal field in order to enhance the recovery of methane	[31]

CO_2-Enhanced Oil Recovery (CO_2-EOR) assumes CO_2 injection into depleted oil fields, to help recovering part of unmineable oil [32,33]. It is a well-established technology, with its biggest potential in USA and the North Sea. The first project of CO_2-EOR was SACROC Unit in West Texas in 1972, using carbon dioxide extracted from natural gas [34]. The possibility of utilization of CO_2 from cheaper, and naturally occurring fields resulted in establishing the net of pipelines connecting New Mexico, Colorado and Mississippi. In 2014, 136 projects of CO_2-EOR were registered in USA [29]. It was established that the CO_2-EOR could potentially produce 2.4 and 3 billion barrels of oil in UK Continental Shelf (UKCS) and in the Danish and Norwegian sectors, respectively [35]. However, the problems associated with the supply of CO_2 to offshore EOR make the investment difficult in this area [29].

CO_2-Enhanced Gas Recovery (CO_2-EGR) is a technology, where CO_2 is injected into a depleted gas field. It has not yet been commercially applied as it is still at an early stage of development. Likewise, they have been only three known field-testing programs, namely, K12-B Reservoir with Gaz de France as operator (the Netherlands), Budafa Szinfeletti Field (Hungary), and in the Krechba gas field in deep Sahara Desert (Algeria) [29,36]. The K12-B is located in the North Sea and it undertakes injection of CO_2 coming from the same field from which it was produced, together with CH_4. The mixture containing 80% of CO_2 and 20% of CH_4 was injected into a depleted gas reservoir. Comparing, the Hungarian reservoir undertakes usage of the offshore gas, which contains 13% of carbon dioxide [30]. In Algeria, CO_2 content in the gas reservoir is 5%-10%. In Krechba, carbon dioxide is injected into a 20 m thick reservoir with moderate permeability from three horizontal wells [36,37].

Using carbon dioxide to extract methane is known as CO_2-enhanced coal bed methane recovery (CO_2-ECBM). An unmineable coal bed may store 3-200 Gt of CO_2, with the simultaneous extraction of natural gas [29]. A number of projects has been conducted, namely, in the San Juan Basin (USA), Fenn Big Valley (Canada), Recopol (Poland) or Hokkaido (Japan) [31]. The ECBM is currently developed, in contrast to the EOR and EGR which are mature technologies.

It must be mentioned, however, that the possible CO_2 leakage is a major concern for geological storage, as well as utilization of CO_2.

Other applications of non-converted CO_2 assume the direct application of this molecule, e.g. as an inert medium in food industry or packaging, in beverage carbonation, during wine production, etc. [17,38]. Carbon dioxide is also used in metal industry, e.g. for chilling parts for shrink fitting and hardening of sand cores, in paper industry to reduce pH during pulp washing operations, or in water treatment for remineralization and for pH control. Furthermore, the gas is used in fire extinguishers, industrial air conditioning and refrigeration units [17,39].

The conversion of CO_2 into chemicals and fuels can be carried out by different routes, such as reactions of hydrocarbons to syngas, hydrogenation to hydrocarbons, alcohols, dimethyl ether and formic acid production, photochemical conversion, electrochemical reactions, biochemical pathways, solar thermochemical conversion, and plasma technologies etc. [40,41].

One of the proposed processes to apply CO_2 is dry reforming of methane ($CH_4 + CO_2 = 2CO + 2H_2$). The stochiometric ratio between the products is 1, but the side reactions occurrence, such as e.g. reverse water-gas shift (RWGS), lowers the H_2/CO ratio to values lower than unity. Dry reforming of methane is an endothermic reaction, posing several problems with finding a proper catalyst which would be active, selective and resistant to catalysts deactivation [42]. Dry reforming of methane can be combined together with partial oxidation of methane (an exothermic reaction), which makes the overall process more favorable thermodynamically. On the other hand, the tri-reforming of methane (TRM), proposed by Song et al. [43], makes use of the gas containing CO_2, H_2O, O_2 and CH_4, the three former products are present in flue gas emitted from combustion.

Carbon dioxide can be hydrogenated to hydrocarbons through direct and indirect routes. For the former a well-known example is CO_2 methanation, for the first time reported by the French chemist Paul Sabatier in 1902 (Sabatier reaction) [44]. The CO_2 methanation takes place at relatively low temperature window (25-400 °C), due to the reaction exothermicity (ΔH^0=-165.3 kJ/mol) [45]. Moreover, other products such as methanol, dimethyl ether, and formic acid may be produced through CO_2 hydrogenation process via the indirect route in (i) a multi-stage approach, e.g. with different reactors, or (ii) a single-stage approach, using hybrid catalysts to perform simultaneously the multi-step transformation [40].

The photochemical reaction uses energy of light to enhance a chemical process and can be realized by one of two routes, via: (i) photovoltaic (PV) cells, which form the adequate photovoltage subsequently supplied to the cathode (for CO_2 reduction) or anode (for water oxidation), or (ii) direct photocatalytic approach where light-absorbing semiconductor particles are dispersed in aqueous solution to attain light harvesting, charge separation and interfacial charge transfer [46].

Electrochemical CO_2 reduction utilizes electric current and redox potential, mainly at ambient conditions used. In a CO_2 electrolyzer, two chambers contain anode and cathode, which are separated with an ionic conducting membrane. In the former, water is oxidized to molecular oxygen, in the latter CO_2 is reduced to carbon species [47].

Biochemical pathways involve conversion of solar energy into chemical energy (via photosynthesis) in order to produce biofuels. The best example is biodiesel production from microalgae. The latter capture carbon dioxide from three different sources: (i) from atmosphere, (ii) from emissions produced by power plants, or (iii) from soluble carbonates [48]. The development of appropriate technologies for high-efficiency algal biodiesel production is relevant also for biohydrogen, biogas, bioethanol and biomass-to-liquid (BTL) approaches [41].

Thermochemical CO_2 conversion assumes the use of thermal energy of solar furnaces or nuclear reactor to supply the required energy to split carbon dioxide, according to the reaction CO_2=CO+½ O_2 [40]. Through this method, methanol and hydrocarbons can be formed if the latter reaction is coupled

with thermochemical water splitting, which results in production of H_2, O_2 and a mixture of H_2/CO. Two types of direct solar energy conversion can be distinguished: (i) thermal conversion (sunlight is absorbed as thermal energy and extracted as work), or (ii) quantum conversion (the work output is taken directly from the light absorber) [41].

Plasma is a fourth state of matter, defined as ionized gas [49]. Two types of plasma are distinguished: (i) thermal (with the high temperature of gas and similar to temperature of electrons), and (ii) non-thermal (low, even ambient temperature, however the temperature of electrons and excited and ionized species is high) [49]. Non-thermal plasma may be used as a reaction medium in catalytic processes. The conversion of CO_2 may be carried out via different plasma catalytic processes, in which ionized gas created by plasma discharge activates carbon dioxide molecule. The efficiency of the plasma catalytic reactions is dependent on the geometry of reactor used, applied parameters and used catalysts [50,51].

Mineral carbonation, is a second route for CO_2 utilization, assuming conversion of this gas (Fig. 1.4). Carbon dioxide reacts with calcium- and/or magnesium-containing minerals to form stable carbonate materials. The reaction is thermodynamically favored at low temperature and results in heat release [52]. Industrial waste, such as ashes, metallurgic slags, mining tailings, asbestos containing materials, can be utilized in the mineral carbonation process [53]. The final products may be used in building industry, in the form of calcite ($CaCO_3$), dolomite ($Ca_{0.5}MgO{\cdot}5CO_3$), magnesite ($MgCO_3$) and siderite ($FeCO_3$) [52–56].

1.2.2.1. *Chemicals production - mature technologies*

From the CO_2 reduction routes, presented above, many chemicals can be produced. The main chemical products manufactured currently from CO_2 on industrial scale are urea, salicylic acid, some cyclic carbonates and polycarbonates [57]. Table 1.2 summarizes these chemicals formed via CCU technologies.

Table 1.2 Examples of chemicals and fuels produced via CCU technologies (full industrial production) [58].

Chemicals and fuels	**Description of carbon dioxide usage**	**Ref.**
Urea	CO_2 reacts with NH_3 via ammonium carbamate Production of urea (100 Mt/year)	[59]
Salicylic acid	CO_2 reacts with sodium phenolate at high pressures and temperatures Production of salicylic acid (0.03 Mt/year)	[60]
Carbonates, Cyclic carbonates, Polycarbonates	Cycloaddition of CO_2 to an alcohol or epoxide, or using liquid ionic solvents which act like catalyst Production of cyclic carbonate (0.05 Mt/year)	[42,61]

The production of urea uses carbon dioxide (from different sources) and ammonia [59,62]. The production of ammonia is based on the Haber-Bosch synthesis process [63]. Urea synthesis is the best-known process of utilizing CO_2. It is an important product, used among others to reduce NOx emission from exhaust gases of power plants or Diesel engines (selective catalytic reduction process), or as a nitrogen fertilizer [57].

The production of salicylic acid is carried out by Kolbe-Schmitt reaction in which sodium phenoxide and carbon dioxide react at 120-140 °C under pressure [60]. Salicylic acid is used in pharmaceuticals, food preservatives, etc. [57].

Traditional synthesis of carbonates, cyclic carbonates and polycarbonates involves the reaction of appropriate alcohols with toxic phosgene [64]. The one of alternative routes is synthesis via cycloaddition of CO_2 to an epoxide [42,58,61]. Another route is a usage of ionic solvents which act as catalysts e.g. in cyclic carbonates or polycarbonates formation [42]. Cyclic carbonates are used as solvents, and components of electrolytes in Li-batteries, while polycarbonates are used for manufacture optical, automotive, and electronic components.

1.2.2.2. *Chemicals production – mature and emerging technologies, and future prospects*

Synthesis gas, also known as syngas, is a mixture of hydrogen and carbon monoxide. As shown in Fig. 1.5, this mixture may be applied in many processes, leading to production of valuable chemical products.

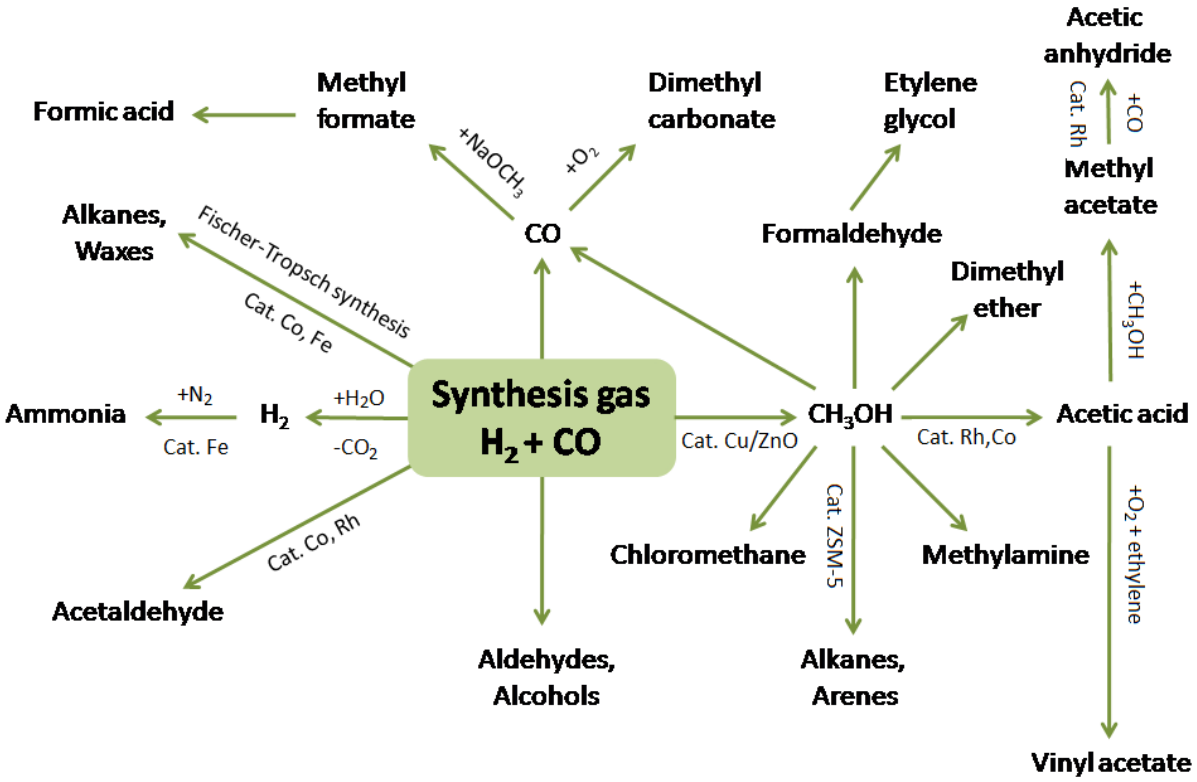

Fig. 1.5 Synthesis gas conversion processes in chemical industry (adapted from [64,65]).

In general, there are six reforming processes proposed in the literature, which produce syngas:

1. Steam reforming of methane (SRM),
2. Partial oxidation of methane (POM),
3. Autothermal reforming (ATR),
4. Dry reforming of methane (DRM),
5. Combined partial oxidation with dry reforming of methane (CRPOM), and
6. Tri-reforming of methane (TRM).

The first three processes are well established and widely used by industry. The synthesis gas in produced via steam reforming of methane (CH_4+H_2O) on nickel-based catalysts [64]. However, the reforming processes which assume conversion of CO_2 are very interesting in terms of utilization of this gas. The last three methods mentioned above (processes 4 to 6) are innovations to minimize this greenhouse gas emissions, minimize energy consumption and improve the reforming process yields. These methods differ in the composition of produced synthesis gas i.e., their H_2/CO molar ratio [66]. The reforming processes will be discussed in detail further in **Subchapter 1.3.2**.

Apart from reforming reactions, syngas may be formed through gasification of coal, and also via an electrochemical process. The former, involves coal conversion into suitable fuel gas by the reaction with air, steam, CO_2 or their mixtures, leading to the production of a mixture of CO, H_2, CO_2 and CH_4 [67,68]. In the electrochemical processes, a mixture of CO and H_2 is produced from the CO_2-water electrochemical reduction [69]. Different metals were studied as catalysts for this purpose. Recently, the researchers from Berkeley (USA) and Toronto (Canada) developed synthesis gas production from a pinch of copper atoms sprinkled atop a gold surface [70]. Moreover, another possibility for conversion of CO_2 is usage of different plasma catalytic processes, in which CH_4 and CO_2 are activated or dissociated by means of high energy electron impact and react with each other at low temperatures [49,50]. The detailed mechanism of plasma excitation in CH_4-CO_2 process was described by Bogaerts et al. [50] and De Bie et al. [71].

As presented in Fig. 1.5, hydrogen, derived from syngas, can be used in fuel cells, or e.g. in the production of urea, etc. However, the biggest consumer of H_2 from syngas is ammonia synthesis. Lately, it is also planned to utilize hydrogen as a fuel for non-polluting vehicles. Carbon monoxide is used in the production of paints, plastics, pesticides, insecticides, etc. [66].

Fischer-Tropsch (F-T) synthesis is a technology to produce hydrocarbons from syngas [72]. Franz Fischer and Hans Tropsch invented this process in 1923 to convert coal into synthetic liquid hydrocarbons at the Kaiser Wilhelm Institute for Coal Research (KWI) in Mulheim Ruhr. First, Fischer and Tropsch hydrocracked the coal by reacting it with steam to produce synthesis gas, and converted

the gases to petroleum-like synthetic liquid [72]. First a cobalt catalyst was designed and developed. The Co-based catalysts are considered the most favorable materials for the synthesis of long chain hydrocarbons due to high activity, high selectivity to linear paraffins and low water–gas shift (WGS) activity [73]. Moreover, cobalt is the best compromise between catalytic performance and cost for the production of hydrocarbons [74]. The water-gas shift reaction (WGS) on Fe-based catalysts in the F-T synthesis is more active than that on Co-based material. The activity of WGS leads to the production of more CO_2 that CO, which at the same time allows the utilization of synthesis gas which contains carbon dioxide or hydrogen depleted syngas [72]. The first commercial Fischer-Tropsch processes were used in Germany. About 14% of motor fuels were produced by the Fischer–Tropsch (FT) method in Germany during World War II [72].

Methanol is the most important product of synthesis gas conversion [75]. It has been estimated that methanol synthesis from catalytic hydrogenation of CO_2 will become commercial within a few years, as it has already been commercially interesting when cheap sources of renewable H_2 are available, or when it was used to store an excess of electrical energy. This development would be pushed by the experience in pilot or pre-commercial industrial plants, such as the Mitsui plant (pilot in Japan, and large unit expected in Singapore) and methanol plant in Iceland (Carbon Recycling International - CRI). The latter produces renewable methanol at a large scale (Vulcanol^{TM}), using CO_2-containing flue gas (from industrial and geothermal emissions) and hydrogen using renewable sources of electricity [76]. Methanol can be used both as a chemical (directly or as an intermediate for other products, including light olefins) and as a fuel (directly, or to produce fuel additives/components)[75].

Table 1.3 Summary of the possibilities for the CO_2 fixation as a function of their maturity (adapted from [64,77]).

		Potential development	Economic perspectives	Potential volume of CO_2	External use of energy	Duration of CO_2 sequestration	Other impacts
Already	Enhanced oil recovery	4	4	2	3	4	4
	Industrial utilization	4	4	3	2	1.5	4
	Organic synthesis	4	3	2	3	3	3
Short	Hydrogenation	3	3	4	4	2	3
	Algae open ponds	3	3	4	4	2	4
Medium	Reforming of hydrocarbon	2	unknown	1	4	2	1
	Algae reactor	2	2	4	4	2	4
Long term	Mineralization	1	1	1	3	4	3
	Thermo-chemical	1	2	4	4	2	3
	Electrolysis	1	unknown	2	4	2	2
	Photo-electro catalysis	1	unknown	4	4	2	2
	Bio catalysis	1	unknown	4	4	2	3

Potential development: 1, more than 10 years → 4, industrial
Economic perspectives: 1, difficult to estimate → 4, available industrial data
External use of energy: 1, difficult to decrease → 4, no need
Potential volume of CO_2: 1, less than 10 Mt → 4, more than 500 Mt

Table 1.3 presents the techno-economic study of the potential as well as currently used technologies for CO_2 utilization. The study was prepared by Thybaud and Lebain [77] for the French Environment and Energy Management Agency. One can note that the reforming of hydrocarbons, hence the reforming of methane processes, are already considered as a medium-term technology with a capability for industrialization. Among them, dry reforming of methane (DRM) is discussed.

A DRM demonstration plant was co-launched by Shanghai Advanced Research Institute of the Chinese Academy of Sciences, Shanxi Lu'an Coal Corporation Limited and Shell Global Solutions International. The plant can produce more than 200,000 Nm^3 of syngas and convert 60 tons of CO_2 per day, and is currently the world's largest test DRM plant [78]. Another example is the JAPAN-GTL demonstration plant located in Niigata City (Japan) with three main units: (i) synthesis gas section, (ii) Fischer-Tropsch synthesis section, and (iii) upgrading section (hydrocracking). The first unit includes steam and dry reforming of methane.

The European example is a DRM pilot plant established in 2015 by the Linde Group at Pullach in Germany [79]. The company is testing two catalysts. A nickel-based catalyst, similar to those used in steam reforming, and a cobalt-based one which has lower tendency to carbon deposition than Ni catalysts [80].

Tri-reforming of methane is a technology with a great potential. The tri-reforming may be especially suited for CO_2, without prior separation. One example may be a usage of non-conventional (CO_2-rich) natural gas, in pilot scale in Korea (KOGAS) for di-methyl-ether (DME) production [81]. This process provides a lower operating temperature, a desirable H_2/CO in the range of 1.2 and 1.5, and lower coke formation.

1.3. Tri-reforming of methane: reactions, mechanism and catalysts

A novel concept of reforming process has been proposed for the first time by Song et al. [43,82], assuming the usage of the gas feed containing CH_4, CO_2, H_2O, and O_2.

The presence of the oxygen and water vapor improve energy efficiency and can positively affect coke mitigation [83]. However, the biggest advantage of the process is the production of synthesis gas which may be further converted into methanol, di-methyl ether (oxo-synthesis) and liquid fuels (via Fischer-Tropsch synthesis). Another application of the tri-reforming of methane could be converting low-quality CO_2-rich natural gas into industrially useful products [83]. The syngas obtained in methane tri-reforming process has molar ratios in the range of 1.5-2.0 [82]. The synthesis gas can be also further

processed into either hydrogen or carbon monoxide alone, so that the obtained gas can be used in other processes, e.g. hydrogenation or carbonylation. It should be stressed, however, that for the future implementation of tri-reforming on industrial scale, an active, stable (free from coke formation), and selective catalyst is a key requirement.

1.3.1. *Two concepts of tri-reforming of methane*

1.3.1.1. *Flue gases from natural gas power station for tri-reforming of methane*

The scenario applies to fossil fuel-fired power plants, where carbon dioxide is one of the components of flue gases. The process does not require the pre-separation of carbon dioxide, and mixtures containing CO_2, H_2O and O_2 (with methane added) may be directly used for the synthesis gas production (H_2 and CO).

Fig. 1.6 shows the visualization of the concept where flue gases from a power station, with natural gas added, are directed to the tri-reformer. As a result, synthesis gas, which is a raw material for a number of chemical syntheses, is obtained. In this concept the direct CO_2 usage, without its pre-separation, is assumed. This results in energy savings, since conventional methods, such as CO_2-MEA absorption, require high energy for absorbent regeneration [84].

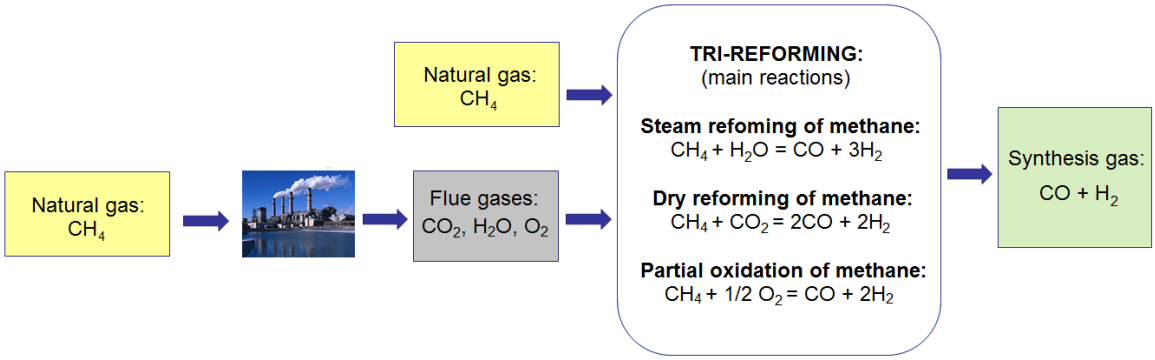

Fig 1.6 Scheme of chemical CO_2 utilization by tri-reforming process implementation in gas-fired power stations.

Typical outlet temperature of flue gases leaving a boiler in a power plant is ca. 1200 °C, and it decreases steadily, as the temperature of flue gases at the tail end is ca. 150 °C [43]. Typical composition from flue gases from natural gas-fired power plants is presented in Table 1.4 [82]:

Table 1.4 Gas composition of flue gases derived from natural gas-fired power station.

Components of flue gases from natural gas-fired power station [vol.%]	**CO_2**	**H_2O**	**O_2**	**N_2**
	8–10	18–20	2–3	67–72

Pollution control installations, such as flue-gas desulfurization and selective catalytic reduction, can remove SOx and NOx, respectively. The particulate matter is also removed in separate units, while, CO_2, H_2O and O_2 remain largely unchanged [83]. Thus, the average composition may be assumed as follows: CO_2–H_2O–O_2–N_2 (9:19:2.5:69.5 parts by volume). Adding 15 vol.% of natural gas and 19 vol.% of air, the condition of thermoneutrality is met at 827 °C and 1 bar pressure by the reaction [84]:

$15\ CH_4 + 9\ CO_2 + 19\ H_2O + 6.8\ O_2 + 85.6\ N_2 = 8.71\ CO_2 + 17.89\ H_2O + 15.29\ CO + 31.1\ H_2 + 0.003\ CH_4 + 85.6\ N_2$

Halmann and Steinfield [84] reported the possible CO_2 emission avoidance, as well CH_4 savings which could be gained when syngas was produced via tri-reforming (instead of traditional steam reforming) and further applied to obtain typical bulk chemicals (methanol, ammonia, etc.), as illustrated by Fig. 1.7. The highest CO_2 emission avoidance (50 %) occurs for methanol production. The largest fuel (natural gas) savings, however, are possible for hydrogen production.

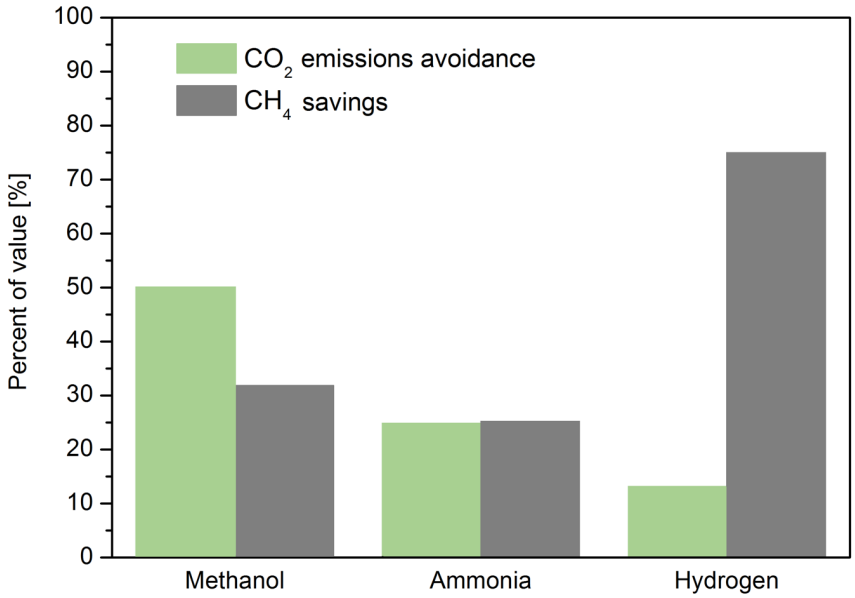

Fig. 1.7 Carbon dioxide emissions avoidance and methane savings when methanol, hydrogen or ammonia are produced with H_2 or syngas obtained via implementation of tri-reforming process in natural gas-fired power stations, instead of current industrial processes. The numerical data taken from [84].

1.3.1.2. *CO_2 separation for tri-reforming of methane*

Another approach to utilization of carbon dioxide flue gases is based on its separation and purification (via absorption, adsorption or membrane separation). Tri-reforming of methane is then a following processes applying pure CO_2. In this case, different molar ratios between the reactants can be used, compared to the ones which are present in the real flue gas. The adjusted mixture should lead to the thermodynamically more favorable results, than in case of the gas mixture typical for flue gases.

Tri-reforming of methane can be carried out with various feed gas compositions as described by Song and Pan [83]. Their thermodynamic calculations showed that high conversions of both CH_4 and CO_2 (respectively over 95, and ca. 80 % at 850 °C) may be obtained, assuming molar ratios of CO_2/H_2O = 1.0, O_2/CH_4 = 0.1, and $(CO_2+H_2O+O_2)/CH_4$ = 1.05. Some experimental catalytic studies of TRM assumed the same and/or very close gas compositions to those proposed in literature calculations [2]. Majewski et al. [85] and Garcia-Vargas et al. [86] studied TRM process with the feed of $CH_4/CO_2/H_2O/O_2$

= 1/0.5/0.5/0.1. Pino et al. [87], worked with feed gas composition of $CH_4/CO_2/H_2O/O_2$ = 1/0.46/0.46/0.1, while Si et al. [88] studied catalysts at $CH_4/CO_2/H_2O/O_2$ = 1/0.5/0.375/0.25., Sun et al. [89] applied in their study $CH_4/CO_2/H_2O/O_2$ = 1/0.45/0.45/0.1, and Song and Pan [43,82,83] assumed $CH_4/CO_2/H_2O/O_2$= 1/0.475/0.475/0.1 and $CH_4/CO_2/H_2O/O_2$= 1/0.56/0.48/0.1. The presence of oxygen may improve catalytic performance of the reforming process. However, it has to be stressed that possible methane ignition should be prevented, and upper and lower flammability limits (UFL, LFL, respectively) have to be considered. Above the upper flammability limit the CH_4 concentration is too high, thus in the presence of spark methane will not combust. The flammability limits are found through calculations, and from methane and oxygen mixture UFL is: 1.57, while for methane in air it is 0.94. On the other hand, when CH_4 concentration is below the LFL its content is too low to start ignition. The lower flammability limits are: CH_4/oxygen = 0.22, and for CH_4/air: 0.05 [90].

1.3.2. *Tri-reforming of methane (TRM): three main reactions*

Tri-reforming of methane is considered as a sum of dry reforming of methane (Eq. 1), steam reforming of methane (Eq. 2) and partial oxidation of methane (Eq. 3), and be written as (Eq. 4):

$$CH_4 + CO_2 = 2CO + 2H_2 \qquad \Delta H^0 = 247 \text{ kJ/mol} \qquad \text{(Eq. 1)}$$

$$CH_4 + H_2O = CO + 3H_2 \qquad \Delta H^0 = 206 \text{ kJ/mol} \qquad \text{(Eq. 2)}$$

$$CH_4 + ½O_2 = CO + 2H_2 \qquad \Delta H^0 = -38 \text{ kJ/mol} \qquad \text{(Eq. 3)}$$

$$3CH_4 + CO_2 + H_2O + ½O_2 = 4CO + 7H_2 \qquad \text{(Eq. 4)}$$

Here some inaccuracy is included, as both the complete oxidation of methane (Eq. 5) and water-gas shift (Eq.6) are not considered.

$$CH_4 + 2O_2 = CO_2 + 2H_2O \qquad \Delta H^0 = 880 \text{ kJ/mol} \qquad \text{(Eq. 5)}$$

$$CO + H_2O = CO_2 + H_2 \qquad \Delta H^0 = -41 \text{ kJ/mol} \qquad \text{(Eq. 6)}$$

During the process many types of side or consecutive reactions take place, involving coke formation, such as direct methane decomposition (Eq. 7) or Boudouard reaction (Eq. 8);

$$CH_4 = C + 2H_2 \qquad \Delta H^0 = 75 \text{ kJ/mol} \qquad \text{(Eq. 7)}$$

$$2CO = C + CO_2 \qquad \Delta H^0 = -171\ kJ/mol \qquad \text{(Eq. 8)}$$

and coke destruction, such as gasification of carbon with CO_2 (Eq. 9), steam (Eq. 10), or oxygen (Eq. 11) [87,91]:

$$C_{(ads)} + CO_2 = 2CO \qquad \Delta H^0 = 172\ kJ/mol \qquad \text{(Eq. 9)}$$

$$C_{(ads)} + H_2O = CO + H_2 \qquad \Delta H^0 = 131\ kJ/mol \qquad \text{(Eq. 10)}$$

$$C_{(ads)} + O_2 = CO_2 \qquad \Delta H^0 = -394\ kJ/mol \qquad \text{(Eq. 11)}$$

Coupling exothermic partial and total oxidation reactions with endothermic CO_2-steam reforming reactions results in generating in situ the heat that can be used to increase energy efficiency and achieve a thermo-neutral balance of reactions [83]. The final H_2/CO ratio can also be adjusted by controlling the amount of steam and CO_2 added to the reaction [92–94]. Moreover, in comparison to dry reforming of methane, catalyst deactivation by carbon formation is lower in this process due to the presence of steam and oxygen [82].

Dry reforming, steam reforming and partial oxidation of methane, considered to take place during the process of tri-reforming of methane are discussed separately in detail below.

1.3.2.1. *Dry reforming of methane (DRM)*

Dry methane reforming (DRM), also called CO_2 reforming, is considered one of the promising processes for chemical CO_2 utilization [44,67,95–100]. The process was introduced by Fischer and Tropsch for the first time in 1928 [101,102]. However, the extensive investigation on the DRM started when increasing concerns about greenhouse effects were raised by the international scientific community in the 1990s [103].

DRM leads to synthesis gas production, a mixture of hydrogen and carbon monoxide that is appropriate for products including Fischer-Tropsch fuels (process on Fe-based catalysts) and dimethyl ether (DME) [104]. In comparison to conventional technologies, i.e., steam reforming and partial

oxidation of methane, the DRM is also suitable for remote natural gas or crude oil fields, where water supplies are limited [105]. Moreover, since natural gas deposits include large amounts of CO_2, its emission to the atmosphere can be avoided if carbon dioxide were used in DRM. This would lower the purification costs [106]. Due to the strong endothermicity of dry reforming of methane, the process can be environmentally valuable only if the required reaction heat comes from nuclear or renewable energy [96,102,103].

Similarly as TRM, the DRM reaction is accompanied by several side reactions, including previously mentioned direct methane decomposition (DMD) (Eq. 7), and Boudouard reaction (Eq. 8). Stoichiometric H_2/CO ratio of dry reforming of methane is 1.0, but it is often lower due to the reverse water-gas shift (RWGS) reaction (Eq. 12).

$$CO_2 + H_2 = CO + H_2O \qquad \Delta H^0 = 41 \text{ kJ/mol} \qquad \text{(Eq. 12)}$$

The main reaction of DRM (Eq. 1) is favored at high temperatures and low pressures, conditions which also favor DMD (Eq. 7). Minimum operating temperatures for DRM and DMD, calculated using the standard free energy, are 645 °C and 557 °C, respectively [103,107–109] (Fig. 1.8). The exothermic character of Boudouard reaction will decrease its role at temperatures higher than 701 °C, while the RWGS accompanies DRM reaction in a wide temperature range [107,109]. In the temperature range of 557-645 °C, where DRM reaction is not favored, both methane decomposition and Boudouard reaction contribute to carbon formation [110]. Therefore, high reaction temperatures (i.e., 700 °C and above) are more favorable [109].

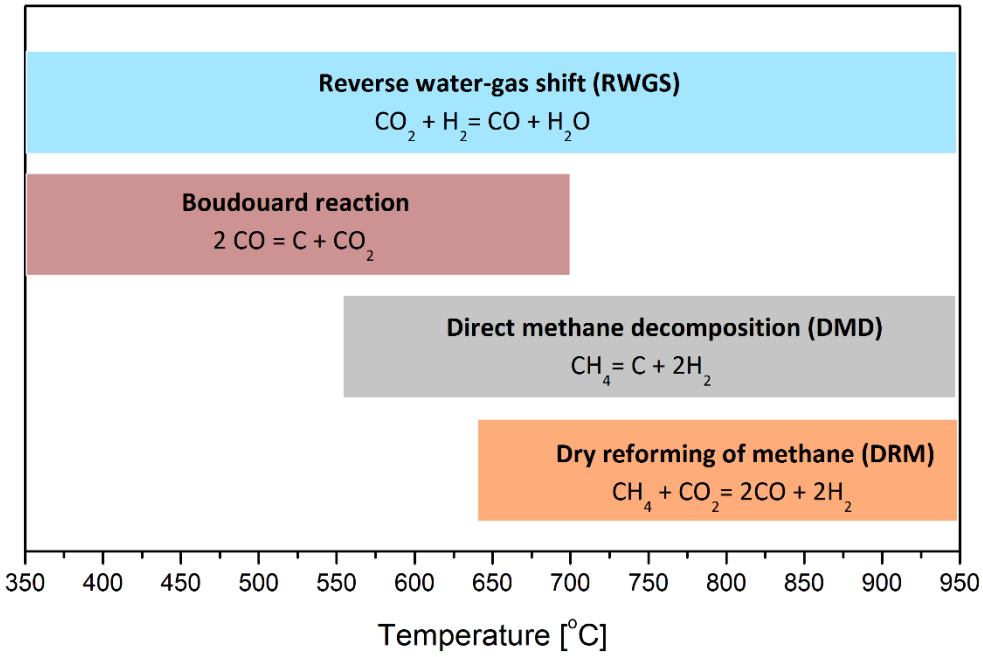

Fig. 1.8 Temperature ranges in which the main side reactions during DRM process are favorable.

Two types of classical heterogenous models are considered for dry reforming of methane, the Eley-Rideal (ER) and Langmuir-Hinshelwood (LH) mechanisms [111,112]. The former assumes that one reactant (CH_4 or CO_2) is associatively adsorbed on the catalyst surface, in an adsorption equilibrium. The adsorbed species of the reactant are subsequently reacting with the other reactant from the gas phase, leading directly to products. The LH mechanism assumes adsorption of both reactants. CH_4 decomposes to CH_x species and hydrogen, whereas CO_2 dissociates producing CO and adsorbed oxygen species. Oxygen species can react with CH_x species leading to H_2 and CO. The Langmuir-Hinshelwood mechanism was most often considered valid in the literature, e.g. for DRM reaction on Ni catalysts [113–115]. The comparison between these two models is presented in Fig. 1.9.

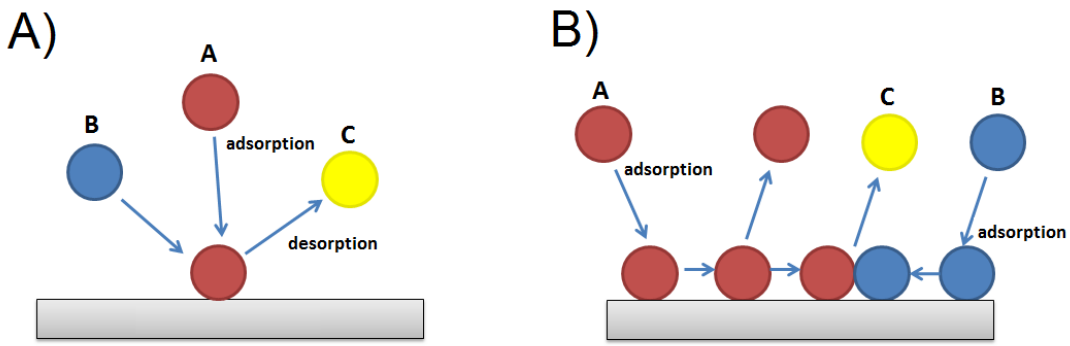

Fig. 1.9 Comparison of (A) Eley-Rideal mechanism and (B) Langmuir-Hinshelwood (adapted from [111]).

The elementary steps may be described as follows [102,116–118]:

Methane activation ("dehydrogenation"):

$$CH_{4\,(gas)} + 2* = CH_3* + H* \quad \text{(Eq. 13)}$$

$$CH_3* + * = CH_2* + H* \quad \text{(Eq. 14)}$$

$$CH_2* + * = CH* + H* \quad \text{(Eq. 15)}$$

$$CH* + * = C* + H* \quad \text{(Eq. 16)}$$

CO_2 activation:

$$CO_2 + * = CO_2* \quad \text{(Eq. 17)}$$

$$CO_2* + * = CO* + O* \quad \text{(Eq. 18)}$$

$$CO* = CO + * \quad \text{(Eq. 19)}$$

Surface reactions:

$$C* + O* = CO* + * \quad \text{(Eq. 20)}$$

$$CO* = CO + * \quad \text{(Eq. 21)}$$

$$H* + H* = H_2 + 2* \quad \text{(Eq. 22)}$$

Methane dehydrogenates step by step, which in the end leads to active carbon (*C) and hydrogen species (*H) adsorbed on metallic active site "*", i.e., Ni^0. CO_2 decomposes to CO and adsorbed oxygen

(O*). Subsequently, C* is oxidized to CO* with adsorbed *O. In the next step CO* desorbs as $CO_{(g)}$, and two H* species recombine to H_2. Hence, the active sites (*) are recovered [117].

The particular conditions needed for DRM are directly linked to its thermodynamic and kinetic barriers that hinder its practical industrial application. Depending on DRM application, the processes differ in operating parameters and feed composition (e.g. SPARG–Sulfur Passivated Reforming or CALCOR–CO through CO_2 Reforming processes) [96,102,119]. Their main goal is, however, to adjust syngas quality to the needs of its subsequent use, and not the valorization of CO_2 itself.

1.3.2.2. *Steam reforming of methane (SRM)*

Steam reforming of methane (Eq. 2) is a chemical process assuming conversion of a hydrocarbon rich feedstock to hydrogen and syngas (hydrogen, carbon monoxide and carbon dioxide). Syngas, as previously mentioned, is an important industrial raw material, and it is used to produce a wide variety of commercially significant products, such as hydrogen (via WGS reaction) for further synthesis, e.g. ammonia [120,121]. Steam reforming of methane produces synthesis gas with high H_2/CO molar ratio of ca. 3, that is higher than the one required for downstream methanol and hydrocarbon conversion processes. SRM was developed at the beginning of the 20th century to produce hydrogen [122]. The main reason for expanding production of hydrogen was connected to the discovery of the Haber-Bosch process, important for the ammonia synthesis. The process was further developed in the 1970's [123].

According to Rostrup-Nielsen [67], replacing carbon dioxide with steam in the reforming reaction has no drastic effect on the mechanism. In the steam reforming process CH_4 is dissociated on the surface of a catalyst, typically Ni-based, molecular hydrogen is formed, and the remaining carbon reacts with water to form additional molecular hydrogen and carbon monoxide [124]. The process takes place at high temperatures and, most economically, if the carbon-to-oxygen ratio in the feed gas is close to stoichiometric. Such conditions, however, lead to the graphitic carbon formation, which deactivates a used catalyst. The rate of carbon formation is known to be far lower on noble metals than on nickel-based catalysts, which is ascribed to a lower dissolution of carbon into these metals

[67]**.** Rostrup-Nielsen [119,125,126] reported a suppression of carbon deposition caused by sulfur poisoning in steam reforming of methane. This effect was explained by a partial blockage of a catalyst surface/sites. The process has been developed industrially by Haldor Topsøe AS, and known as the SPARG process [127].

Typically nickel-based catalysts are used for industrial steam reforming [128]. The catalysts are heated to temperatures of up to 900 °C to obtain a satisfying conversion of methane [128,129]. The demand for high throughput, low pressure drop and high pressures in synthesis loops dictates the 20–40 bar pressure in reforming units [129].

1.3.2.3. *Partial oxidation of methane (POM)*

In the 1940s, Prettre et al. [130] first reported the formation of synthesis gas by the catalytic partial oxidation of CH_4. In contrast to dry and steam reforming of methane, methane partial oxidation is mildly exothermic, leading to savings in energy use. On the other hand, the partial oxidation requires pure oxygen, which is produced in expensive air separation units that are responsible for up to 40% of the cost of a synthesis gas plant. It should be additionally taken into account that the two reagents (CH_4 and O_2) are explosive if the reaction is not conducted under appropriate conditions. Therefore, the catalytic partial oxidation of methane did not attract much interest for nearly half a century, and steam reforming of methane remained the main commercial process to manufacture synthesis gas [131–133]. The H_2/CO molar ratio of POM is close to 2, which is suitable for Fischer-Tropsch process (over cobalt-based catalysts) and methanol synthesis [104]. Moreover, the POM can be performed under very high gas hourly space velocities (GHSV) of 100,000-500,000 h^{-1} [134]. The application of POM in chemical technology up to date are gas-to-liquids (GTL) plants operated by the Royal Dutch Shell PLC [135].

There are two mechanisms of partial oxidation of methane discussed in literature, is: (i) total combustion and the following reforming reactions mechanism (CRR), or (ii) direct partial oxidation

(DPO). The former was suggested for the first time by Prettre et al. [130] and assumes the following steps:

1. The initial reaction of total oxidation of part of the methane consuming all oxygen in the gas feed, and
2. The reduction of water and carbon dioxide with residual methane, amounting to approximately three quarters of that originally taken, leading to the production of carbon monoxide and hydrogen.

The second pathway, direct partial oxidation mechanism (DPO), was discussed by Hickman and Schmidt [136–138]. It consists of the following steps:

1. Methane first dissociates to generate hydrogen and carbon,
2. Hydrogen desorbs and carbon is oxidized to carbon monoxide by surface oxygen species. H_2 and CO are the primary products in this mechanism.

1.3.2.4. *Autothermal steam reforming (ATR)*

To avoid the high energy demand for SRM, the concept of autothermal reforming (ATR) was developed. The autothermal steam reforming is a hybrid of steam reforming (Eq. 2) and partial oxidation of methane (Eq. 3) [128]. Autothermal reforming was introduced in the 1950s by the Danish catalyst company Haldor Topsøe AS [139]. Typically, the values of H_2/CO between 1 and 2 are obtained. The main drawback of ATR process is high cost of oxygen separation [128].

1.3.2.5. *Combined dry reforming and partial oxidation of methane (CRPOM)*

Ashcroft et al. [140], Choudhary et al. [141], and Ruckenstein and Hu [142] have studied the combined process of dry reforming and partial oxidation of methane, in contrast to the other researchers who concentrated on autothermal steam reforming.

The combined reactions of dry (CO_2) reforming (Eq. 1) and partial oxidation of methane (POM) (Eq. 3) have a number of advantages. Firstly, by coupling the exothermic partial oxidation reaction with the endothermic reforming reaction, the methane-to-syngas conversion can be operated in a safer manner than partial oxidation, and more energy-efficient manner than CO_2 reforming. Secondly, the H_2/CO ratio and the selectivity for various Fischer-Tropsch synthesis products can be tailored to the customers' needs. Thirdly, the addition of oxygen to the CRPOM process can reduce the carbon deposition on the catalytic surface and to increase the methane conversion, although this can also cause the reduction in the process selectivity. Finally, the raw material of this process is readily and easily available from those numerous natural gas reserves, which contain substantial amounts of CO_2 [143,144].

1.3.3. *Catalysts for tri-reforming of methane*

According to literature, a proper catalyst for tri-reforming catalyst must be thermally stable, have a high surface area, good redox properties, high oxygen storage capacity (OSC), provide resistance to coke formation, and be economically advantageous in order to be feasible as a renewable energy alternative [91,145,146].

Ni-based catalysts have shown good potential for reforming of methane and provide a more economical option than noble metals. However, the main drawback for their application is susceptibility to carbon formation leading to fast deactivation [96,147]. Since the addition of oxygen and steam limit the carbon formation, this drawback may be greatly limited. Deactivation is directly related to catalyst structure and composition (various promoters) and, therefore, research is aimed at producing a suitable catalyst.

The tri-reforming process requires an efficient catalyst which would be catalytically active in three processes separately. Djéga-Mariadassou [148] considers the process over Ni-based catalysts, as follows (* abbreviation for free radical):

1. CH_4 is chemisorbed dissociatively on reduced metallic Ni^0 (dry and steam reforming, partial oxidation of methane),
2. CO_2 is activated via dissociative chemisorption; the used catalyst requires basic properties (dry reforming),
3. H_2O activation proceeds with the formation of radical O and gaseous hydrogen (steam reforming),
4. surface reactions are: (i) carbon radical *C reacts with oxygen radical *O (or hydroxyl radical *OH) in order to form CO of syngas, and (ii) two hydrogen radicals form hydrogen gas (2 *H = H_2) via associative desorption (dry and steam reforming).

In case of partial oxidation of methane (POM), it has been shown by Djéga-Mariadassou [148] and Nishimoto et al. [149] that total CH_4 oxidation takes place on reduced metal: metal oxide MO (thanks to oxygen sites O□) interface, followed by dry reforming, and steam reforming (thanks to Ni^0). DRM proceeds satisfactorily either on precious metals (Pt, Rh, Ru, Ir) or metallic Ni, the latter preferred because it is much cheaper and more available [9]. SRM uses Ni-based catalysts. The summary of TRM reactions and the required properties of possible catalysts, together with catalytically active component are presented schematically in Fig. 1.10. The presence of H_2O and O_2 can positively influence the stability of the used catalyst, by the inhibition of catalytic coking, thus decreasing or avoiding deactivation problem common for dry reforming process, and improving lifetime of the catalyst [82,91,146].

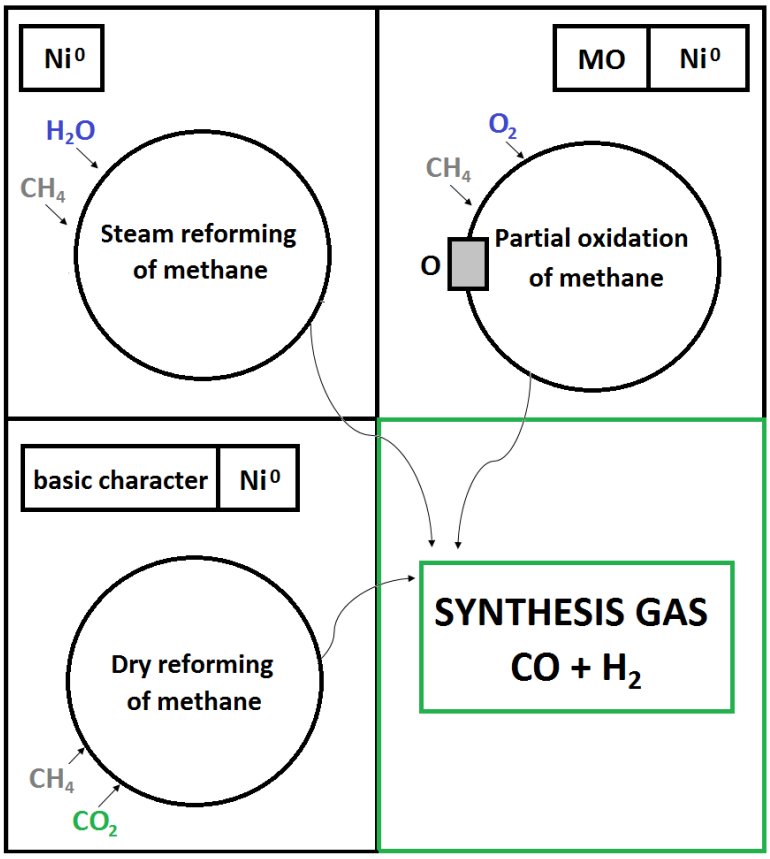

Fig. 1.10 Major components of tri-reforming of methane catalyst (based on: [148,149])

The stability problem observed for Ni-based catalysts may be, however, solved by the approaches proposed in literature. Dębek et al. [96] listed the most important of them, namely:

1. Employing an appropriate preparation method in order to control Ni crystal size and thus inhibit coke growth,
2. Using metal oxides with strong Lewis basicity as supports or promoters, since basic sites enhance CO_2 adsorption. Metal oxides can promote the oxidation of carbon deposits (i.e., via the reverse Boudouard reaction), but, on the other hand, the supports exhibiting Lewis acidity enhance formation of coke deposits,
3. Addition of a second metal, i.e., a noble metal, which may enhance the transport of hydrogen and/or oxygen between active sites and support by spillover, and can influence the mechanism

of coke formation. Addition of promoters, such as Ce, Zr or La, with the aim of modifying the selectivity of the DRM process and/or enhancing the gasification of the carbon deposits,

4. Sulphur passivation of Ni catalysts, which blocks the step edge sites where coke build-up is initiated,
5. Changing reaction conditions by the addition of oxidizing agents, such as water or oxygen, which can help oxidize carbonaceous deposits.

Some studies attempted to design a catalyst that would be active, stable and selective in TRM. The patented catalyst for tri-reforming of methane is a Ni-based impregnated zirconia support, with zirconia doped with yttrium and another metal (cerium) in order to distort the crystal lattice of zirconia [150]. The proposed yttrium content was 5-10 mol.% relative to zirconia. It was identified, that when the Y amount was less than 5 mol.%, the lattice of zirconia could not be deformed and the mobility of oxygen ion was not sufficient. If the amount was higher than 10 mol.%, the activity of catalyst in the tri-reforming reaction of methane was decreased due to too high deformation of zirconia lattice. It was also reported that zirconia could at high temperature undergo the transformation into a more stable fluorite structure, by adding 8 wt.% of yttria. Moreover, the addition of 8 mol.% yttria exhibited the highest ionic conductivity of oxygen [150].

There are only a few literature reports on catalysts investigated for TRM. Table 1.5 shows examples of such catalysts, where Ni was the active component based on various supports, with or without a promoter.

Table 1.5 Ni-based catalysts studied in tri-reforming of methane process.

Support	Ni loading [wt.%]	Promoter	Performance	Ref.
MgO, MgO/CeZrO, CeO_2, ZrO_2, CeZrO, Al_2O_3 (ICI)	6 ; Expect for Ni/MgO (8), Ni/ZrO_2 (3.8)	none	Mg improved CO_2 adsorption, NiO-MgO solid solution increased contact between Ni and Mg	Song et al. [83]
Ce-ZrO_2	3	none	Ce improved catalyst stability by increasing the mobility of oxygen ions on the surface	Lee et al. [151]
ZrO_2	4.8	none	Strong interaction between Ni-ZrO_2 resulted in high activity; the best results for 4.8% Ni-loaded catalyst at 800°C	Singha et al. [152]
ZrO_2	n.d.	MgO [2)]	Mg improved CO_2 adsorption resulted in high activity; and increase of thermal stability	Sun et al. [89]
ZrO_2	n.d.	CaO [2)]	Samples calcined at 700°C, and co-precipitated at pH of 10–12 gave the best catalytic results	Si et al. [88]
SiO_2 spheres	11.0	none	11% Ni/SiO_2 showed stable activity at 750 °C (4 hours) without deactivation. Presence of oxygen impacted positively coke formation and improved catalytic performance	Majewski et al. [85]
β-SiC	5.0	Mg [1)]	Adding Mg to the Ni/β-SiC (molar ratio Mg/Ni = 1/1) decreased coke formation, increased basicity, and improved Ni-Mg interaction. The sequence of Ni–Mg impregnation was important	García-Vargas et al. [86]
CeO_2	5.0 [4)]	La [3)]	Adding La (10 at.%) resulted in strong interactions between Ni–La; Ce provided surface oxygen vacancies	Pino et al. [87]

n.d. – no data

[1)] impregnation

[2)] co-precipitation,

[3)] combustion synthesis.

[4)] expressed in [at.%]

The first authors who tested different Ni supported catalysts for tri-reforming were Song et al. [83]. In this study, the decreasing activity was observed for different supports: Ni/MgO > Ni/MgO/CeZrO > Ni/CeO_2 ≈ Ni/ZrO_2 ≈ Ni/Al_2O_3(ICl) > Ni/CeZrO. The higher CO_2 conversion for Ni/MgO and Ni/MgO/CeZrO in tri-reforming was related to the interaction of CO_2 with MgO and more contact between Ni and MgO resulting from the formation of NiO/MgO solid solution. The applied feed composition of $CH_4/H_2O/CO_2/O_2$ = 1/0.56/0.48/0.1 gave the highest conversion results between 700 and 850 °C. The CH_4 conversion reached a maximum of 87% at 850 °C with a H_2/CO ratio of 1.67. Nevertheless, the most important drawback of these supports was their textural properties, i.e., the low surface area. Moreover, these supports had weak acid sites, high oxygen storage capacity and strong metal support interaction.

Lee et al. [151] examined Ni-based catalysts supported on cerium-zirconia oxides. The major role was ascribed to weak acidic sites, strong basic sites, and high redox ability of Ce-ZrO_2. The catalyst showed very good catalytic behavior, expressed by inhibition of the coke formation on the surface of catalyst, as well as on the reactor walls. The oxidant (steam or oxygen) positively influenced the inhibition of carbon deposition, while the addition of cerium increased the mobility of oxygen ions on the catalyst surface.

Singha et al. [152] examined Ni supported on ZrO_2 without any additional promoter. It was noted that the rising Ni loading resulted in increasing Ni particle size. 4.8 wt.% Ni was reported as optimal for the used reaction conditions. High metal dispersion and strong metal support interactions (due to Ni–ZrO_2 presence) were found to be the most important factors in achieving high activity and stability. The authors showed that the catalyst was stable for more than 100 h time on stream with high conversions of 95% at 800 °C. The H_2/CO ratio (1.9) was almost constant.

Similar observations were reported by Sun et al. [89]. The catalyst with Ni-Mg-ZrO_2 exhibited strong metal–support interactions. The addition of Mg improved the basic character of the catalyst, and, as a consequence, improved CO_2 chemisorption. High temperature also had a positive impact on the conversion of CH_4 and CO_2.

Other authors focused on the conditions of the preparation of catalysts, such as pH of co-precipitation and calcination temperature as factors which influence the catalytic performance. Si et al. [88] observed that under the certain preparation conditions (pH value of 10–12 and the following thermal treatment in the air at 700 °C) it was possible to obtain proper surface area, nano-sized Ni particles, and very good Ni–ZrO_2 interaction which resulted in the more than 70% conversion of CH_4 (measurement at 700 °C, 1 atm).

Majewski et al. [85] tested silica spheres which were covered by three–dimensional nickel. This resulted in a shell structure which allowed the catalyst to encapsulate, and prevented the migration of nanoparticles during the catalytic reactions. In the catalytic tests an increase in oxygen content resulted in coke reduction and CH_4 conversion improvement (to 90%). The catalyst containing 11% Ni showed stable activity at 750 °C (4 hours) without deactivation.

García-Vargas et al. [153] studied the influence of the impregnation order (of nickel and magnesium on silicon carbide SiC) on catalyst properties. Materials with Mg impregnated in the first step were more stable and showed good catalytic performance. When Ni impregnation was the first step, weaker interaction between Ni and Mg was observed which, according to the authors, could have explained the blockage of Ni particles by Mg, the reduction of the number of Ni active sites and inferior catalytic results. The Ni-Mg/SiC (1Ni:1Mg) catalyst was very active and stable in tri-reforming, with low coke formation. The highest conversion of 97.9%, reached at 800 °C, was stable during 25 h on stream.

Pino et al. [87] studied Ni–CeO_2 materials loaded additionally with lanthanum (10 at.%). These catalysts showed strong interactions between Ni and La, and better Ni dispersion. Due to lanthanum loading, the CH_4 conversion increased from 93% to 96%, as well as CO_2 conversion from 83% to 86.5%.

1.3.3.1. *Dry reforming of methane (DRM)*

Similarly as TRM, the dry reforming of methane shows very good properties on Ni as the active material. The latest DRM studies are mainly focused on stability increase because of the coke formation problem. In recent years, reviews were published by Pakhare and Spivey [114], Kawi et al.

[147], Dębek et al. [96], Taniewski et al. [57], Seo et al. [154] and Aramouni et al. [155]. The studied DRM catalysts were mainly Ni, supported on Al_2O_3 [156,157], MgO [158–161], CeO_2 [157,162–164], ZrO_2 [157,161,164], SiO_2 [165–167], ordered mesoporous silica SBA-15 [168–171] and KIT-6 [172], La_2O_3 [157,173], TiO_2 [174,175], mixed oxides (MgO–Al_2O_3 [176–178], CeO_2–ZrO_2 [164], CeO_2–Al_2O_3 [179]), zeolites (zeolite Y, zeolite A, zeolite X, ZSM-5, clinoptolite) [180–183], clays (diatomite [184], vermiculite [185], montmorillonite [186], hydrotalcites [187–192], natural Tunisian clays [193–195]), and carbon-based materials (activated carbon [196]). Below, some selected examples of literature studies are discussed in more detail.

Alumina shows excellent textural properties. Under appropriate conditions Ni/Al_2O_3 catalyst can form a spinel phase ($NiAl_2O_4$), which can considerably hinder carbon formation. On the other hand, such phase was reported by Becerra et al. [156], as leading to low catalytic activity, especially at relatively low temperatures.

MgO is a support with high Lewis basicity. Therefore, Ni/MgO catalysts have high CO_2 sorption capacity. However, the activation of side reactions, such as reverse water-gas shift is very likely on this kind of materials [158–160]. Ni/MgO-Al_2O_3 catalysts also showed good catalytic behavior. Modification with 20 wt.% of nickel led to increased catalytic activity, although enhanced formation of carbon deposit was reported [177]. The possible reason of the latter could be inferior Ni dispersion, originating from modifying the support with high contents of Ni.

$MgAl_2O_4$ spinel was also considered as a support. Alvar and Rezaei [178] examined this mesoporous material modified with nickel, in dry reforming of methane. The catalyst showed high specific surface area and nanocrystalline structure, which benefited catalytic activity, as well as stability of DRM catalysts (no deactivation after 50 h).

CeO_2 is known to have high oxygen storage capacity. Its use as support for nickel DRM catalysts led to improved stability through the participation of labile oxygen in the oxidation of carbon deposits [162]. Asami et al. [163] reported almost negligible deactivation of a Ni/CeO_2 catalyst during DRM at 850 °C. At lower reaction temperatures, i.e., 700 °C, a decrease in stability was, however, registered.

Cerium can be also used as a promoter in DRM process. As studied by Dębek et al. [188] the addition of this metal to Ni-based Mg/Al-mixed oxides derived from hydrotalcites resulted in better activity compared to non-promoted material. According to the authors, cerium contributed to the enhanced reduction of nickel species. The authors also tested Zr-promoted hydrotalcite catalysts [188]. The addition of zirconium significantly improved stability in the DRM test at 550 °C. The improvement originated from the inhibition of direct methane decomposition. However, the modification with both Ce and Zr resulted in better stability, though, in the same time, decreased catalytic activity. This was ascribed to higher amount of strong basic sites [197].

Zirconium oxides were also studied as carriers for DRM because of their appropriate basicity and weak acid properties. As reported by Rezaei et al. [198], zirconia supports promoted with K_2O showed improved catalytic activity and stability, which was due to enhanced basicity in the materials.

Natural clays may also find application as supports of DRM catalysts. Liu et al. [193] examined the influence of ceria or zirconia promotion of Cu- or Fe-pillared clays. Such modification increased the number of medium and weak basic sites, together with increasing Ni^0 crystalline size, which resulted in increased catalytic activity during DRM test, but also a presence of carbon forming reactions.

Mesoporous silica was also considered an attractive carrier due to its high specific surface area, porosity in the mesopore region and good thermal stability [165]. Huang et al. [165] studied SiO_2 supports loaded with Ni. The use of SiO_2 allowed to obtain very high dispersion of the Ni phase and controlled crystallite sizes, leading to improved catalytic performance. Lovell et al. [167] studied SiO_2 supports, which were prepared through flame spray pyrolysis and subsequently loaded with nickel. The best catalytic performance in DRM was registered for the catalysts with the highest specific surface area and the smallest Ni crystallite size of the series.

Recently, considerable attention was also been paid to the ordered mesoporous silica SBA-15. Gálvez et al. [168] studied Ni/SBA-15 catalysts, which were synthesized by three different ways (impregnation, co-precipitation and co-precipitation with ascorbic acid). The pre-reduction of the Ni-phase using ascorbic acid resulted in a very accurate control of Ni-crystallite size, leading to Ni particles

placed inside the mesopores of the SBA-15 structure, resulting in enhanced activity, selectivity and stability.

Promotion with a second metal can also positively influence catalytic behavior of DRM catalyst. Several different promoters were tested: (i) noble metals – Pt, Pd, Rh, Ru and Ir (ii) alkali, or alkaline earth metals – K, Li, Mg, Ca, Ba, (iii) rare earth metals – Ce, Zr, La, Y and (iv) other metals – Au, Ag, Sn, Bi, As, Pb, Cu.

Table 1.6 presents some examples of metals used as promoters.

Table 1.6 Ni-supported catalysts promoted with different metals studied in dry reforming of methane.

Support	Ni (loading [wt.%])	Promoter (loading [wt.%])	Effect of promoter addition	Ref.
Al_2O_3	6.0	Pt (1.0)	Improved activity and selectivity; inhibited formation carbon whisker-like deposits	Gould et al. [199]
CeO_2-ZrO_2	4.5	Rh (0.5)	Increased activity and stability	Koubaissy et al. [200]
MgAlO hydrotalcite	10.0	Rh (1.0)	Increased dispersion of active sites, increased Ni reducibility	Lucrédio et al. [201]
MgO-ZrO_2	3.0	Co (3.0)	High conversion and resistance to coke formation	Fan et al. [113]
SBA-15	4.0	Co (1.0)	Increased activity and stability, significant inhibition of carbon formation	Erdogan et al. [202]
MgAlO hydrotalcite	17.3	Zr (2.5)	Enhanced stability due to inhibition of direct methane decomposition, decreased activity	Dębek et al. [188,203,204]
MgAlO hydrotalcite	17.9	Ce (3.7)	Good activity, selectivity and stability, gasification of carbon deposits	Dębek et al. [188,204,205]
MgAlO hydrotalcite	12.0	Ce (2.84)	High activity and enhanced stability due to the surface oxygen taking part in oxidation of formed carbon deposits	Niu et al. [206]
MgAlO hydrotalcite	15.0	La (4.0)	Increased stability due to gasification in situ of amorphous carbon deposits	Liu et al. [207]
α-Al_2O_3	4.3	Y (1.5)	Increased catalytic activity and stability, small degree of graphitic carbon	B. Li et al. [208]

SBA-15	9.0	Y (9.0)	Increased activity and superior stability due to low carbon formation	J.F. Li et al. [209]

Gould et al. [162] studied Pt promoted Ni/alumina catalysts. No formation of whiskers-type of carbon deposits was observed for the Pt-Ni catalyst which was synthesized by atomic layer deposition method. The improved catalytic behavior of this bimetallic catalyst was ascribed to the fact that Ni-Pt surfaces formed Ni-terminated surfaces which were associated with higher DRM rates than Pt-terminated surfaces. The presence of Pt on the edges of Ni crystallites inhibited carbon diffusion and thus resulted in higher resistance towards coking.

Koubaissy et al. [159] reported that Rh addition to Ni/CeO_2-ZrO_2 catalyst enhanced its stability and activity. However, carbon deposits were still present on the catalyst surface after DRM test. Thermogravimetric experiments revealed that the addition of Rh had influenced the type of formed carbon deposits. Amorphous carbon was detected, which did not decrease conversions of CH_4 and CO_2.

Lucrédio et al. [201] related that Ni dispersion increased by Rh addition when Mg(Al)O hydrotalcite-derived material was the support, while Rh led to the aggregation of Ni supported on γ-Al_2O_3. When γ-Al_2O_3 was used as a carrier the addition of Rh did not increase catalyst stability.

The influence of Co, Ca, Ba, K, La, Mn or Ce promotion on Ni/MgO-ZrO_2 catalyst was studied by Fan et al. [166]. The activity of the prepared materials tested in DRM at 750 °C decreased in the sequence: Ni-Co > Ni-La ≈ Ni-Ce > Ni-Ba > Ni-Mn > Ni-K > Ni-Ca. The best catalytic performance of Ni-Co catalyst was attributed to the Ni-Co solid solution which led to the reduced carbon formation and improved both CH_4 and CO_2 conversions. Ni-La and Ni-Ce catalysts showed similar performance. The activity of Ni-Ba and Ni-Mn catalyst decreased within 40 h on stream. On the other hand, a moderately stable performance was shown by Ni-K and Ni-Ca catalysts. The activity sequence followed that of metal dispersion. Carbon deposits were detected in all studied catalysts after 40 h catalytic tests, with the highest amount of C registered for Ni-Mn catalyst.

Erdogan et al. [202] examined the effect of nickel and cobalt addition to SBA-15 support. The co-impregnation of Ni (4 wt.%) and Co (1 wt.%) on SBA-15 resulted in the formation of Ni-Co alloy that hindered the agglomeration of nickel particles, resulting in the suppressed carbon deposit formation. High CH_4 and CO_2 conversions were obtained.

Dębek et al. [188,203,204] examined the promotion of Zr in Ni/Mg/Al hydrotalcites-derived catalysts. Zirconia was found to strongly influence both activity and selectivity. Zr considerably inhibited the direct methane decomposition reaction, favoring the interaction of methane with CO_2 (DRM reaction). The catalytic activity was, however, lower than the one reported for unmodified catalyst (Ni/Mg/Al hydrotalcite).

Dębek et al. [188,204,205] found that the addition of Ce, by ion-exchange with $[Ce(EDTA)]^-$ complexes, to Ni-containing hydrotalcite-derived catalysts enhanced reducibility of nickel species and resulted in the formation of new strong basic sites, which improved catalytic stability in the 5-hour catalytic test). The increased basicity led to the higher CO_2 adsorption capacity. Additionally, ceria led to the gasification of carbon deposits by the reverse Boudouard reaction [38].

Niu et al. [206] examined CeO_2, ZrO_2 or ZnO modified Ni/Mg/Al hydrotalcites. All metals were introduced by incipient wetness impregnation. The best results were observed for CeO_2-Ni. The improved performance was linked with a higher concentration of surface oxygen which allowed to oxidize the carbon deposits, thus prolonging the lifetime of the material. The activity, however, was lower than that of the unpromoted catalyst.

La-promoted Ni-containing hydrotalcite-derived catalysts were studied by Liu et al. [207]. Lanthanum contributed to the gasification of amorphous carbon deposits, through the formation of oxycarbonate species, thus resulting in overall lower carbon formation during 5-hour isothermal experiments performed at 550 °C. Unfortunately, the presence of La resulted also in the promotion of undesirable side reactions, such as direct methane decomposition.

B. Li et al. [208] tested Ni-Y modified Al_2O_3 catalysts prepared by different methods. The catalyst prepared via sequential-impregnation had better stability than the one prepared by co-impregnation.

The better performance of Ni/Y-Al_2O_3 catalyst (first impregnated with Y nitrate, then with Ni nitrate) was linked to smaller metallic nickel particles and more basic sites. Low degree of graphitization and the lower amount of carbon deposit was registered for this catalyst. On the contrary, in case of Co/Al_2O_3 catalyst, Y_2O_3 addition negatively affected DRM catalytic performance, as it led to inadequate reduction, as well as metal sintering in reduced and spent catalysts.

J.F. Li et al. [209] also reported a positive effect of Y-promotion in case of Ni (9 wt.%)/SBA-15 catalysts. 6, 3 and 9 wt.% yttrium containing materials were prepared. The 9%Y-Ni/SBA-15 catalyst showed superior stability and low carbon deposition during 50 h on stream, as well as the highest catalytic activity of the studied series.

1.3.3.2. *Steam reforming of methane (SRM)*

Steam reforming of methane is a well-known process on large industrial scale. This process is focused on hydrogen production, and usually operates in the 750-1450 °C and 5 to 25 atm in the presence of nickel catalyst supported on alumina (Ni/Al_2O_3) [210].

According to Sehested [211], nickel-based catalysts for steam reforming of methane are facing four main challenges: (i) activity, (ii) sulfur poisoning, (iii) carbon formation, and (iv) sintering. Firstly, Ni catalyst for SRM must be catalytically active. Secondly, catalyst should be tolerant to sulfur containing feeds poison, as exposed to sulfur the catalysts creating H_2S compounds blocking active sites on the nickel surface. Next, the material should be resistant to coke formation, as the latter leads to blocking of active sites, increased pressure drops, and decreased heat transfer. Finally, sintering resistant material should be used, as high temperatures causes growth and aggregation of nickel particles, which lowers activity.

The endothermic nature of steam reforming of methane results in poor conversion at low temperatures. However, in the literature may be found one example described by Nieva et al. [212], where good catalytic performance was reported at relatively low temperatures between 500 and 600 °C. The authors used Ni/Zn/Al catalyst, which showed high conversions and only low formation of amorphous carbon. This improved behavior was ascribed to a better interaction of small metal nickel

particles with the non-stoichiometric zinc aluminate-like phase formed during thermal treatments of the catalyst precursor than for conventional catalysts studied in this temperature range.

Numerous Ni/Al-based catalysts were examined in SRM process, in combination with other metals. Hufschmidt et al. [213] studied Ni/La/Al catalysts using Ni/La perovskite. Near full conversion of methane at 850 °C was registered using a steam to carbon ratio (S/C) of 1.24, with very low carbon deposition, proving very good long-term stability.

Ni/Al promoted by molybdenum was found to have better stability than pure Ni/Al catalysts [214]. For a catalyst with Ni/Al molar ratio of 3 with 0.05% Mo and a steam to carbon ratio of 4, stable conversion of ca. 85% was obtained. With increased Mo loading a decrease in specific surface area was found leading to a decrease in conversion. For S/C ratio of 2, rapid deactivation occurred during the first three hours, followed by the stabilization at ca. 60% conversion.

Xu et al. [215] tested 15 wt.% Ni/γ-Al_2O_3 promoted with 0.5 and 1.0 wt.% boron. The latter content was found to increase the initial methane conversion and decreased deactivation of Ni/Al catalysts by decreasing coke formation. The addition of boron 1.0 wt.% also reduced the first order deactivation rate coefficient by a factor of 3, and the activity loss after 10 h from 70 to 30% (GHSV=660,000 $cm^3/(h \cdot g_{cat})$.

Takeguchi et al. [216] compared the performance of Ni-based hydrotalcite catalyst (Ni-HT) with commercial Ni/Al_2O_3. The former showed high activity and a higher resistance to coke formation than the latter. The selectivity of coke formation on this catalyst was as low as 0.2% at a steam to carbon (S/C) ratio of 0.45.

1.3.3.3. *Partial oxidation of methane (POM)*

It was shown that Ni-based catalysts were also efficient in partial oxidation of methane, although the optimal support is still searched. The following oxides, or mixed oxides, were investigated as carriers [90]: Al_2O_3 [134,217–222], $MgAl_2O_4$ [223], MgO [224], SiO_2 [225], CeO_2 [132,226], ZrO_2 [226], CeO_2–ZrO_2

[226,227], perovskite [117,228], phosphate [229],TiO_2 [230], hydrotalcites [231–235], SiC [236], Y_2O_3 [237–239], ZSM-5 zeolite [240] BEA zeolite [241], and more.

In the literature on POM, different promoters of Ni-based catalysts were considered: (i) noble metals – Pt, Pd, Ru, Rh, Ir, (ii) alkali, earth alkali metals – Na, K, B, Ca, Mg, Li, and (iii) rare earth metals – Ce, Zr, La, Y, Sm. Table 1.7 presents selected examples of promoters used for Ni catalysts supported on different carriers studied in partial oxidation of methane.

Table 1.7 Ni-supported catalysts promoted with different metals in partial oxidation of methane process.

Support	Ni (loading [wt.%])	Promoter (loading [wt.%])	Effect of promoter addition	Ref.
Al_2O_3	18.7	Pt Pd (0.1, 0.5, 2.5)	Decrease of ignition temperature, improvement in selectivity	Choudhary et al. [242]
Al_2O_3	7.56	Yb (Ni/Yb/Al=1:1:10)[1)]	Improved methane conversion and minimizing carbon deposition	Ding et al. [218]
γ-Al_2O_3	10.0	Li (1.25) La (n.d.)	Improved stability – suppression of carbon and inhibition of sintering	Liu et al. [243]
MgAlO hydrotalcite	18.06	La (6.5)[2)]	Inhibition of nickel sintering and carbon formation	Zhang et al. [234]
MgAlO hydrotalcite	6.0	Rh (0.1)[3)]	Enhanced the resistance to carbon deposition	Basile et al. [235]

n.d. – no data
1) as atomic ratio
2) expressed in [mol.%]
3) expressed in [at.%]

Choudhary et al. [242] illustrated the beneficial effect of noble metal promotion on the ignition temperature over Ni/Al_2O_3. Promoting with 0.1 wt.% noble metal reduced the ignition temperature from 790 to 605 °C with Pt, and to 520 °C with Pd. At 0.5 wt.% noble metal loading the ignition temperature decreased further to 530 °C with Pt and 460 °C with Pd promotion. With 2.5 wt.% Pt, Pd or Ru promotion the ignition temperature was about the same as for the Ni-free catalyst containing noble metal with the same loading.

Ding et al. [218] examined ytterbium addition to Ni/Al_2O_3 catalysts in POM reaction. It reduced effectively the Lewis acidity of Al_2O_3 and improved resistance towards coking. It also improved the interaction of Ni with the support, thus preventing the growth of Ni nanoparticles, and minimizing coke formation. The 1Ni1Yb10Al catalyst proved to be the most active, with CH_4 conversion of 98%, CO selectivity of 98% and H_2 selectivity of 83% (800 °C, space velocity of 50,000 mL/g·h). Yb contributed also to the methane combustion and adsorption of CO_2, improving methane conversion and minimizing the carbon deposition.

Liu et al. [243] reported that when Li and La were added to alumina-supported Ni, they improved the stability of the support and suppressed sintering and loss of Ni, as well as they enhanced the resistance to carbon deposition. $LiLaNiO/\gamma\text{-}Al_2O_3$ catalyst not only possessed excellent reaction performance (CH_4 conversion ca. 95%, CO selectivity ca. 98%), but also had comparatively stable pore structure and stable crystalline phase during a 500 h-test at at 850 °C, with natural gas/O_2 ratio of 1.90 and space velocity of 270,000 L/(kg·h).

Zhang et al. [234] studied La/Ni/Mg/Al-hydrotalcites in POM. The addition of 6.5 mol.% La^{3+} gave rise to the strong basicity and small Ni particle sizes. This catalyst showed the highest catalytic performance (CH_4 conversion of 99%, CO selectivity of 93% and H_2 selectivity of 96%), which was mainly attributed to inhibition of both carbon deposition and nickel sintering. Almost no deactivation was observed even after 86 h-test at 780 °C.

Basile et al. [34] studied Ni, Rh and Ni–Rh catalysts derived from Mg–Al hydrotalcite precursors. A synergistic effect of promoting Ni with Rh was reported in partial oxidation of methane. Adding 0.1 at.% Rh to 6.0 at.% Ni was shown to maintain Ni in a reduced state, even when the conversion of oxygen was not complete. The presence of Rh also enhanced the resistance to carbon deposition.

1.3.4. *Double layered-hydroxides as potential catalysts for tri-reforming of methane*

Double-layered hydroxides (DLHs), also known as hydrotalcites (HTs), are natural layered minerals and can be described by the following formula $[M^{II}_{1-x}M^{III}_{x}(OH)_2]^{x+}(A^{n-})_{x/n}\cdot mH_2O$, where M^{II} and M^{III} are

divalent and trivalent cations of metals, respectively, A^{n-} is an n-valent anion and m is the number of molecular water [96,244,245]. In this structure, the Mg^{2+} cations are partially substituted by Al^{3+} cations resulting in a positive charge. A^{n-} represents an inorganic or organic anions and x is the molar ratio of cations usually between $0.20 \leq x \leq 0.33$. The counter-anions A^{n-} are intercalated in the interlayer space, together with molecular water, to compensate the charge introduced by the cations. (Fig. 1.11). Typically, M^{II}/M^{III} ratios in double-layered hydroxides vary from 2.0-3.0 [244,246].

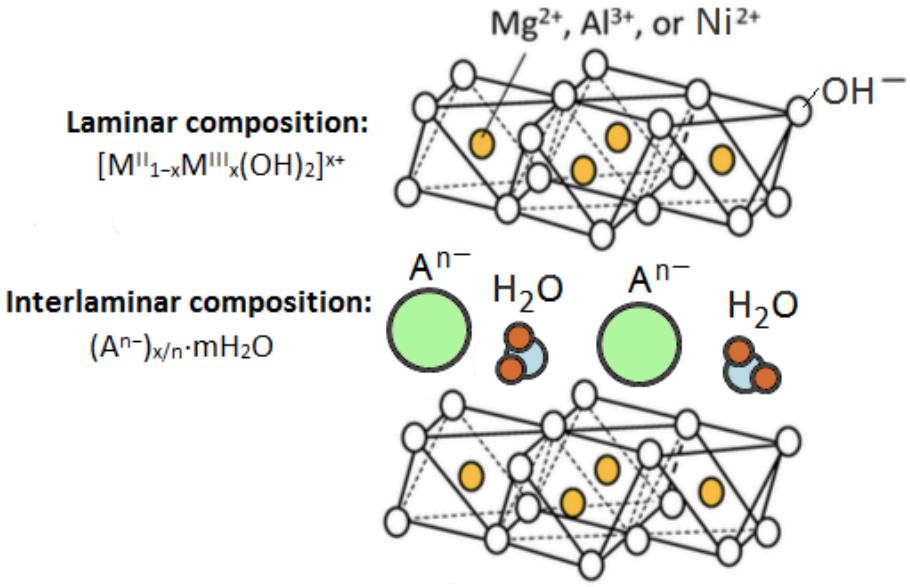

Fig. 1.11 Schematic representation of the double-layer hydroxide/hydrotalcite structure.

From a crystallographic point of view, the ordering of hydroxide layers is similar to that of brucite $Mg(OH)_2$, where each Mg^{2+} cation is octahedrally surrounded by six OH^- anions and the different octahedra $[Mg(OH)_6]^{4-}$ (Fig. 1.11) [245]. As with brucite, octahedral units are linked by edges. It results in hydroxide layers with a net positive charge, which has to be neutralized by interlayer anionic species. Depending on the arrangement of the layers, the hydrotalcite structure may have rhombohedral or hexagonal symmetry, in which the unit cell is built up of three and two hydrotalcite layers, respectively. For both naturally occurring and synthetic hydrotalcite materials, the rhombohedral symmetry is generally more common.

1.3.4.1. *Properties, synthesis and application*

In double-layered hydroxides some of the Mg^{2+}, as well as Al^{3+} ions, can be replaced, respectively, by other divalent (e.g. Ni, Cu, Co, Zn) and/or trivalent (Fe, Co, Ce, Cr, Y) cations. Moreover, it is possible to produce hydrotalcites containing large variety of different interlayer anions (e.g. CO_3^{2-}, NO_2^{3-}, SO_4^{2-}, Cl^-, ClO_4^-, WO_4^{2-}, CrO_4^{2-})[247–250].

The structure and catalytic properties after calcination depend on the chemical composition of the LDH precursor, as well as temperature and atmosphere of calcination.

The heating of freshly synthesized DLHs results in structural changes. The materials may undergo four phase transformations: (i) from room temperature to ca. 200 °C, (ii) at 200 °C, (iii) from ca. 300 to ca. 600 °C and (iv) over 600 °C [251]. The layered structure of HTs can turn to almost amorphous at around 200 °C and only the structural water is lost, followed by the formation of mixed (nano-)oxides of the periclase-like structure at 300-600 °C. The spinel structure is formed at the temperature over 900 °C. As mentioned above, hydrotalcites lose their layered structure which results in the formation of amorphous nano-oxides. This process is reversible, and DLHs are characterized by the so-called *memory effect*, if the applied heating temperature does not exceed 550-600 °C [252]. It was reported that the thermal treatment, in the range of 450-500 °C, results in a modest increase in specific surface area reaching about 120 to 200 m^2/g (N_2 sorption) and the pore volume increasing to about 0.6 to 1.05 cm^3/g (Hg intrusion). At this temperature region a change in the XRD pattern from that of hydrotalcite to a poorly crystalline magnesium oxide (brucite-like) happens [252]. So calcined materials exhibit also thermal stability, good homogeneity and high dispersion of metals [1].

Synthesis of hydrotalcite is simple and inexpensive to carry out in the laboratory. Seven main methods of DLHs preparation were proposed in literature: co-precipitation, urea method, sol-gel method, salt-oxide method (induced hydrolysis), reconstruction, anionic exchange and hydrothermal treatment [64,244]. Co-precipitation is the method most often used. It gives compositions optimal for hydrotalcite like-compounds. It is carried out by the addition of a mixture of di- and tri-valent cations to a base. The synthesis may be performed at variable or constant pH. The latter is recommended

when hydrotalcite-like material with high chemical homogeneity is required [64]. The co-precipitation method was shown to result in double-layered hydroxides-like materials with high specific surface area, high average pore diameter, high crystallinity, and small particle sizes, making these materials suitable for industrial applications. The co-precipitation method is especially appropriate for non-noble metal-based catalysts.

Double-layered hydroxides are used as adsorbents (water treatment), in medicines (stabilizer), as an additive to polyvinyl chloride polymers (PCV), as molecular sieves, ion exchangers, flame retardants, etc. [96,244]. Moreover, hydrotalcite-based metal oxides are potentially useful as catalysts or catalyst precursors due to their unique properties. The following description is focused on applications of DLHs in catalysis.

The mixed oxides derived from DLHs were studied in various base catalyzed and redox reactions, such as DeNOx with ammonia [253,254], DeSOx process [255], decomposition of N_2O [256], CO_2 hydrogenation [257–260], methanol incineration [261], Fischer-Tropsch synthesis [262,263], isomerization of glucose [264,265], epoxidation [266], esterification of aldehydes [267], cyanoethylation [246,268], aminohydroxylation [269], aldol condensation [270], and most importantly, in reforming reactions. The next section is devoted to the description of these materials in dry reforming, steam reforming and oxidative reforming processes.

1.3.4.2. *Double layered-hydroxides in methane reforming processes*

Hydrotalcites (double-layered hydroxides DLHs) were found to be especially interesting for methane reforming processes as it was already described in the previous section of this thesis. These materials contain Mg and Al and the desired metal cation/s in their structure, thus fulfilling the requirements for appropriate redox and basic properties.

Ni-based HTs are the main focus of this chapter, although noble metals and cobalt are also active in reforming processes [271–275]. Nickel may be incorporated into DLHs by different methods, i.e. by co-precipitation, ion exchange or simply by impregnation, as illustrated examples in Table 1.8 [96].

Table 1.8 Examples of Ni-supported double-layered hydroxides with Ni introduced by the different methods in catalysts for methane reforming processes (adopted from [96]).

Ni (loading [wt.%])	Method of hydrotalcite synthesis	Calcination conditions	DRM test conditions			Catalytic performance			Ref.
			GHSV [h^{-1}]	Temp [°C]	TOS [h]	CH_4 [%]	CO_2 [%]	H_2/CO [mol/mol]	
Dry reforming of methane									
63	Co-precipitation at constant pH	550 °C, 4 h, air	20,000	550	1	48	57	2.7	Dębek et al. [276]
0.8	Adsorption of $[Ni(EDTA)]^{2-}$	550 °C, 4 h, air	20,000	550	1	25	38	1.6	Dębek et al. [277]
n.d.	Co-precipitation with $[Ni(EDTA)]^{2-}$	500 °C, 16 h, air	n.d.	800	150	98	95	1.0	Tsyganok et al. [190]
10	Co-precipitation at constant pH	900 °C, 5 h, air	50,000	750	10	85	93	0.98	Guo et al. [278]
25.1	Co-precipitation at constant pH	650 °C, 14 h, air	54,000	800	6	94	n.d.	n.d.	Shishido et al.[279]
25.1	Impregnation of Ni^{2+} on MgAl HT	850 °C, 14 h, air	54,000	800	6	92	n.d.	n.d.	Shishido et al. [279]
15	Sol-gel method	750 °C, 5 h, air	36,000	800	40	84	89	n.d.	Min et al. [280]
Steam reforming of methane									
16.3	Co-precipitation at constant pH	850 °C, 5 h, air	2,500	800	600	90	n.d	n.d.	Takehira et al. [281]
Combined steam and dry reforming									
75	Co-precipitation at constant pH	500 °C, 15 h, air	14,000	850	2	65.1	60	1.1	Bhattacharyya et al. [187]
Partial oxidation of methane									
10 [1)]	Co-precipitation at constant pH	900 °C, 16 h, air	n.d.	750	8	n.d.	-	35%2)	Basile et al. [282]
25.1	Co-precipitation at constant pH	650 °C, 14 h and 580 °C, 5 h	1.0500[3)]	800	6	94	-	n.d.	Shishido et al. [231]

n.d.- no data

[1)] atomic ratio percentage,

[2)] selectivity of both H_2 and CO,

[3)] expressed in [ml/(h· g)]

Dębek et al. [276,277] examined the influence of the method of nickel introduction into hydrotalcite-based materials. The authors also compared the catalytic behavior of Ni-Al-co-precipitated mixed oxides with the ones containing Mg and Al onto which Ni was introduced via the adsorption of $[Ni(EDTA)]^{2-}$ complexes. Both types of prepared materials were active in DRM at 550 °C. However, the nickel introduction via $[Ni(EDTA)]^{2-}$ chelates resulted in the higher activity per gram of active material, as compared to the catalysts into which nickel was introduced into the brucite-like layers by co-precipitation method.

Tsyganok et al. [190] studied the Ni introduction into HTs by co-precipitation with a solution of $[Ni(EDTA)]^{2-}$ chelates. The nickel-EDTA species were present in the interlayer spaces of the HT structure. The reduction pre-treatment was not required, but the stabilization of the catalytic systems needed from 30 to 90 min induction time. The tested material showed stable conversions in DRM tests at 800 °C during 150 h. Various types of carbonaceous deposits were detected on the surface of the spent catalysts, indicating the presence of carbon-forming reactions. The carbon formation did not, however, affect the catalytic activity.

A conventional co-precipitation method with Ni was applied in the study of Guo et al. [278]. The authors prepared nickel supported on $MgAl_2O_4$ spinels, the latter obtained from Mg/Al hydrotalcite precursors upon calcination at 800 °C. Catalytic activity of such materials was compared to similarly prepared Ni/γ-Al_2O_3 and Ni/MgO-Al_2O_3 catalysts. Using the $MgAl_2O_4$ spinel resulted in a highly active catalytic system with excellent stability under reaction conditions. Highly dispersed Ni species and low acidity of $MgAl_2O_4$, as compared to Al_2O_3, as well as strong interactions between Ni and $MgAl_2O_4$ were found responsible for high activity and stability of such catalysts.

Shishido et al. [279] compared the co-precipitated Ni/Mg/Al hydrotalcite-derived catalyst with those obtained by impregnation of Ni onto $MgAl_2O_4$, Mg/Al hydrotalcite-derived, and two other conventional Ni/MgO and Ni/Al_2O_3 materials. The first mentioned exhibited the highest activity at 800 °C, which was ascribed to the highly dispersed and stable nickel species on the catalyst surface.

Min et al. [280] compared the catalytic behavior of two Ni-containing catalysts, one prepared by a sol-gel, and the second by a co-precipitation method. Both catalysts showed high conversions of CH_4 and CO_2 and were stable for 40 h on stream. The catalysts did not differ in catalytic activity; however, the characterization of spent materials proved that Ni crystallites had larger size (metal clusters) in the co-precipitated catalyst than the one prepared via the sol-gel method. The bigger crystal size points a higher deactivation degree due to sintering. As a consequence, lower resistance to coke formation was registered for the co-precipitated catalyst.

Takehira et al. [281] tested Ni-containing hydrotalcites in the steam reforming of CH_4. No decrease in the catalytic activity was observed for 600 h of reaction time, even under a low steam to carbon ratio of 1.6. The CH_4 conversion and the distribution of products followed thermodynamic equilibrium during the reaction. The obtained results were compared to a commercial Ni/α-Al_2O_3 catalyst, which showed a clear decline in the activity. The Ni dispersion was enhanced after the co-preparation method, resulting in the recorded high activity for this catalyst when Ni/Mg was larger than 0.2, and the most suitable ratio of Mg/Al was 1/3.

Bhattacharyya et al. [187] reported on hydrotalcite-derived Ni/Al and Ni/Mg/Al mixed oxides as catalysts for combined steam/dry reforming. The authors compared their catalytic behavior to that of commercial Ni/Al_2O_3 or Ni/$MgAl_2O_4$ catalysts at 815 °C and 300 psi pressure. The DLHs derived catalysts showed identical performance as the commercial ones. Additionally, the catalysts based on double-layered hydroxides were more active under more severe reaction conditions (higher gas hourly space velocity (GHSV), and lower H_2O/CH_4).

Basile et al. [282] tested Ni/Mg/Al DLHs catalysts in partial oxidation of methane, with a mixture containing $CH_4/O_2/He=2/1/4$. The residence time dependence of the reactivity features was examined. Calcination of the precursors generated materials in which the Ni species were differently distributed between NiO, (Ni,Mg)Al_2O_4 phases and NiO–MgO periclase structures. The relative amount of the different phases depended on Ni content and affected the reduction behavior as well as reactivity in POM. The catalysts with high Ni-content (71, 61 and 34 atomic ratio percentage) completely

deactivated after 2-3 hours of time-on-stream due to carbon formation. On the contrary, catalysts with low Ni-content (10 atomic ratio percentage) did not show any deactivation during an 8 h test.

Shishido et al. [231] examined POM over Ni/Mg-Al mixed oxides derived from hydrotalcites. The materials were prepared by co-precipitation from appropriate metal nitrates. The obtained material showed high activity and selectivity to synthesis gas even at high space velocity. When Ni was supported by impregnation on Mg-Al mixed oxide prepared from Mg-Al HT, its activity was higher than that of Ni/α-Al_2O_3 and Ni/MgO and close to the activity of co-precipitated-Ni/Mg-Al.

Based on the above-mentioned literature studies, it may be concluded that the co-precipitation method allows to obtain DLHs materials with the good catalytic performance in methane reforming processes.

Chapter 2 – Experimental part

Chapter 2 – Experimental part

2.1. Catalyst preparation

The catalysts studied in this thesis were synthesized by the following methods:

- Co-precipitation technique,
- Co-impregnation technique,
- Incipient wetness impregnation.

2.1.1. *Co-precipitation technique*

The co-precipitation can be applied for the preparation of precursors (such double-layered hydroxides/hydrotalcites) with definite stoichiometry, which further can be easily converted to catalyst, or the catalysts themselves. Thermal treatments, such as e.g. calcination or reduction, lead to well mixed agglomerates of the components. Such dispersion of catalyst components is hard to achieve with other types of precipitation, which makes co-precipitation an important technique in solid catalyst synthesis [244,283,284].

Four series of catalysts were prepared with the co-precipitation technique: *(i) Y-promoted double-layered hydroxides, (ii) Zr-promoted double-layered hydroxides, (iii) Zr- and Y-promoted double-layered hydroxides and (iv) Ce-promoted double-layered hydroxides.*

Table 2.1 Chemical reagents used in the synthesis of the studied materials.

Symbol	**Name**	**Provider**
$Mg(NO_3)\cdot 6H_2O$	Magnesium nitrate hexahydrate	Sigma Aldrich, 99% pure
$Al(NO_3)_2\cdot 9H_2O$	Aluminum nitrate nonahydrate	Fluka, 98% pure
$Ni(NO_3)_2\cdot 6H_2O$	Nickel (II) nitrate hexahydrate	Sigma Aldrich, 98.5% pure
$Y(NO_3)_3\cdot 6H_2O$	Yttrium (III) nitrate hexahydrate	Aldrich, 99.8% pure
$ZrO(NO_3)_2\cdot xH_2O$	Zirconium (IV) oxynitrate hydrate	Sigma Aldrich, 99% pure

$Ce(NO_3)_3 \cdot 6H_2O$	Cerium (III) nitrate hexahydrate	Sigma Aldrich, 99% pure
NaOH	Sodium hydroxide	ACS reagent, 97% pure
Na_2CO_3	Sodium carbonate	AnalaR NORMAPUR, 99.9% pure

(i) Y-*promoted double-layered hydroxides:* Two solutions were prepared, one containing $Mg(NO_3) \cdot 6H_2O$, $Al(NO_3)_2 \cdot 9H_2O$, $Ni(NO_3)_2 \cdot 6H_2O$ and $Y(NO_3)_3 \cdot 6H_2O$ (listed in Table 2.1), and the second a 2M solution of NaOH to control pH. These two solutions were added dropwise to sodium carbonate solution (25 wt. %). The pH of a mixture was kept in the range of 9.8-10.2. The molar ratios of Ni^{2+}/Mg^{2+} and M^{2+}/M^{3+} were adjusted to 0.33 and ca. 3.0, respectively. Five samples were prepared with the assumed yttrium content of 0.2, 0.4, 0.6, 2.0 and 3.0 wt.%. After co-precipitation, the mixture was aged for 24 h, and the slurry was then filtered and washed with distilled water. The final product was calcined in air at 550 °C for 5 h. The temperature of 550 °C was found to result in complete transformation of the layered structure to mixed nano-oxides, as reported in literature for hydrotalcites with various compositions [197,203,251,276,285]. So prepared catalysts were labeled **HTNi, HTNi-Y0.2, HTNi-Y0.4, HTNi-Y0.6, HTNi-Y2.0** and **HTNi-Y3.0.**

(ii) Zr-promoted double-layered hydroxides: An aqueous solution of following salts was used: $Mg(NO_3) \cdot 6H_2O$, $Al(NO_3)_2 \cdot 9H_2O$, $Ni(NO_3)_2 \cdot 6H_2O$, and $ZrO(NO_3)_2 \cdot xH_2O$ for the co-precipitation of Zr-modified catalysts (the parameters the same above for Y-promoted catalysts). The nominal amount of Zr was 5 wt.%, whereas 20 wt.% of Ni, 30 wt.% of Mg and 12 wt.% of Al were assumed. After calcination at 550 °C for 5 h, the catalyst was designated **HTNi-Zr**.

(iii) Zr- and Y-promoted double-layered hydroxides: An aqueous solution of: $Mg(NO_3) \cdot 6H_2O$, $Al(NO_3)_2 \cdot 9H_2O$, $Ni(NO_3)_2 \cdot 6H_2O$, $ZrO(NO_3)_2 \cdot xH_2O$, and $Y(NO_3)_3 \cdot 6H_2O$ were used for the co-precipitation of Zr- and Y-promoted catalyst. 5.0 wt.% of Zr, 0.4 wt.% of Y, 20 wt.% of Ni, 30 wt.% of Mg and 12 wt.% of Al were presumed. The ratio between Al/Zr was assumed as 5.0. The material was calcined at 550 °C for 5 h. The catalyst was designated **HTNi-ZrY0.4**.

(iv) Ce-promoted double-layered hydroxides: Co-precipitation method was carried out with the aqueous solution of following nitrates: $Mg(NO_3)\cdot 6H_2O$, $Al(NO_3)_2\cdot 9H_2O$, $Ni(NO_3)_2\cdot 6H_2O$, and $Ce(NO_3)_3\cdot 6H_2O$. 3 wt.% was presumed in the Ce-containing samples. The Ni/Mg/Al solid support assumed 20 wt.% of Ni, 30 wt.% of Mg and 12 wt.% of Al. After calcination at 550 °C for 5 h, the material was labelled **HTNi-Ce**.

2.1.2. *Co-impregnation technique*

For comparison, selected materials were prepared by co-impregnation.

Zr- and Y-promoted double-layered hydroxides: A mixture of aqueous solutions of $ZrO(NO_3)_2\cdot xH_2O$ and $Y(NO_3)_3\cdot 6H_2O$ was used for the incipient wetness impregnation on the dried Ni/Mg/Al solid support (20 wt.% of Ni, 30 wt.% of Mg and 12 wt.% of Al). The nominal amount of Zr was 5 wt.% and that of yttrium was 0.2, 0.4 or 0.6 wt.%, this corresponding to Y/Zr molar ratio of 0.05, 0.08 and 0.12, respectively. The final solid product was calcined in air at 550 °C for 5 h. The prepared catalysts were labelled **HTNi/Zr**, **HTNi/ZrY0.2**, **HTNi/ZrY0.4** and **HTNi/ZrY0.6**, respectively.

2.1.3. *Incipient wetness impregnation*

The co-precipitated Ni/Mg/Al double-layered hydroxides samples containing either Zr or Ce were impregnated with Y.

Co-precipitated Zr-containing catalyst impregnated with Y: The dried **HTNi-Zr** (not calcined) was divided into four portions and three of them were impregnated with aqueous solution of $Y(NO_3)_3$, with the assumed Y content of 0.2, 0.4, and 0.6 wt.%. The designation of the catalysts was: **HTNi-Zr/Y0.2**, **HTNi-Zr/Y0.4**, **HTNi-Zr/0.6**.

Co-precipitated Ce-containing samples impregnated with Y: The freshly synthesized material was divided into four portions, and three of them were impregnated with yttrium nitrate, assuming Y

content of 0.2, 0.4 or 0.6 wt.%. The dried materials were calcined at 550 °C for 5 h, and labelled **HTNi-Ce, HTNi-Ce/Y0.2, HTNi-Ce/Y0.4** and **HTNi-Ce/Y0.6**.

The full list of the prepared materials is presented in Table 2.2.

Table 2.2 List of the prepared catalysts. All catalysts assumed 20 wt.% of Ni, 30 wt.% of Mg and 12 wt.% of Al. The nominal contents of the promoters (yttrium, zirconium and cerium) are given in brackets.

Designation	**Co-precipitation**	**Co-impregnation**	**Incipient wetness impregnation**
HTNi	Ni^{2+}, Mg^{2+}, Al^{3+}	-	-
HTNi-Y0.2	Ni^{2+}, Mg^{2+}, Al^{3+}, Y^{3+} (0.2 wt.%)	-	-
HTNi-Y0.4	Ni^{2+}, Mg^{2+}, Al^{3+}, Y^{3+} (0.4 wt.%)	-	-
HTNi-Y0.6	Ni^{2+}, Mg^{2+}, Al^{3+}, Y^{3+} (0.6 wt.%)	-	-
HTNi-Y2.0	Ni^{2+}, Mg^{2+}, Al^{3+}, Y^{3+} (2.0 wt.%)	-	-
HTNi-Y3.0	Ni^{2+}, Mg^{2+}, Al^{3+}, Y^{3+} (3.0 wt.%)	-	-
HTNi-Zr	Ni^{2+}, Mg^{2+}, Al^{3+}, Zr^{4+} (5.0 wt.%)	-	-
HTNi-Zr/Y0.2	Ni^{2+}, Mg^{2+}, Al^{3+}, Zr^{4+} (5.0 wt.%)	-	Y^{3+} (0.2 wt.%)
HTNi-Zr/Y0.4	Ni^{2+}, Mg^{2+}, Al^{3+}, Zr^{4+} (5.0 wt.%)	-	Y^{3+} (0.4 wt.%)
HTNi-Zr/Y0.6	Ni^{2+}, Mg^{2+}, Al^{3+}, Zr^{4+} (5.0 wt.%)	-	Y^{3+} (0.6 wt.%)
HTNi-ZrY0.4	Ni^{2+}, Mg^{2+}, Al^{3+}, Zr^{4+} (5.0 wt.%), Y^{3+} (0.4 wt.%)	-	-
HTNi/Zr	Ni^{2+}, Mg^{2+}, Al^{3+}	Zr^{4+} (5.0 wt.%)	-
HTNi/ZrY0.2	Ni^{2+}, Mg^{2+}, Al^{3+}	Zr^{4+} (5.0 wt.%), Y^{3+} (0.2 wt.%)	-
HTNi/ZrY0.4	Ni^{2+}, Mg^{2+}, Al^{3+}	Zr^{4+} (5.0 wt.%), Y^{3+} (0.4 wt.%)	-
HTNi/ZrY0.6	Ni^{2+}, Mg^{2+}, Al^{3+}	Zr^{4+} (5.0 wt.%), Y^{3+} (0.6 wt.%)	-
HTNi-Ce	Ni^{2+}, Mg^{2+}, Al^{3+}, Ce^{3+} (3.0 wt.%)	-	-
HTNi-Ce/Y0.2	Ni^{2+}, Mg^{2+}, Al^{3+}, Ce^{3+} (3.0 wt.%)	-	Y^{3+} (0.2 wt.%)
HTNi-Ce/Y0.4	Ni^{2+}, Mg^{2+}, Al^{3+}, Ce^{3+} (3.0 wt.%)	-	Y^{3+} (0.4 wt.%)
HTNi-Ce/Y0.6	Ni^{2+}, Mg^{2+}, Al^{3+}, Ce^{3+} (3.0 wt.%)	-	Y^{3+} (0.6 wt.%)

"-" not used

2.2. Characterization methods

Catalysts described in this PhD thesis were characterized by the following methods:

- X-ray diffraction (XRD),
- X-ray fluorescence (XRF),
- Low temperature nitrogen sorption,
- Temperature programmed reduction in H_2 (TPR-H_2),
- Temperature programmed desorption of CO_2 (TPD-CO_2),
- H_2 chemisorption,
- Transmission electron microscopy (TEM),
- High-resolution transmission electron microscopy (HRTEM),
- Thermogravimetric analysis (TGA) or thermogravimetric analysis coupled by mass spectrometry (TGA/MS), and
- Raman spectroscopy.

2.2.1. *X-ray diffraction (XRD)*

X-ray diffraction is a characterization method commonly used to identify bulk structures crystalline structures of solids [286,287].

XRD analysis is typically limited to the identification of specific lattice planes that produce reflections at their corresponding angular positions 2θ, determined by Bragg's law (Eq. 1):

$$2d \sin \theta = n\lambda \quad \text{(Eq. 1)}$$

where:

n - the order of the reflection,

λ - the wavelength of the beam,

d - the distance between diffracting planes,

θ - the Bragg angle.

The technique can only identify crystalline phases, and fails to provide information on the amorphous or highly dispersed solid phases commonly met in catalysts. Additionally, due to its low sensitivity, the concentration of the crystalline phase needs to be high enough in order to be detected. Moreover, XRD probes bulk phases, and is not able to selectively identify the surface structures where catalytic reactions take place [286,287].

On the other hand, the medium size of crystallites can be determined based on the Scherrer equation (Eq. 2):

$$< L > = \frac{K\lambda}{\beta \cos\theta} \qquad \text{(Eq. 2)}$$

where:

L – a measure of the dimension of the crystal in the direction perpendicular to the reflecting plane,

λ – the X-ray wavelength,

β – the half-width of the reflection used in the calculation,

θ – the Bragg angle,

K – the dimensionless shape factor, assumed as 0.9 [245].

X-ray diffraction (XRD) patterns were registered to analyze phase composition of the obtained catalysts and the crystallite size of Ni. PANalytical-Empyrean diffractometer, equipped with CuKα (λ = 0.15406 nm) radiation source was used. The XRD patterns were registered within the range of 2θ from 3.0066° to 89.9766°, with the step of 0.013°, and 68.5950 sec for each scan. The measurements were carried out at room temperature.

Phase identification was carried out by comparing the collected spectra with the database of the HighScore Plus software. Ni crystallite size was calculated basing on Scherrer equation and the half-width of 2θ = 52°.

2.2.2. *X-ray fluorescence (XRF)*

X-ray fluorescence (XRF) is a widely used method for qualitative, quantitative and non-destructive spectroscopic analyzes. The technique can analyze both solid and liquid samples, and reveals the

atomic compositions of a material [288]. It allows to detect elements from Na to U using energy-dispersive X-ray fluorescence spectrometry (EDXRF), whereas the application of wavelength-dispersive spectrometers (WDXRF) allows efficient determination of low-Z elements down to even Be [289]. Most commercially available instruments show limitations in their ability to precisely and accurately measure the abundances of elements with Z<11 in most natural earth materials [290].

The principle of XRF technique is the usage of X-ray beam, which causes excitation of electrons and their ionization. Firstly, the electrons in the inner shells eject to outer shells, which later transit to the vacant positions of the exited electrons. The emitted radiation is known as fluorescent X-rays [290]. This radiation is typical for the element and proportional to the atomic mass and the concentration of the element [291].

X-Ray Fluorescence (XRF) analysis was used to examine elemental composition of the studied catalysts after calcination. The analysis was carried out by Wavelength Dispersive X-Ray Fluorescence (WDXRF) using a Supermini200 instrument. 50 mg of the calcined materials were diluted in 2 g of boric acid and pelletized under a press (10 bar) for 15 min. The pellets were deposited in sample holders, and covered with 6 µm polypropylene film. The analyzes were carried out under vacuum at 36.5 °C in the presence of P-10 gas (a mixture of 10% CH_4 in Ar with 24.7 cm^3/min of flow). The contents of metals were calculated by ZSX software.

2.2.3. *Low temperature nitrogen sorption*

The most common method used to describe the textural parameters of solids is the analysis of adsorption–desorption isotherms of either nitrogen or argon [286]. Six types of adsorption isotherms have been identified according to a classification made by IUPAC. The most common met in catalysis are types II, IV, I, VI [286,292].

- Type II – macroporous solids, where the prevailing adsorption processes are the formation of a monolayer at low relative pressures,

- Type IV – mesoporous solids, in which condensation occurs sharply at a pressure determined by Kelvin-type rules. It is present for most oxides used as carriers,
- Type I – microporous solids. Typical examples of microporous solids are active carbons, zeolites and zeolite-like crystalline solids,
- Type VI – uniform ultramicroporous solids, at which adsorption takes place on surface adsorbate interaction, and shows isotherms with various steps, each corresponding to adsorption on one group of energetically uniform sites.

The Brunauer-Emmett-Teller (BET) method is the most widely used procedure to calculate the textural parameters. The monolayer capacity is determined from the following equation (Eq. 3) (in the linear form):

$$\frac{p}{n^a \cdot (p^0 - p)} = \frac{1}{n_m^a \cdot C} + \frac{(C-1) \cdot p}{n_m^a \cdot C \cdot p^0} \quad \text{(Eq. 3)}$$

where:

p – partial pressure of N_2,

p^0 – saturation pressure at a given temperature,

n^a – amount of adsorbed at the relative pressure p/p^0,

n_m^a – the monolayer capacity,

C – constant.

Monolayer capacity is used to calculate specific surface area S_{BET} according to equation (Eq. 4).

$$S_{BET} = \frac{n_m^a \cdot N \cdot a}{m \cdot 22400} \quad \text{(Eq. 4)}$$

where:

N – Avogadro constant ($6.023 \cdot 10^{23}$ mol^{-1}),

a – effective cross-sectional area of one adsorbate molecule, in square meters (e.g. 0.162 nm^2 for nitrogen)

m – mass of the tested sample,

22400 – volume occupied by one mole of the adsorbate gas at standard temperature and pressure.

The Barrett, Joyner and Halenda (BJH) method is a procedure for calculating pore size distribution from experimental isotherms. It uses the modified Kelvin model of pore filling, in order to relate the amount of absorbent removed from the pores of the material to the size of the pores. The method applies only to the mesopore and small macropore size range [293,294].

Nitrogen sorption was measured by a Micromeritics TriStar II 3020 in order to determine textural properties of the materials. The isotherms were determined at liquid N_2 temperature (-196 °C) within p/p_0 rage of 0.0 to 1.0. 100 mg of samples were degassed for 3 h at 110 °C in VacPrep 061 Degasser unit before the measurements. The specific surface area was calculated using BET equation, while the mesopore volume and pore diameter were calculated by the Barrer, Joyner and Halenda (BJH desorption method).

2.2.4. *Temperature programmed reduction (TPR-H_2)*

TPR-H_2 is mostly used to investigate the reduction behavior of the bulk of solids and to find out the efficient reduction conditions of supported reducible species, solid solutions, promoted metal catalysts, metals in zeolites, and of supported sulfides and of nitrides etc. [283]. The experiments are carried out under controlled heating in hydrogen flow. The information obtained from the TPR analysis is the temperature required for the complete reduction of the sample, and the presence of different reducible species of the same element over the catalyst surface [295].

In order to measure the reducibility of the Ni based double-layered hydroxides, temperature-programmed reduction (TPR-H_2) experiments were carried out in a BEL Japan BELCAT-M equipped with a thermal conductivity detector (TCD). 60 mg of a calcined sample were first treated in helium at 100 °C for 2 h and then reduced in 5 % H_2/Ar mixture with a heating rate of 10 °C/min starting from 100 to 900 °C.

2.2.5. *Temperature programmed desorption (TPD-CO_2)*

Temperature-programmed desorption (TPD) is employed to gain information about specific sites in catalysts. The temperature at which desorption occurs indicates the strength of adsorption, whereas either the amount of gas consumed in the uptake or the amount of desorption upon heating gives information on the concentration of the surface sites [286,296]. The peak temperatures can be correlated to the basic or acid strength of the adsorption sites, depending on the type of used probe adsorbate. Commonly used molecules are NH_3, CO and CO_2.

Temperature programmed desorption (TPD-CO_2) measurements were carried out in order to determine basicity of the catalysts. The measurements were performed after TPR-H_2 runs, using BEL Japan BELCAT-M. CO_2 was adsorbed at 80 °C for 1 h from a mixture of 10% CO_2/He. Then gas flow was switched to helium for 15 min at 80 °C, in order to desorb weakly adsorbed CO_2. Finally, the materials were heated from 80 to 800 °C in helium to determine the temperature of CO_2 desorption. TPD profiles were deconvoluted into three Gaussian peaks corresponding to weak, medium and strong basic sites, in agreement with literature [207,259,285,297].

2.2.6. *H_2 chemisorption*

Chemisorption requires strong bond between the probe molecule and the surface site and negligible interaction with the support at the chosen temperatures and pressures. H_2, CO, NO, and N_2O are used as probes at or above room temperature [283]. The reactive gas is injected repeatedly into the reactor in the form of pulses, and gets chemisorbed on a catalyst. The principle of the method is to measure the chemisorbed amount of gas as a function of the equilibrium pressure, and consequently to obtain an adsorption isotherm. The adsorbed amount corresponding to one monolayer, is determined by extrapolating the linear part of the isotherm to zero pressure. If the chemisorption stoichiometry is known, dispersion, which is directly related to particle size and particle size distribution, can be calculated [283].

Hydrogen chemisorption was used to determine nickel dispersion (the number of surface metal atoms divided by the total number of metal atoms present in the catalyst) using a Micromeritics, ASAP 2020S. 200 mg of a calcined material was placed between quartz wool and loaded into a U-shaped quartz reactor. Prior to the experiments, evacuation at 40 °C for 1 h and *in situ* reduction in pure H_2 at 900 °C for 1 h was applied (heating ramp 10 °C/min). After reduction, the sample was treated in helium of 50 cm^3/min for 30 min at 900 °C and subsequently for 1 h at 40 °C. Then the sample was continuously evacuated for 30 min at 40 °C. Adsorption isotherm was recorded at 40 °C and the metal dispersion was calculated based on the hydrogen uptake. For Ni-based catalysts theoretical amount of hydrogen that would be used for full reduction of Ni was assumed. The stoichiometric ratio of H:Ni was taken as 1. It was also assumed that neither Y, Zr, Ce nor the support contributed to chemisorption.

The percentage metal dispersion (D) was calculated from Eq. 5, assuming that reduced part of the nickel was present in a separate dispersed layer in intimate contact with the support [298]:

$$\mathrm{D} = \frac{1.17 \cdot \mathrm{X}}{\mathrm{W} \cdot \mathrm{f}} \ [\%] \qquad \text{(Eq. 5)}$$

where:

D – dispersion,

X – hydrogen uptake in micromoles per gram of the catalyst,

W – weight percentage of nickel,

f – fraction of nickel reduced to the metal.

From the above formula (Eq. 5), the crystallite size was calculated, assuming spherical metal crystallites with a uniform size (Eq. 6). The calculation method was similar to that described by Mustard et al. [298]:

$$\mathrm{D} = \frac{97.1}{\mathrm{D}} \ [\mathrm{nm}] \qquad \text{(Eq. 6)}$$

where:

d – average nickel crystallite diameter.

2.2.7. *Transmission Electron Microscopy (TEM)*

In Transmission Electron Microscopy (TEM), electromagnetic lenses are used to focus an electron beam on the specimen. Two modes are available in TEM, a bright-field mode where the intensity of the transmitted beam provides a two-dimensional image of the density or thickness of the sample, and a dark-field mode, where the electron diffraction pattern is recorded. A combination of topographic and crystallographic information, including particle size distributions, can be obtained in this way [286].

The micrographs obtained from Transmission Electron Microscopy (TEM, JOEL JEM-100XCII) were used for the determination of Ni crystallite size distribution, and the type of formed carbon deposits in the spent catalysts. The samples were prepared by the dropwise addition of a colloidal solution in ethanol onto a copper grid covered with amorphous carbon film. 400 particles were measured in the ImageJ software in order to obtain the average Ni particle size in the reduced and spent catalysts. TEM analyzes were performed by Sandra Casale (Sorbonne Université).

2.2.8. *High-Resolution Electron Microscopy (HRTEM)*

High-Resolution Transmission Electron Microscopy (HRTEM) is capable of imaging individual planes in crystalline particles, and can provide more detailed structural information on the surface of the catalysts than TEM [299]. However, the electron microscopy has some limitations. The technique requires special sample preparations. Any electron beam-induced effects (such as changes in the specimen due to local heating), electronic excitations, or deposition of contaminants during observation, must be minimized [286]. Additionally, statistical analysis of a large number of micrographs is needed to get meaningful information on particle size distributions. Thus it is best to correlate such results with information obtained by other characterization methods [286].

High-Resolution Transmission Electron Microscopy (JEOL JEM-2010 with EDS) was used to characterize carbon deposits and to obtain precise analysis of the planes registered at the nanometer

scale. The specimens were prepared in the same way as for TEM analysis. HRTEM analyzes were performed by Patricia Beaunier (Sorbonne Université).

2.2.9. *Thermogravimetric analysis coupled by mass spectroscopy (TGA/MS)*

Thermogravimetry is associated with the changes in sample weight under inert, reduced and oxidative atmosphere. The experiments are carried out as a function of temperature. The temperature increases linearly over time, while the weight changes are recorded. Sometimes, it is coupled with MS (Mass Spectrometer) in order to identify the gaseous composition of the sample [286].

Thermogravimetric analyzes were carried out by a TGA-MS (TGA: Netzsch STA 449C Jupiter, MS: Netzsch Aërlos QMS 403C) in order to evaluate the catalytic coke formation on the spent catalysts. A mixture of air flow of 100 cm^3/min and argon protective gas flow of 20 cm^3/min were applied. 10 mg of a spent sample was heated starting from room temperature to 900 °C with a heating rate of 10 °C/min. The amount of the formed carbon deposits was estimated by mass loss in TGA analysis, and confirmed by CO_2 formation derived from MS results.

2.2.10. *Raman spectroscopy*

Raman spectroscopy is a vibrational characterization method, which is used to study the structure of solids, liquids and gases. Raman scattering is a function of the molecular vibrations and symmetries of chemical bonds. It offers a high spatial resolution in the micrometer range [300]. Among other possibilities, Raman spectroscopy gives information on disordered and heterogeneous carbonaceous materials, by revealing the presence of characteristic D bands and G bands [301]. The D band (ca. 1330 cm^{-1}) indicates structural imperfections of graphite, while the G band (ca. 1590 cm^{-1}) is ascribed to in-plane carbon–carbon stretching vibrations of graphite layers [166].

The technique does suffer from some limitations. Firstly, Raman intensities of surface species are often quite low. Also, the high laser intensity required for Raman characterization tends to heat the sample,

and often causes changes in the physical properties of the solid [286]. Finally, the heterogeneity can constitute a severe limitation to a quantitative characterization of the materials [301].

Raman measurements were performed using a Horiba Jobin Yvon LabRam HR800 spectrophotometer in order to characterize carbon deposition on the spent catalysts after DRM. The spectra were recorded in range of 3000-1000 cm^{-1} at room temperature. The excitation source was 633 nm of Ne-Ne laser. The spectra were recorded with an accumulation of 3 and an acquisition time of 20 s. A diffraction grating of 1800 gr/mm and a 50x objective were applied.

2.3. Catalytic tests

All catalytic tests, dry reforming of methane (DRM), partial oxidation of methane (POM), combined partial oxidation with dry reforming of methane (CRPOM) and tri-reforming of methane (TRM), were performed using a U-shaped reactor presented in Figure 2.1 A. A precise mass of a catalyst, corresponding to GHSV (20,000 h^{-1}) was placed in the reactor. Quartz wool was used to retain catalyst powder inside the reactor. K-type thermocouple was used to control the temperature in the catalytic bed.

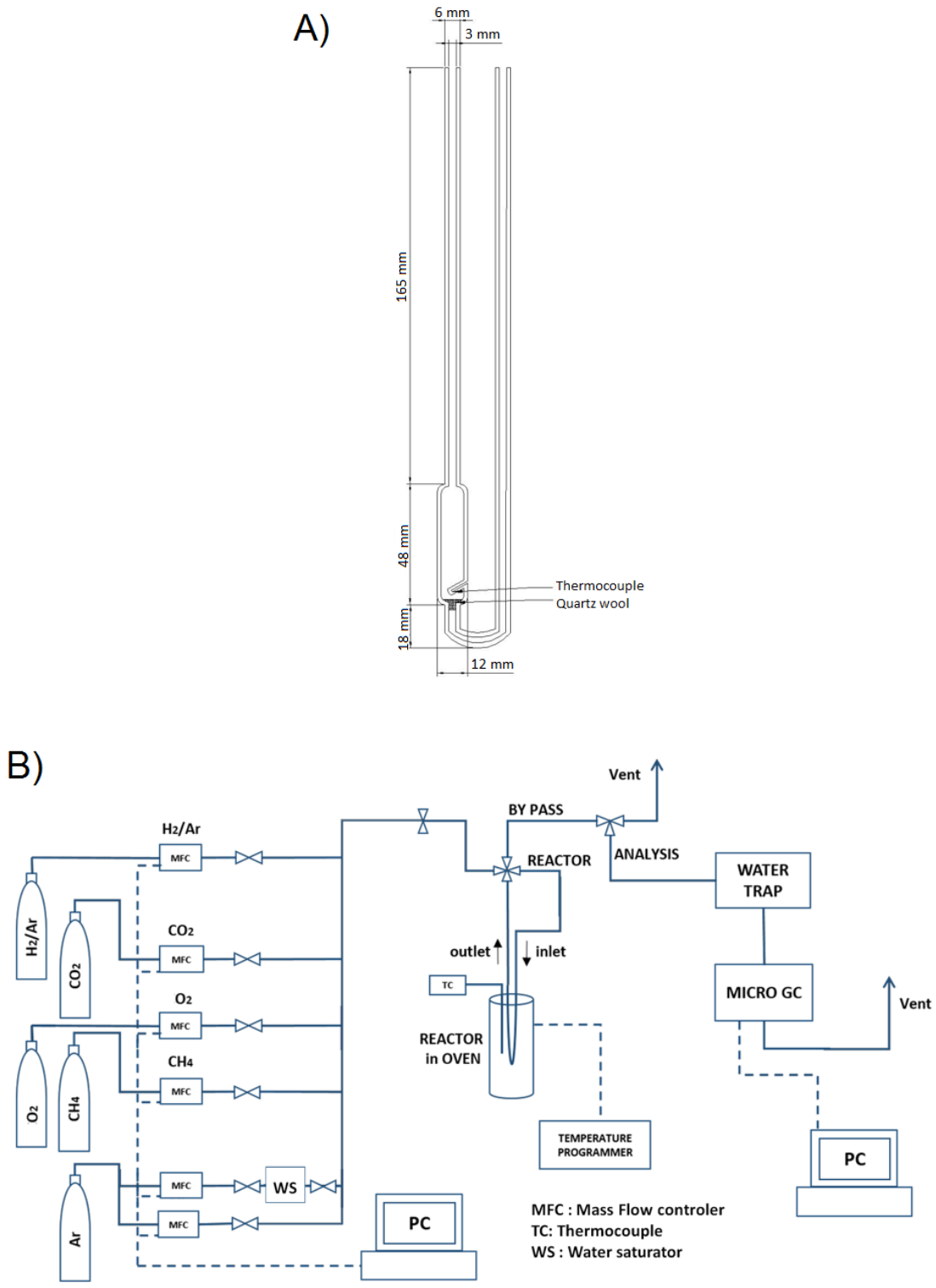

Fig. 2.1 Set-up of catalytic reactor (A) and catalytic test (B)

Catalytic experiments were performed in a fixed bed reactor. Flow rate of each reactant was controlled by mass flow controllers (BROOKS Instruments) (Fig. 2.1 B). All experiments were conducted

at total flow rate of 100 cm^3/min. The following reagents were used: CH_4 (Air Liquide, N45 purity), CO_2 (Air Liquide, N45 purity), O_2 (Air Liquide, Alphagaz 1), H_2 (Air Liquide, Alphagaz 1), Ar (Air Liquide, Alphagaz 1).

For the SRM and TRM experiments using steam, the water content in the reaction mixture was controlled using the vapor pressure of H_2O at the temperature of the saturator (52 °C). All lines downstream of the saturator were heated to temperature above 100 °C to prevent condensation.

The following substrates/products: CH_4, CO_2, H_2 and CO were analyzed by a 490 Varian Micro-GC equipped with injector, COX column, and a micro thermal conductivity detector (μTCD) installed in separate small temperature-controlled compartments.

Prior a catalytic test, a catalyst was reduced *in situ* at 900 °C for 1 h with 5% H_2/Ar gas mixture (flow 100 cm^3/min). The gas composition used for tests were as follows:

- Dry reforming of methane $CH_4/CO_2/Ar=1/1/8$ ($10\%CH_4/10\%CO_2/80\%Ar$),
- Partial oxidation of methane $CH_4/O_2/Ar=1/0.5/8.5$ ($10\%CH_4/5\%O_2/85\%Ar$),
- Combined partial oxidation with dry reforming of methane $CH_4/CO_2/O_2/Ar=1/1/0.5/7.5$ ($10\%CH_4/10\%CO_2/5\%O_2/75\%Ar$).
- Tri-reforming of methane $CH_4/CO_2/H_2O/O_2/Ar=1/0.5/0.5/0.1/7.9$ ($10\%CH_4/5\%CO_2/5\%H_2O/1\%O_2/79\%Ar$), and $CH_4/CO_2/H_2O/O_2/Ar=3/1/2/0.3/3.7$ ($30\%CH_4/10\%CO_2/20\%H_2O/3\%O_2/37\%Ar$),

  Additionally, direct methane decomposition (DMD) was also studied in order to examine selectivity towards this important carbon forming reaction, using a mixture of $CH_4/Ar= 2/8$.

There were two types of tests:

- A first series of the experiments was performed in the temperature range of 850-600 °C (starting from 850 °C) with a temperature step every 50 °C, and the cooling time of 15 min

between the steps. The duration of the test at each temperature was 30 minutes corresponding to steady-state measurements, as presented in Fig. 2.2.

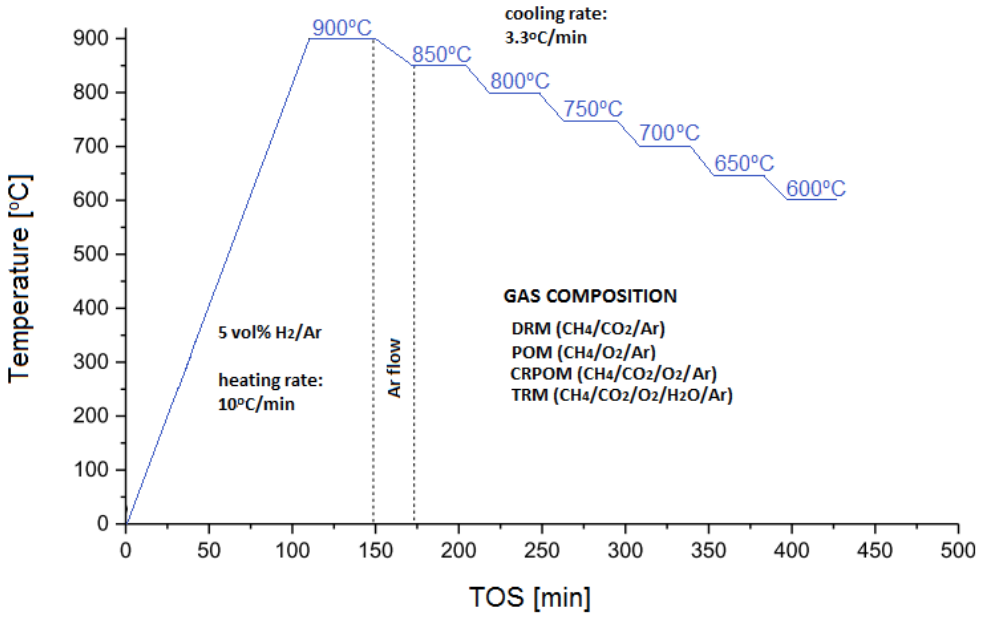

Fig. 2.2 Scheme of methodology used in catalytic tests, with different temperatures of reactions (TPSR).

- Experiments at the second series were carried out in isothermal conditions at 700 °C for 5 hours in order to evaluate the catalysts stability, as presented in Fig. 2.3.

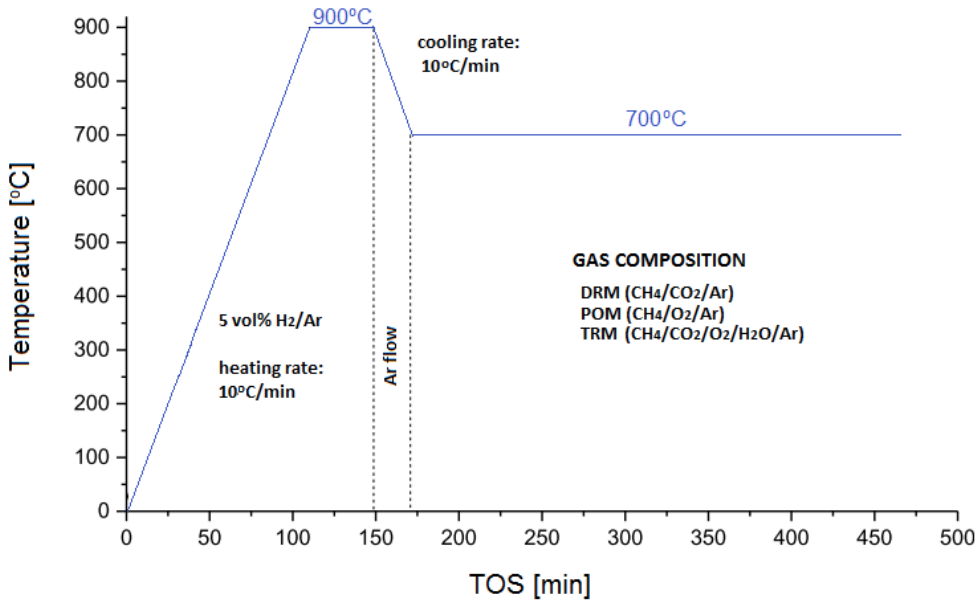

Fig. 2.3 Scheme of methodology used in catalytic tests under isothermal conditions.

Conversions of CH_4 and CO_2, and H_2/CO ratios were calculated using the following equations (7), (8), (9):

$$X_{CH_4} = \left[\frac{\boldsymbol{n}_{CH_4^{in}} - \boldsymbol{n}_{CH_4^{out}}}{\boldsymbol{n}_{CH_4^{in}}}\right] \cdot 100 \qquad [\%] \qquad \text{(Eq. 7)}$$

$$X_{CO_2} = \left[\frac{\boldsymbol{n}_{CO_2^{in}} - \boldsymbol{n}_{CO_2^{out}}}{\boldsymbol{n}_{CO_2^{in}}}\right] \cdot 100 \qquad [\%] \qquad \text{(Eq. 8)}$$

$$H_2/CO = \left[\frac{\boldsymbol{n}_{H_2^{out}}}{\boldsymbol{n}_{CO^{out}}}\right] \qquad \text{(Eq. 9)}$$

Where $n_{CH4,initial}$ and $n_{CO2,initial}$ are the inlet numbers of moles of methane and carbon dioxide, respectively. And $n_{CH4,final}$, $n_{CO2,final}$, $n_{H2,final}$, $n_{CO,final}$ are outlet number of moles of methane, carbon dioxide, hydrogen and carbon monoxide, respectively.

CH_4 conversion in direct methane decomposition was calculated based on Eq. 10:

$$X_{DMD,CH_4} = \left[\frac{\boldsymbol{n}_{CH_4^{in}} - \boldsymbol{n}_{CH_4^{out}}}{\boldsymbol{n}_{CH_4^{in}}}\right] \cdot 100 \qquad [\%] \qquad \text{(Eq. 10)}$$

2.4. Thermodynamic calculations

2.4.1 *Minimization of Gibbs free energy*

The Gibbs free energy analysis was used to study the equilibrium of the system containing several species. The total Gibbs free energy is expressed in Eq. 11 [115,302,303]:

$$G_{total} = \sum_{i=1}^{N} n_i \left(G_i^0 + \mathrm{RTln}\left(\frac{f_i}{f_0}\right)\right) \qquad \text{(Eq. 11)}$$

Where the G_i^0 is standard Gibbs free energy of formation of species *i*, *R* stands for molar gas constant, *T* is temperature of the system, and a number of moles is assigned to n_i of species *i*. Standard-state is expressed as 25 °C and 1 bar, while f_i is a fugacity at this state of species *i*, and f_0 refers to operating state. In view of Eq. 11, n_i moles of species has to fulfill the following relation:

$$\sum_{i=1}^{N} a_{ji} n = b_j \quad \text{(Eq. 12)}$$

Where the number of element *j* expressed in grams or atoms of molecule *i* is assigned to a_{ji}. b_{ji} is a total number of moles of element *j* in the feed. Additionally, the following equality: 1≤j≤M, where *M* is the number of elements in the mixture, has to be fulfilled.

2.4.2. *Calculation method*

Thermodynamic calculations were carried out by HSC Chemistry 5 software. The minimization of Gibbs free energy method was used. The influence of temperature and feed gas composition were examined in an isobaric system in order to calculate the equilibrium amount of CO_2, CH_4, CO, H_2, H_2O, C, and equilibrium conversions of CO_2, CH_4, and H_2/CO molar ratio.

For the calculations, the chemical reactions in methane reforming processes were considered (Table 2.3) [302,304,305]. The following reactants were taken into account: $Ar_{(g)}$, $CH_{4(g)}$, $CO_{2(g)}$, $CO_{(g)}$, $H_{2(g)}$, $H_2O_{(g)}$, $O_{2(g)}$ (only for POM and TRM), $C_{(s)}$, $C_2H_{2(g)}$, $C_2H_{4(g)}$, $C_2H_{6(g)}$, $CH_3OCH_{3(g)}$, $CH_3OH_{(g)}$, $HCOOH_{(g)}$, while the substrates were assumed as: $CH_{4(g)}$, $CO_{2(g)}$ and $Ar_{(g)}$ for DRM; $CH_{4(g)}$, $O_{2(g)}$ and $Ar_{(g)}$ for POM; $CH_{4(g)}$, $H_2O_{(g)}$ and $Ar_{(g)}$ for SRM; $CH_{4(g)}$, $CO_{2(g)}$, $O_{2(g)}$, $H_2O_{(g)}$ and $Ar_{(g)}$. All calculations were performed with constant pressure of 1 bar.

Table 2.3 The list of reactions present in tri-reforming of methane [302,304,305].

Number	Name	Reaction	ΔH^0 [kJ/mol]
1	**Dry reforming of CH_4**	$CH_4 + CO_2 = 2CO + 2H_2$	247
2	**Steam reforming of CH_4**	$CH_4 + H_2O = CO + 3H_2$	206
3	**Partial oxidation of CH_4**	$CH_4 + ½O_2 = CO + 2H_2$	-36
4	Total oxidation of CH_4	$CH_4 + 2O_2 = CO_2 + 2H_2O$	-880
5	Oxidation of CH_4	$CH_4 + O_2 = CO_2 + 2H_2$	-319
6	Reverse water-gas shift	$CO_2 + H_2 = H_2O + CO$	41
7	Methanation of CO_2	$CO_2 + 4H_2 = CH_4 + 2H_2O$	-165
8	Methanation of CO	$CO + 3H_2 = CH_4 + H_2O$	-206

9	Hydrogenation of CO_2	$CO_2 + H_2 = HCOOH$	15
10	Hydrogenation of CO_2	$CO_2 + 3H_2 = CH_3OH + H_2O$	-49
11	Hydrogenation of CO	$CO + 2H_2 = CH_3OH$	-91
12	Hydrogen oxidation	$H_2 + ½O_2 = H_2O$	-58
13	Oxidation of CO	$CO + ½O_2 = CO_2$	-283
14	Dehydration of CH_3OH to CH_3OCH_3	$2CH_3OH = CH_3OCH_3 + H_2O$	-37
15	Reforming of CH_3OCH_3	$CH_3OCH_3 + H_2O = 2CO + 4H_2$	205
16	Reforming of CH_3OCH_3	$CH_3OCH_3 + CO_2 = 3CO + 3H_2$	258
17	Oxidative coupling of CH_4	$2CH_4 + CO_2 = C_2H_6 + CO + H_2O$	106
18	Reforming of C_2H_6	$C_2H_6 + 2CO_2 = 4CO + 3H_2$	430
19	Oxidative coupling of CH_4	$2CH_4 + 2CO_2 = C_2H_4 + 2CO + 2H_2O$	284
20	Reforming of C_2H_4	$C_2H_4 + 2CO_2 = 4CO + 2H_2$	290
Reactions of coke			
21	Methane decomposition	$CH_4 = C_{(s)} + 2H_2$	75
22	Boudouard reaction	$2CO = C_{(s)} + CO_2$	-172
23	Hydrogenation of CO_2	$CO_2 + 2H_2 = C_{(s)} + 2H_2O$	-90
24	Steam on C	$C_{(s)} + H_2O = CO + H_2$	131
25	Partial oxidation of C	$C_{(s)} + ½O_2 = CO$	-110

Chapter 3 - Thermodynamic analysis of DRM, SRM, POM, TRM

Chapter 3 - Thermodynamic analysis of DRM, SRM, POM, TRM

In this chapter, thermodynamic equilibrium calculations are presented for dry reforming of methane (DRM). A comparison of DRM with thermodynamic results obtained for steam reforming of methane (SRM), partial oxidation of methane (POM), and tri-reforming of methane (TRM) was also carried out. Finally, for tri-reforming of methane, a feed composition was examined, which may be useful for a natural gas-based power plant.

The analyzes assumed the volumetric ratios of feed compositions considering two scenarios described in the **Subchapters 1.3.1.1**. and **1.3.1.2:**

(i) CO_2 can be separated from flue gases, and TRM reaction may be carried out according to the gas composition suggested in the literature [85,86]: ($CH_4/CO_2/H_2O/O_2$/Ar= 1/0.5/0.5/0.1/7.9), and

(ii) direct usage of CO_2 from flue gases from a power plant fired with natural gas, and the gas composition suggested for the first time in this thesis.

Table 3.1 presents the feed compositions which were proposed for the calculations. The following compositions refer to the volumetric ratios of the components: (1) DRM: $CH_4/CO_2/H_2O/O_2$/Ar = 1/1/0/0/8, (2) SRM: $CH_4/CO_2/H_2O/O_2$/Ar = 1/0/1/0/8, (3) POM: $CH_4/CO_2/H_2O/O_2$/Ar = 1/0/0/0.5/8.5, and (4) TRM: $CH_4/CO_2/H_2O/O_2$/Ar = 1/0.5/0.5/0.1/7.9.

Table. 3.1 Feed gas compositions used for the thermodynamic calculations.

Number	Process	Feed gas composition					
		CH_4	CO_2	H_2O	O_2	Ar	CH_4/O_2 ratio
1	DRM	1	1	0	0	8	-
2	SRM	1	0	1	0	8	-
3	POM	1	0	0	0.5	8.5	2
4	TRM	1	0.5	0.5	0.1	7.9	10

The second part of this chapter describes thermodynamic calculations which were proposed based on the assumption that tri-reforming process may be introduced on industrial scale. A typical flue gas composition from natural gas-fired power plant was used in order to simulate the TRM (8–10% CO_2, 18–20% H_2O, 2–3% O_2, and 67–72% inert). The following feed gas compositions were proposed, assuming four different methane volumetric share in the mixture of the gases i.e., 1, 1.5, 2.0 and 3.0 mol as presented in Table 3.2. The obtained CH_4/O_2 ratios are above upper flammability limit (UFL) and should not cause ignition of the mixture in the presence of spark [90].

Table 3.2 Feed gas compositions of tri-reforming of methane used for the thermodynamic calculations.

Number	TRM Process	Feed gas composition					
		CH_4	CO_2	H_2O	O_2	Ar	CH_4/O_2 ratio
1		1	1	2	0.3	5.7	3.33
2		1.5	1	1	0.3	5.2	5
3		2	1	2	0.3	4.7	6.67
4		3	1	2	0.3	3.7	10

3.1. Thermodynamic equilibrium analysis of methane reforming processes

3.1.1. *Dry reforming of methane calculations*

Fig. 3.1 presents the equilibrium of reactants as a function of temperature for dry methane reforming ($CH_4/CO_2/H_2O/O_2/Ar$ = 1/1/0/0/8, p = 1 bar). The results are in good agreement with literature [114,306]. Due to the endothermic nature of the process, and the fact that DRM is accompanied by many parallel reactions, a large variation in the quantity of components is observed with the temperature increase (from 0 to 1000 °C). At 500 °C, a large amount of carbon is formed, together with water, and a higher amount of H_2 than that of CO.

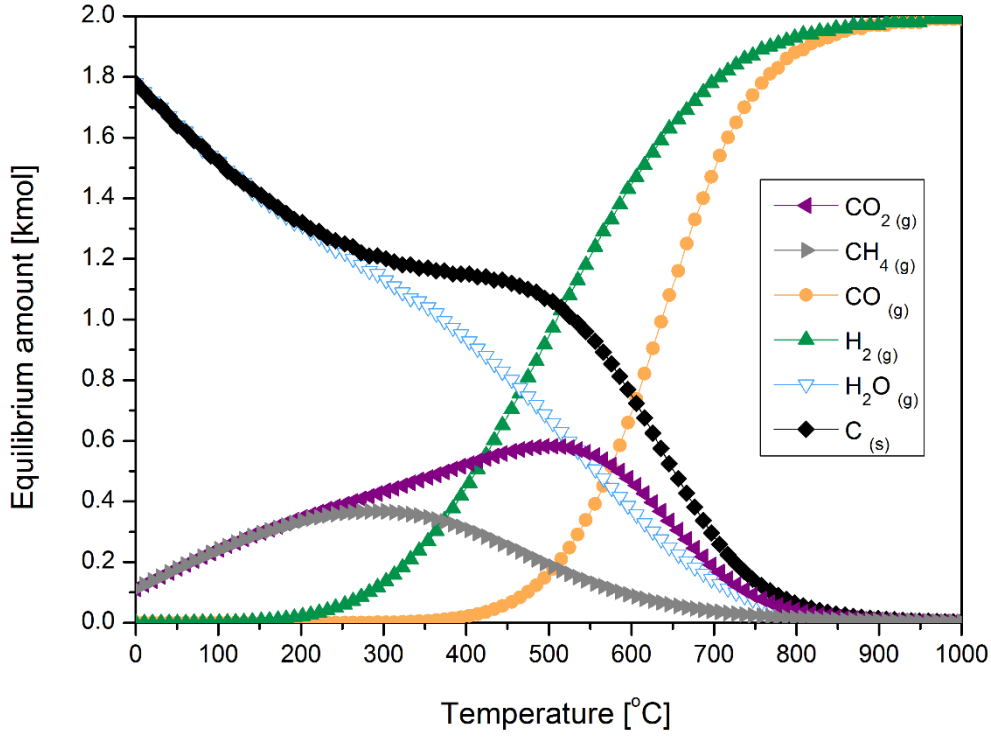

Fig. 3.1 Equilibrium amounts for gaseous components and coke in the dry reforming of methane process (CH_4/CO_2/Ar=1/1/8, p= 1 bar).

At 500 °C, CO_2 equilibrium reaches a maximum, which refers to the lowest conversion of this gas in the entire temperature range (0-1000 °C) (Fig. 3.2). This suggests a high probability of the occurrence of parallel reactions other than methane dry reforming. Above this temperature (ca. 600 °C and more), a fast decrease in carbon and water formation is observed. In addition, H_2 and CO, which represent a sufficient value of molar ratio (around 1) for further use in fuel production, are observed. It is consistent with generally accepted opinion that DRM is likely to proceed efficiently at very high temperature (over 700 °C), although from the economical point of view it would be desirable to run the process at lower temperature with a very active and stable catalyst.

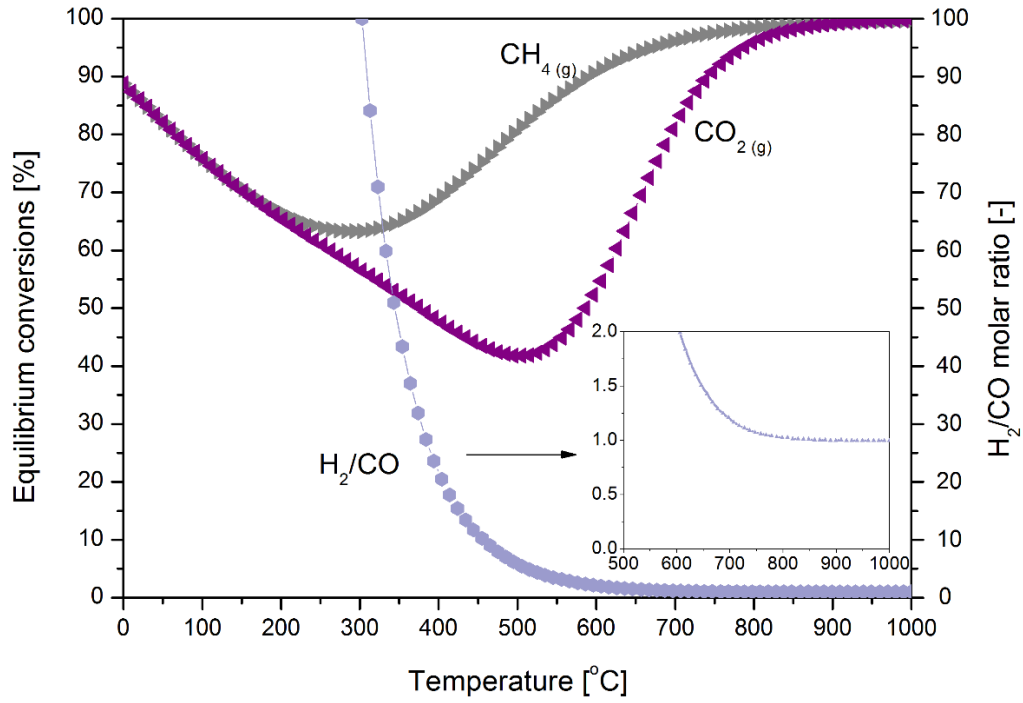

Fig. 3.2 Equilibrium conversions of CH_4, CO_2, and H_2/CO molar ratio in the dry reforming of methane process (CH_4/CO_2/Ar=1/1/8, p= 1 bar).

3.1.2. *Dry reforming of methane versus other reforming processes*

Syngas formation from methane may be realized in three different reacting mixtures. Dry methane reforming (DRM), also called CO_2-reforming, has long been considered as one of the prospective operations for the valorization of carbon dioxide ($CH_4+CO_2=2CO+2H_2$, ΔH^0 = 247 kJ/mol)[44,100,154]. However, it does not give a satisfactory H_2/CO molar ratio for the e.g., methanol production. Therefore, is it recommended to perform dry reforming combined with steam reforming (SRM) [2], the latter being the currently used commercial method producing synthetic gas with a higher H_2/CO ratio, around 3.0 ($CH_4 + H_2O = CO + 3H_2$, ΔH^0= 206 kJ/mol). The partial oxidation of methane (POM) is a slightly exothermic reaction which may give a H_2/CO ratio equal to 2.0 ($CH_4 + ½\ O_2 = CO + 2H_2$, ΔH^0 = -36 kJ/mol). For this reason, the POM is very advantageous from the application point of view. A new process, which is a combination of DRM, SRM and POM, was proposed in literature [2]. This process is called tri-reforming of methane and allows CO_2 utilization and the production of synthesis gas with

molar ratio of H_2/CO=1.5-2.0. The presence of H_2O and O_2 in the process improves stability of a catalyst by the removal of carbon deposits [2].

The influence of temperature on methane reforming processes was examined for four feed gas compositions presented in Table 3.1. For TRM the following gas composition was investigated $CH_4/CO_2/H_2O/O_2/Ar$ = 1/0.5/0.5/0.1/7.9, and compared with DRM, SRM and POM.

Figure 3.3 shows CH_4 equilibrium conversion versus temperature. As it may be seen, all results are relatively high (above 65% at the temperature range from 550 to 900 °C). For all methane reforming processes a significant increase in CH_4 conversion may be observed in the range of 550 to 720 °C, with a smaller increase over 720 °C. In the temperature range from 850-900 °C, CH_4 conversion was almost 100%.

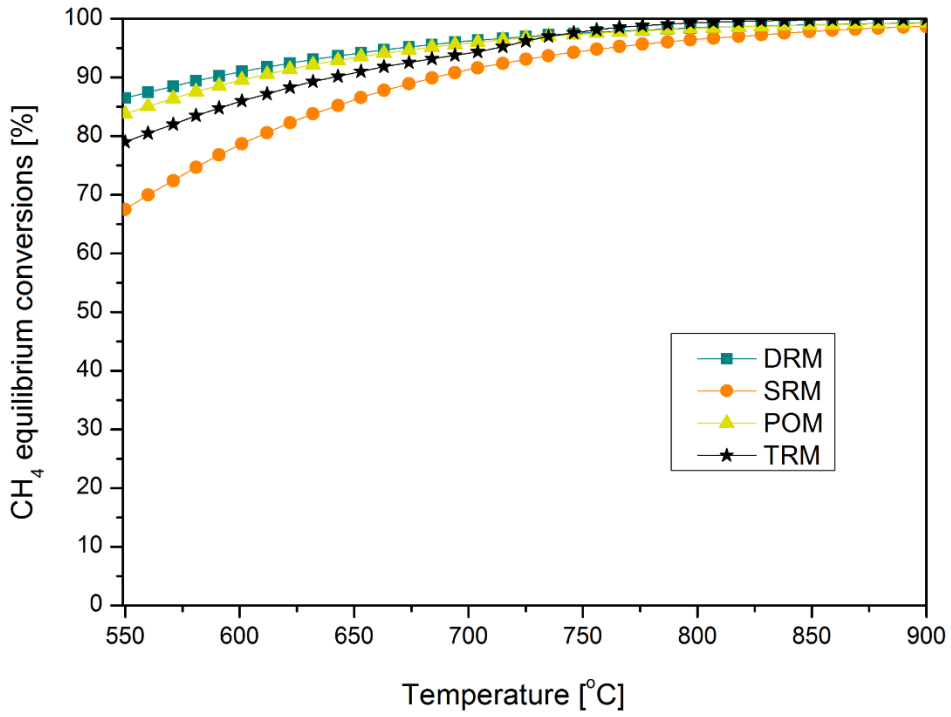

Fig. 3.3 Influence of temperature on the equilibrium concentration of methane (DRM: $CH_4/CO_2/Ar$=1/1/8, SRM: $CH_4/H_2O/Ar$=1/1/8, POM: $CH_4/O_2/Ar$=1/0.5/8.5, TRM: $CH_4/CO_2/H_2O/O_2/Ar$=1/0.5/0.5/0.1/7.9; p= 1 bar).

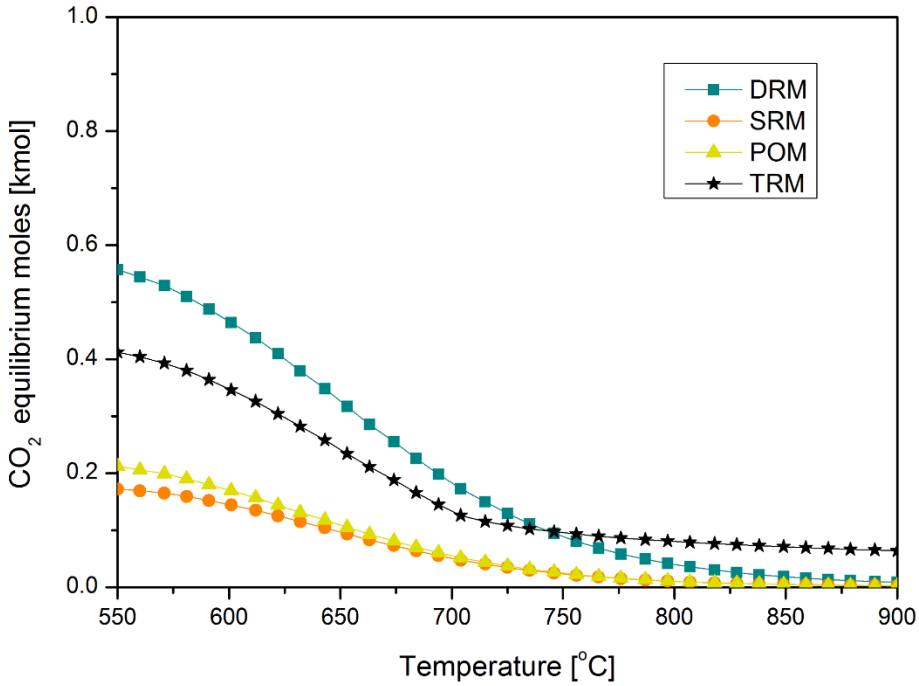

Fig. 3.4 The influence of temperature on the reforming of carbon dioxide (DRM: $CH_4/CO_2/Ar=1/1/8$, SRM: $CH_4/H_2O/Ar=1/1/8$, POM: $CH_4/O_2/Ar=1/0.5/8.5$, TRM: $CH_4/CO_2/H_2O/O_2/Ar=1/0.5/0.5/0.1/7.9$; p= 1 bar).

The changes in CO_2 content as a function of temperature are shown in Fig. 3.4. The results originate from CO_2 conversion, as well as the occurrence of the CO_2 producing side reactions (listed in Table 1 in **Chapter 2**). The equilibrium carbon dioxide content declines with the increase in temperature. Only negligible amounts of CO_2 are observed for SRM and POM over 800 °C. Theoretically, carbon dioxide is not the main substrate in SRM and POM. Thus, it may be assumed that in case of SRM the amount of CO_2 in the system was linked with the reverse water-gas shift process, i.e., reaction 6 in Table 2.3 (**Chapter 2**). In POM, carbon dioxide could be produced via CH_4 oxidation (reaction 5), or CO oxidation (reaction 13). In dry reforming and tri-reforming, the carbon dioxide was present as a reactant, hence significantly higher equilibrium amounts were recorded. For all methane processes, the CO_2 conversion was calculated as a difference between inlet and outlet number of moles divided by initial number of moles (**Subchapter 3.1.2**.; Eq. 4.)

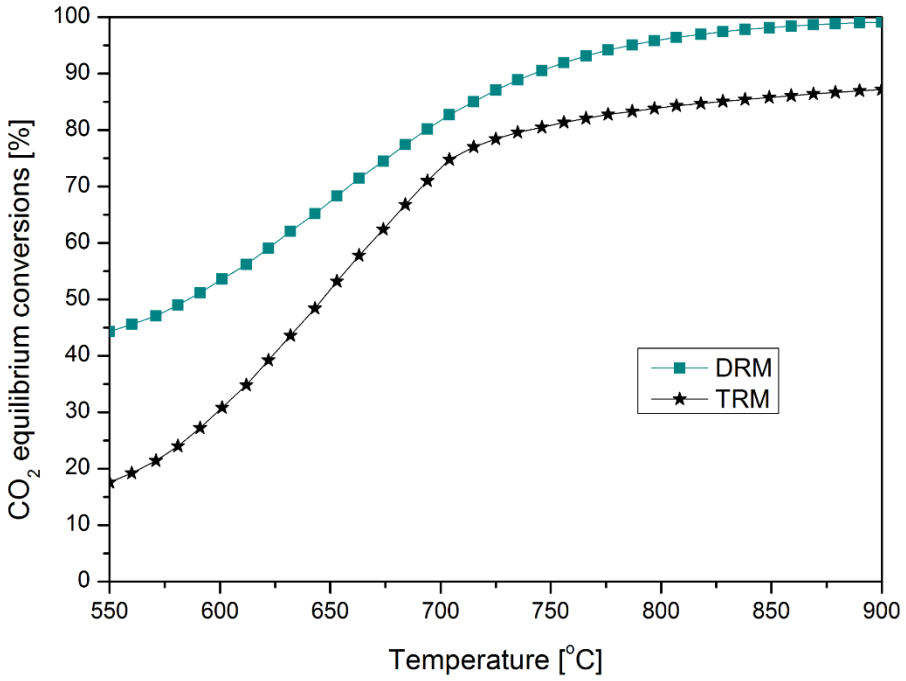

Fig. 3.5 The influence of temperature on the equilibrium concentration of carbon dioxide. (DRM: $CH_4/CO_2/Ar=1/1/8$, TRM: $CH_4/CO_2/H_2O/O_2/Ar=1/0.5/0.5/0.1/7.9$; p= 1 bar).

In Fig. 3.5 a comparison between carbon dioxide equilibrium conversion for DRM and TRM are presented. For both processes, conversion increased with the temperature growth. For DRM process CO_2 conversion was always higher than for TRM, in the whole temperature range. The highest conversions were obtained at 850 °C and 900 °C, where CO_2 conversion was close or equal to 100%, respectively. Nevertheless, the TRM results are relatively good, since ca. 73% of CO_2 may be converted at 700 °C.

Synthesis gas may be used directly in the liquid fuels production, e.g. Fischer-Tropsch or methanol synthesis followed by Methanol To Gasoline (MTG) process, when the H_2/CO ratio is in the range of 1.5-2.0. According to the calculations performed by HSC Chemistry 5.0, the desired ratio may be received for POM and TRM feed gas compositions presented in the Fig. 3.6 at temperatures 700 to 900 °C. Steam reforming of methane and dry reforming have, respectively, too high or too low molar ratios of the considered gaseous components. Therefore, the idea of the combination of these two reforming reactions may be promising in terms of receiving desired H_2/CO ratio.

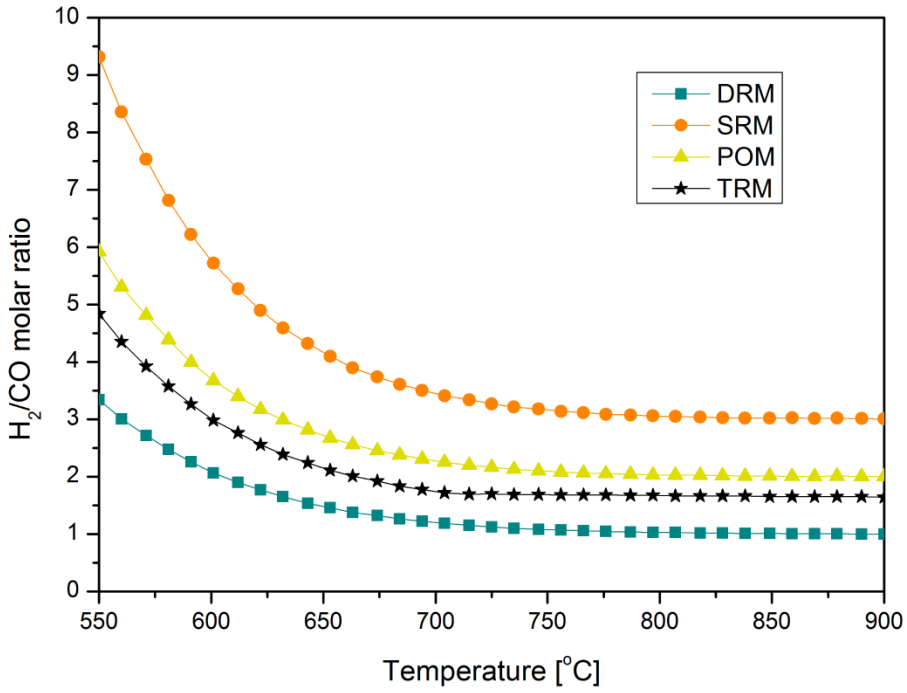

Fig. 3.6 The influence of temperature on the H_2/CO molar ratio (DRM: CH_4/CO_2/Ar=1/1/8, SRM: CH_4/H_2O/Ar=1/1/8, POM: CH_4/O_2/Ar=1/0.5/8.5, TRM: $CH_4/CO_2/H_2O/O_2$/Ar=1/0.5/0.5/0.1/7.9; p= 1 bar).

3.1.3. *The influence of feed gas composition on carbon deposition*

Fig. 3.7 presents equilibrium carbon content as a function of temperature. Almost no carbon formation was observed over 900, 850, 830 or 715 °C for DRM, POM, SRM or TRM, respectively. This result proves the positive influence of H_2O and O_2 in the feed on carbon formation, in good agreement with conclusions drawn by Song and Pan [83].

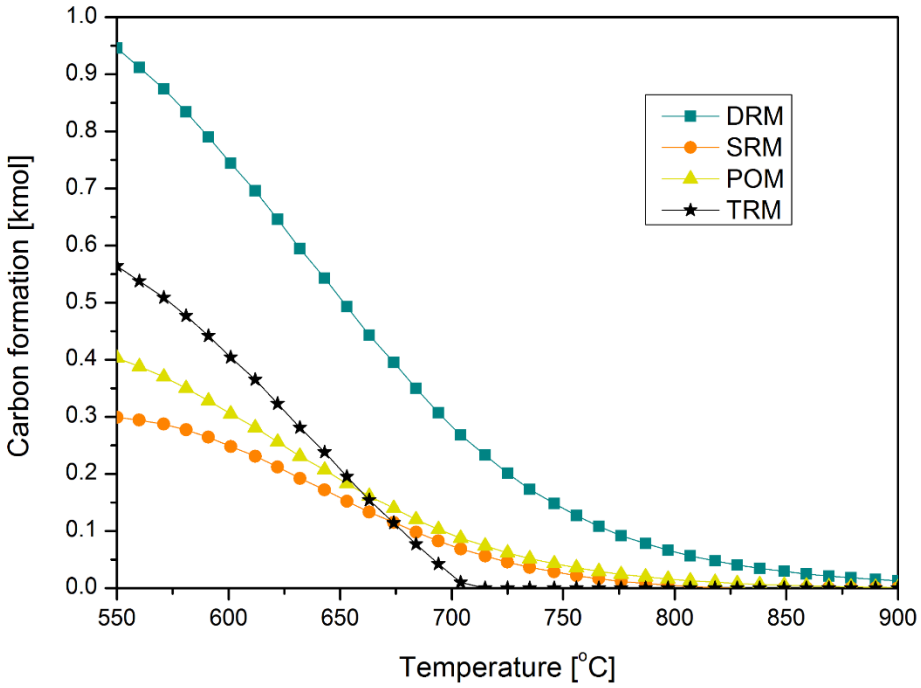

Fig. 3.7 Equilibrium carbon content as a function of temperature (DRM: $CH_4/CO_2/Ar=1/1/8$, SRM: $CH_4/H_2O/Ar=1/1/8$, POM: $CH_4/O_2/Ar=1/0.5/8.5$, TRM: $CH_4/CO_2/H_2O/O_2/Ar=1/0.5/0.5/0.1/7.9$; p= 1 bar).

3.2. Thermodynamic calculations for tri-reforming of methane assuming direct application of CO_2 from flue gases

In order to examine the industrial feasibility of tri-reforming of methane process, a calculation was carried out for typical flue gas compositions from natural gas-fired power station, assuming different amounts of methane added. The gas compositions used in the calculations are listed in cp. Table 3.2, i.e.:

(i) $CH_4/CO_2/H_2O/O_2/Ar = 1/1/2/0.3/5.7$,

(ii) $CH_4/CO_2/H_2O/O_2/Ar = 1.5/1/2/0.3/5.2$,

(iii) $CH_4/CO_2/H_2O/O_2/Ar = 2/1/2/0.3/4.7$,

(iv) $CH_4/CO_2/H_2O/O_2/Ar = 3/1/2/0.3/3.7$.

Fig. 3.8 presents methane conversion as a function of temperature. Different conversions can be obtained considering lower or higher CH_4 content. Generally, with the higher methane content in the system, the 100% conversion may be reached at higher temperatures of the process.

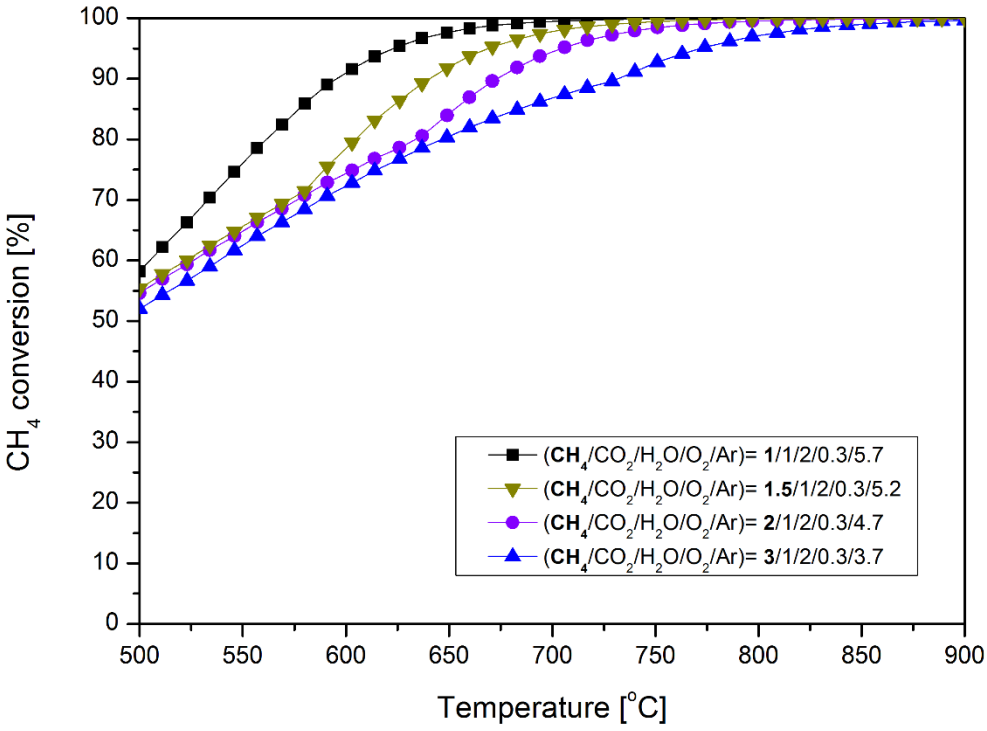

Fig. 3.8 CH_4 conversion as a function of temperature for TRM, assuming flue gas content of CO_2, H_2O and O_2 in the range typical for a natural gas-fired power station with different amounts of methane added.

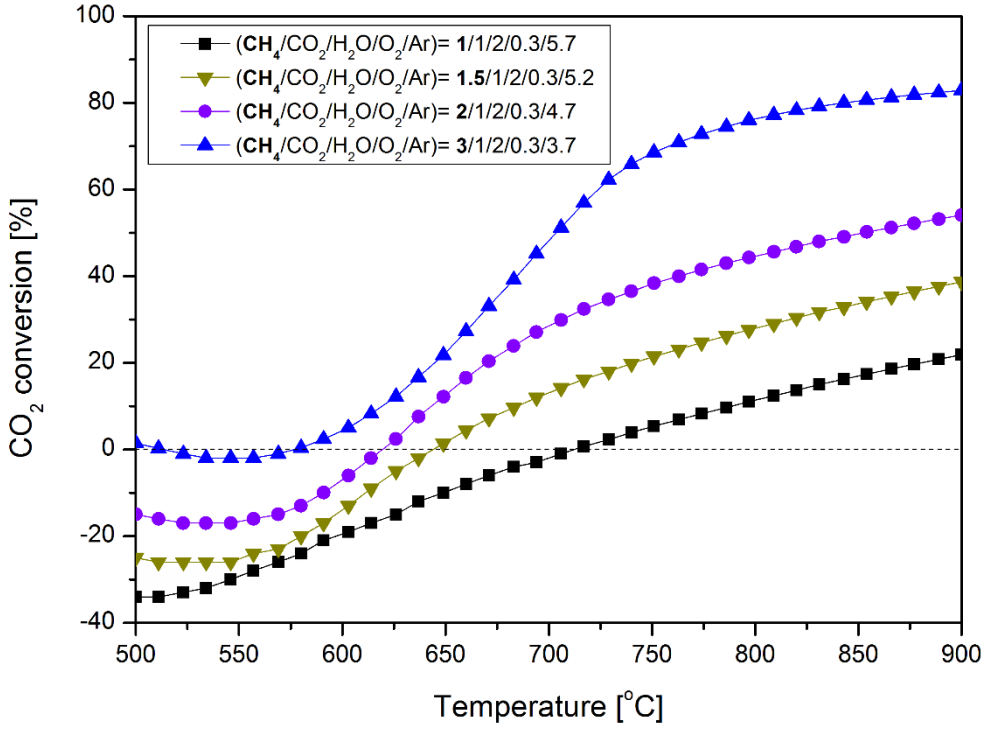

Fig. 3.9 CO_2 conversion as a function of temperature for TRM, assuming flue gas content of CO_2, H_2O and O_2 in the range typical for a natural gas-fired power station with different amounts of methane added.

CO_2 conversion as a function of temperature is reported in Fig. 3.9. Significant effect of the addition of methane may be observed. Higher amount of CH_4 allows to convert more CO_2. For the composition of $CH_4/CO_2/H_2O/O_2/Ar$ = 3/1/2/0.3/3.7, carbon dioxide started to be converted at temperature of 575 °C. When the mixture contained lower CO_2/CH_4 ratio higher temperature was required, i.e., 2, 1.5 and 1 at 625, 649 and 717 °C, respectively. At 700 °C, from the thermodynamic point of view, it is possible to convert ca. 15, 30 or 50% of CO_2, with respectively 1.5, 2 or 3 mol of CH_4 (per 1 mol of CO_2) in the gas feed.

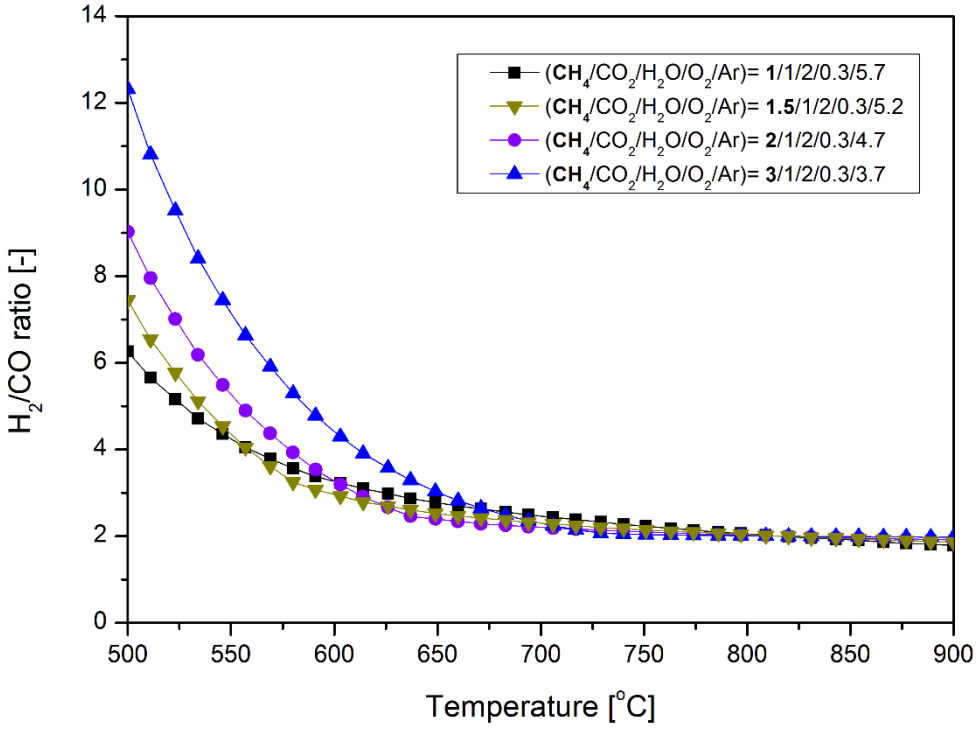

Fig. 3.10 H_2/CO molar ratio as a function of temperature for TRM, assuming flue gas content of CO_2, H_2O and O_2 in the range typical for a natural gas-fired power station with different amounts of methane added.

The H_2/CO molar ratio was calculated for the assumed gas compositions. A significant decrease in H_2/CO ratio may be observed with the increase in temperature. The most desired ratio, ca. 2.0, is observed at temperatures starting from 700 °C.

Fig. 3.11 presents carbon formation during TRM process. No carbon is formed at 500 °C when $CH_4/CO_2/H_2O/O_2/Ar$ = 1/1/2/0.3/5.7. The appropriate amount of methane added can lead to the suppression of carbon formation at the respectively higher temperatures. For feed gas composition containing 1.5, 2.0 and 3.0 vol.% of CH_4 respectively, 580, 637 and 740 °C is required.

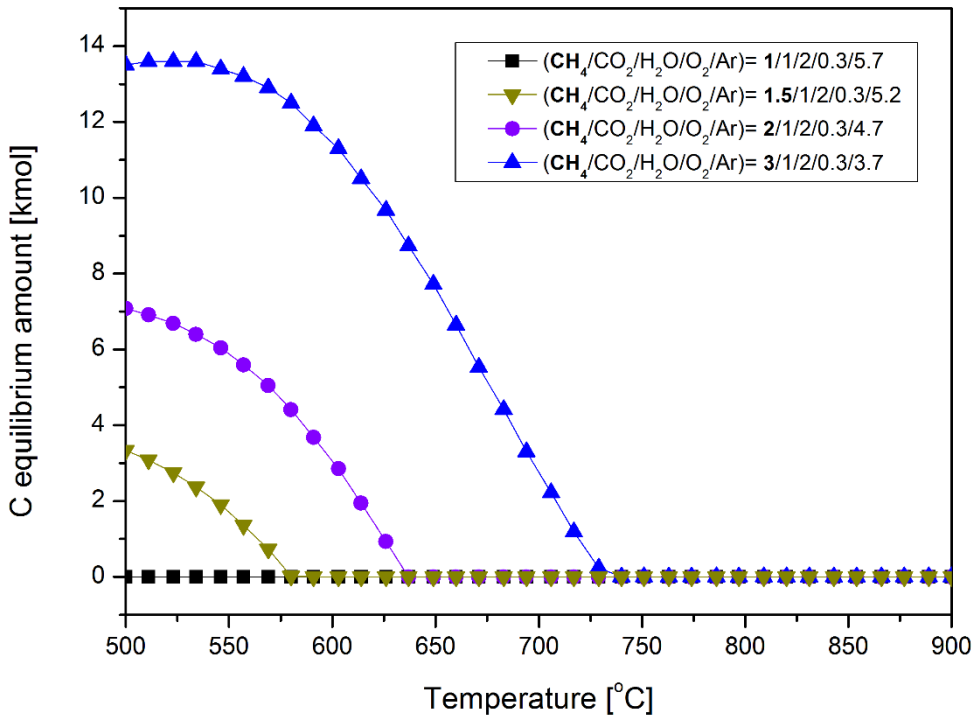

Fig. 3.11 Carbon equilibrium amount as a function of temperature for TRM, assuming flue gas content of CO_2, H_2O and O_2 in the range typical for a natural gas-fired power station with different amounts of methane added.

3.3. Conclusions

Thermodynamic equilibrium analysis was performed to examine possible conversions of CH_4 and CO_2. The thermodynamic calculations for the processes, such as dry reforming of methane (DRM), steam reforming of methane (SRM), partial oxidation of methane (POM), and tri-reforming of methane (TRM) were carried out.

Dry reforming of methane is likely to occur with high efficiency at very high temperature (over 700 °C), thus 700 °C was selected as a condition parameter for the catalytic experiments, in order to avoid carbon deposition, mainly taking place at low temperature (below 650 °C), and to limit possible metal sintering, likely the increase with the increase of temperature. Moreover, inhibition of side reactions, taking place at high temperature (higher than 800 °C), was considered.

The thermodynamic analysis of tri-reforming of methane carried out for typical flue gas composition from natural gas-fired power plant showed that it is possible to obtain at 700 °C high conversions of CH_4 (from 87 to 99%) and reasonable conversion of CO_2 (from 15 to 50%), as well as to avoid carbon formation even at 500 °C. The amount of natural gas (source of methane) added to the flue gases determined the conversion of CO_2 and the obtained H_2/CO ratio. There is a growing CO_2 conversion with higher contents of CH_4 in the feed. A possible suppression of carbon formation required at least 740 °C when $CH_4/CO_2/H_2O/O_2/Ar$ = 3/1/2/0.3/3.7, which is a higher temperature that the ones registered for other gas feed compositions. Also, 30 vol.% of methane allowed to obtain the highest possible conversion of CO_2. However, the key role for such gas conditions would be finding a stable catalyst, which would prevent deactivation caused by carbon deposition.

Chapter 4 – Dry reforming of methane (DRM)

4.1. Yttrium promotion of nickel-based double layered-hydroxides

4.2. Co-impregnation with zirconium and yttrium of nickel-based double layered-hydroxides

4.3. Co-precipitation with zirconium and impregnation with yttrium versus co-precipitation with zirconium and yttrium

4.4. Co-precipitation with cerium and impregnation with yttrium of nickel-based double layered-hydroxides

Chapter 4 – Dry reforming of methane (DRM)

4.1. Yttrium promotion of Ni-based double layered-hydroxides

Yttrium is a rare-earth element that has recently attracted large interest for catalytic applications. As reported by Francis and Whitlow [307] yttrium oxides show high temperature oxidation resistance in the presence of carbon dioxide. Many literature studies are focused on yttrium oxide studied as a support for DRM catalysts [308–310]. However, there are only a few literature reports describing the role of yttrium as a possible promoter in the DRM reaction [172,311–313]. B. Li et al. [311] observed high resistance towards carbon deposition for Y-promoted Ni-SBA-15 catalysts, which was attributed to high dispersion of yttrium with nickel nanoparticles, and the ability of yttrium to create oxygen vacancies. Similar properties were also observed in Y-$Ce_{0.75}Zr_{0.25}O_2$ catalysts [312]. Taherian et al. [313] reported a positive influence on controlling the nickel size and its dispersion into the mesopores of Ni/SBA-15 catalyst after modification with Y_2O_3. Moreover, Ni-Y/KIT-6 catalyst exhibited better dispersion of nano-sized Ni particles inside the pores of the support as compared to Ni/KIT-6 material [172]. Also, the formation of coke was lower for Y-modified catalyst in the initial stability test at 700 °C. Furthermore, B. Li et al. [208] studied Ni/Y/Al_2O_3 catalyst with yttrium introduced via different types of impregnation, and observed improved stability of the modified samples. However, in a recent study by Huang et al. [314] the impregnated NiO-Y_2O_3-Al_2O_3 mesoporous catalysts were reported to be less stable than the samples prepared with a one-pot evaporation-induced self-assembly method. The former resulted in the creation of loosely attached Ni particles on the support, which was the reason for fast deactivation of the catalyst due to graphitic carbon formation. The second method revealed the presence of Ni particles strongly anchored to the Al_2O_3 support. This resulted in an improvement of catalytic activity and stability. The best results were obtained for a catalyst containing ca. 2 wt.% of yttrium, which was attributed to the high surface area, small nickel particles and very high nickel dispersion.

No studies concerning the influence of yttrium on Ni-Mg-Al double-layered hydroxides have been reported in the literature. Only a few studies have dealt with Mg-Al hydrotalcites modified with Y for epoxidation [266], cyanoethylation [268] and aldol condensation [270].

Thus, the aim of the work presented in this subchapter was to examine the influence of Y promotion on the physico-chemical properties of the resulting catalysts, their structure and performance in DRM. Five yttrium-modified catalysts, containing 0.2, 0.4, 0.6, 2.0 and 3.0 wt.% of Y were prepared.

4.1.1. *Physicochemical properties*

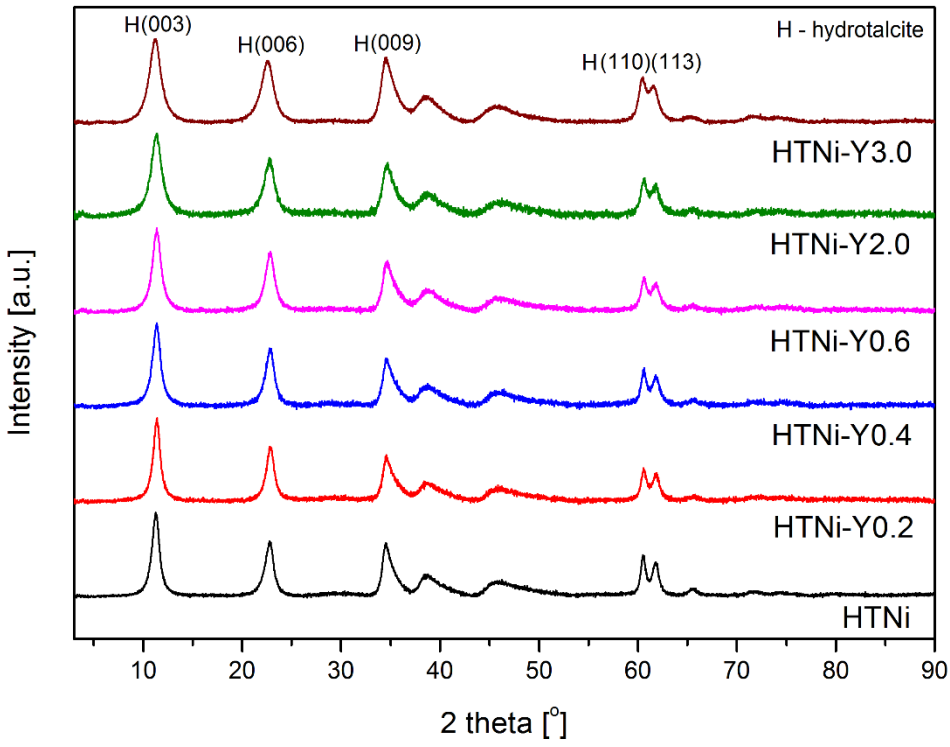

Fig. 4.1 XRD patterns of fresh synthesized catalysts HTNi, HTNi-Y0.2, HTNi-Y0.4, HTNi-Y0.6, HTNi-Y2.0 and HTNi-Y3.0.

XRD diffractograms of freshly synthesized catalysts are presented in Figure 4.1. The layered rhombohedral structure of $Mg_6Al_2(OH)_{16}CO_3{\cdot}4H_2O$ (ICOD 00-014-0191) was registered at 2θ = 11, 22, 35, 61 and 62°, corresponding to (003), (006), (009), (110) and (113) planes, respectively. A small shift of the d_{003} and d_{006} towards lower angles was registered after promotion with 2 wt.% and 3 wt.% of

yttrium, indicating the presence of intercalation anions. This shift indicates that CO_3^{2-} was not the only anion in the interlayer regions [248–250,284].

Table 4.1 Structural parameters of the freshly synthesized materials. Elemental composition and textural properties for the calcined materials. The numbers in brackets are nominal values.

Catalyst	XRD			XRF			N_2 sorption		
	Structural parameters Fresh materials			Elemental composition Calcined materials			Textural properties Calcined materials		
	a [Å][1)]	c [Å][2)]	c' [Å]	Ni^{2+} [wt.%]	Y^{3+} [wt.%]	M^{2+}/M^{3+} [-]	S_{BET} [m^2/g][3)]	V_p [cm^3/g][4)]	d_p [nm][5)]
HTNi	3.06	23.45	7.8	20	-	3.6 (3.0)	120	0.6	19
HTNi-Y0.2	3.06	23.36	7.8	19	0.2 (0.2)	3.2 (3.0)	127	0.5	16
HTNi-Y0.4	3.06	23.38	7.8	21	0.4 (0.4)	3.5 (3.0)	120	0.5	15
HTNi-Y0.6	3.06	23.37	7.8	19	0.6 (0.6)	3.5 (3.0)	162	0.5	11
HTNi-Y2.0	3.06	23.42	7.8	18	1.8 (2.0)	3.4 (3.0)	192	0.6	14
HTNi-Y3.0	3.06	23.54	7.8	17	2.8 (3.0)	3.8 (3.0)	142	0.5	13

[1)] calculated from (110) spacing $a=2d_{(110)}$ as suggested by Cavani et al. [244]

[2)] calculated from XRD patterns of the fresh catalysts, from the position of the three first reflections $c=d_{(003)} + 2d_{(006)} + 3d_{(009)}$, as suggested by Liu et al. [207]

[3)] specific surface areas calculated from the BET equation

[4)] mesopore volumes derived from the BJH desorption calculation method

[5)] pore size distribution obtained from the BJH desorption calculation method

The values of the unit cell parameters *a* and *c* (for non-calcined materials) are shown in Table 4.1. The obtained values of *c*, which refers to the triple distance between brucite-like layers, remained practically unchanged after Y-modification as compared to the non-modified material, except for HTNi-Y3.0. For the latter catalyst some deposition of Y compound on the external surface may be assumed. Pavel et al. [266] studied Ni-free Mg/Al hydrotalcites modified with Y (0.49 and 1.25 wt.%). For both materials the authors found an increase of *c* parameter suggesting Y aggregation on the external

surface. The *c´* parameter, equal to one brucite-like sheet and one interlayer (*c´=c/3*), is 7.8 Å and constant for our HTNi-Y catalysts, indicating the presence of interlayer CO_3^{2-} (7.65 Å) and NO_3^- (8.79 Å) anions [244,248–250]. According to Kuśtrowski et al. [248], in theory the calculated values are in agreement with the size of the anions intercalated into the interlayer space. It should be noted, however, that the gallery heights are slightly lower than the corresponding free anions diameters due to a high content of Al^{3+} in the hydrotalcites, leading to the strong interaction of the interlayer anions with the brucite-like sheets. The lattice parameter *a* is stable for all catalysts (3.06 Å), although García-García et al. [315] assumed that the introduction of yttrium into DLHs layers, considering its ionic radius bigger than that of Mg and Al (Y^{3+}=1.04 Å, Mg^{3+}=0.86 Å, Al^{3+}=0.675 Å) [316], may cause lattice distortions, i.e. changes in the lattice parameter *a*. On the other hand, Fernández et al. [316], reported that only yttrium loading higher than 4 wt.%, could result in distortions in the DLHs layers, recognised as very low crystallinity observed in XRD patterns. As the amount of Y introduced into the studied catalysts was lower, the stability of the lattice parameter *a* does not contradict the possibility of introduction of Y into the structure of double-layered hydroxides.

Fig. 4.2 presents XRD patterns of the calcined materials, showing reflections of Ni-Mg-Al periclase-mixed oxides (ICOD 00-045-0946) (2θ ca. 36.7, 43 and 62.5°), which are characteristic for double-layered hydroxides after thermal treatment at 550 °C [203,285,317]. For the HTNi-Y3.0 catalyst calcination at 550 °C resulted in the stabilization of the $Mg_6Al_2(OH)_{16}CO_3{\cdot}4H_2O$ phase (ICOD 00-014-0191), as evidenced by reflections at 2θ of ca. 11, 22 and 35°, corresponding to crystal planes of (003), (006), (009), respectively [285]. No separate yttrium phase was registered in XRD patterns, either due to low loading of this metal or the presence of Y-compound in amorphous form.

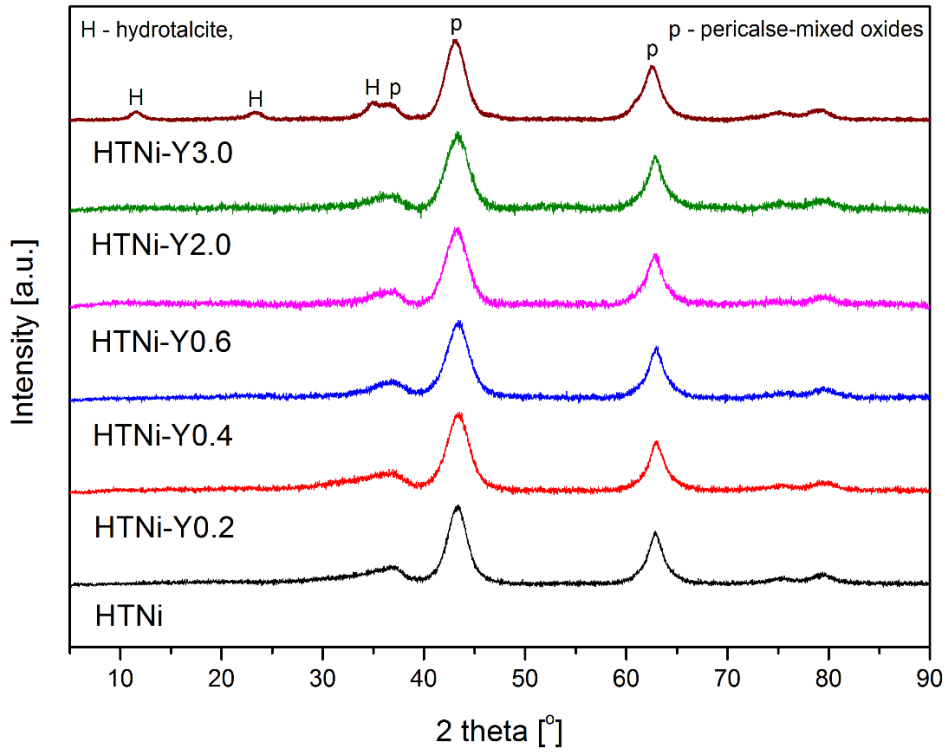

Fig. 4.2 XRD patterns of the calcined catalysts HTNi, HTNi-Y0.2, HTNi-Y0.4, HTNi-Y0.6, HTNi-Y2.0 and HTNi-Y3.0.

The contents of Ni and Y, together with the assumed M^{2+}/M^{3+} ratio, are listed in Table 4.1. The studied catalysts contained ca. 20 wt.% of Ni and yttrium contents close to the nominal values, i.e., 0.2, 0.4, 0.6, 1.8 and 2.8 wt.%. The calculated ratios of M^{2+}/M^{3+}, i.e., (Ni+Mg)/(Al+Y), were relatively close to the values which were assumed during the synthesis step.

Fig. 4.3 shows IV type isotherms for the calcined materials, which are characteristic for mesoporous structures [206,260]. The obtained hysteresis loop indicates the presence of slit shaped pores with nonuniform size and shape [292]. The adsorbed amounts decreased with the increasing doping with yttrium (up to 0.4 wt.%), which possibly may be related to the observed decrease in pore size. After promotion with 0.6 and 2.0 wt.% of yttrium an increase in amount adsorbed was registered, and for the catalyst containing 3.0 wt.%-loading again a decrease was found. Specific surface area for the calcined catalysts varied from 120 to 192 m^2/g, with the highest S_{BET} observed for HTNi-Y2.0 (Table 1.1). As presented in Fig. 4.4, small contents of yttrium did not change the S_{BET} (within experimental error), higher amounts of 0.6 and 2.0 % increased the specific surface area while doping with 3 wt.%

resulted in decreased S_{BET}. Total pore volume remained stable after modification with yttrium. However, pore diameters slightly decreased as compared to HTNi catalyst.

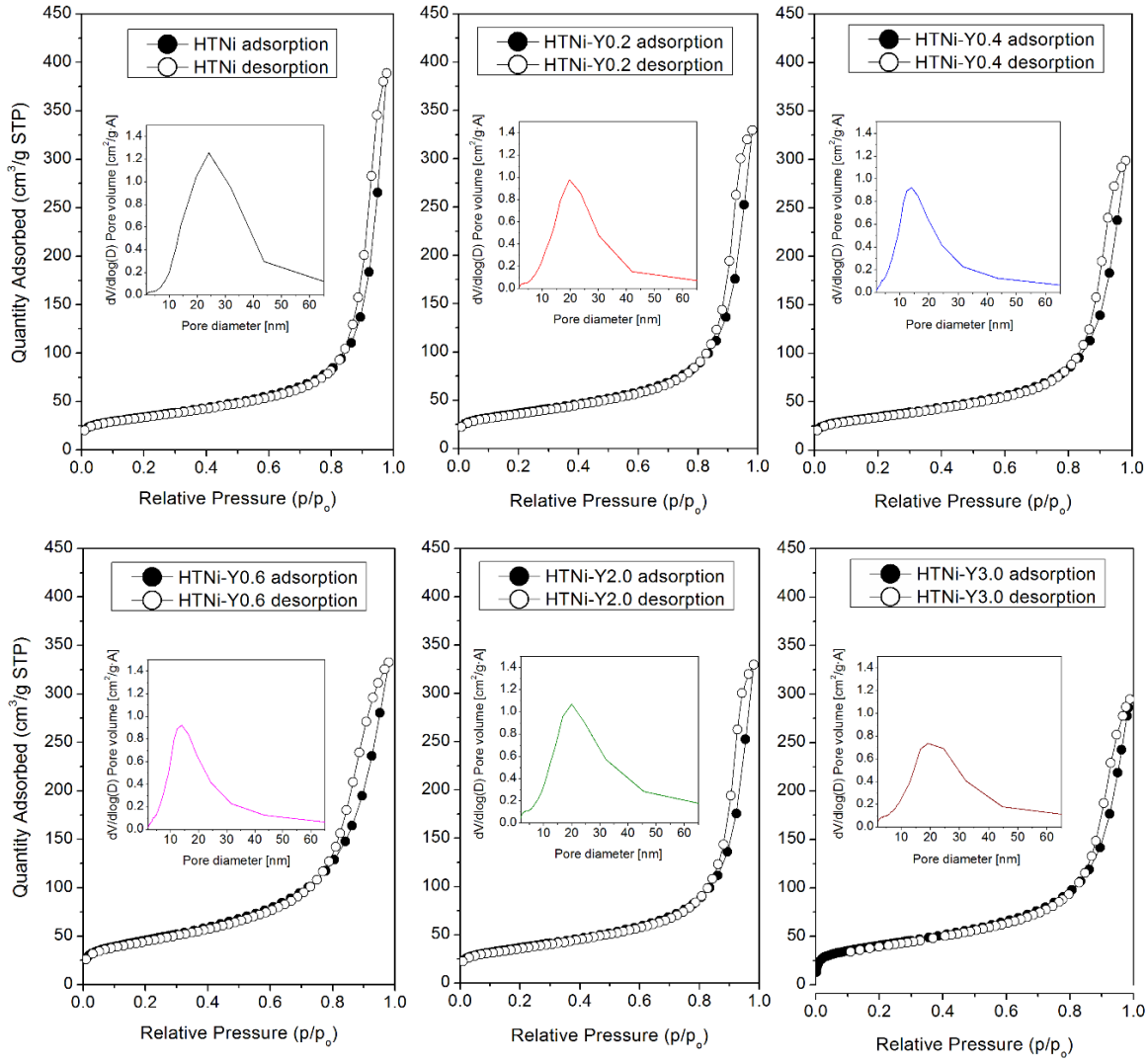

Fig. 4.3 N_2 adsorption/desorption isotherms and pore size distribution for HTNi, HTNi-Y0.2, HTNi-Y0.4, HTNi-Y0.6, HTNi-Y2.0 and HTNi-Y3.0.

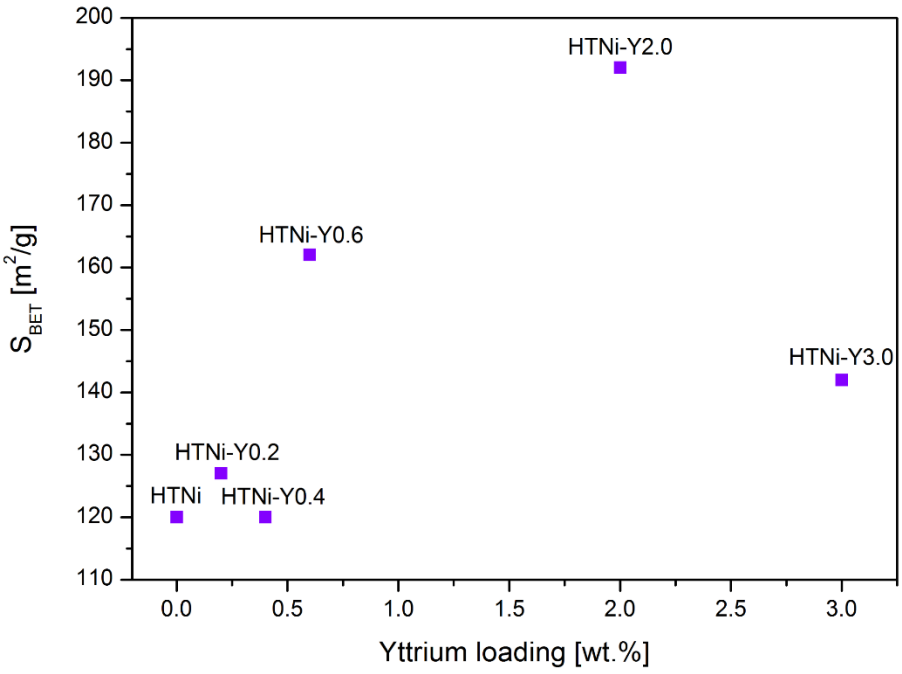

Fig. 4.4 Correlation between nominal yttrium loading and specific surface area.

The significant increase in S_{BET} for the catalysts promoted with 0.6 wt.% and 2 wt.% Y, positively influences the textural properties of Ni-based catalyst and is supported by literature findings. As reported by Kim et al. [318] a partial crystal deformation of double-layered hydroxides occurs upon calcination, in which octahedral Al^{3+} ions migrate to tetrahedral positions resulting in the enhancement of S_{BET} and in evolution of mesopores. Similar effect was observed by Huang et al. [314], who reported that the modification of NiO-Al_2O_3 supports within yttrium loading of 1.3-2.44 wt.% led to the S_{BET} enhancement. On the other hand, the decrease in S_{BET} observed for HTNi-Y3.0 suggests a possible partial blocking of porous system, and together with the increase in the lattice parameter *c* for HTNi-Y3.0, may indicate that some yttrium aggregates were deposited on the external surface of this catalyst, similarly as suggested by Pavel et al. [266]. Thus the improvements in the catalytic performance in dry reforming of methane can be expected for HTNi-Y2.0, as suggested by the relation between specific surface area and stability in DRM reported in the article of Huang et al. [314].

4.1.2. *Reducibility, basicity, Ni dispersion and crystallite size*

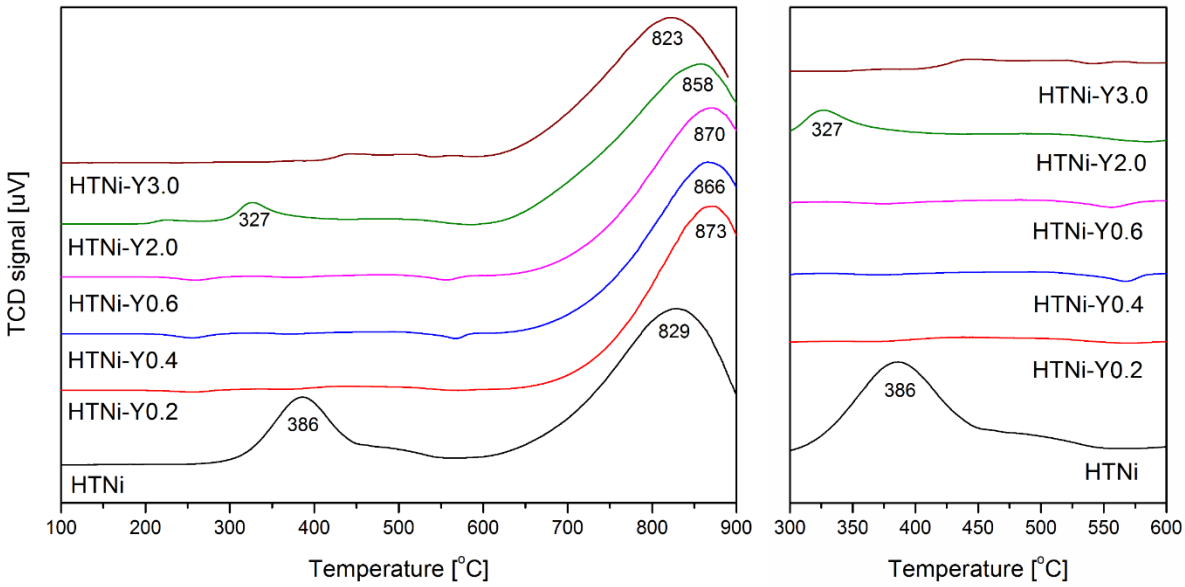

Fig. 4.5 Temperature-programmed reduction (TPR-H_2) profiles of the calcined catalysts.

TPR-H_2 profiles of calcined Y-modified Ni/Mg/Al double-layered hydroxides are presented in Fig. 4.5. The profile for HTNi shows two wide peaks with maxima at 386 and 829 °C, respectively, which may be attributed to NiO weakly-bonded to the mixed oxides structure and NiO present in the structure of mixed oxides, respectively [197,205,207,319]. According to Hu et al. [320] only a part of nickel can be reduced, i.e., Ni–O–Ni species, while the Ni–O–Mg species are almost impossible to reduce. After the yttrium addition, the temperature of the maximum of the peak at the high temperature region (T_{max}) showed a shift to higher values, indicating stronger interaction of Ni species with the support as compared to HTNi catalyst. The shift depended on the amount of introduced yttrium and the T_{max} formed a sequence: 873 °C (Y 0.2 wt.%) > 866 °C (Y 0.4 wt.%) ≈ 870 °C (Y 0.6 wt.%) > 858 °C (Y 2.0 wt.%) > 829 °C (HTNi). For the catalyst modified with 3.0 wt.% of yttrium a minimal shift to lower temperature was observed (823 °C). The shift of the T_{max} towards higher temperatures, together with the presence of NiO, was also observed by Huang et al. [314] for NiO-Al_2O_3 materials modified with similar amounts of Y_2O_3 (1.30 and 2.44 wt.%). However, when higher amounts of Y were introduced (4.86 wt.%) the T_{max} had lower value, in good agreement with the presented results (cp. Fig. 4.5). Different trends in reducibility changes depending on the amount of introduced promoter were reported for other

studied catalysts based on double-layered hydroxides [203], e.g. when double-layered hydroxide-derived catalysts were modified with low amounts of zirconia a decrease in reducibility was observed, in contrast to reducibility increase caused by higher ZrO_2 loadings [203]. The authors ascribed this effect to the location of ZrO_2 in or out of hydrotalcite structure. Higher loading of zirconia led to its deposition outside the periclase structure, resulting in weaker interactions with Ni, and the presence of weakly bonded NiO, in agreement with the observations for the here studied HTNiY-catalysts. Then, this supports the hypothesis of Y-compound at least partly deposited on the outer surface of HTNi-Y3.0, discussed above.

Additionally, Y-modification influenced the amount of weakly bonded Ni (low temperature peak, shown in more detail in the right hand-side enlargement of Fig. 4.5). For HTNi an additional medium-strong peak may be observed at 386 °C, which was reported for numerous catalysts with Ni introduced onto a support by e.g. impregnation [297,321–323], or co-precipitation method [205,285,324,325]. A shorter peak at this temperature region may be observed only for HTNi-Y2.0. Additionally, very weak peaks appear at ca. 450 and 500 °C for HTNi, HTNi-Y2.0 and even for HTNi-Y3.0. They arise from either weakly-bonded NiO or bulk NiO [259]. For the latter Mile et al. [326] reported that two reduction peaks may arise from reduction of bulk NiO: (i) at ca. 250 °C from Ni^{3+} reduction, and (ii) reduction of Ni^{2+} at ca. 400 °C. Similar was reported by Kadkhodayan et al. [327], who observed a double peak arising from the reduction of bulk NiO species at the temperature range of 300-400 °C.

Hydrogen consumption values obtained during reduction of the calcined materials are listed in Table 4.2. The highest consumption of 0.209 mmol H_2/g was observed for non-modified HTNi catalyst. After promotion with yttrium, the values of hydrogen uptake decreased to 0.143, 0.151, 0.145, 0.165 and 0.148 mmol H_2/g for HTNi-Y0.2, HTNi-Y0.4, HTNi-Y0.6, HTNi-Y2.0 and HTNi-Y3.0 catalysts, respectively. The higher H_2 consumption in the HTNi catalyst, together with lower temperature of reduction maximum, may be due to the weaker interaction between Ni and the support, as well as the presence of bigger NiO crystallites loosely attached to the surface for the HTNi catalyst.

Table 4.2 Hydrogen consumption and chemisorption results for the Y-promoted catalysts.

Catalyst	TPR-H_2 Calcined materials	H_2 chemisorption Calcined materials	N_2 sorption Reduced materials		
	H_2 consumption [mmol H_2/g]	Ni dispersion [%]	S_{BET} [m^2/g][1)]	V_p [cm^3/g][2)]	d_p [nm][3)]
HTNi	0.209	8.9	68	0.4	21
HTNi-Y0.2	0.143	9.5	50	0.3	14
HTNi-Y0.4	0.151	10.7	51	0.4	11
HTNi-Y0.6	0.145	17.7	44	0.3	9
HTNi-Y2.0	0.165	19.8	67	0.6	12
HTNi-Y3.0	0.148	11.9	117	0.4	13

[1)] specific surface areas calculated from the BET equation

[2)] mesopore volumes derived from the BJH desorption calculation method

[3)] pore size obtained from the BJH desorption calculation method

The dispersion of metallic nickel calculated from H_2 chemisorption is shown in Table 4.2. Fig. 4.6 shows the relation between dispersion and the content of promoting Y. Thus, a positive influence of yttrium promotion resulting in higher Ni dispersion may be clearly seen. The dispersion values are 8.9, 9.5, 10.7, 17.7, 19.8 and 11.9 % for HTNi, HTNi-Y0.2, HTNi-Y0.4, HTNi-Y0.6, HTNi-Y2.0 and HTNi-Y3.0, respectively. However, it may be also observed (Fig. 4.6) that there is an optimal amount of Y-promotion where the increase in dispersion is concerned (2.0 wt.%). For too high amounts of Y, which, as suggested by other results discussed above, is at least partly deposited on the outer surface of the catalysts, the increase in dispersion is similar as that for HTNi-Y0.4. As reported by Huang et al. [314], enhanced dispersion leads to more stable catalytic performance in dry reforming of methane, since a higher number of accessible metallic sites are created on the surface of the catalyst. So, it may be expected that HTNi-Y0.4 and HTNi-Y3.0 may show similar activity. However, it should be taken into account that apart from dispersion, also the size of crystallites and basicity play a very important role in DRM.

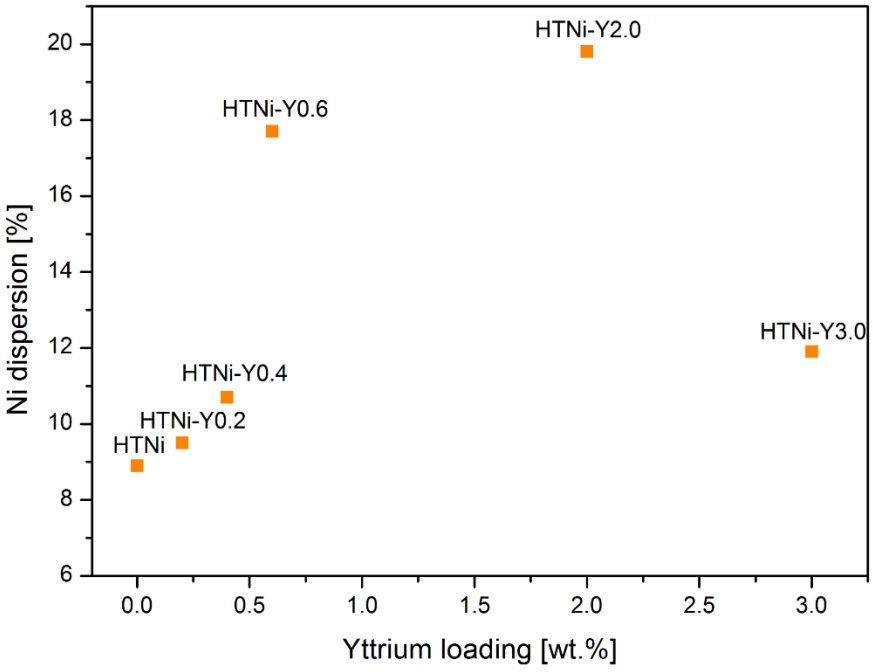

Fig. 4.6 Correlation between nominal yttrium loading and metallic Ni dispersion.

The textural properties of the reduced materials are listed in Table 4.2. The specific surface area decreased twice for the unmodified material HTNi. Comparable effect was observed for the Y-promoted catalysts, for which much lower S_{BET} than for the calcined samples were registered (cp. Table 4.1). The decrease in the specific surface area is related to the transformation of the NiO-MgO-Al_2O_3-(Y_2O_3) mixed-oxides into Ni^0-MgO-Al_2O_3-(Y_2O_3). The nickel oxide was reduced and partially covered the surface with its metallic phase. Only a small S_{BET} decrease was observed for HTNi-Y3.0, i.e., 142 m^2/g for the calcined sample versus 117 m^2/g for the reduced one. This could have arisen from the stabilization of hydrotalcite structure (as described further in the text in XRD section). For all samples the mesopore volume and pore diameters decreased in contrast to the porous properties recorded for calcined samples.

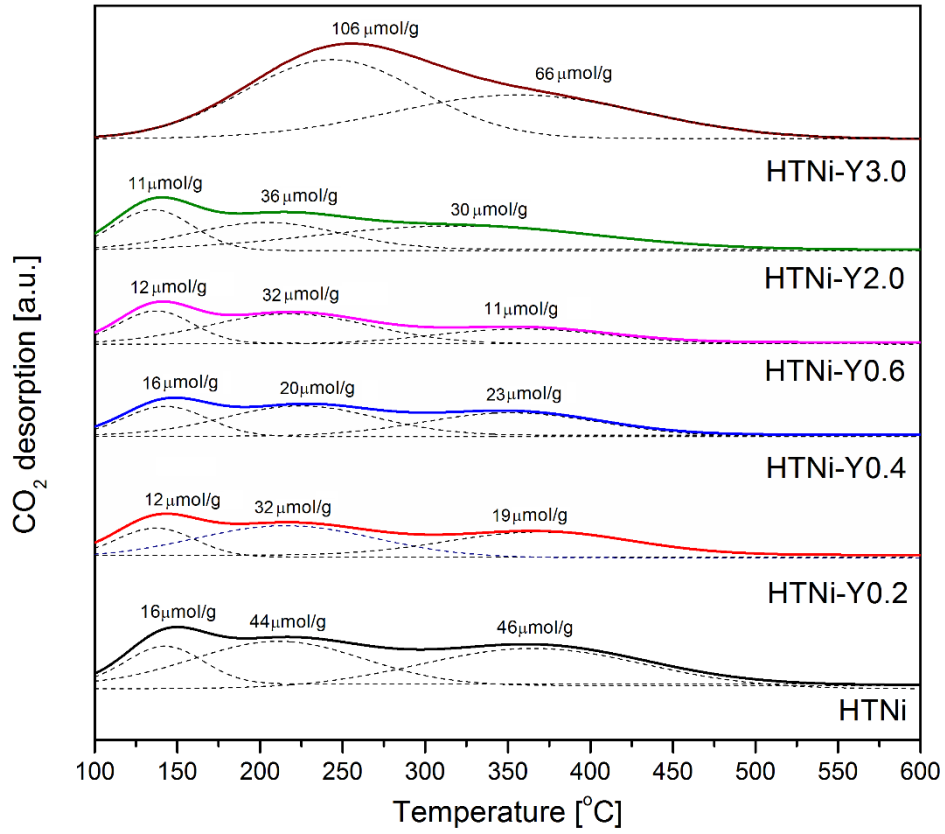

Fig. 4.7 Temperature-programmed desorption (TPD-CO_2) profiles for the reduced materials.

Table 4.3 The number of basic sites and their percentage distribution derived from TPD-CO_2.

Catalyst	TPD-CO_2						
	Number of basic sites [μmol/g]				Percentage distribution [%]		
	Weak	Medium	Strong	Total basicity	Weak	Medium	Strong
HTNi	16	44	46	107	15	41	43
HTNi-Y0.2	12	32	19	63	18	45	34
HTNi-Y0.4	16	20	23	59	28	34	38
HTNi-Y0.6	12	32	11	55	22	58	20
HTNi-Y2.0	11	36	30	77	15	47	38
HTNi-Y3.0	-	106	66	173	-	62	38

Basicity of the reduced catalysts, measured by TPD-CO_2, is shown in Fig. 4.7. Three types of basic sites can be distinguished with maxima at (i) 135-150 °C, (ii) 203-247 °C and (iii) ca. 316-367 °C, respectively. According to literature, they are ascribed to weak (Brønsted basic sides, such as hydroxyl groups), medium (Lewis acid-base sites), and strong basic sites (Lewis basic sites associated with oxygen anions) [205,207]. The data in Table 4.3 show that total basicity was the highest for the non-modified HTNi catalyst, and similar in value to a comparable HT-25Ni studied by Dębek et al. [285]. The latter was found to have optimal basicity for DRM. It should be mentioned additionally, that the dependence of CO_2 conversion on the basicity of double-layered hydroxides with different basicity was rather weak, with the exception of the catalyst containing low amount of Ni (5 wt.%) (Fig. 4.8). The catalysts studied by Dębek et al. (cp. Fig. 4.8) containing 25 to 100% Ni showed CO_2 conversion between ca. 37 and 40 %, despite a large difference in basicity. This indicates that a certain level of basicity is necessary for DRM, but other factors, such as reducibility, dispersion and the size of crystallites also play an important role, so an appropriate balance of all must be kept.

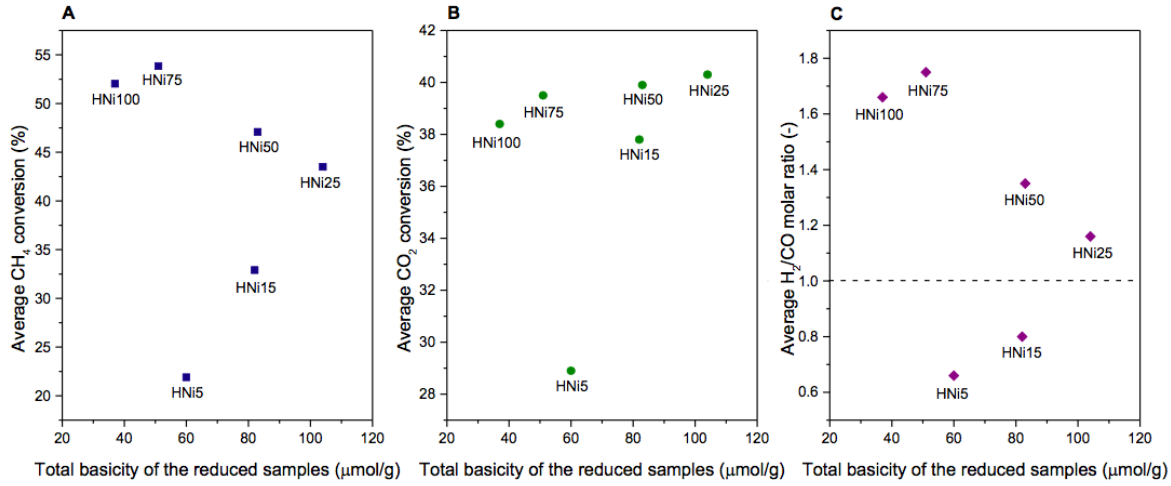

Fig. 4.8 Average conversions of methane (A), carbon dioxide (B) and H_2/CO molar ratio (C) registered during 5 h DRM catalytic tests (CH_4/CO_2/Ar=1/1/8, 550 °C, GHSV= 20,000 h^{-1}) as a function of catalysts basicity in the study of Dębek [64]. Reprinted with permission of the author.

The addition of Y modified both the number and the distribution of basic sites. After promotion with this metal in the range of 0.2-2.0 wt.%, the total basicity decreased, showing the lowest value of 55

µmol/g for HTNi-Y0.6, and slightly higher for other catalysts, i.e., 59, 63, and 77 µmol/g for HTNi-Y0.4, HTNi-Y0.2 and HTNi-Y2.0, respectively. The amount of each type of sites (weak, medium and strong) in the HTNi-Y materials studied in this work also decreased compared to HTNi. A decrease of total basicity caused by Zr or Ce promotion was also reported elsewhere [188,203,204]. Although the basicity was lower, it did not negatively affect DRM performance of the promoted catalysts. Indeed, the modification with Zr or Ce resulted in better stability and/or activity. On the other hand, the HTNi-Y3.0 showed different basicity distribution compared to the materials having 0.2-2.0 wt.% of Y. A shift to stronger sites was recorded, significantly increasing a number of medium ones, at the expense of the weak sites. As a result, the HTNi-Y3.0 catalyst showed the highest total basicity among all studied catalysts, i.e., 173 µmol/g (Table 4.3). Similar results were reported by Wierzbicki et al. [259] for La-promoted Ni-based double-layered hydroxides. As suggested by these authors, low loading of promoter may cause a partial blocking of the basic sites in the mixed oxides of DLHs, and only higher loading of metal can result in the creation of new basic sites.

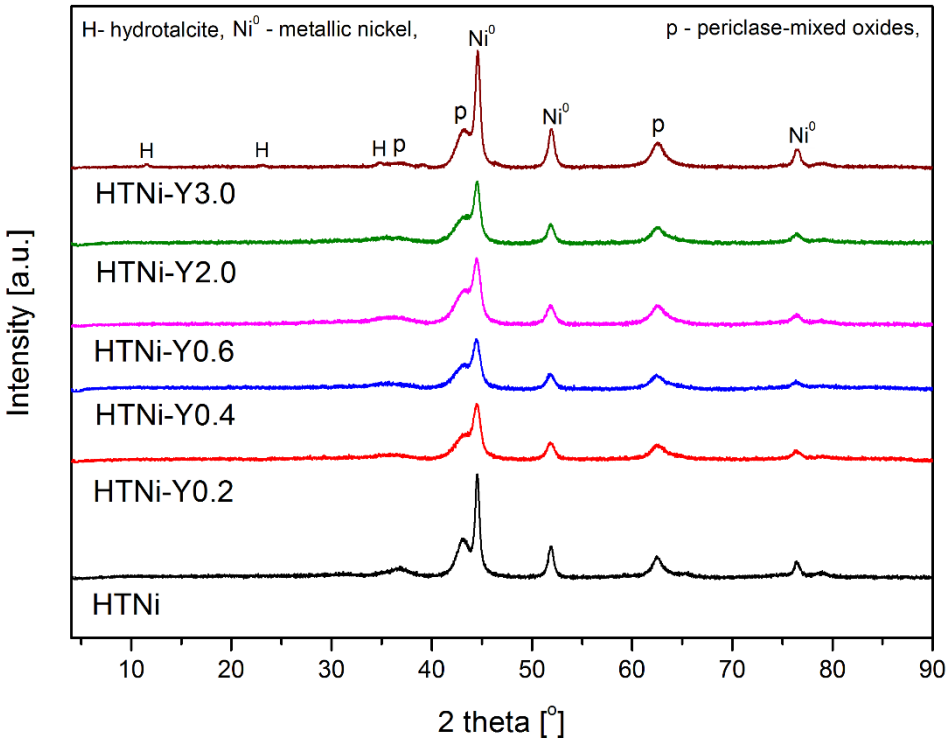

Fig. 4.9 XRD patterns for the reduced catalysts HTNi, HTNi-Y0.2, HTNi-Y0.4, HTNi-Y0.6, HTNi-Y2.0 and HTNi-Y3.0.

Fig. 4.9 shows XRD diffractograms of the reduced catalysts, in which characteristic metallic nickel phase (ICOD 01-087-0712) is evidenced by the presence of reflections at 2θ ca. 44.5, 53, 76.5°, corresponding to crystal planes of (111), (200), (220). Also, a periclase-mixed oxides phase (2θ ca. 36.7, 43, 62.5°) is observed [172,205,207,328]. Table 4.4 compares the size of Ni particles, calculated from the 2θ diffraction peak at ca. 53° (corresponding to (200) crystal plane of Ni^0) using the Scherrer equation. It may be seen that the yttrium addition resulted in a decrease of nickel crystallites from ca. 8 nm for the unpromoted HTNi to ca. 6 nm for HTNi-Y (Table 4.4), with the exception of HTNi-Y3.0 catalyst which showed Ni crystallite size similar to that of HTNi (ca. 8 nm). A similar effect was observed for the Ni-Y-Al_2O_3 catalysts and better performance in DRM was attributed to the formation of these smaller Ni^0 particles [208,314]. The difference observed for HTNi-Y3.0 agrees well with the hypothesis that at least part of introduced yttrium formed aggregates on the external surface of the catalysts and was in poor contact with Ni.

Table 4.4 Average diameters of nickel particles in the reduced HTNi-Y catalysts.

Catalyst	**d_{Ni} from XRD [nm]**[1)]	**d_{Ni} from H_2 chemisorption [nm]**[2)]	**d_{Ni} from TEM [nm]**[3)]
HTNi	8	11	27
HTNi-Y0.2	6	10	n.m.
HTNi-Y0.4	5	9	n.m.
HTNi-Y0.6	6	5	16
HTNi-Y2.0	6	5	14
HTNi-Y3.0	8	8	n.m.

n.m. – not measured

[1)] based on the Scherrer equation, from the width at half-maximum of the XRD reflections at 2θ ca. 53°

[2)] calculated from d = 97.1/(%D) based on the assumption of spherical crystallites of uniform size

[3)] average diameter of Ni particles obtained from TEM image

The smaller Ni crystallite size is linked with improved dispersion, as confirmed by calculation carried out assuming spherical crystallites of the uniform size (Table 4.4). These values are in good agreement

with XRD calculations (Scherrer equation). A number of other studies also showed that H_2 or CO chemisorption results were in line with the values obtained from XRD [329–332].

In order to verify the Ni particle size, TEM analysis was carried out for three selected catalysts: HTNi, HTNi-Y0.6 and HTNi-Y2.0. For the reduced catalysts, randomly distributed Ni particles are observed (dark spots in the micrographs presented in Fig. 4.10). Smaller nickel particle sizes were registered for Y-promoted catalysts. The average particle size varies from 27 nm for the unpromoted HTNi, to 16 nm and 14 nm for HTNi-Y0.6 and HTNi-Y2.0, respectively (Table 4.4).

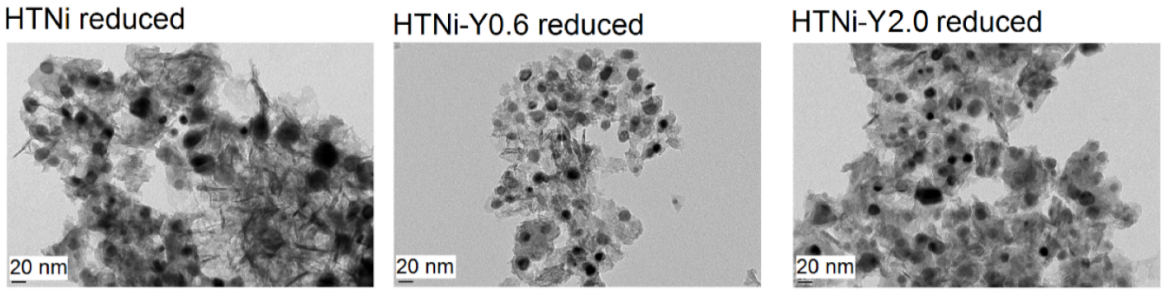

Fig. 4.10 TEM micrographs of HTNi reduced.

The reason for obtaining higher values from TEM analysis, as compared to XRD, may lie in differences in measurement techniques. By TEM, the particle size of all nickel aggregates is measured, irrespective if they are crystalline or amorphous. On the other hand, XRD data gives information on the average size of crystalline nickel particles.

The Ni crystallite size, calculated from the data obtained in these three characterization techniques, clearly shows a decrease in Ni particle size with Y addition (Table 4.4), with the exception of HTNi-Y3.0. The accuracy of these characterization methods was examined by Mustard et al. [298]. The authors described the application of TEM, H_2 adsorption and XRD for the determination of Ni crystallite size on supported catalysts, such as Ni/SiO_2, Ni/Al_2O_3 and Ni/TiO_2. As stated by the authors, the precision of each technique depends on Ni loading and its dispersion, as well as the textural properties of the used support.

4.1.3. *Catalytic activity and stability in DRM*

The discussion of the results of catalytic tests was divided into two parts, i.e., (i) promotion with yttrium of 0.2 and 0.4 wt.%, and (ii) promotion with yttrium of 0.6 and 2.0 wt.%, and compared to the performance of the unmodified material.

Figs. 4.11 A and 4.11 B present the CH_4 and CO_2 conversions of HTNi, HTNi-Y0.2 and HTNi-Y0.4 catalysts for DRM as a temperature programmed surface reaction (TPSR) in the range of 850-600 °C. The yttrium doping positively affected the activity of Ni-containing double-layered hydroxides, which is proven by higher conversion. It should be mentioned that experimental error (indicated by bars) is ca. 5%. The difference is higher in CH_4 conversion results (up to 700 °C), with the non-modified HTNi showing the lowest activity (Fig. 4.11 A). For CO_2 conversion, the catalysts reached values close to the equilibrium, and the differences were smaller for the discussed catalysts. It may be concluded that the addition of Y significantly improved catalytic performance, and a correlation between the increase of catalytic activity and the increasing Y content is clearly observed. In the temperature range of 600-700 °C, the materials doped with 0.2 and 0.4 wt.% of Y presented conversions higher than the one reported for the unmodified catalyst. However, at temperatures of 700 °C and higher, the positive influence of Y-promotion on CH_4 conversion decreased. At 700 °C HTNi and HTNi-Y0.2 showed similar activity, while HTNi-Y0.4 was still more active. CO_2 conversion was slightly higher than that of CH_4, and the H_2/CO ratio is presented in Fig. 4.11 C. Moreover, the values of H_2/CO ratio were lower than 1. The latter may be ascribed to the occurrence of reverse water-gas shift, which is a side reaction usually accompanying DRM [314]. Additionally, when more CH_4 than CO_2 was converted, the other side reactions such as direct methane decomposition and Boudouard reaction could have taken place [205], as discussed in **Chapter 1** (**Subchapter 1.3.2.1**).

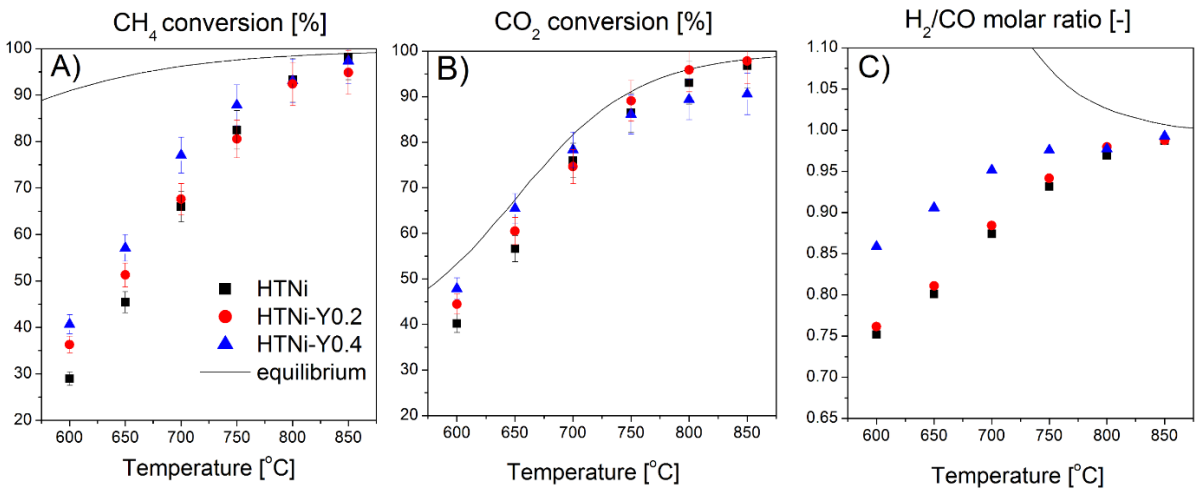

Fig. 4.11 Catalytic activity of HTNi-Y catalysts (with 0.2 and 0.4 wt.% of yttrium) in the temperature range of 850 to 600 °C: CH_4 conversion (A), CO_2 conversion (B), and H_2/CO molar ratio (C) versus temperature in DRM process ($CH_4/CO_2/Ar$=1/1/8, GHSV= 20,000 h^{-1}). The solid line represents the thermodynamic equilibrium (cp. Chapter 3).

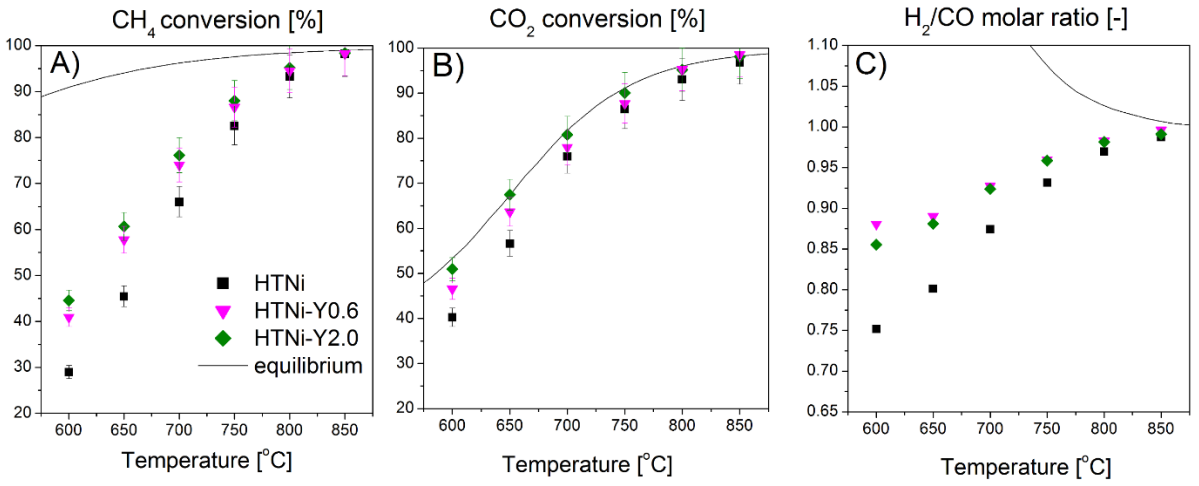

Fig. 4.12 Catalytic activity of HTNi-Y catalysts (with 0.6 and 2.0 wt.% of yttrium) in the temperature range of 850 to 600 °C: CH_4 conversion (A), CO_2 conversion (B), and H_2/CO molar ratio (C) versus temperature in DRM process ($CH_4/CO_2/Ar$=1/1/8, GHSV= 20,000 h^{-1}). The solid line represents the thermodynamic equilibrium (cp. Chapter 3).

Figs. 4.12 A-C show catalytic performance of Ni-based double-layered hydroxides modified with 0.6 or 2.0 wt.% yttrium (HTNi-Y0.6 and HTNi-Y2.0). The same positive trend may be observed as for the

materials doped with low amounts of yttrium (0.2 or 0.4 wt.%). Again, the non-modified HTNi had the lowest activity, both for CH_4 and CO_2 conversions (Figs. 4.12 A and B). The addition of Y significantly improved catalytic performance, and a correlation between the increase of catalytic activity and the increasing Y content can be observed. For example, at 700 °C, CH_4 conversion was 66, 74 and 76.2%, while CO_2 conversion was 76, 78 and 80.8%, respectively for HTNi, HTNi-Y0.6 and HTNi-Y2.0 catalysts. The same activity sequence was observed at 750 °C. Comparing the performance of HTNi-Y0.6 with HTNi-Y2.0, it may be observed that the one promoted with 2.0 wt.% Y is the most efficient in the whole temperature range of the experiment. Fig. 4.12 C presents H_2/CO molar ratio, with a similar trend as observed for 0.2 or 0.4 wt.% Y-doped materials, i.e., Y-modification led to values higher than for HTNi. Differences in the produced H_2/CO ratios at the lowest studied temperature of 600 °C are the highest. Most probably, other side reactions started to be more dominant than the dry reforming reaction, resulting in a slowly increasing fraction of CO compared to H_2 [313].

Comparing the catalytic results carried out for the whole series of the Y-modified catalysts, i.e., HTNi-Y(0.2-2.0), one can note that yttrium addition enhances the catalytic performance in dry reforming of methane (CH_4/CO_2=1) giving conversions for both CH_4 and CO_2 from 5% to 15% higher than for the unpromoted HTNi catalyst. However, no clear correlation between increasing yttrium loading and increasing activity may be drawn from this type of test.

Considering the experimental error, the conversions are only slightly different from each other. The differences are the highest in the moderate temperature range (600-700 °C), with HTNi-Y2.0 catalyst showing the highest activity. Considering thermodynamic limitations of the DRM reaction, and the decreasing carbon formation with the rising temperature (as discussed in **Chapter 3**, **Subchapter 3.2.2.**), longer experiments were carried out at 700 °C, in which the conversions could be ca. 10% higher than at 650 °C.

The isothermal runs were carried out at 700 °C for 5 hours under the same GHSV (flow, catalysts volume), as in the previously discussed experiments. The catalysts containing 0.4 or 2.0 wt.% Y and

additionally, in order to examine the influence of higher Y loading, the catalyst modified with 3 wt.% of Y were studied.

As shown in Figs. 4.13 A-C in the isothermal test, catalytic activity formed a sequence: HTNi < HTNi-Y2.0 < HTNi-Y0.4 < HTNi-Y3.0. All studied catalysts revealed relatively stable conversion values for 5 h. The conversion change, expressed as $\Delta = (|x_i - x_{5h}|/x_i \cdot 100)$, where "$x_i$" and "$x_{5h}$" relate to the initial values and those after 5 hours, respectively, are listed in Table 4.5. The initial and final gas conversions were considered. The initial CH_4 conversions recorded respectively for HTNi, HTNi-Y0.4, HTNi-Y2.0 and HTNi-Y3.0 were 74.0, 83.9, 74.4 and 90.2 %. In case of CO_2 conversion, the following initial values were obtained: 75.7% for HTNi, and 87.0%, 78.6 % and 84.9 % for HTNi-Y0.4, HTNi-Y2.0, and HTNi-Y3.0, respectively. Both increase and decrease in CH_4 and CO_2 conversions were observed. The extent was dependent on the catalyst. The highest stability, expressed by the lowest relative change were registered for HTNi-Y2.0 with Δ values of only 0.7 and 0.4%, respectively for CH_4 and CO_2 conversions. These relative changes were much smaller than for the unpromoted HTNi (2.3 and 1.8%, respectively), proving the positive influence of Y promotion on the catalyst's stability. For HTNi-Y0.4 catalyst, activity increase online with Δ values of 0.4 and 1.6%, respectively for CH_4 and CO_2 conversions. On the other hand, HTNi-3.0 catalyst showed Δ value for CO_2 conversion higher than that for HTNi (2.7 versus 1.8 %). This may be due to different distribution of basic sites, with the absence of weak sites.

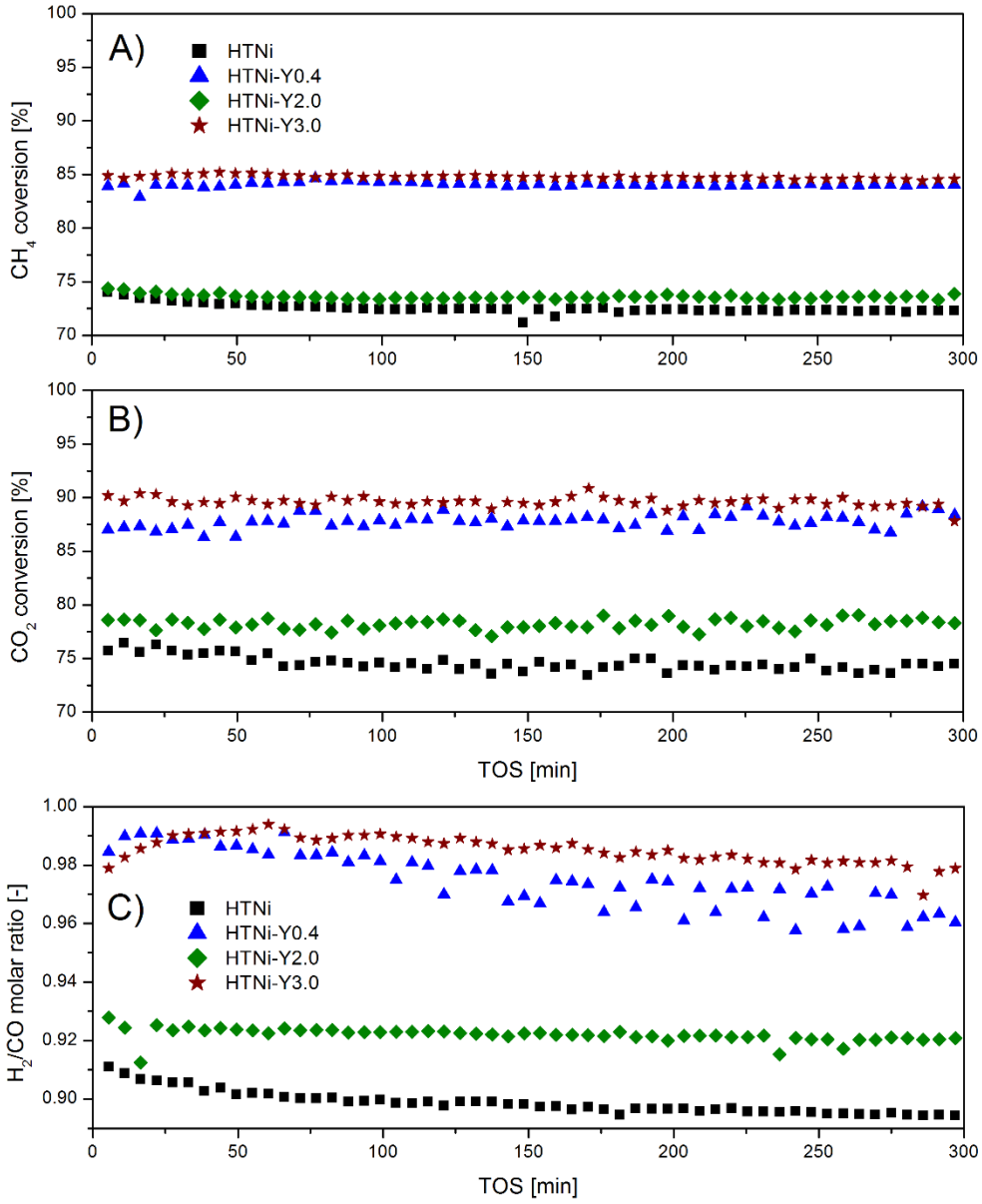

Fig. 4.13 Catalytic activity of HTNi-Y catalysts (with 0.4, 2.0 and 3.0 wt.% of yttrium) in the isothermal experiments at 700 °C: CH_4 conversion (A), CO_2 conversion (B), and H_2/CO molar ratio (C) versus temperature in DRM process ($CH_4/CO_2/Ar$=1/1/8, GHSV= 20,000 h^{-1}).

It should be mentioned, however, that there were some differences between the values of CO_2 and CH_4 conversions, as well as H_2/CO ratios registered in the TPSR and isothermal tests. This may have originated from differences in the methodology of the experiments, due to a possible slight initial deactivation of the catalysts, which in TPSR were examined first at temperatures higher than 700 °C.

Table 4.5 Stability results showing initial and final (after 5 hours) activity, and the relative changes ascribed to deactivation.

Catalyst	**CH_4 conversion [%]**	**CO_2 conversion [%]**	**H_2/CO [-]**
HTNi			
Initial	74.0	75.7	0.90
After 5h	72.3	74.3	0.89
Δ : relative change after 5h [%][1)]	↓2.3	↓1.8	
HTNi-Y0.4			
Initial	83.9	87.0	0.98
After 5h	84.1	88.4	0.96
Δ : relative change after 5h [%] [1)]	↑0.2	↑1.6	
HTNi-Y2.0			
Initial	74.4	78.6	0.92
After 5h	73.9	78.3	0.92
Δ : relative change after 5h [%] [1)]	↓0.7	↓0.4	
HTNi-Y3.0			
Initial	84.9	90.2	0.99
After 5h	84.6	87.8	0.97
Δ : relative change after 5h [%][1)]	↓0.4	↓2.7	

[1)] calculated as ($|x_i-x_{5h}|/x_i \cdot 100$), where x is CH_4 or CO_2 conversion expressed in percentage, and subscripts stand for i – initial, 5 h – after 5 h catalytic test; symbols ↓and ↑ denote that appropriate conversion respectively decreased or increased after 5 hours on line

The trends discussed above are in good agreement with those reported in literature for other Y-promoted DRM catalysts. A positive effect of the Y promotion was also observed for Ni,Y-Al_2O_3 [208], Ni-Y/SBA-15 [311,313], Ni-Y/KIT-6 [172], NiO-Y_2O_3-Al_2O_3 [314] and Y-$Ce_{0.75}Zr_{0.25}O_2$ [312]. Similarly as shown above, CO_2 conversion was reported to be slightly higher than that of CH_4, and the values of H_2/CO ratio lower than 1, which was ascribed to the occurrence of the reverse water-gas shift side reaction ($CO_2+H_2=CO+H_2O$) [98,172,313,314,333,334]. According to literature, other side reactions such as gasification of carbon deposits and the Boudouard reaction could have also taken place

[172,205,334]. On the other hand, Li et al. [311] observed CH_4 conversion higher than that of CO_2 for SBA-15 supported catalysts with Y/Si molar ratio of 0.02, 0.06 and 0.08 and ascribed it to methane decomposition. Such result was not registered in our study. This explains possible enhanced stability of the Y modified double-layered hydroxides. As reported by Dębek et al. [285] the methane decomposition (which causes catalyst deactivation) was less pronounced for smaller Ni particles. Thus, the fact that Y promotion resulted in smaller crystallites may play an important role in suppression of this unwanted reaction.

As discussed above, the yttrium modification resulted also in better dispersion of metallic Ni, enhanced specific surface area and changes in basicity. The better dispersion of nickel is of importance for catalytic performance, as better distribution of smaller Ni particles makes them more accessible to CH_4 in DRM process [155,314]. The increased specific surface area is another positive factor. As reported by Huang et al. [314], the enhanced S_{BET} of NiO-Y_2O_3-Al_2O_3 materials was linked with the good catalytic behavior in CO_2 reforming. On the other hand, the weak and medium basic sites may be also of advantage for DRM reaction rather than the strong sites, as suggested by Liu et al. [207]. Dębek et al. [285] found that high basicity hinders carbon formation and/or contributes to oxidation of formed coke. In contrast, too strong CO_2 adsorption, which results in carbon formation, was reported as originating from the presence of the strongest basic sites [197].

The mechanism of DRM can be shorty described as (i) decomposition of methane on Ni active site and (ii) dissociative adsorption of carbon dioxide on the metal surface and metal-surface interface [154,155]. During the first step, carbon atoms are formed on the Ni surface as a product of CH_4 decomposition ($CH_4 = C + 2H_2$). The carbon atom can be oxidized by atomic oxygen derived from CO_2. It was reported that doping with Y^{3+} improved the rate of carbon removal due to oxygen vacancies, which induced oxygen radicals from CO_2 to react with coke [209,309,313,335,336]. Thus, a possible removal of carbon could have taken place (to some extent) according to the reverse Boudouard reaction ($CO_2 + C = 2CO$) (cp. Table 4.5) [209].

In order to better understand the catalysts behavior in terms of side reactions and thus avoid deactivation, the direct methane decomposition (DMD) was studied for two selected catalysts, HTNi and HTNi-Y0.4. The latter catalyst was selected because it showed the highest decrease in H_2/CO molar ratio during the isothermal test (cp. Fig. 1.13). HTNi was chosen for comparison to elucidate the role of Y promotion. CH_4 conversion is presented in Fig. 4.14. As it may be seen, HTNi is more active in methane decomposition (DMD) than the catalyst promoted with yttrium. Moreover, stable methane conversion was registered for HTNi catalyst, whereas HTNi-Y0.4 showed decreasing values after first 30 min, pointing to an evolution of surface properties resulting in the suppression of this reaction. Small size of Ni crystallites present in the Y-promoted material could have contributed to this phenomenon, similar as reported in the study of Dębek et al. [285]. Thus, it may be concluded that the Y promotion inhibited the direct methane decomposition, and thus the C formation via this reaction. The carbon suppression was also reported for other Y-promoted materials [172,209].

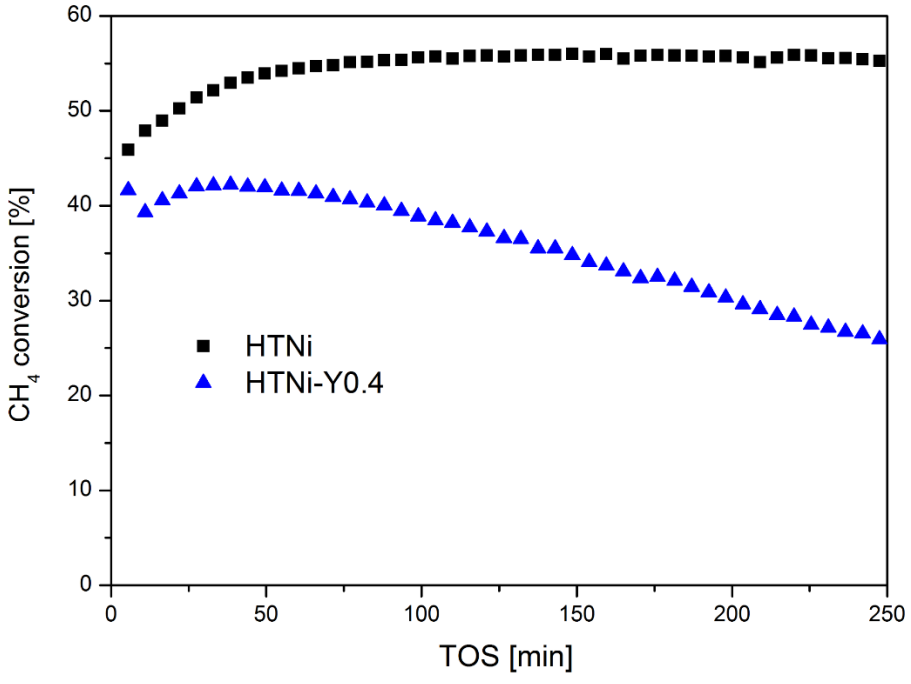

Fig. 4.14 Catalytic test of direct methane decomposition for HTNi and HTNi-Y0.4 as a function of temperature (GHSV=20,000 h^{-1}, CH_4/Ar=2/8, total flow rate 100 cm^3/min).

4.1.4. *Characterization of the spent catalysts*

Table 4.6 summarizes selected properties of the spent catalysts: (i) texture – S_{BET}, total pore volume and medium pore diameter, (ii) Ni crystallite size, as well as (iii) I_D/I_G intensity ratio obtained from Raman spectrum and (iv) the mass loss registered in TGA.

Specific surface area of the unpromoted spent catalyst was 125 m^2/g, and increased in comparison to the reduced sample. Similar effect was observed for the 0.4 wt.% Y-promoted spent catalyst. The partial reconstruction of the hydrotalcites may explain this fact (discussed further in the text). On the other hand, S_{BET} decreased for HTNi-Y2.0 and HTNi-Y3.0. No significant changes in pore volumes and diameters of pores were registered.

Table 4.6 Textural and structural properties of the spent catalysts. Numbers in brackets {..} relate respective values for the reduced samples (taken from Table 4.2).

Catalyst	**Textural properties** **Spent materials**			**XRD** **Spent materials**	**Raman** **Spent materials**	**TGA** **Spent materials**
	S_{BET} [m^2/g][1)]	**V_p [cm^3/g][2)]**	**d_p [nm][3)]**	**Ni^0 crystallite size [nm][4)]**	**I_D/I_G [-]**	**Mass loss [mg]**
HTNi	125 {68}	0.3	10	7	1.83	2.0
HTNi-Y0.4	95 {51}	0.3	10	6	1.65	2.6
HTNi-Y2.0	51 {67}	0.4	11	7	1.23	1.7
HTNi-Y3.0	85 {117}	0.6	14	8	0.84	2.8

[1)] specific surface areas calculated from the BET equation

[2)] mesopore volumes derived from the BJH desorption calculation method

[3)] pore size obtained from the BJH desorption calculation method

[4)] based on the Scherrer equation, calculated from the half-width of the XRD reflections at 2θ ca. 52°

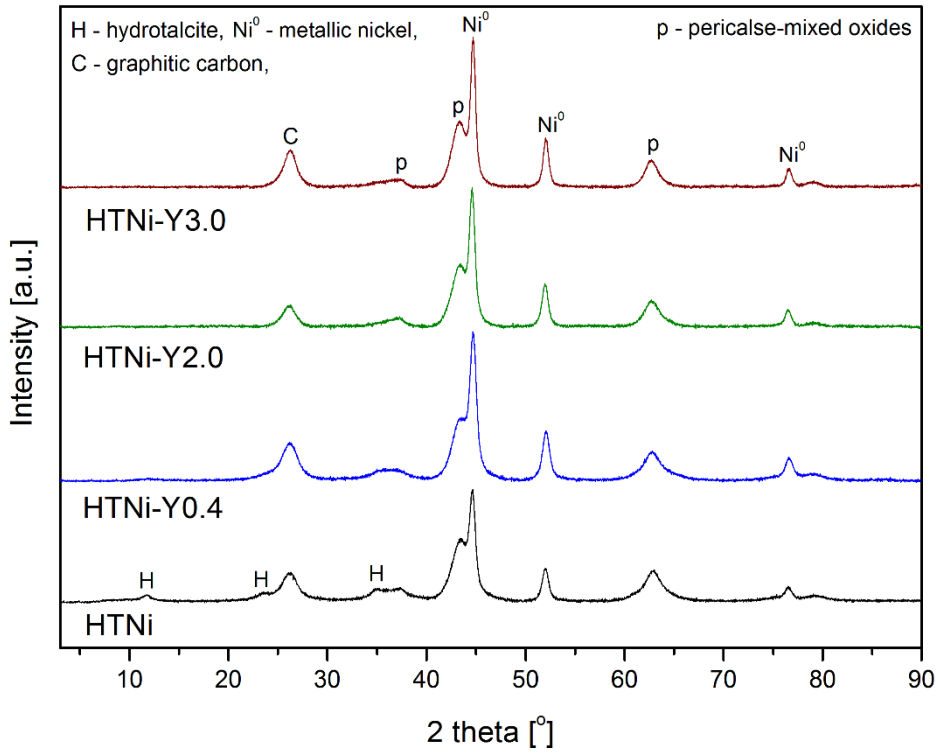

Fig. 4.15 XRD diffractograms of the spent catalysts (CH_4/CO_2/Ar=1/1/8, 700 °C for 5 h).

XRD diffractograms were recorded for the spent catalysts in order to verify the Ni^0 crystallite size, the possible changes in the support after the catalytic process, and the carbon formation. The results are presented in Fig. 4.15, where reflections typical for metallic nickel phase (ICOD 01-087-0712) and periclase-like mixed oxides phase can be found (ICOD 00-045-0946) [172,205,207,328], similarly as for the reduced catalysts (cp. Fig. 1.9). Crystallite size of Ni^0 did not change significantly after the tests. For all catalysts the values are close to those recorded for the reduced catalysts (cp. Table 4.6). This suggests the lack of sintering of the nickel particles upon DRM and thus confirms the stability of the Y doped catalysts during DRM in stability runs. Additionally, the reflections of graphite carbon (ICOD 01-075-2078) at 2θ=26.6° were registered for all catalysts (Fig. 4.15), which shows that the studied materials had suffered from carbon deposition during time on stream experiments. For the HTNi catalyst additional reflections of $Mg_6Al_2(OH)_{16}CO_3{\cdot}4H_2O$ (ICOD 00-014-0191) were registered at 2θ=11.5 and 22.9°. The partial reconstruction cannot be excluded for HTNi-Y0.4 sample, as small

shoulders were recorded at 2θ = 11.5 and 22.9°, and the S_{BET} increased (cp. Table 4.6). The $Mg_6Al_2(OH)_{16}CO_3{\cdot}4H_2O$ phase is typical for DLHs after synthesis and before calcination at around 500 °C [259,285,337]. The presence of hydrotalcite phase (H) was reported before for Ni-based LDHs after DRM tests, and indicates a partial regeneration of the support in the presence of water. This property, so-called memory effect of DLHs, facilitates reconstruction of mixed oxides to the original DLHs phase or meixnerite [318,338]. The partial reconstruction could have been produced by side reactions during DRM, such as RWGS or hydrogenation, as reported elsewhere [285]. The reflections of $Mg_6Al_2(OH)_{16}CO_3{\cdot}4H_2O$ were not observed in the spent HTNi-Y3.0, in contrast to both the calcined (cp. Fig. 4.2) and reduced catalysts (cp. Fig. 4.9). A possible explanation could be that the catalyst was fully transformed into the periclase phase during dry reforming of methane experiment, and the occurrence of side reactions did not lead to the partial regeneration of hydroxides.

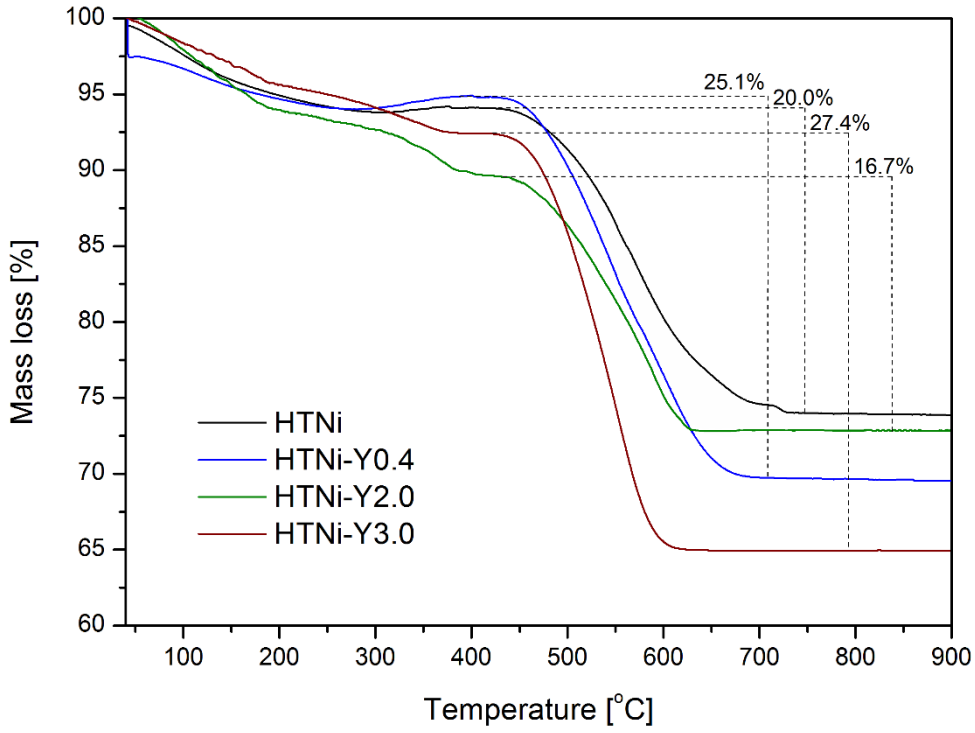

Fig. 4.16 TGA over the spent catalyst (CH_4/CO_2/Ar=1/1/8, 700 °C for 5 h).

TGA data are presented in Fig. 4.16, where 20.0, 25.1, 16.7 and 27.4 % weight losses were recorded for HTNi, HTNi-Y0.4, HTNi-Y2.0 and HTNi-Y3.0, respectively. Additionally, a weight increase may be observed at 300 °C for the spent HTNi and HTNi-Y0.4 catalysts. According to Tsyganok et al. [191], this increase arises from Ni^0 oxidation to NiO. The registered weight decrease at ca. 600 °C was linked to CO_2 formation, which occurs due to the oxidation of carbonaceous species, formed upon dry reforming of methane [191,206]. The registered temperature suggests the formation of carbon filaments [317]. The formation of carbon filaments cannot be, however, linked directly to the CH_4 decomposition because, as discussed in the previous subchapter, the activity of HTNi-Y0.4 for this reaction was lower than for HTNi (cp. Fig. 4.14).

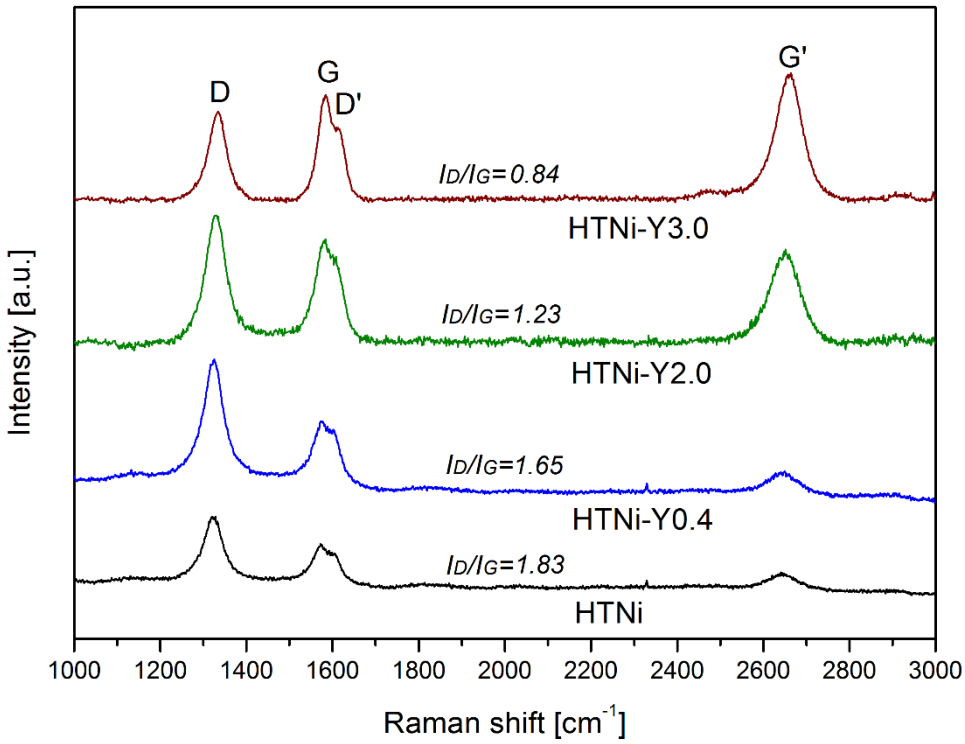

Fig. 4.17 Raman spectra of the spent catalysts (CH_4/CO_2/Ar=1/1/8, 700 °C for 5 h). The I_D/I_G ratio describes the degree of crystallinity of the formed carbon.

In order to examine the properties of carbonaceous species on the spent catalysts Raman spectroscopy was used. For HTNi and the Y-promoted materials, four bands were registered: D band, G band, D' band and G' band (Fig. 4.17). The D and D' bands arise from a disorder in graphite structure and they were ascribed to the non-zone centered phonons associated to the disorder-induced vibration of C–C bond. The G and G' bands refer to the stretching vibrations in the aromatic layers of graphite and they are only present in perfect crystalline graphite [339]. Table 4.6 presents the calculated ratios of the intensity of D and D' bands to the intensity of G and G' bands, I_D/I_G, which describe the graphitization degree of carbon and the disorder in its structure. The relative intensity of the D and G bands (I_D/I_G) gives valuable information about the crystallinity degree of the carbon formed during the DRM. The lower I_D/I_G ratio refers to a high crystallinity and high graphitization degree due to the higher contribution of the graphitized carbon fractions formed [340,341]. The Y-modified materials showed decreasing I_D/I_G ratios with 1.83 for HTNi versus 1.65, 1.23 and 0.84 for HTNi-Y0.4, HTNi-Y2.0 and HTNi-Y3.0, respectively (Table 4.6). Therefore, it can be concluded that different carbon structures were formed on the studied catalysts, and the carbon deposited on Y promoted materials is more graphitic [179]. The graphitic carbon is mainly responsible for deactivation, and acts like a shell covering the Ni particle layer by layer [334]. This shows that yttrium promotion influenced the DRM mechanism in favoring side reactions, such as for example CO_2 hydrogenation.

4.1.5. *Conclusions*

Ni-containing Mg/Al double-layered hydroxides (DLHs) were promoted with Y. The catalysts were tested in dry reforming of methane in the temperature range of 850-600 °C, and in the stability tests at 700 °C for 5 h.

The promotion with yttrium did not result in a separate crystalline phase formation but led to a decrease in the size of Ni crystallites as compared to non-modified Ni-DLHs. Also, a decrease in H_2 consumption was reported (Ni species strongly interacting with the periclase structure). In the HTNi-Y2.0 and HTNi-Y3.0 catalysts, a stabilization of weakly bonded NiO was also observed. After

modification with yttrium amount of 0.2 to 2.0 wt.% the total basicity decreased, whereas the promotion with 3 wt.% led to a significant increase in the total number of basic sites, with mainly the number of Lewis pairs increased. The best material features were observed for Ni-based double-layered hydroxides modified with 2.0 wt.% of Y. This catalyst, as compared to unmodified Ni-double layered hydroxide, showed: (i) smaller Ni crystallite size, (ii) higher specific surface area, and (iii) enhanced dispersion of Ni^0.

During DRM for HTNi-Y2.0, carbon formation was minimized as evidenced by TGA analysis. However, the presence of graphitic carbon formation was still proven by the XRD and Raman characterization techniques.

During isothermal experiments the catalyst modified with 2.0 wt.% yttrium revealed the highest and the most stable values of H_2/CO molar ratio. For all studied materials the H_2/CO ratio was always lower than 1.0, with the lower ratios for HTNi-Y0.4 and HTNi-Y3.0 catalysts. This may have arisen from the consumption of H_2 caused by the side reactions occurrence. Considering that HTNi-Y0.4 showed suppression of direct methane decomposition ($CH_4 = C_{(s)} + 2H_2$), it suggests that the formed carbon deposits could have originated from e.g. CO_2 hydrogenation ($CO_2 + 2H_2 = C_{(s)} + 2H_2O$), which, in consequence, led to the decrease in H_2 content in the product stream and the decrease of H_2/CO ratio during DRM. It should be also mentioned that a partial reconstruction of the support was registered only in case of the unpromoted catalyst HTNi, and possibly HTNi-Y0.4, and manifested itself in the presence of $Mg_6Al_2(OH)_{16}CO_3 \cdot 4H_2O$ reflections in XRD patterns. As this reconstruction requires the presence of CO_2 and water, this shows that Y promotion leads to a better structural resistance to the side reactions which produce H_2O, such as e.g. reverse water-gas shift reaction or CO_2 hydrogenation.

4.2. Co-impregnation with zirconium and yttrium of Ni-based double layered-hydroxides

The promotion with zirconium oxide was reported as beneficial in terms of catalytic stability. Dębek et al. [203] studied three different concentrations of added zirconia (2.5, 5.4 and 9.7 wt.%) into Ni/Mg/Al hydrotalcites. The addition of Zr (2.5 wt.%) to the catalyst composition resulted in the enhancement of stability, which originated from the suppression of direct methane decomposition. On the other hand, this improvement resulted in the decrease in activity, together with a lower H_2/CO product molar ratio. The catalyst modified with 5.4 wt.% of Zr provided satisfactory activity results, but it suffered in terms of stability [203]. Thus, to find a balance between activity and stability, stabilization of the catalytic system with zirconia (5 wt.% phase) was considered. The properties of ZrO_2 can be tailored by the introduction of a cation with valence lower than 4+, e.g. Y^{3+} [309,342,343]. This results in the formation of defects in the crystal structure of zirconia, together with oxygen vacancies in its oxygen sub-lattice, which are known as beneficial in the minimization of carbon deposits [309,329,344,345]. The ZrO_2-Y_2O_3 solid solution was studied in the past in different reforming processes [329,345–347]. Bellido et al. [309] prepared different Y/Zr catalysts with a varying mole fraction of Y (4 to 12 mol.%). The synthesized supported nickel 8YZ catalyst showed the best results in terms of activity and stability in the DRM [9]. The authors ascribed these properties to the increased formation of oxygen vacancies in the synthesized support.

The aim of the study presented in this subchapter was to examine the influence of Ni/Mg/Al double-layered hydroxides co-impregnated with a mixture of zirconium and yttrium, on the final physico-chemical features of the resulting catalysts, their structure and catalytic behavior in DRM. Three zirconium and yttrium-modified catalysts were examined assuming 5.0 wt.% of Zr and 0.2, 0.4 or 0.6 wt.% of Y. Moreover, a sample only impregnated with Zr was prepared in order to analyze the differences between Y-free and Y-promoted material.

4.2.1. *Physicochemical properties*

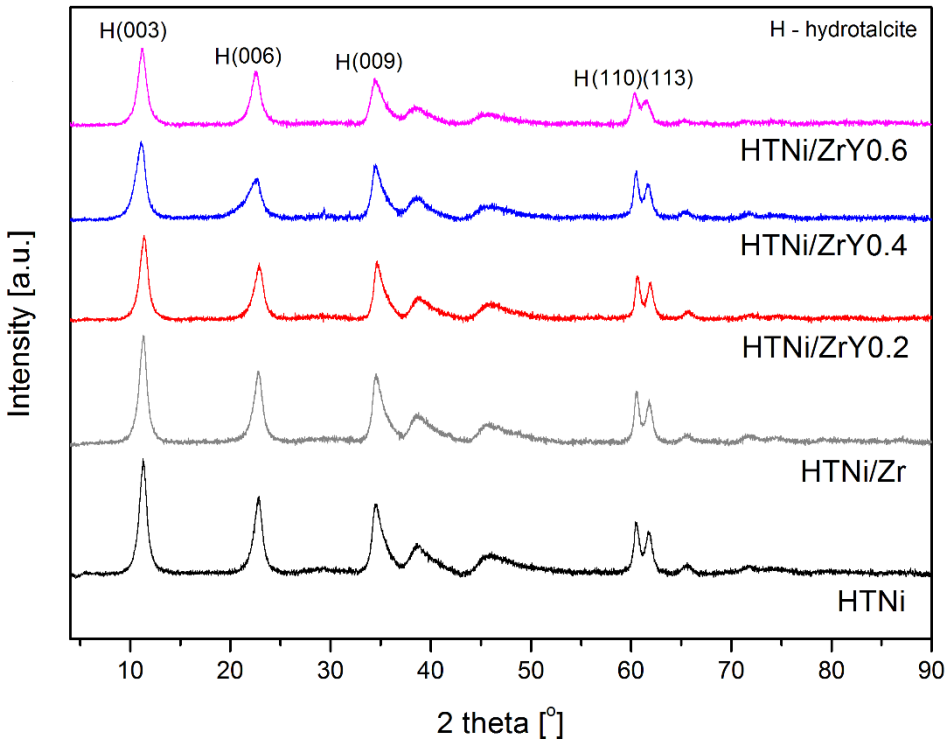

Fig. 4.18 XRD diffractograms of the freshly synthesized materials promoted with Zr and Y (HTNi/Zr, HTNi/ZrY0.2, HTNi/ZrY0.4, HTNi/ZrY0.6) compared to HTNi.

Fig. 4.18 presents XRD diffractograms of the freshly synthesized catalysts HTNi/Zr, HTNi/ZrY0.2, HTNi/ZrY0.4, HTNi/ZrY0.6 compared to HTNi. All materials showed a typical layered structure of hydrotalcite (ICOD 00-014-0191), which is recognized by the presence of (003), (006), (009), (110) and (113) planes reflections at 2θ=11, 22, 35, 60 and 62°, respectively [197,205,244,316]. After modification with 0.4 and 0.6 wt.% yttrium, small shifts towards lower angles were registered, in the reflections arising from (003) and (006) planes. This indicates that the existing interlayer anions were not only carbonates but possibly also nitrate anions [197,248–250,284]. It is important to note that no additional reflections were observed, either for nickel or promoting zirconium and yttrium. Table 4.7 presents the structural parameters of the freshly synthesized materials. The unit cell parameters *a* (cation-cation distance) remained stable after modification with Zr and Y. The obtained values of *c* (the

triple distance between brucite-like layers) slightly increased after promotion with metals, as Zr and Y were placed on the surface of catalysts. Based on the latter parameter, the *c'* parameter was calculated. The value of 7.77-7.91 Å was obtained for all materials, indicating the presence of CO_3^{2-} (7.65 Å) and NO_3^- (8.79 Å) between the layers of hydrotalcite [197,244,248].

Table 4.7 Structural parameters of the freshly synthesized materials.

Catalyst	XRD					
	d(003)	**d(006)**	**d(009)**	**a [Å]**[1)]	**c [Å]**[2)]	**c' [Å]**
HTNi	7.84	3.91	2.60	3.06	23.45	7.82
HTNi/Zr	7.84	3.91	2.58	3.06	23.40	7.80
HTNi/ZrY0.2	7.79	3.89	2.58	3.06	23.31	7.77
HTNi/ZrY0.4	8.02	3.97	2.59	3.06	23.72	7.91
HTNi/ZrY0.6	7.91	3.94	2.59	3.07	23.56	7.85

[1)] calculated from (110) spacing $a=2d_{(110)}$ as suggested by Cavani et al. [244]

[2)] calculated from XRD patterns of the fresh catalysts, from the position of the three first reflections $c=d_{(003)} + 2d_{(006)} + 3d_{(009)}$, as suggested by Liu et al. [207]

Fig. 4.19 presents XRD patterns for the catalysts after calcination at 550 °C with characteristic reflections of nano-oxides having a periclase-like structure (ICOD 00-045-0946) (2θ ca. 36.7, 43 and 62.5°). Additionally, a separate phase of tetragonal zirconia (ICOD 01-079-1765) was recorded in HTNi/Zr sample [203,348]. This indicates the deposition of this oxide on the surface of the support. Similar observations were made by Dębek et al. [203]. The authors examined different concentrations of Zr (ca. 3, 5 and 10 wt.%) introduced into Ni/Mg/Al-hydrotalcites, and found that only the lowest amount of this metal could be introduced into the periclase-like structure, while the loading higher than 3 wt.% resulted in the formation of a separate phase of zirconia. On the other hand, the modification with yttrium did not result in the formation of a separate phase, which may be due to either the low loading of this metal or the presence of amorphous Y-compound. However, the existence of the ZrO_2-Y_2O_3 phase (ICOD 01-070-4426) cannot be excluded. The position of the

reflection at 2θ of ca. 30° differs for each sample, and is 30.66, 30.34, 30.28 and 30.30° for HTNi/Zr, HTNi/ZrY0.2, HTNi/ZrY0.4, and HTNi/ZrY0.6, respectively. The shift towards lower Bragg angles after the addition of yttrium, can arise from formation of ZrO_2-Y_2O_3 phase [309,342,349–351]. This will be further examined in more detail for the reduced and spent materials.

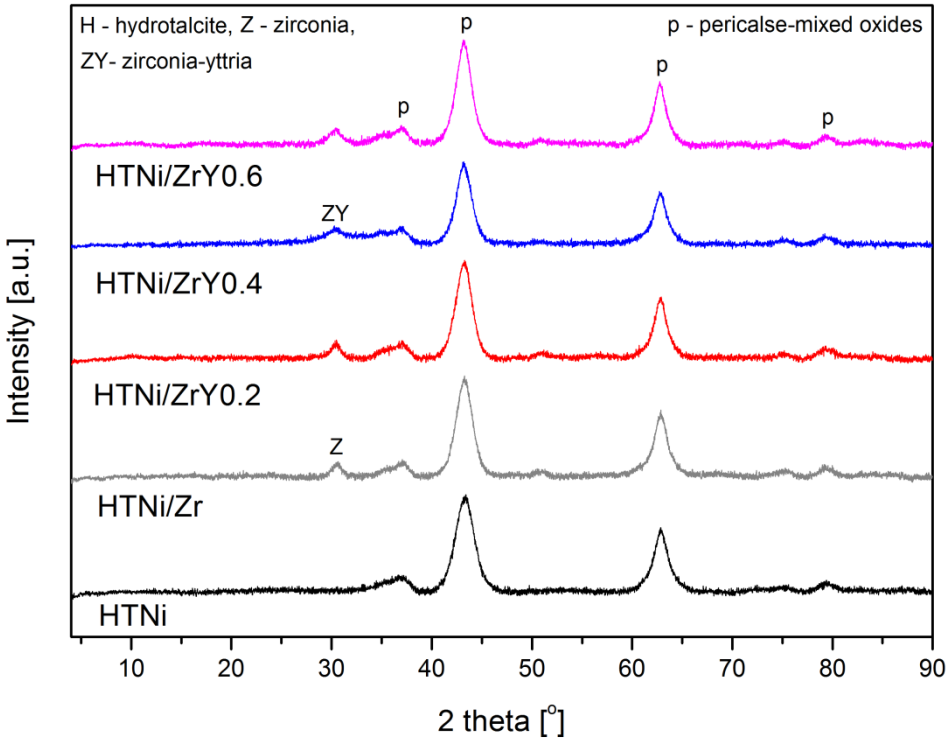

Fig. 4.19 XRD diffractograms of the calcined samples co-impregnated with Zr and Y (HTNi/Zr, HTNi/ZrY0.2, HTNi/ZrY0.4, HTNi/ZrY0.6) compared to HTNi.

The elemental analysis of the calcined materials revealed the Ni content within 15-20 wt.% (Table 4.8). During the synthesis step, 5 wt.% of Zr and Al^{3+}/Zr^{4+}=5.0 nominal values were assumed. However, the content of Zr and the Al^{3+}/Zr^{4+} molar ratio were, respectively, 2.5, 2.7, 2.6, 2.4 wt.% and 15.3, 14.1, 15.9, 16.1 for HTNi/Zr, HTNi/ZrY0.2, HTNi/ZrY0.4 and HTNi/ZrY0.6. These results show that Zr was only partially incorporated into the double-layered hydroxides structure, similarly as described by Dębek et al. [203]. The yttrium content was found to be the same as the nominal values, i.e., 0.2, 0.4 and 0.6 wt.%. The Ni^{2+}/Mg^{2+} molar ratio is close to the nominal values only for the unmodified material. The

values lower than 0.33 for other studied catalysts (containing zirconium and yttrium) suggest that Mg^{2+} ions were only partly substituted by assumed number of Ni^{2+}.

Table 4.8 Structural parameters, elemental composition, and textural properties for the calcined samples (HTNi, HTNi/Zr, HTNi/ZrY0.2, HTNi/ZrY0.4, HTNi/ZrY0.6). The values in brackets are nominal ones.

Catalyst	XRF							N_2 sorption		
	Mg [wt.%]	Al [wt.%]	Ni [wt.%]	Zr [wt.%]	Y [wt.%]	Ni^{2+}/Mg^{2+} molar ratio	Al^{3+}/Zr^{4+} molar ratio	S_{BET} [m^2/g] 1)	V_p [cm^3/g] 2)	d_p [nm] 3)
HTNi	30	12	20	-	-	0.29 (0.33)	-	120	0.6	19
HTNi/Zr	31	12	16	2.5 (5.0)	-	0.21 (0.33)	15.3 (5.0)	105	0.6	18
HTNi/ZrY0.2	30	11	18	2.7 (5.0)	0.2 (0.2)	0.24 (0.33)	14.1 (5.0)	107	0.6	18
HTNi/ZrY0.4	32	12	15	2.6 (5.0)	0.4 (0.4)	0.19 (0.33)	15.9 (5.0)	107	0.5	19
HTNi/ZrY0.6	32	12	15	2.4 (5.0)	0.6 (0.6)	0.20 (0.33)	16.1 (5.0)	107	0.5	18

1) specific surface areas calculated from the BET equation
2) mesopore volumes derived from the BJH desorption calculation method
3) pore size distribution obtained from the BJH desorption calculation method

The modification of HTNi with zirconium caused a slight decrease of the specific surface area S_{BET}, from 120 m^2/g to ca. 105 m^2/g for HTNi/Zr (Table 4.8). This may be linked to the formation of the surface phase of ZrO_2, which was registered in the XRD analysis. No significant changes of the textural properties were observed after the modification with yttrium. S_{BET} had the same value of 107 m^2/g for each of the Y-modified catalysts. Specific mesopore volume varied from 0.5 to 0.6 cm^3/g, and pore diameters from 18 to 19 nm in all prepared catalysts.

4.2.2. *Reducibility, basicity, Ni dispersion and crystallite size*

TPR-H_2 profiles of the calcined materials showed a wide reduction peak starting from 600 °C and centered at ca. 850 °C (Fig. 4.20). According to the literature, this peak corresponds to NiO incorporated within the structure of periclase [203]. Zr and Zr/Y addition resulted in a rightward shift of the peak maximum, together with lower H_2 consumption, and these features reflect the decrease of reducibility of the studied solids. The samples modified with 0.2% and 0.6% of Y show a peak maximum at ca. 847 °C. A more pronounced shift was observed for the Y0.4-promoted catalyst, which suggests stronger interaction of Ni particles with the support [285]. At lower temperatures, additional small peaks were registered. The one observed at 385 °C for HTNi catalyst is assigned to weakly-bonded NiO [197]. After modification with Zr the doublet at 330 and 394 °C is probably due to the presence of bulk NiO [326,327]. The subsequent modification with 0.2 and 0.6 wt.% yttrium resulted in the stabilization of bulk NiO. This was not observed in the HTNi/ZrY0.4 catalyst, in which only one reduction peak centered at 400 °C was registered, indicating the absence of bulk NiO.

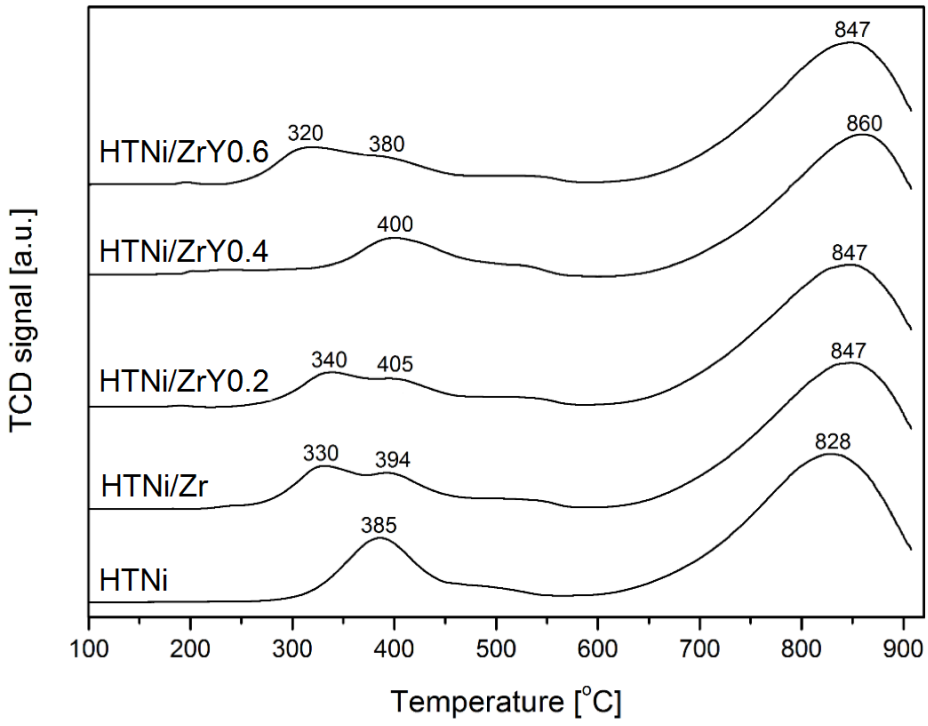

Fig. 4.20 TPR-H_2 profiles registered for HTNi/Zr, HTNi/ZrY0.2, HTNi/ZrY0.4 and HTNi/ZrY0.6 compared to HTNi.

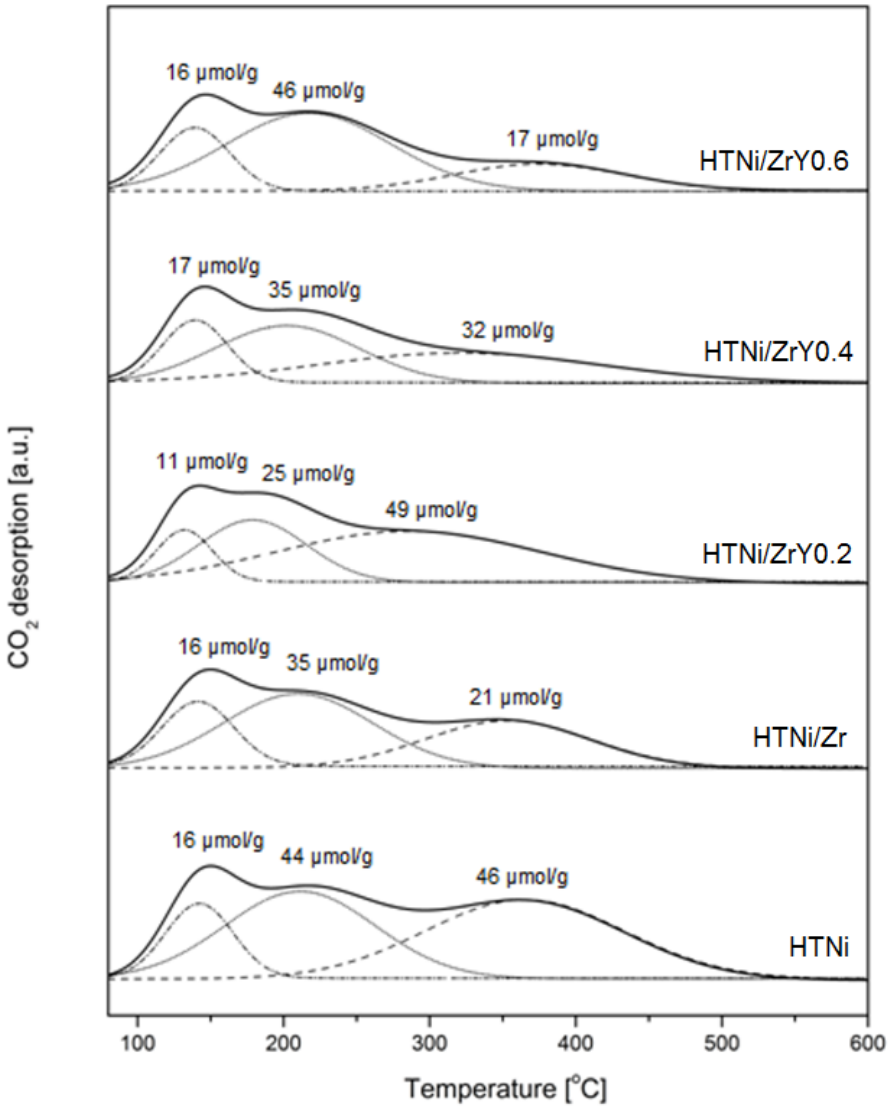

Fig. 4.21 TPD-CO_2 profiles of HTNi/Zr, HTNi/ZrY0.2, HTNi/ZrY0.4 and HTNi/ZrY0.6 compared to HTNi.

Basicity was examined by TPD-CO_2 technique. The obtained profiles are presented in Fig. 4.21, and the calculated values in Table 4.9. The total basicity decreased after promotion of HTNi material, from 107 to, 72, 84, 85 and 79 µmol/g for HTNi/Zr, HTNi/ZrY0.2, HTNi/ZrY0.4 and HTNi/ZrY0.6, respectively. The promotion with Zr decreased the percentage of strong surface basic sites and slightly increased the percentage of medium and weak sites. After promotion with 0.2 wt.% of yttrium, the percentage of strong sites increased again from 29% for HTNi/Zr to 57%. This sample had the highest percentage of the strong basic sites. Higher yttrium loading caused gradual decrease of the percentage of the

strong sites, to 38% and 22% for HTNi/ZrY0.4 and HTNi/ZrY0.6, respectively. The opposite tendency was observed for the percentage of the medium basic sites, which increased after yttrium loading of 0.4 and 0.6 wt.%. The basic sites of medium strength have been already reported to play a significant role in DRM [207].

Table 4.9 Basic properties, Ni^0 crystallite size and Ni^0 dispersion for catalysts co-impregnated with Zr and Y.

Catalyst	TPR-H_2	TPD-CO_2				XRD	H_2 chemisorption	
	H_2 uptake [mmol H_2/g]	Weak [%]	Medium [%]	Strong [%]	Total basicity [µmol/g]	Ni^0 crystallite size [nm][1)]	Ni^0 dispersion [%]	Ni^0 crystallite size [nm][2)]
HTNi	0.209	16	41	43	107	8	8.9	11
HTNi/Zr	0.179	22	49	29	72	10	7.8	12
HTNi/ZrY0.2	0.174	13	30	57	84	10	9.8	10
HTNi/ZrY0.4	0.154	20	42	38	85	11	10.0	10
HTNi/ZrY0.6	0.177	20	58	22	79	10	11.1	9

[1)] based on the Scherrer equation, from the width at half-maximum of the XRD reflections at 2θ ca. 53°

[2)] calculated from d = 97.1/(%D) based on the assumption of spherical crystallites of uniform size

XRD patterns of the reduced samples are presented in Fig. 4.22. Characteristic reflections of periclase mixed oxides, metallic nickel Ni^0 and ZrO_2 are observed [204,285,352]. Additionally, XRD analysis revealed the possible presence of magnesium-zirconium oxide and aluminum-zirconium oxide, indicating strong interactions of Zr with the support. No separate phase of yttrium was registered, probably due to its low content, which makes it undetectable by XRD. However, Y-doping with 0.4 and 0.6 wt.% resulted in a shift of the reflection at 2θ of ca. 30° (originating from ZrO_2-Y_2O_3 tetragonal phase: ICOD 01-070-4426), towards lower Bragg angles, which suggests an increase in the interlayer distance of zirconia, as reported elsewhere [309,342,349–351]. Yttrium ions can enter the zirconia crystal lattice, resulting in the formation of ZrO_2-Y_2O_3 solid solution, and this was confirmed by HRTEM analysis over the spent materials, discussed further in the text. The size of ZrO_2 crystallites

(calculated from the Scherrer equation using the half-width of the 2θ diffraction line at 31°), was 11 nm for the Zr-containing materials. Asencios et al. [329] studied $NiO/Y_2O_3/ZrO_2$ catalysts in which a decrease of the ZrO_2 crystal size was observed after yttrium promotion (4.87-29.52 wt.%). As the content of Y introduced into the Zr,Y-co-impregnated catalysts was lower, the stable crystallite size of ZrO_2 does not contradict the possibility of Y^{3+} introduction into the ZrO_2 lattice to form the solid solution. The calculated mean size of Ni crystallites (based on at reflection at 2θ ca. 52°) was found to be practically the same for all studied catalysts. No shift of Ni^0 reflections was observed for any of the tested materials, indicating the absence of either Y_2O_3-NiO or ZrO_2-NiO solid solutions [329].

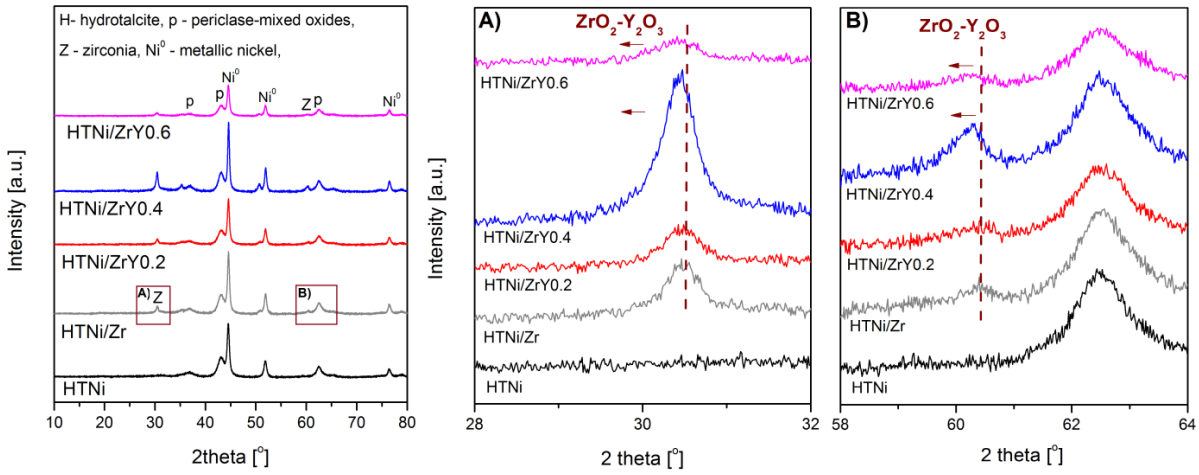

Fig 4.22 XRD patterns recorded for Zr,Y-impregnated catalysts reduced in a mixture of H_2/Ar at 900 °C.

The dispersion of nickel for the HTNi material slightly decreased after the modification with zirconium, from 8.9% for HTNi to 7.8% for HTNi/Zr (Table 4.9). After further promotion with yttrium an increase of Ni dispersion was observed, showing the highest value for HTNi/ZrY0.6 catalyst. Such increase of dispersion after Y-promotion was also reported by Huang et al. [314] and Li et al. [311], as well as observed for the hydrotalcite HTNi samples (without Zr promotion) as discussed in **Subchapter 4.1**.

4.2.3. *Catalytic activity and stability in DRM*

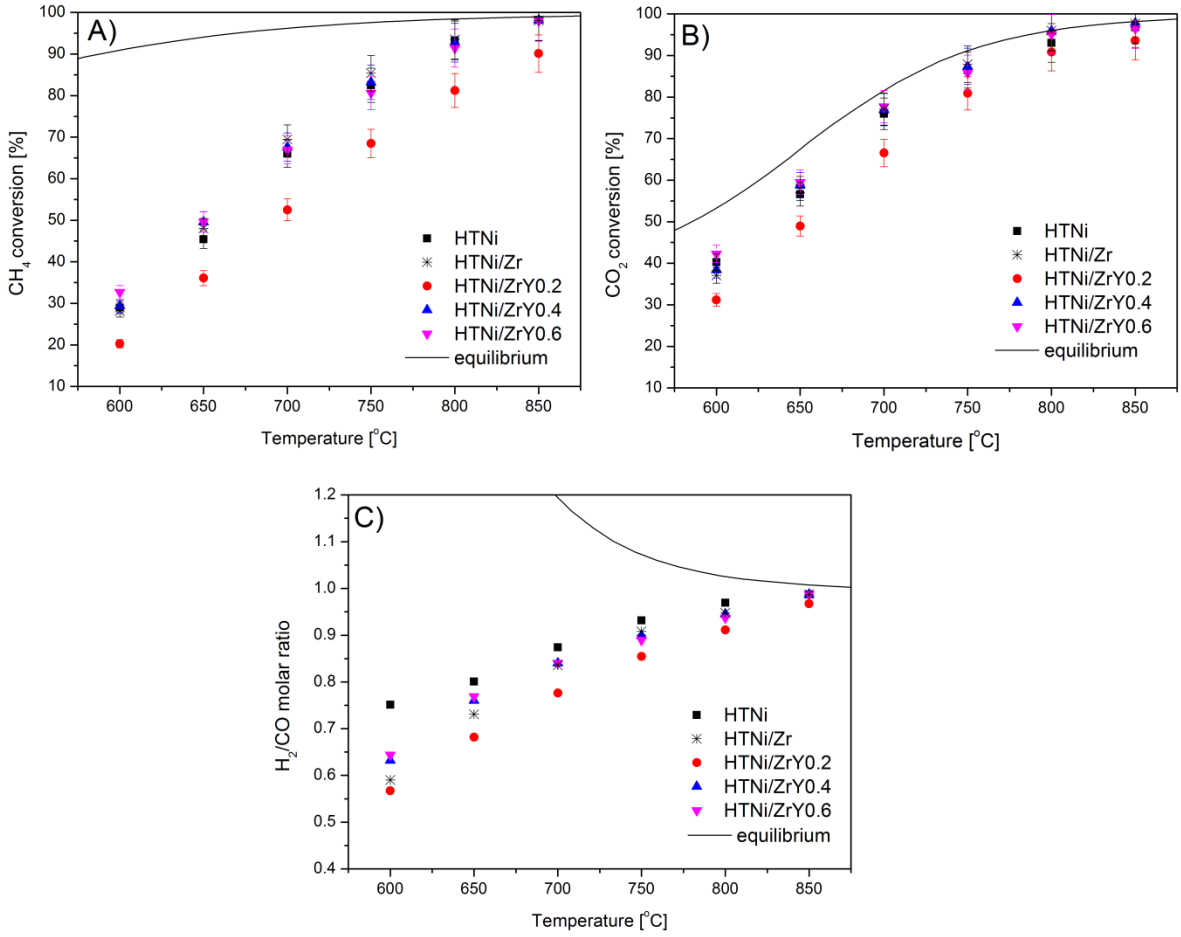

Fig. 4.23 DRM performance tests (CH_4- and CO_2-conversion, H_2/CO molar ratio) conducted for co-impregnated Zr- and Y- Ni/Mg/Al hydrotalcites; tests conditions: $CH_4/CO_2/Ar$=1/1/8, GHSV=20,000 h^{-1}, the temperature range 600-850 °C. Solid lines represent thermodynamic equilibrium.

Fig. 4.23 presents catalytic results of the DRM in terms of CH_4 and CO_2 conversion and H_2/CO product ratio in the 600-850 °C range. All catalysts were active under the tested DRM conditions, showing within experimental error, a similar methane and carbon dioxide conversion, with the exception of HTNi/ZrY0.2 catalyst with a worse performance. The CO_2 conversion was higher than that of CH_4, indicating the occurrence of side reactions, mainly RWGS, which is in agreement with the obtained H_2/CO ratio which was lower than unity [96,114,329].

Stability tests were carried out at 700 °C for 300 min (5 h) for HTNi/Zr and HTNi/ZrY0.4 catalysts and compared to unpromoted HTNi (Fig. 4.24). For the HT/ZrY0.4 catalyst, the conversions were higher than for HTNi/Zr. For the latter, the conversions constantly increased with TOS during the first 75 min of DRM. This may suggest unstable performance of the Zr-impregnated catalyst, and a possible enhancement of the stability due to the yttrium addition since HTNi/ZrY0.4 did not show such behavior. The worst catalytic performance was obtained for the unmodified material, where after 75 min of DRM CH_4 and CO_2 conversions of respectively 72.7% and 74.7%, were registered. These results are in contrast to those reported by Dębek et al. [197,203], which were obtained for Ni-based hydrotalcites at 550 °C (CH_4/CO_2=1, GHSV=20,000 h^{-1}). The latter study reported that the unpromoted catalyst (HT) showed considerable selectivity towards direct decomposition of CH_4, which led to increasing H_2/CO ratio due to the excess hydrogen. Also, the HT catalyst presented higher activity than the Zr-modified materials (3-10 wt.%). A similar trend was observed in other activity tests of Dębek et al. [203] carried out at 650 and 750 °C, over the HNi and HNiZr3 samples. Thus, in this study, it is shown that impregnation of Ni/Mg/Al double-layered hydroxides with Zr (5 wt.%) and Y (0.4 wt.%) not only enhanced the stability in DRM but also improved the catalytic activity as compared to the unmodified Ni-based catalyst.

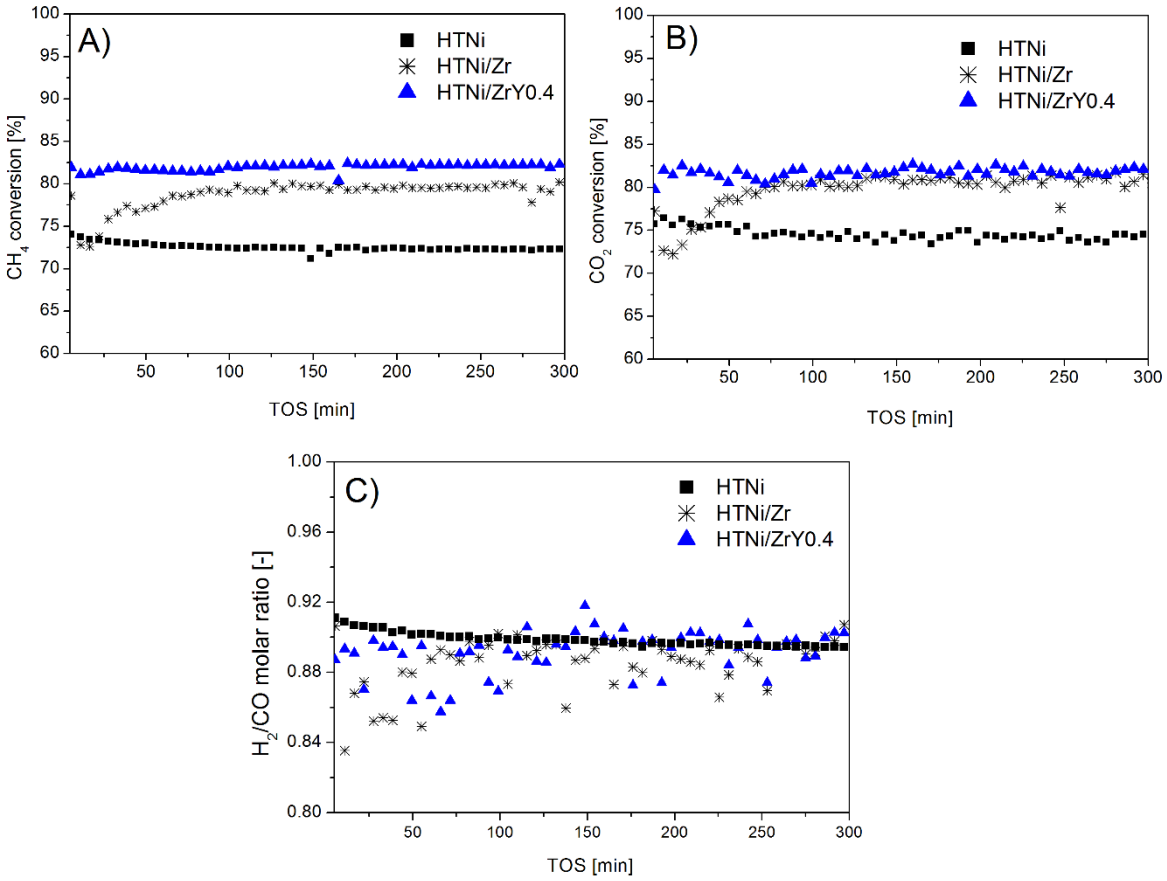

Fig. 4.24 DRM performance tests (CH_4- and CO_2-conversion, H_2/CO molar ratio) conducted for Zr,Y-promoted Ni/Mg/Al hydrotalcites; tests conditions: $CH_4/CO_2/Ar$=1/1/8, GHSV= 20,000 h^{-1} at 700 °C for 5 h.

The differences in catalysts stability are related with the improvement of Ni dispersion (H_2 chemisorption) and changes in basicity (TPD-CO_2). Both were reported to contribute to better catalytic performance [154,161,205].

The formation of ZrO_2-Y_2O_3 solid solution (observed in XRD for HTNi/ZrY0.4 and HTNi/ZrY0.6) did not lead to an increased reducibility of the Y-loaded materials, in contrast to the previously reported other materials containing Zr and Y oxides [311,329,345]. The increase of H_2 uptake observed in TPR could be explained by the possible formation of oxygen vacancies. However, the identification and characterization of oxygen vacancies is still challenging and requires more sophisticated techniques, such as: scanning tunneling microscopy (STM), atomic force microscopy (AFM), or electron paramagnetic resonance (EPR) [353]. The oxygen vacancies (called by Pacchioni [354] “the invisible

agents on oxide surfaces") are believed to increase the rate of removal of carbon located in the vicinity of active nickel. This can be realized via the reverse Boudouard reaction ($CO_2 + C = 2\ CO$) [355]. Although the decreased reducibility was observed in the HTNi/ZrY0.4 catalyst, the detected ZrO_2-Y_2O_3 phase was largely able to lead to the reduction of the surface NiO by decreasing the formation of bulk NiO. This may contribute to the better stability and less coke formation.

4.2.4. *Characterization of the spent catalysts after the TPSR test*

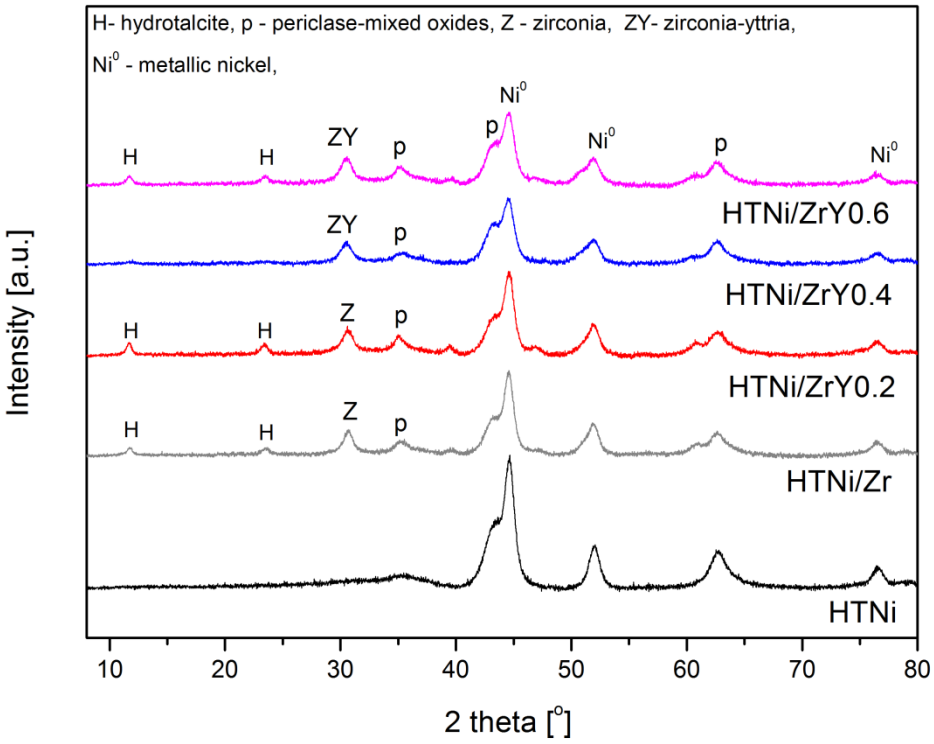

Fig. 4.25 XRD diffractograms recorded for the spent catalysts (after TPSR catalytic test).

XRD patterns of the spent catalysts after TPSR tests are presented in Fig. 4.25. Apart from the reflections arising from Ni^0, ZrO_2, ZrO_2-Y_2O_3 and periclase phases, the ones resulting from hydrotalcite (H) are also observed for HTNi/Zr, HTNi/ZrY0.2 and HTNi/ZrY0.6 catalysts. This indicates a partial regeneration of the support during DRM, which may be observed in hydrotalcite-derived materials in the presence of water [285]. This suggests that one of the side reactions, such as RWGS ($CO_2 + H_2 = CO$

+ H_2O), had a significant involvement in the DRM of these catalysts. On the other hand, the HTNi/Zr-Y0.4 did not reveal the presence of (003), (006) and (009) planes characteristic for hydrotalcite, proving a better stability of this material.

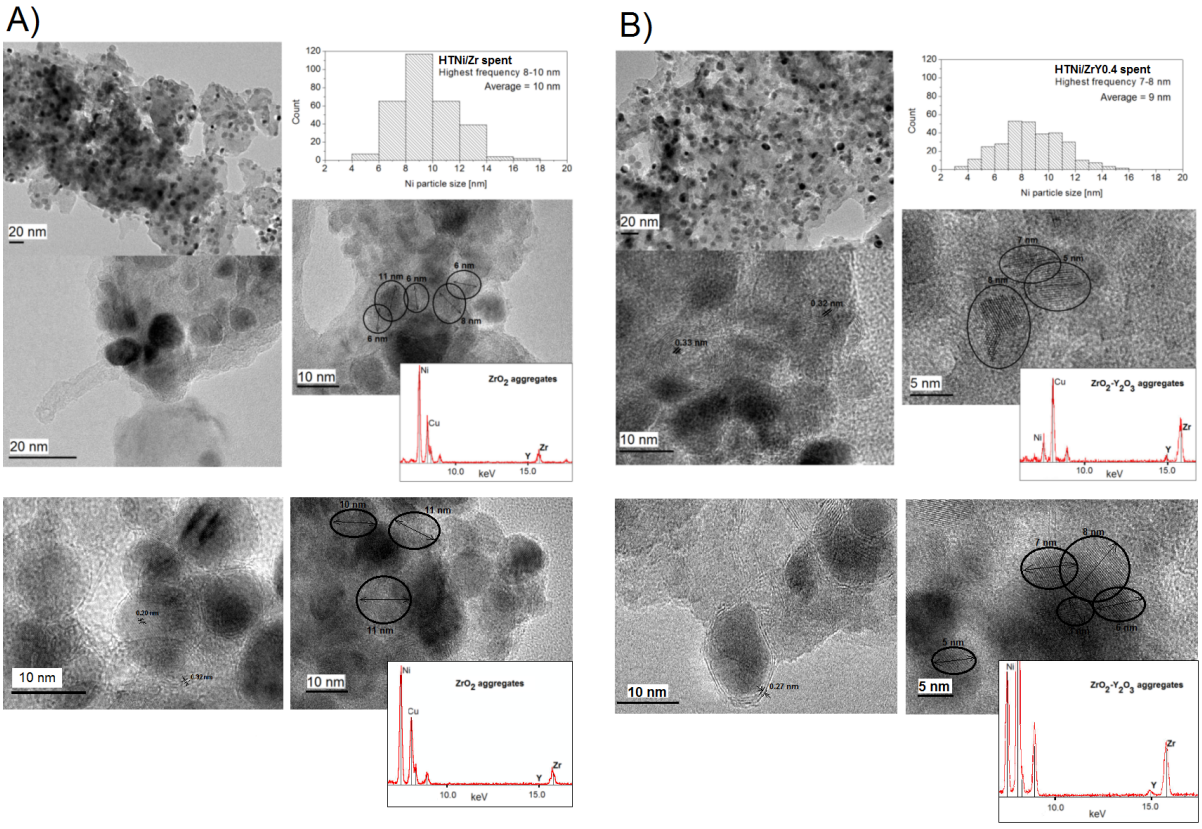

Fig. 4.26 HRTEM micrographs with EDS analysis for the spent HTNi/Zr (A) and HTNi/ZrY0.4 (B) catalysts.

HRTEM images of the spent catalysts are shown in Figs. 4.26 A and B. On the left-hand side (Fig. 4.26 A), the micrographs of the spent HTNi/Zr catalyst are presented. The histogram of Ni particles size showed values in the range of 4 to 18 nm. Carbon nanotubes were also registered in this material. The EDS analysis proved the existence of Ni and Zr. A detailed examination showed the presence of ZrO_2 aggregates with the particle sizes in the range of 6 to 11 nm, and interplanar distance in the 0.29-0.30 nm range. No ZrO_2-NiO solid solution was found. On the right-hand side (Fig. 4.26 B), the images of the spent HTNi/ZrY0.4 catalyst are presented. The histogram of Ni particles revealed similar average size of Ni aggregates as for HTNi/Zr. These values are also similar to Ni^0 crystallite size for both HTNi/Zr and HTNi/ZrY0.4 reduced samples (cp. Table 4.9). For the latter sample, the EDS analysis revealed the

presence of zirconium in the direct vicinity of yttrium. ZrO_2-Y_2O_3 solid solution (with d-spacing of 0.29, 0.28, 0.30 nm) was observed in the form of aggregates. For both HTNi/Zr and HTNi/ZrY0.4 spent catalysts, graphitic carbon was registered with an interlayer distance of 0.27 to 0.32 nm [356,357]. It can be observed that certain Ni crystallites are encapsulated in carbon, which is considered as one of the main reasons for catalysts deactivation in DRM [96].

4.2.5. *Characterization of the spent catalysts after the isothermal tests*

The phase composition, carbon formation, and crystallite size of the active metal (Ni^0) were examined by XRD. XRD diffractograms are presented in Fig. 4.27 for HTNi/Zr and HTNi/ZrY0.4 catalysts after isothermal tests, and compared with the XRD pattern of HTNi (also after DRM reaction). The reflections characteristic for the thermal decomposition of hydrotalcite (periclase-mixed oxides) at 2θ, ca. 37, 43 and 63° (ICOD 00-045-0946), metallic nickel at 2θ ca. 44, 53° (ICOD 01-087-0712) and graphitic carbon at 2θ ca. 27° (ICOD 01-075-2078) were recorded. For the latter, the intensities of the XRD reflections differ for HTNi, HTNi/Zr and HTNi/ZrY0.4 samples. As suggested by Dębek et al. [197] lower intensity of graphite reflections may be linked with better stability of the catalyst, and in the current study, the lowest intensity was observed for HTNi/ZrY0.4 sample. The crystallite sizes of metallic nickel calculated by Scherrer equation (using the half-width of reflection at 2θ ca. 53°) are presented in Table 4.10. For all the catalysts the Ni crystallite size did not change as compared to the reduced materials (cp. Table 4.9). Thus, the deactivation of catalysts was not linked with the sintering of nickel particles.

Moreover, the separate phases of ZrO_2 and ZrO_2-Y_2O_3 were recorded, similarly as for the reduced materials (cp. Fig. 4.22). Also, the same as for the spent catalysts after TPSR tests, no partial reconstruction of hydrotalcite was found for the catalysts promoted with 0.4 wt.% yttrium, indicating an increased structural resistance, i.e., only the unmodified material HTNi as well as HTNi/Zr catalyst showed hydrotalcite reflections after 5 h-catalytic runs at 700 °C. Thus, it can be concluded that the promotion with 0.4 wt.% Y considerably stabilized the periclase phase (solid solution NiO-MgO-Al_2O_3).

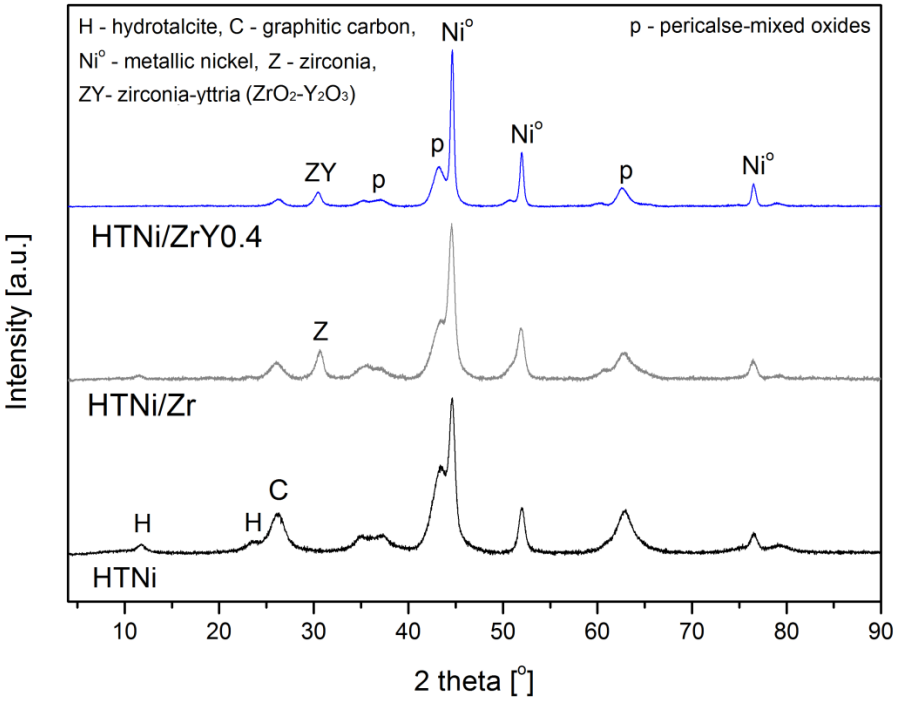

Fig. 4.27 XRD diffractograms of the HTNi/Zr and HTNi/ZrY0.4 spent catalysts (after isothermal catalytic test) compared to HTNi.

Table 4.10 Properties of the spent catalysts (HTNi/Zr and HTNi/ZrY0.4) compared to unmodified HTNi.

Catalyst	XRD	TGA		Raman	Type of carbon (based on XRD, TGA and Raman)
	Ni^0 crystallite size [nm] [1)]	Mass loss due to carbon oxidation [%]	Mass loss [mg] [2)]	I_D/I_G [-]	
HTNi	7	20.0	2.0	1.83	Graphite-like carbon (with low order) + filamentous carbon
HTNi/Zr	9	13.9	1.5	1.47	Graphite-like carbon + filamentous carbon
HTNi/ZrY0.4	12	18.2	1.9	1.02	Graphite-like carbon (with high order) + filamentous carbon + amorphous carbon

[1)] based on the Scherrer equation, from the width at half-maximum of the XRD reflections at 2θ ca. 52°

[2)] resulting from carbon oxidation, calculated assuming the initial mass of the analyzed sample, i.e., 10.5-10.0 mg

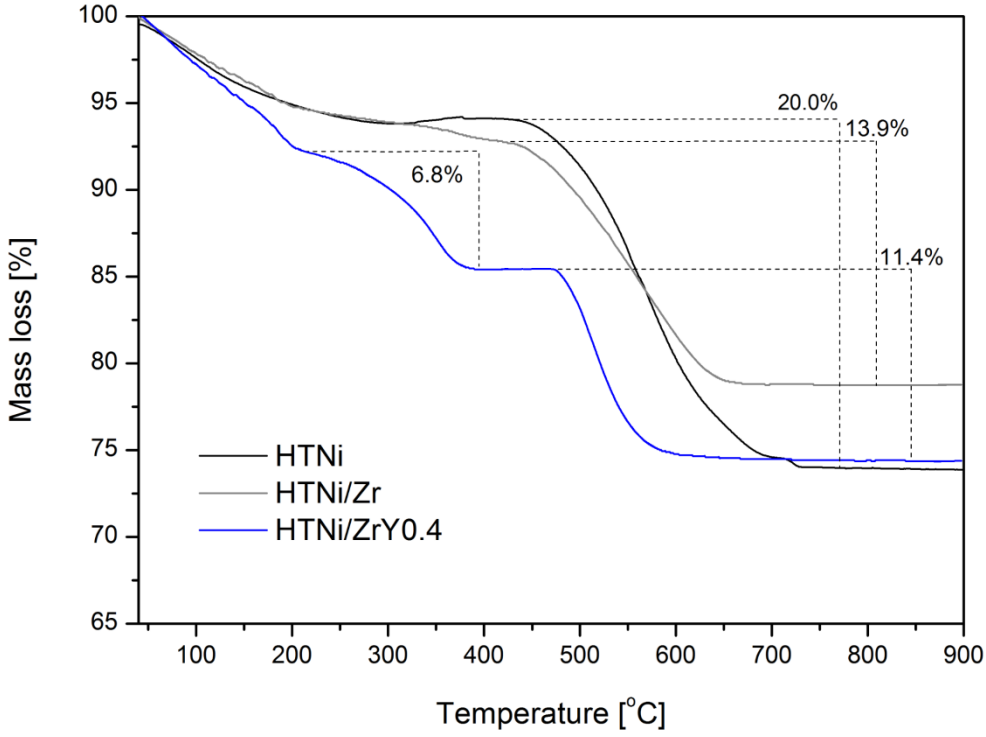

Fig. 4.28 TGA plots for the HTNi/Zr and HTNi/ZrY0.4 spent catalysts (after isothermal catalytic test) compared to HTNi.

TGA plots for the spent catalysts after isothermal tests are presented in Fig. 4.28. Three regions of carbon removal may be distinguished basing on the oxidation temperature: (i) amorphous carbon (T < 300 °C), (ii) ordered carbon nanotubes (400–700 °C), and (iii) graphite (>800 °C) [358–360]. According to Zhang et al. [173] amorphous carbon can participate in the formation of synthesis gas via gasification with CO_2 or H_2O, while graphite leads to catalysts deactivation. Additionally, in Fig. 4.28 the mass loss from ambient temperature to ca. 200 °C is assigned to the removal of adsorbed water [172,285,360]. The weight loss, from 200 to 380 °C, was only recorded for the spent HTNi/ZrY0.4 catalyst (6.8%), and resulted from the oxidation of amorphous carbon [361]. In all samples, the main mass loss occurred between ca. 450 °C and ca. 600, 650 or 750 °C for HTNi, HTNi/Zr or HTNi/ZrY0.4 catalysts, respectively. This mass loss results from oxidation of filamentous carbon, such as for example carbon nanotubes and carbon nanofibers (CNTs and CNFs) [334]. Respectively for HTNi, HTNi/Zr and HTNi/ZrY0.4 catalysts

this mass loss was 20.0%, 13.9% and 11.4%. No mass change in the TGA plot at ca. 800 °C was registered.

The properties of the formed carbon deposit were investigated by Raman spectroscopy (Fig. 4.29). Five peaks at 1328 cm^{-1} (D band), 1590 cm^{-1} (G band), 1603 cm^{-1} (D' band), 2648 cm^{-1} (G' band) and 2911 cm^{-1} (D+G band) were detected for all samples. The first two peaks are typical for CNTs [334,362]. The D band indicates structural imperfections of graphite, while the G band is ascribed to in-plane carbon–carbon stretching vibrations of graphite layers [166]. Another disorder, known as D'-band, appears as a shoulder of the classical G-band. The D' mode is observed for graphitic defects or disordered carbons, and does not exist in pure graphite [334]. The G' band is the most intense peak in the spectrum of crystalline graphite and graphene, whereas the G+D band is a combination of the G and D modes, typical for disturbed graphitic structures [341,363]. The degree of crystallinity of the formed carbon was determined by estimation of the relative intensity of the D and G-bands (I_D/I_G). An I_D/I_G ratio near zero indicates well-structured hard carbon, whereas high value of I_D/I_G suggests the formation of soft carbon with amorphous character [179]. The calculated values are presented in Table 4.10, and follow the order HTNi (I_D/I_G=1.83) > HTNi/Zr (I_D/I_G=1.47) > HTNi/ZrY0.4 (I_D/I_G=1.02). This shows that different carbon structures were formed on the spent catalysts. Although the oxidation of amorphous carbon was only reported in HTNi/ZrY0.4 (cp. Fig. 4.28), on the whole this sample showed the highest degree of graphitization. The differences between TGA and Raman spectroscopic results may originate from the heterogeneity of the studied catalysts, similarly as reported by Saché et al. [179], who found, at two different spots of the Ni-Sn sample, totally different I_D/I_G ratios, of 2.01 (amorphous character) and 0.61 (well-structured hard carbon). The value given in Table 4.10 and Fig. 4.29, is an average of the I_D/I_G values obtained at four different points on the sample.

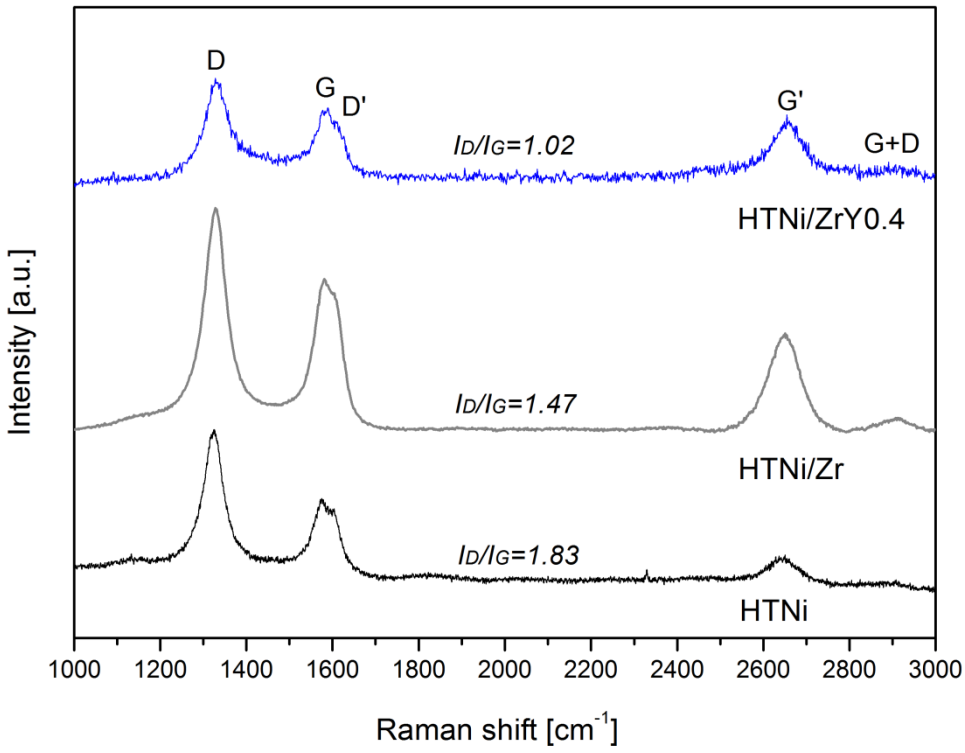

Fig. 4.29 Raman spectra for the spent HTNi/Zr and HTNi/ZrY0.4 catalysts compared to HTNi. The I_D/I_G ratio describes the degree of crystallinity of the formed carbon.

4.2.6. *Conclusions*

In this subchapter, Ni/Mg/Al hydrotalcites (HT) were co-impregnated with Zr and Y (0.2, 0.4, 0.6 wt.%) and tested in the two types of dry reforming of methane (DRM) tests, i.e., in the temperature range of 850-600 °C (TPSR), and in the stability tests at 700 °C for 5 h.

Dry impregnation of HT with a mixture of Zr and Y nitrates resulted in the formation of segregated phase of ZrO_2 in all Zr-containing samples, and ZrO_2-Y_2O_3 solid solution in these samples which were promoted with 0.4 or 0.6 wt.% Zr and Y. A decrease in reducibility, together with lower H_2 consumption and stronger interactions of nickel with the modified-HT support were observed. All Zr- and Y-promoted catalysts showed presence of bulk NiO, except the HTNi/ZrY0.4 catalyst. The promotion with Zr led to the decreased basicity as well as changes in basicity distribution. The percentage of medium basic sites was increasing with the increasing yttrium loading, whereas the opposite effect was

observed for the strong sites. For the latter, higher yttrium loading caused gradual decrease of the percentage of the strong sites.

During the DRM test, all catalysts showed similar catalytic behavior (within experimental error), except the sample modified with 0.2 wt.% Y for which CH_4 and CO_2 conversions were lower. However, only HTNi/ZrY0.4 presented structural resistance to the products of the RWGS side reaction, as supported by the absence of hydrotalcite reflections in the XRD patterns of the spent catalyst. The material promoted with Zr and 0.4 wt.% of Y was catalytically active and stable in DRM (CH_4/CO_2=1) at 700 °C. Moreover, the improvement of catalyst stability was clearly shown at 700 °C for 5 h of TOS, where the HTNi/ZrY0.4 catalyst was more stable than the Y-free material. The observed better stability may have arisen from favorable changes in the distribution of surface basic sites, reduction of bulk NiO, improved Ni dispersion and formation of ZrO_2-Y_2O_3 solid solution.

The characterization of the spent catalysts showed the formation of graphite-like carbon, filamentous and amorphous carbon deposits. The latter was observed to a higher extent in the HTNi/ZrY0.4 catalyst.

4.3. Co-precipitation with zirconium and impregnation with yttrium versus co-precipitation with zirconium and yttrium

This subchapter is a continuation of the study focused on the Zr and Y promotion discussed in **Subchapter 4.2**. The aim of the study was to examine the influence of the method of introduction of promoters on physico-chemical features of the resulting catalysts, their structure and catalytic behavior in dry reforming of methane (DRM). Ni/Mg/Al double-layered hydroxides promoted with Zr and Y introduced via co-precipitation of Ni, Mg, Al and Zr compounds and impregnation with yttrium were prepared, while in **Subchapter 4.2** the catalysts promoted via impregnation of both Zr and Y onto Ni/Mg/Al hydrotalcite were discussed. Five catalysts were prepared. Three were modified with zirconium (5.0 wt.%) and yttrium (0.2, 0.4 or 0.6 wt.%) via co-precipitation of Ni/Mg/Al/Zr and by incipient wetness impregnation with Y. The fourth catalyst was prepared similarly, without Y. The fifth catalyst was prepared by co-precipitation of all Ni, Mg, Al, Zr and Y components, and contained (assumed) 5.0 wt.% of Zr and 0.4 wt.% of Y. The 0.4 wt.% concentration of yttrium was chosen taking into account the following experimental findings (discussed in more detail in **Subchapter 4.2.**): (i) high catalytic activity and significantly better stability than for HTNi/Zr, (ii) the structural resistance towards the side reaction products (water), and the lack of the partial reconstruction of the hydrotalcite structure, and (iii) the considerable presence of amorphous carbon, which can contribute to the synthesis gas production via gasification. The mentioned materials were compared with Ni/Mg/Al/Zr co-precipitated catalyst.

4.3.1. *Physicochemical properties*

The XRD of fresh double-layered hydroxides is presented in Fig. 4.30. All recorded diffractograms have reflections typical for double-layered hydroxides (hydrotalcite) at 2θ ca. 11, 22, 35, 61 and 62°, originating from (003), (006), (009), (110) and (113) planes, respectively. Structural parameters *a*, *c*, and *c'* are summarized in Table 4.11. Unit cell parameter, indicating the average cation-cation

distances, slightly increased after the addition of Zr (3.6 versus 3.7 Å). Since ionic radius of Zr^{4+} (0.72 Å) is bigger than Al^{3+} (0.675 Å), this suggests a partial substitution of alumina by zirconia ions increasing the distance between the cations in periclase layers [203,316,364,365]. The values for the *c* and *c'* parameters of the unit cell are respectively in the range of 23.43-23.62 Å and 7.81-7.87 Å, indicating the presence of carbonate anions between the layers of hydrotalcite (7.65 Å). The slight increase of parameter *c* suggests the deposition of yttrium on the catalysts surface. As described in **Subchapters 4.1** and **4.2**, a slight shift towards lower angles of d_{003} was registered, indicating, additionally, the possible presence of interlayer NO_3^{2-} anions [248–250,284].

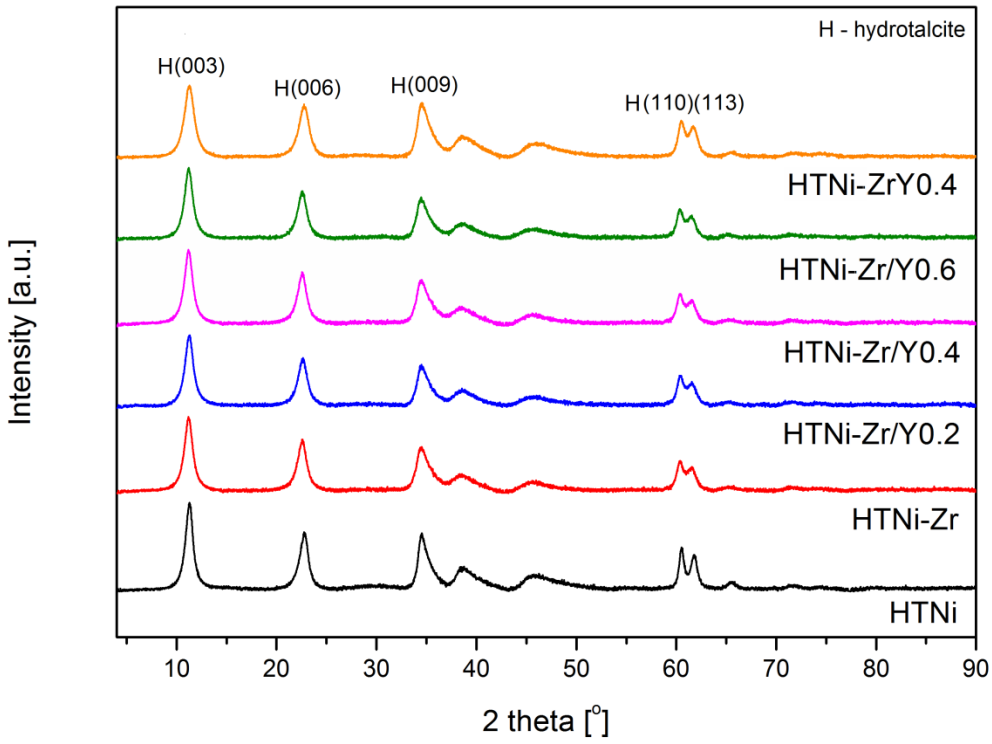

Fig. 4.30 XRD diffractograms of the freshly synthesized materials co-precipitated with Zr and impregnated with Y (HTNi-Zr, HTNi-Zr/Y0.2, HTNi-Zr/Y0.4, HTNi-Zr/Y0.6) compared to HTNi. "-" in the name of the sample designates the introduction of promoter/s via co-precipitation with Ni, Mg and Al; "/" designates the introduction via impregnation of Y onto HTNi-Zr.

The textural features of the studied catalysts are summarized in Table 4.11. Specific surface area was between 120-150 m^2/g, typical for this kind of materials [197,203,253,258]. Co-precipitation with Zr resulted in an increase of S_{BET} and a decrease in pore size diameter, similarly as reported in the literature [188,203], while no change in mesopore volume was registered. After promotion of HTNi-Zr sample with yttrium, specific surface area decreased from 150 m^2/g to 131, 126 and 122 m^2/g for HTNi/ZrY0.2, HTNi/ZrY0.4 and HTNi/ZrY0.6, respectively, as a consequence of the metal deposition on the catalyst surface and blockage of the pores. The co-precipitation with Zr and 0.4 wt.% Y also led to a decrease of S_{BET} and the volume of the mesopores was slightly reduced.

Table 4.11 Structural parameters of the freshly synthesized materials and textural features of calcined materials.

Catalyst	XRD			N_2 sorption		
	a [Å][1)]	c [Å][2)]	c' [Å]	S_{BET} [m^2/g][3)]	V_p [cm^3/g][4)]	d_p [nm][5)]
HTNi	3.06	23.45	7.82	120	0.6	19
HTNi-Zr	3.07	23.56	7.85	150	0.5	11
HTNi-Zr/Y0.2	3.07	23.48	7.83	131	0.5	10
HTNi-Zr/Y0.4	3.07	23.62	7.87	126	0.4	10
HTNi-Zr/Y0.6	3.07	23.55	7.85	122	0.4	10
HTNi-ZrY0.4	3.07	23.43	7.81	95	0.3	6

[1)] calculated from (110) spacing $a=2d_{(110)}$ as suggested by Cavani et al. [244]

[2)] calculated from XRD patterns of the fresh catalysts, from the position of the three first reflections $c=d_{(003)} + 2d_{(006)} + 3d_{(009)}$, as suggested by Liu et al. [207]

[3)] specific surface areas calculated from the BET equation

[4)] mesopore volumes derived from the BJH desorption calculation method

[5)] pore size distribution obtained from the BJH desorption calculation method

The co-precipitation with both Zr and Y led to the different porosity than that registered after the Zr,Y-co-impregnation (Table 4.12), with much lower average pore dimeter and pore volume registered for the former. This shows that the way of yttrium introduction influences the volume of the pores and average pore diameter. Possibly upon Zr and Y co-precipitation synthesis, not only Zr, but also yttrium

was incorporated in the framework of periclase-like structure, leading to the creation of smaller mesopores with less volume (Table 4.12).

Table 4.12 Comparison of textural properties of the calcined samples depending on the way of Zr and Y introduction.

Catalyst	**Promoter introduced via:**			
	Zr-coP	**Zr-Y-coP**	**Zr-Y-Imp**	**Zr-coP, Y -Imp**
Designation	HTNi-Zr	HTNi-ZrY0.4	HTNi/ZrY0.4	HTNi-Zr/Y0.4
S_{BET} [m^2/g]	150	95	107	126
V_p [cm^3/g]	0.5	0.3	0.5	0.4
d_p [nm]	11	6	19	10

coP - co-precipitation

Imp - dry impregnation

The composition of the studied catalysts is given in Table 4.13. The calcined materials had Ni contents within 20-25 wt.%, which is close to the value assumed during the synthesis step. The zirconia content differs from the nominal value of 5.0 wt.%, and for the Zr-containing materials the following values were recorded: 3.6, 2.8, 3.5, 4.6 and 4.1 wt.% for HTNiZr, HTNiZr/Y0.2, HTNiZr/Y0.4, HTNiZr/Y0.6, HTNiZrY0.4, respectively. According to Dębek et al. [203], lower values of detected zirconia content may arise from the loss of Zr to another oxide phase. Moreover, as mentioned in **Subchapter 4.2.**, the presence of magnesium-zirconium oxide and aluminum-zirconium oxide cannot be excluded. The Ni^{2+}/Mg^{2+} molar ratio is close to the nominal values only for the unmodified material HTNi, and HTNi-Zr, HTNi-Zr/Y0.2 catalysts. The impregnation with 0.4 and 0.6 wt.% Y resulted in the increased Ni^{2+}/Mg^{2+} molar ratio. The value below 0.33 for HTNi-ZrY0.4 indicates that Mg^{2+} ions were only partly substituted by the assumed number of Ni^{2+}. The M^{2+}/M^{3+} molar ratio was only slightly higher than assumed 3.0.

Table 4.13 Structural parameters, elemental composition, and textural properties for the calcined samples (HTNi-Zr, HTNi-Zr/Y0.2, HTNi-Zr/Y0.4, HTNi-Zr/Y0.6 and HTNi-ZrY0.4) compared to unpromoted HTNi. The numbers in brackets are nominal values.

Catalyst	XRF							
	Mg [wt.%]	**Al [wt.%]**	**Ni [wt.%]**	**Zr [wt.%]**	**Y [wt.%]**	**Ni^{2+}/Mg^{2+} molar ratio**	**M^{2+}/M^{3+} molar ratio**	**Al^{3+}/Zr^{4+} molar ratio**
HTNi	30	12	20	-	-	0.29 (0.33)	3.6 (3.0)	-
HTNi-Zr	26	9	23	3.6 (5.0)	-	0.36 (0.33)	3.8 (3.0)	8.9 (5.0)
HTNi-Zr/Y0.2	29	9	20	2.8 (5.0)	0.2	0.29 (0.33)	3.7 (3.0)	10.8 (5.0)
HTNi-Zr/Y0.4	23	8	25	3.5 (5.0)	0.4	0.46 (0.33)	3.8 (3.0)	8.0 (5.0)
HTNi-Zr/Y0.6	23	9	24	4.6 (5.0)	0.7	0.44 (0.33)	3.4 (3.0)	6.7 (5.0)
HTNi-ZrY0.4	32	13	20	4.1 (5.0)	0.5	0.26 (0.33)	3.4 (3.0)	10.9 (5.0)

Upon calcination, the double-layered hydroxides were transformed into mixed oxides with a periclase-like structure (Fig. 4.31). The co-precipitation with Zr led to the formation of a separate phase of tetragonal ZrO_2 (ICOD 01-079-1765), similarly as shown in the diffractograms for HTNi/Zr, HTNi/ZrY0.2, HTNi/ZrY0.4, HTNi/ZrY0.6 (**Subchapter 4.2.**).

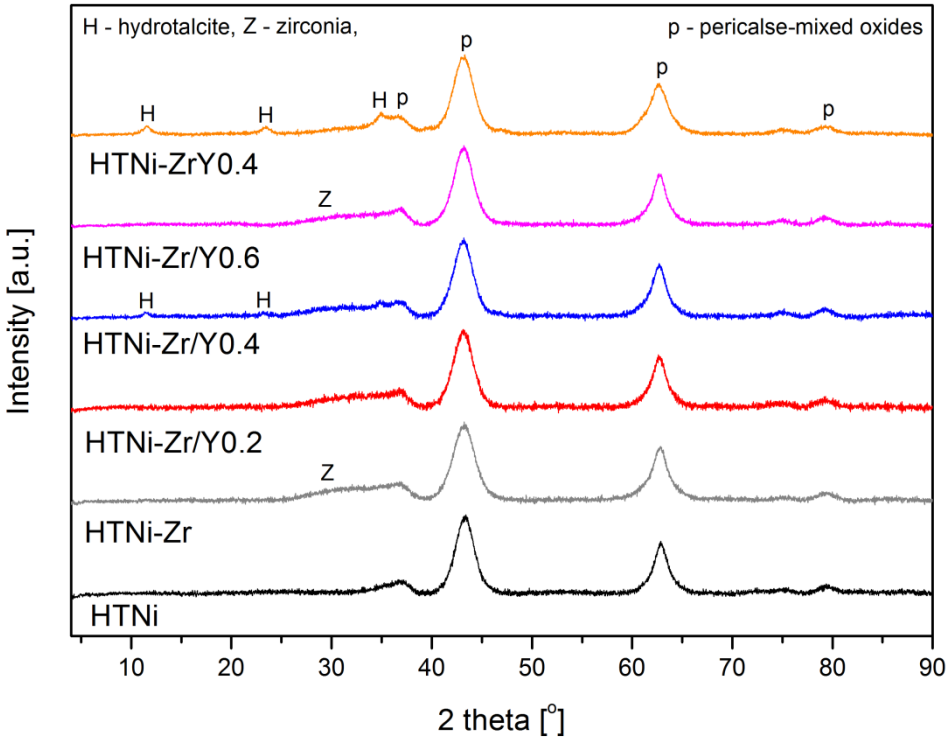

Fig. 4.31 XRD patterns for Zr- and Y-promoted catalysts calcined at 550 °C for 5 h.

Table 4.14 presents the comparison of the phases registered during XRD analysis. The XRD patterns for HTNi-Zr/Y0.4 and HTNi-ZrY0.4 samples still reveal three reflections which are characteristic for hydrotalcite structure. This shows that for both materials a higher calcination temperature is required to fully transform their structure into periclase-mixed oxides. This was not observed for the samples co-precipitated with Zr and co-impregnated with Zr and Y. For the latter, more crystalline form of ZrO_2 was recorded, as more sharp reflections were registered at 2θ ca. 30° and 50° (cp. Fig. 4.19 in **Subchapter 4.2.**). For the Zr co-precipitated catalysts, however, only a small shoulder was observed in XRD patterns (Fig. 4.31). Similar shoulder was observed elsewhere [203] for calcined HNiZr5 sample.

Table 4.14 Comparison of phase composition of the calcined samples depending on the way of Zr and Y introduction.

Catalyst	**Promoter introduced via:**			
	Zr-coP	**Zr-Y-coP**	**Zr-Y-Imp**	**Zr-coP, Y -Imp**
Designation	HTNi-Zr	HTNi-ZrY0.4	HTNi/ZrY0.4	HTNi-Zr/Y0.4
Hydrotalcite (H)	-	+	-	+
Periclase (p)	+	+	-	+
Zirconia (Z)	+	+	+	+
Zirconia-Yttria (ZY)	-	-	+	-

coP - co-precipitation

Imp - dry impregnation

"+" indicates the presence, "-" the absence

4.3.2. *Reducibility, basicity, Ni dispersion and crystallite size*

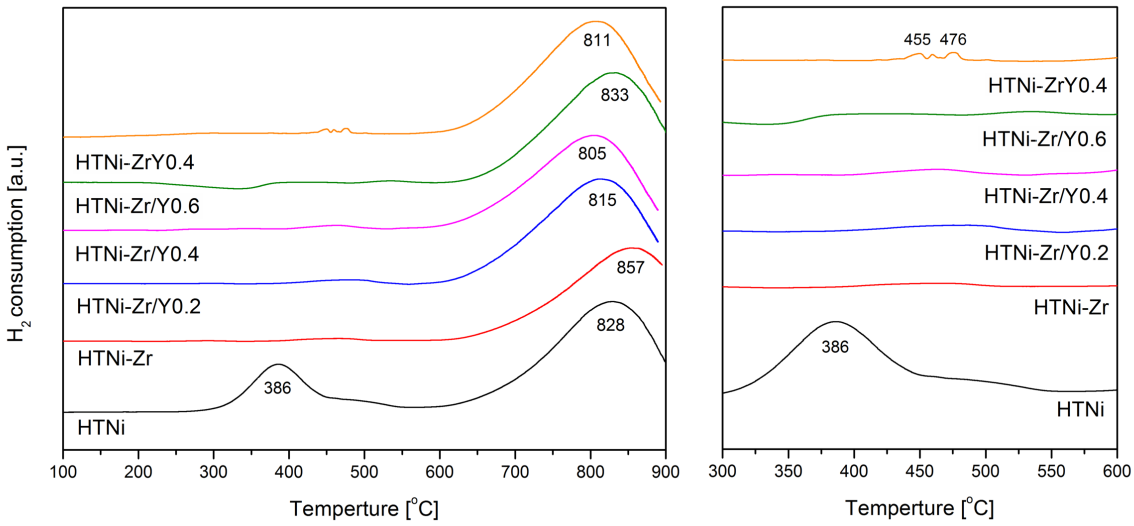

Fig 4.32 TPR-H_2 profiles for Zr- and Y-modified catalysts.

Fig. 4.32 presents the TPR-H_2 profiles for the calcined double-layered hydroxides modified with Zr and Y. All profiles exhibit a wide asymmetric peak at temperatures between 805 and 857 °C, arising from the reduction of nickel oxide species in the periclase-like structure. The maximum temperature for these peaks is shifted to higher values after introduction of Zr via co-precipitation with Ni, Mg and Al, pointing to stronger interactions of NiO, due the formation of a highly stable NiO–MgO solid

solution. Similar observation was reported in the study of Dębek et al. [203]. In case of the Y-doped catalysts presented in Fig. 4.32, a shift towards lower reduction temperatures was observed for the Ni-phase, pointing to easier NiO reduction upon the introduction of yttrium species. The shifts towards lower temperature were more distinct after promotion with 0.2 and 0.4 wt.% Y, with values even lower than that for the unpromoted HTNi catalyst. After addition of 0.6 wt.%, the temperature was only slightly higher than for the unmodified catalyst, i.e., 833 versus 828 °C for HTNi. The increased reductivity arising from yttrium addition was not observed for co-impregnated catalysts (cp. **Subchapter 4.2.**). H_2 uptake values, calculated from the area under the TPR-H_2 profiles, are listed in Table 4.15. Zr modification resulted in the decreased H_2 consumption in comparison to the one registered for HTNi catalyst, due to the stronger interactions of Ni species with the support. However, after further promotion with yttrium (0.2-0.6 wt.%) only small differences in H_2 consumption were registered. The HTNi-Zr/Y0.2 and HTNi-ZrY0.4 catalysts which had the lowest reduction temperature (cp. Fig. 4.32), did not show the highest H_2 consumption. Similar observation was reported for the HTNi-Y3.0 catalyst discussed in **Subchapter 4.1**. The hydrogen consumption formed the following sequence: 0.110, 0.142, 0.133, 0.148 and 0.196 mmol H_2/g respectively for HTNi-Zr, HTNi-Zr/Y0.2, HTNi-Zr/Y0.4, HTNi-Zr/Y0.6 and HTNi-ZrY0.4. Thus, the promotion with metals decreased the H_2 uptake in contrast to unpromoted HTNi.

Table 4.15 Hydrogen uptake, textural properties, basicity and Ni dispersion for Zr and Y-modified catalysts.

Catalyst	TPR-H_2 Calcined materials	N_2 sorption Reduced materials			TPD-CO_2 Reduced materials				H_2 chemisorp-tion Calcined materials[4)]
	H_2 uptake [mmol H_2/g]	S_{BET} [m^2/g][1)]	V_p [cm^3/g][2)]	d_p [nm][3)]	Weak [%]	Medium [%]	Strong [%]	Total basicity [µmol/g]	Ni dispersion [%]
HTNi	0.209	68	0.4	21	15	42	43	107	8.9
HTNi-Zr	0.110	90	0.4	16	24	50	26	62	8.6
HTNi-Zr/Y0.2	0.142	91	0.4	16	7	30	63	114	5.1
HTNi-Zr/Y0.4	0.133	79	0.4	11	14	35	51	43	6.9
HTNi-Zr/Y0.6	0.148	101	0.5	15	13	47	41	64	6.6
HTNi-ZrY0.4	0.196	n.m	n.m	n.m	-	58	42	153	10.2

n.m. – not measured

[1)] specific surface areas calculated from the BET equation

[2)] mesopore volumes derived from the BJH desorption calculation method

[3)] pore size distribution obtained from the BJH desorption calculation method

[4)] before H_2 chemisorption the samples were reduced *in situ*

XRD diffractograms acquired for the reduced catalysts are presented in Fig. 4.33. Similarly, as for the co-impregnated Zr and Y materials, characteristic reflections of periclase-mixed oxides, metallic nickel and ZrO_2 were recorded. The reduced materials showed sharper reflections of tetragonal zirconia than the calcined materials (cp. Fig. 4.31). Crystallite size calculated for ZrO_2 (at 2θ=30°) was 5 nm for HTNi-Zr, HTNi-Zr/0.2, HTNi-Zr/Y0.4, HTNi-Zr/Y0.6 and HTNi-ZrY0.4 catalysts. This value is lower than the one registered for co-impregnated Zr,Y materials described in previous **Subchapter 4.2.** (ZrO_2 crystallite size of 11 nm). This suggests that co-precipitation led to the formation of smaller particle size of this promoter, thus its better dispersion, which, as discussed later, influenced the catalytic performance. Moreover, neither impregnation nor co-precipitation with yttrium resulted in the formation of its segregated phase, thus indicating the deposition of yttrium on the surface of the studied materials. Similarly as described in the previous chapters, the lack of the yttrium separate

phase may arise from either the low content of the metal and/or its high dispersion. No shift of the reflection arising from Zr was observed, indicating that ZrO_2-Y_2O_3 solid solution was not formed.

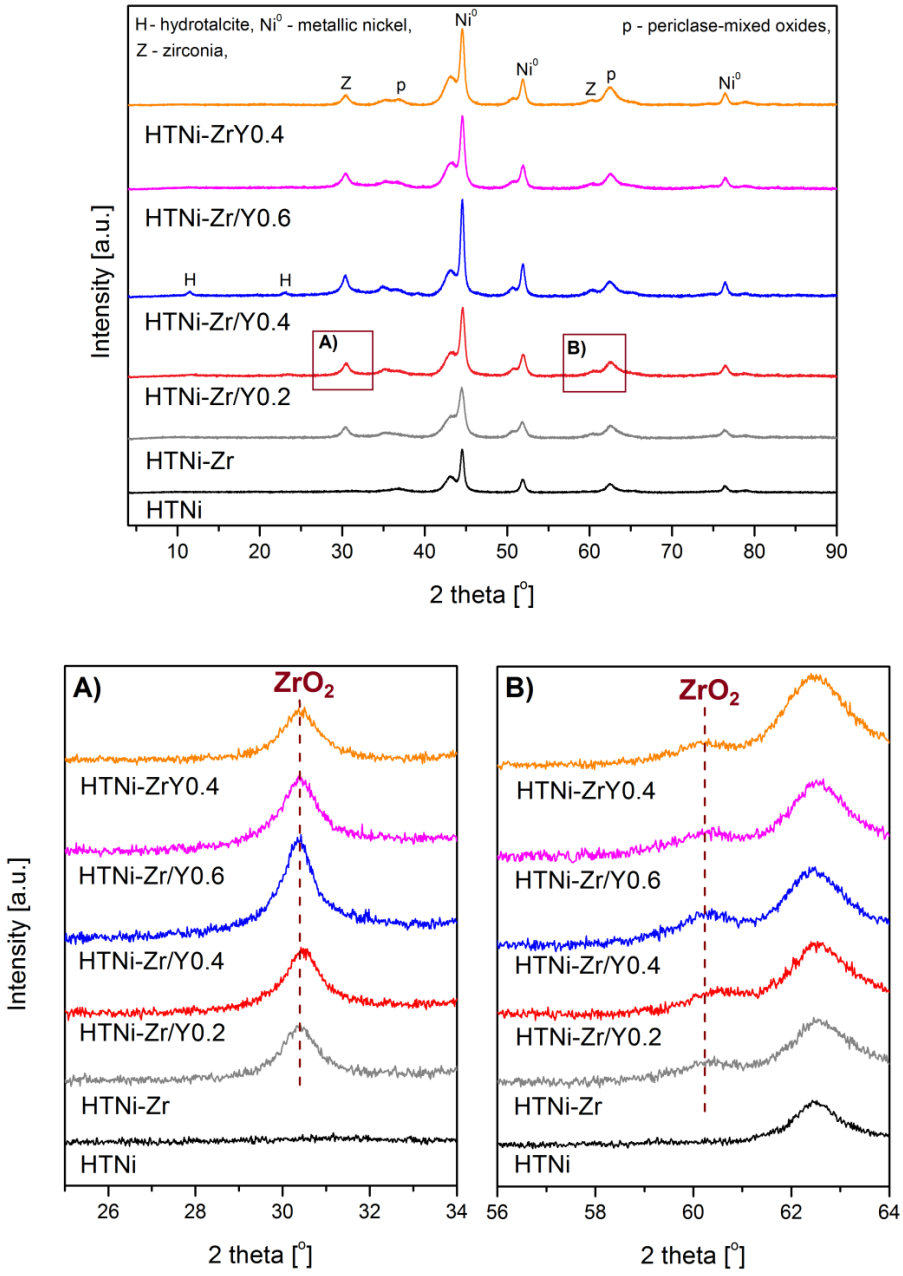

Fig 4.33 XRD patterns for Zr,Y-modified catalysts reduced in a mixture of H_2/Ar at 900 °C. "-" in the name of the sample designates the introduction of promoter/s via co-precipitation with Ni, Mg and Al; "/" designates the introduction via impregnation of Y onto HTNi-Zr.

The Ni^0 crystallite sizes calculated for the reduced samples are listed in Table 4.16. Co-precipitation with Zr resulted in the decreased crystallite size in contrast to HTNi catalyst (6 nm versus 8 nm, respectively). The further impregnation with yttrium nitrate led to the creation of bigger crystallites (9 nm), as detected by XRD. A comparable result was recorded for the sample co-precipitated with Zr and Y 0.4 wt.%.

Table 4.16 Average diameters of nickel particles in the reduced catalysts modified with Zr and Y.

Catalyst	**d_{Ni} from XRD [nm] [1)]**	**d_{Ni} from H_2 chemisorption [nm] [2)]**	**d_{Ni} from TEM [nm] [3)]**
HTNi	8	11	27
HTNi-Zr	6	11	12
HTNi-Zr/Y0.2	8	19	n.m.
HTNi-Zr/Y0.4	9	15	17
HTNi-Zr/Y0.6	8	15	n.m.
HTNi-ZrY0.4	8	10	n.m.

n.m. – not measured

[1)] based on the Scherrer equation, from the width at half-maximum of the XRD reflections at 2θ ca. 52°

[2)] calculated from d = 97.1/(%D) based on the assumption of spherical crystallites of uniform size

[3)] average diameter of Ni particles obtained from TEM images

The recorded values are slightly lower than for the sample co-impregnated with both Zr and Y (Table 4.17). For the latter, Ni crystallite size was 11 nm, which is the highest value among the Zr,Y-modified materials.

Table 4.17 Comparison of Ni^0 crystallite size (XRD) in the reduced samples depending on the way of Zr and Y introduction.

Catalyst	**Promoter introduced via:**			
	Zr-coP	**Zr-Y-coP**	**Zr-Y-Imp**	**Zr-coP, Y -Imp**
Designation	HTNi-Zr	HTNi-ZrY0.4	HTNi/ZrY0.4	HTNi-Zr/Y0.4
Ni crystallite size [nm]	6	8	11	9

coP - co-precipitation

Imp - dry impregnation

The textural properties of the materials reduced in a mixture of 5 vol.% of H_2 in Ar are presented in Table 4.15. A considerable decrease of the S_{BET} was observed for all catalysts in contrast to the results acquired for the calcined materials. Additionally, a slight increase in average pore diameter was observed, while there were no changes in mesopore volume. The changes within textural features may be attributed to the transformation of NiO into Ni^0.

To determine the strength and number of basic sites in the reduced Zr/Y-promoted mixed-oxides, TPD-CO_2 was applied. The results are presented in Fig. 4.34 and Table 4.13. All catalysts presented three desorption peaks, except the HTNi-ZrY0.4 material with only two (the lack of weak basic sites). The total basicity decreased after the modification with metals in a sequence: HTNi-ZrY0.4 (153 µmol/g) > HTNi-Zr/Y0.2 (114 µmol/g) > HTNi (107 µmol/g) > HTNi-Zr (62 µmol/g) ≈ HTNi-Zr/Y0.6 (64 µmol/g) > HTNiZr/Y0.4 (43 µmol/g). The number of total basic sites of HTNi-Zr is in agreement with the value registered by Dębek et al. [203] for HZrNi5 (61 µmol/g). The presence of zirconium affected also the distribution of the weak, medium and strong basic sites. Similarly as in case of Zr and Y co-impregnated materials, the gradual increase of the yttrium content (added via impregnation), led to the decreased percentage share of strong basic sites, while the opposite trend was observed for the medium-strength sites which % increased after doping with yttrium. Furthermore, the content of yttrium and the way of its introduction (impregnation and co-precipitation) also influenced the basic properties of catalysts. The co-precipitation with both Zr and Y resulted in the formation of new basic sites, mostly in the form of Lewis acid-base pairs (medium strength sites) and low coordinated oxygen species (strong sites). Moreover, the maximum temperatures of desorption peaks were shifted towards higher values, pointing to the increased strength of the basic sites for HTNi-ZrY0.4 catalyst [9,10]. Among all the tested materials, the number of total basic sites was the highest for the HTNi-ZrY0.4, i.e., the one with both promoters introduced into HTNi via co-precipitation (Table 4.13).

Comparing the results registered in this study with the series presented in **Subchapter 4.2.**, the total number of basic sites were two times higher after having both Zr and Y on the surface (HTNi/ZrY0.4) than only yttrium (HTNi-Zr/Y0.4) (Table 4.18). The introduction of Zr within the

framework of the structure obviously decreased the total basicity, as Zr may strongly interact with Mg and Al. However, when zirconia was incorporated together with yttrium the effect was opposite, resulting in an increased basicity. The calculated number is almost two times higher for HTNi-ZrY0.4 than HTNi/ZrY0.4.

Table 4.18 Comparison of basic properties for the reduced samples depending on the way of Zr and Y introduction. The total basicity for unmodified HTNi catalyst was 107 µmol/g.

Catalyst	**Promoter introduced via:**			
	Zr-coP	**Zr-Y-coP**	**Zr-Y-Imp**	**Zr-coP, Y -Imp**
Designation	HTNi-Zr	HTNi-ZrY0.4	HTNi/ZrY0.4	HTNi-Zr/Y0.4
Weak [%]	24	-	20	14
Medium [%]	50	58	42	35
Strong [%]	26	42	38	51
Total basicity [µmol/g]	62	153	85	43

coP - co-precipitation

Imp - dry impregnation

"-" indicates the absence

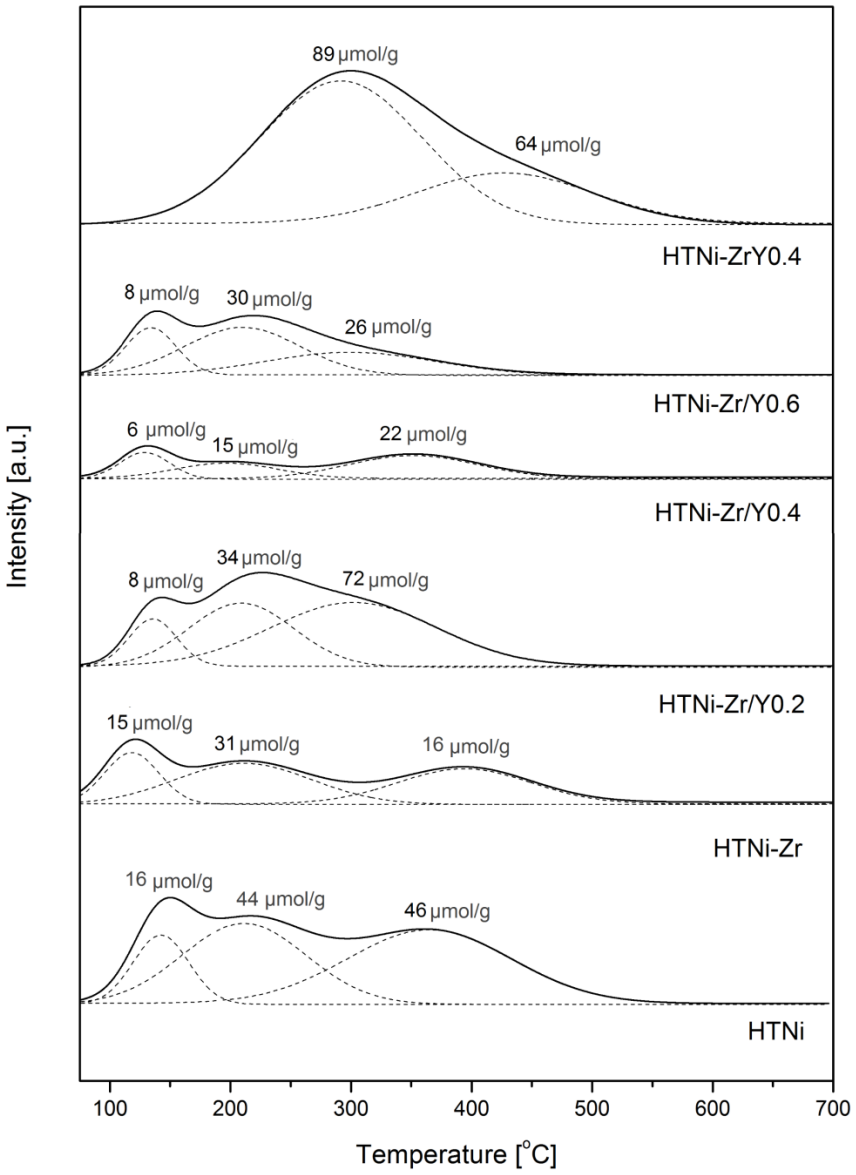

Fig 4.34 TPD-CO_2 profiles for the reduced Zr and Y promoted catalysts. "-" in the name of the sample designates the introduction of promoter/s via co-precipitation with Ni, Mg and Al; "/" designates the introduction via impregnation of Y onto HTNi-Zr.

Hydrogen chemisorption allowed to determine metal dispersion which is presented in Table 4.13. It can be seen that the modification with Zr did not affect the Ni dispersion as compared to the unpromoted HTNi material. Similar observation was reported by Yu et al. [366] for NiZr hydrotalcite. However, the promotion with both Zr and Y resulted in a decrease of this parameter. The latter may be explained by the presence of yttrium species on the surface of the material, covering a part of the

available Ni active sites [367]. Yu et al. [368] also reported a decrease of Ni dispersion for La-Ni/Mg/Al hydrotalcites for hydrotalcite with La/Al molar ratio=0.18, as well as an increase of Ni^0 crystal size. The observations of these authors are in agreement with the current study, in which the addition of yttrium led to the formation of bigger Ni crystallites. After co-precipitation with Zr and Y the dispersion of Ni increased, possibly as a consequence of yttrium presence inside the structure.

TEM images (Figs. 4.35 A,B) confirmed the presence of well dispersed Ni particles (darkest places, as indicated by the arrows). Better dispersion may be observed for HTNi-Zr than for HTNi-Zr/Y0.4, in agreement with H_2 chemisorption results (cp. Table 4.13). Moreover, according to the recorded micrographs the Ni particle size was smaller for HTNi-Zr catalyst than for HTNi-Zr/Y0.4. For the former, the particle size ranged from 1 nm to 33 nm, while after the yttrium impregnation the registered particles were bigger (from 1 nm to 50 nm). A possible sintering upon reduction at 900 °C of the metallic nickel particles may explain this fact.

Table 4.14 summarizes the average particle size of the metallic nickel calculated via three different characterization techniques (XRD, H_2 chemisorption and TEM). The differences between these methods were discussed in **Subchapter 4.1.** It is important to note that for each technique, the impregnation with yttrium resulted in the increased crystallite size of Ni^0 as compared to the HTNi-Zr catalyst.

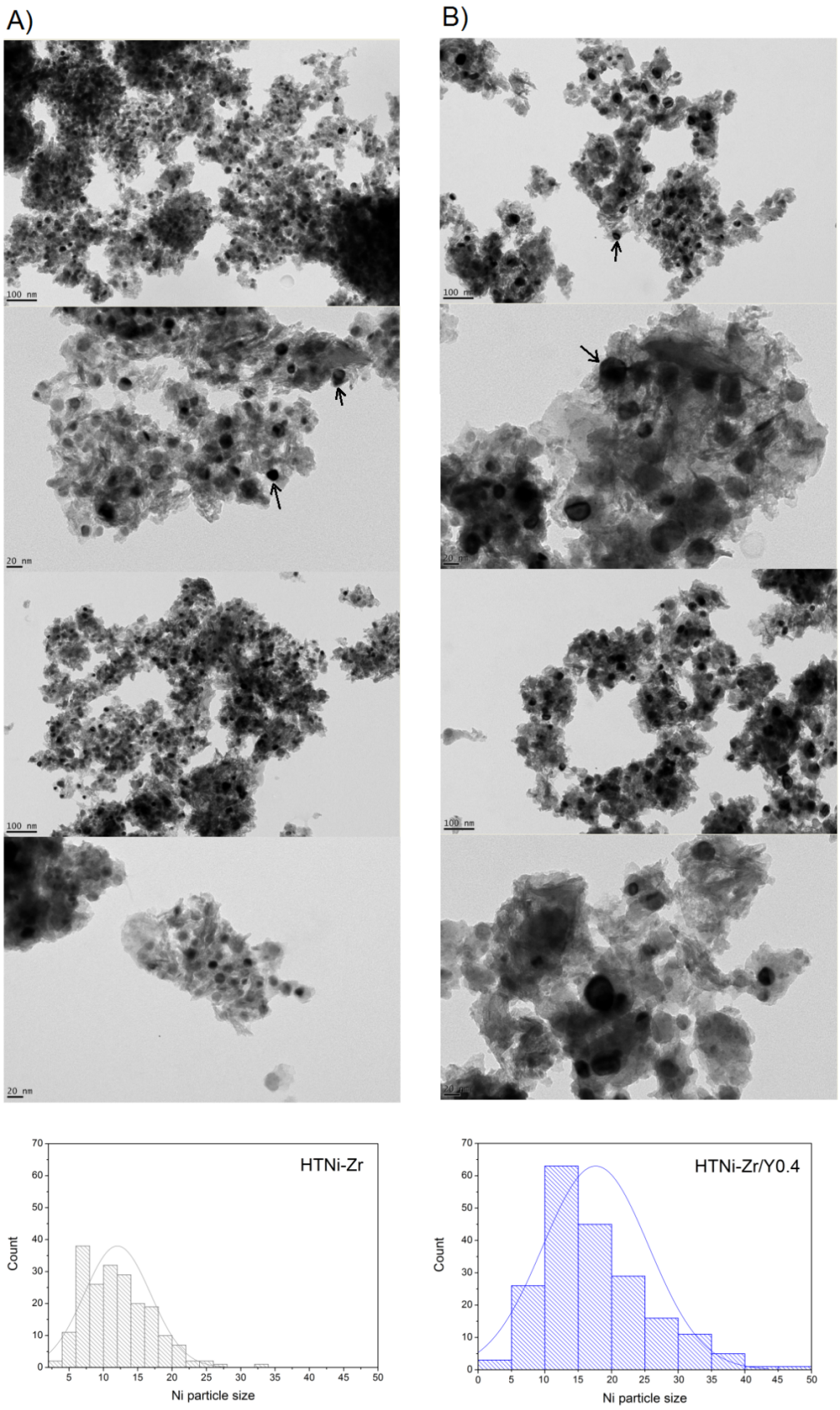

Fig. 4.35 TEM images for the reduced HTNi-Zr and HTNi-Zr/Y0.4 catalysts and the distribution of Ni particle sizes.

4.3.3. *Catalytic activity and stability in DRM*

The activity of all catalysts was examined in the dry reforming of methane process in the temperature range of 850-600 °C. The CH_4 conversion as a function of temperature is presented in Fig. 4.36 A. The highest methane conversion was registered for HTNi-Zr catalyst, followed by HTNi-Zr/Y0.4, HTNi-Zr/Y0.2, HTNi-Zr/Y0.6 and HTNi. A similar trend was observed for CO_2 conversion (Fig. 4.36 B). The decrease of conversion caused by yttrium addition is a consequence of a partial blockage of the available nickel sites as confirmed by the obtained Ni dispersion values. Moreover, as mentioned in the previous chapters, the proper basicity contributes to the enhanced CO_2 adsorption and thus higher CO_2 conversion. However, there is no straight correlation between the basicity and the obtained catalytic activity results. According to Dębek et al. [203], both surface basicity and reducibility of Ni species in Zr-containing Ni/Mg/Al double-layered hydroxides influence the catalytic performance of hydrotalcites in DRM and a proper balance between both have to be found. In the study of these authors, the increasing Zr content led to the decreased basicity and increased maximum reduction temperature. This shows that stronger interactions of Ni with support improved the catalytic performance in DRM. For the tested Zr,Y-modified series, the increasing activity sequence is in the good agreement with the decreasing H_2 consumption acquired from TPR-H_2 (cp. Table 4.13). This correlation is significant at the temperatures of 600 and 650 °C. Among the studied yttrium-impregnated catalysts, the 0.4 wt.% loading resulted in the best conversion. On the other hand, the highest catalytic activity registered for Zr co-precipitated material, is in contrast with the results of both Yu et al. [366] and Dębek et al. [203]. Both articles related that Zr led to the decreased catalytic activity compared to the unmodified material. Nevertheless, in the study of Dębek et al. [203] the low CH_4 and CO_2 conversions were accompanied with the enhanced stability as proven by the less carbon deposit on the surface of the Zr-modified catalyst.

The H_2/CO molar ratio (Fig. 4.36 C) was always lower than unity, which confirms the coexistence of parallel reactions, resulting in the formation of excess CO, e.g. reverse-water gas shift (RWGS).

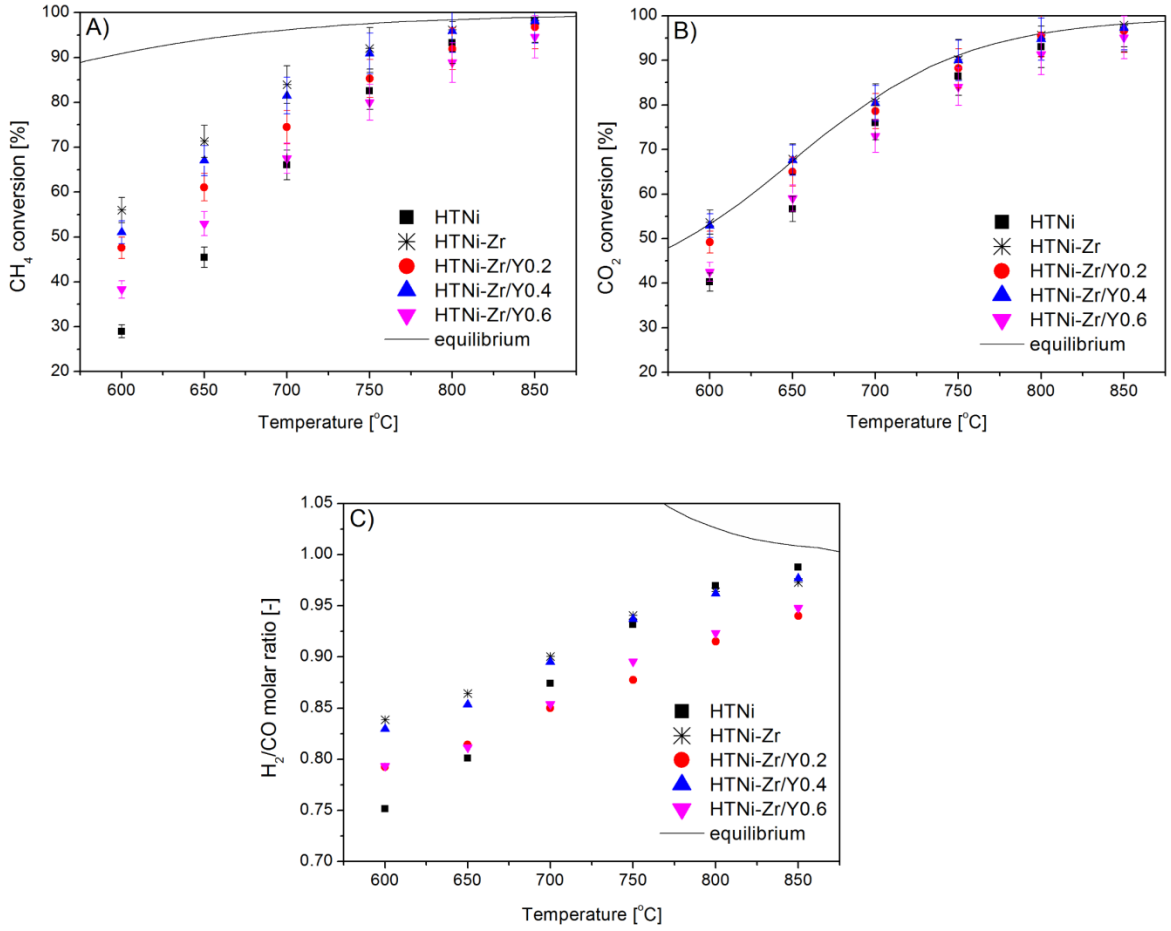

Fig. 4.36 DRM performance tests (CH_4- and CO_2-conversion, H_2/CO molar ratio) modified with Zr and Y using different methods; "-" in the name of the sample designates the introduction of promoter/s via co-precipitation with Ni, Mg and Al; "/" designates the introduction via impregnation of Y onto HTNi-Zr. Tests conditions: $CH_4/CO_2/Ar$=1/1/8, GHSV= 20,000 h^{-1}, the temperature range 600-850 °C. Solid lines represent thermodynamic equilibrium.

Activity tests were additionally carried out at 700 °C for 5 h in order to evaluate the stability of the catalysts. For this test HTNi, HTNi-Zr and HTNi-Zr/Y0.4 were chosen, and additionally zirconium and yttrium co-precipitated material (HTNi-ZrY0.4). The conversions of CH_4 and CO_2, and H_2/CO molar ratios are shown in Figs. 4.37 A, B, C. The unmodified catalyst showed the lowest CH_4 and CO_2 conversions. The sequence of both was: HTNi < HTNi-Zr/Y0.4 ≈ HTNi-Zr < HTNi-ZrY0.4. For the HTNi-ZrY0.4 catalyst an increase in CH_4 and CO_2 conversions with time on stream was registered, pointing to a further evolution of Ni-species with TOS. The HTNi, HTNi-Zr, HTNi-Zr/Y0.4 catalysts showed more

stable performance, though conversions were lower. The H_2/CO molar ratio was also enhanced for the catalyst with Zr and Y promoted by the co-precipitation (HTNi-ZrY0.4). After first 50 min the ratio reached the value of 1.0, and constantly increased with TOS up to 1.02 after 88 minutes, followed by a gradual decrease till molar ratio of 0.99 was reached after 237 minutes. The values slightly above unity point to the occurrence of side reactions which result in higher H_2 production, such as e.g. CH_4 decomposition.

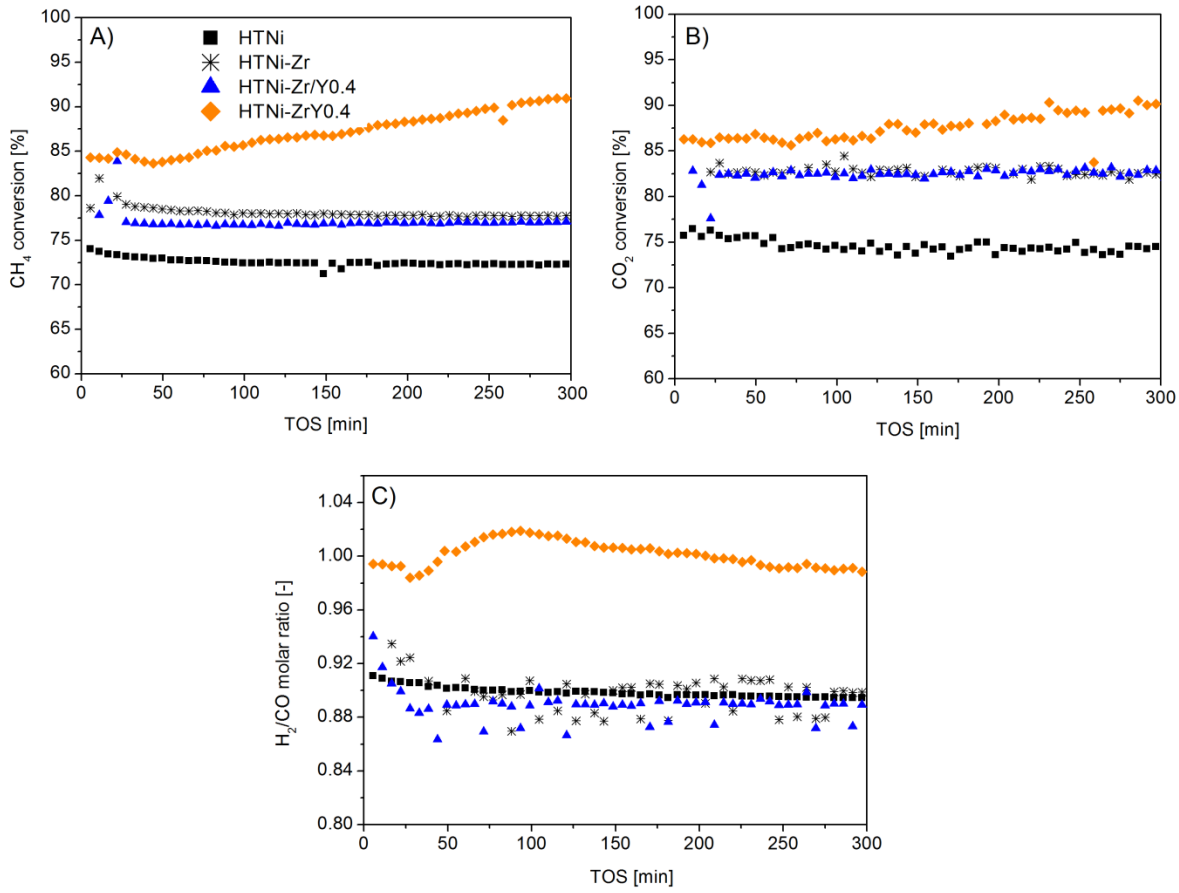

Fig. 4.37 DRM performance tests (CH_4- and CO_2-conversion, H_2/CO molar ratio) modified with Zr and Y using different methods; "-" in the name of the sample designates the introduction of promoter/s via co-precipitation with Ni, Mg and Al; "/" designates the introduction via impregnation of Y onto HTNi-Zr. Tests conditions: CH_4/CO_2/Ar=1/1/8, GHSV= 20,000 h^{-1} at 700 °C for 5 h.

In general, the promoting effect of zirconia may be related to the enhanced catalyst stability by inhibiting carbon nanofibers formation through direct decomposition of methane [203]. It was also

reported in literature that ZrO_2 may increase the content of oxygen vacancies on the catalysts surface, which plays an important role in the dissociative adsorption of CO_2 [200,206]. An introduction of yttrium into zirconia lattice results in the stabilization of tetragonal phase of ZrO_2 and formation of oxygen vacancies that are believed to contribute to the carbon removal [309]. In the current study, the addition of zirconia led to the improved catalytic activity and stability (as further confirmed by the characterization of the spent materials). The impregnation with 0.2 and 0.6 wt.% of yttrium, however, did not have such positive effect because of a partial blockage of the available nickel sites and decreased dispersion.

Table 4.19 Comparison of catalytic results in the isothermal DRM tests at 700 °C for 5 h for Zr,Y-modified catalysts.

Catalyst	**Promoter introduced via:**			
	Zr-coP	**Zr-Y-coP**	**Zr-Y-Imp**	**Zr-coP, Y-Imp**
Designation	**HTNi-Zr**	**HTNi-ZrY0.4**	**HTNi/ZrY0.4**	**HTNi-Zr/Y0.4**
CH_4 conversion [%]				
Initial	78.6	84.3	81.9	76.9
After 5h	77.7	90.9	82.3	77.1
Δ : relative change after 5 h [%] [1)]	↓1.14	↑7.83	↑0.50	↑0.26
CO_2 conversion [%]				
Initial	82.7	86.3	79.7	82.8
After 5h	82.6	90.2	82.1	82.0
Δ : relative change after 5 h [%] [1)]	↓0.12	↑4.52	↑3.00	↓0.97
H_2/CO molar ratio [-]				
Initial	0.99	0.99	0.88	0.90
After 5 h	0.98	0.98	0.90	0.88

[1)] calculated as $(|x_i-x_{5h}|/x_i \cdot 100)$ [%], where x is CH_4 or CO_2 conversion expressed in percentage, and subscripts stand for i – initial, 5 h – after 5 h catalytic test; symbols ↓ and ↑ denote that appropriate conversion respectively decreased or increased after 5 hours on line

Table 4.19 shows the comparison of the initial results and results after 5 h for CH_4 and CO_2 conversions and H_2/CO molar ratio. From the activity point of view, the co-precipitation with both Zr and Y resulted in the best catalytic performance, giving the highest initial and after-5 h CH_4 and CO_2

conversions. The conversions for this catalyst increased with TOS, whereas the H_2/CO ratio remained stable around 1. For the other catalysts, the sequence of the activity was: HTNi/ZrY0.4 > HTNi-Zr > HTNi-Zr/Y0.4. However, the H_2/CO ratio results did not follow the same sequence, pointing out to different side reactions during DRM.

4.3.4. *Characterization of the spent catalysts after the isothermal tests*

Textural properties of the spent materials are presented in Table 4.20. The specific surface area increased after reaction in comparison to the reduced materials, obtaining values similar to those registered for the calcined materials (cp. Table 4.11). The mesopore volume and average diameter of the pores were also similar to the values registered for the materials after calcination.

Table 4.20 Textural and structural properties, and types of formed carbon for the spent Zr,Y-modified catalysts. Numbers in brackets {..} relate respective values for the reduced samples (taken from Table 4.15).

Catalyst	N_2 sorption			XRD	TGA	Raman	Type of carbon (based on XRD, TGA and Raman)
	S_{BET} [m^2/g][1)]	V_p [cm^3/g][2)]	d_p [nm][3)]	Ni^0 crystallite size [nm][4)]	Mass loss [%][5)]	I_D/I_G [-]	
HTNi	125 {68}	0.3	10	7 {8}	20.2	1.83	Graphite-like carbon (with low order) + filamentous carbon
HTNi-Zr	124 {90}	0.4	11	4 {6}	7.3	2.08	Trace amount of graphite-like carbon + filamentous carbon + amorphous carbon
HTNi-Zr/Y0.4	98 {79}	0.3	10	7 {9}	11.9	1.67 2.24[6)]	Graphite-like carbon (with low order) + filamentous carbon + amorphous carbon
HTNi-ZrY0.4	98 {n.m.}	0.3	8	7 {8}	18.8	n.m.	Graphite-like carbon + filamentous carbon

[1)] specific surface areas calculated from the BET equation

[2)] mesopore volumes derived from the BJH desorption calculation method

[3)] pore size distribution obtained from the BJH desorption calculation method

[4)] based on the Scherrer equation, from the width at half-maximum of the XRD reflections at 2θ ca. 52°

[5)] due to carbon oxidation, calculated assuming the initial mass of the analyzed sample, i.e., 10.5-10.0 mg

[6)] Raman spectrum was registered at two different places of the catalyst. At these two places the registered ratios were different

Diffractograms for the materials after isothermal tests are shown in Fig. 4.38. After catalytic tests the reflections typical for hydrotalcite-derived materials were recorded, i.e., periclase-mixed oxides phase at 2θ of ca. 37, 43 and 63° (ICOD 00-045-0946), metallic nickel at 2θ of ca. 44, 53° (ICOD 01-087-0712) and graphitic carbon at 2θ of ca. 27° (ICOD 01-075-2078).

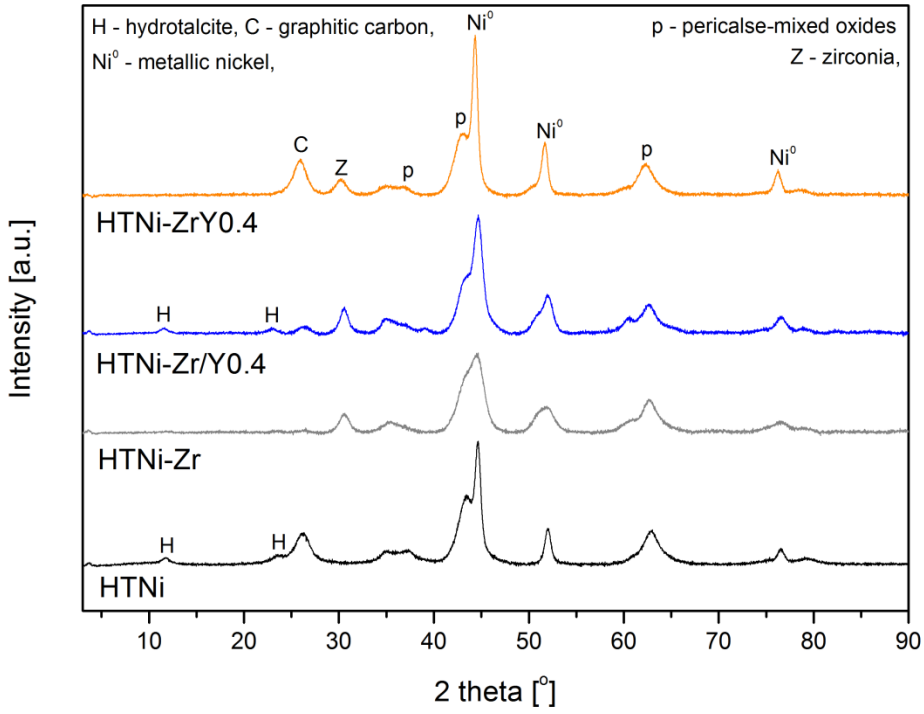

Fig. 4.38 XRD diffractograms of the spent catalysts modified with Zr and Y using different methods (after isothermal catalytic test) compared to HTNi. "-" in the name of the sample designates the introduction of promoter/s via co-precipitation with Ni, Mg and Al; "/" designates the introduction via impregnation of Y onto HTNi-Zr.

The reflection of graphitic carbon registered for spent HTNi-Zr has very low intensity, indicating the enhanced stability of this material. After impregnation with 0.4 wt.% yttrium intensity of C reflection was still low, while the co-precipitation of all components, including Zr and Y, resulted in the presence of sharper and more intense graphite line.

All zirconia containing materials revealed additionally the presence of the tetragonal ZrO_2 phase (ICOD 01-079-1765) at 2θ of ca. 30 and 50°. Moreover, the hydrotalcite reflections were observed for the spent HTNi and HTNi-Zr/Y0.4 materials. Very small hydrotalcite reflections were also observed for

HTNi-Zr. This is in contrast to the results described in **Subchapter 4.2.**, where the co-impregnation with Y0.4 and Zr stabilized the periclase-mixed solid solution. Metallic nickel crystallite size calculated for the spent catalysts are listed in Table 4.15. A significant decrease of the Ni crystal size was observed after reaction for the material co-precipitated with Ni, Mg, Al and Zr, i.e., 4 nm, versus 6 nm registered for the reduced sample. The catalysts containing Y, irrespective of the method of introduction, were also smaller after reaction than for the reduced samples, and reached the same values as for the spent unpromoted HTNi (cp. Table 4.20). Dębek et al. [203] reported a similar effect for the spent HNiZr3, HNiZr5, and HTNiZr10 catalysts, and explained it by a possible re-dispersion having taken place during DRM. Considering CO_2 as a source of oxygen, once it is adsorbed on the catalyst surface, it may be involved in the oxidation of Ni^0 sites to NiO. By adsorption of H_2, CO or perhaps H-species originating from methane molecules activated on the catalyst surface, the Ni-sites are subsequently reduced and thus ready to participate in the DRM reaction. The oxidation of Ni sites may lead to the regeneration of mixed NiMg oxides that, in the presence of the reducing atmosphere generated under reaction conditions, may yield Ni^0 species of smaller crystallite size than those present on the catalyst upon reduction pre-treatment prior to the catalytic tests. The balance between Ni^0 and NiO in DRM remains a possible hypothesis explaining the re-dispersion observed in XRD.

Thermogravimetric analysis (TGA) profiles of the spent materials are presented in Fig. 4.39. The results show two main weight loss regions, (i) < 300 °C and (ii) 300-800 °C, the former connected with sample dehydration and amorphous carbon oxidation; the latter with filamentous and graphitic type of carbon removal. Additionally, a small increase of the mass observed is related to oxidation of metallic nickel to nickel oxide [191]. The oxidation of filamentous carbon occurred for the studied materials at the following temperature ranges: 335-660 °C, 374-617 °C, 438-673 °C and 418-732 °C for HTNi-Zr, HTNi-Zr/Y0.4, HTNi-ZrY0.4 and HTNi, respectively. The shift towards lower temperature of carbon removal for Zr and Zr/Y0.4 samples indicates the type, which is easier to remove via oxidation. The same sequence as for the oxidation temperatures was observed for the percentage mass loss (cp. Fig. 4.39).

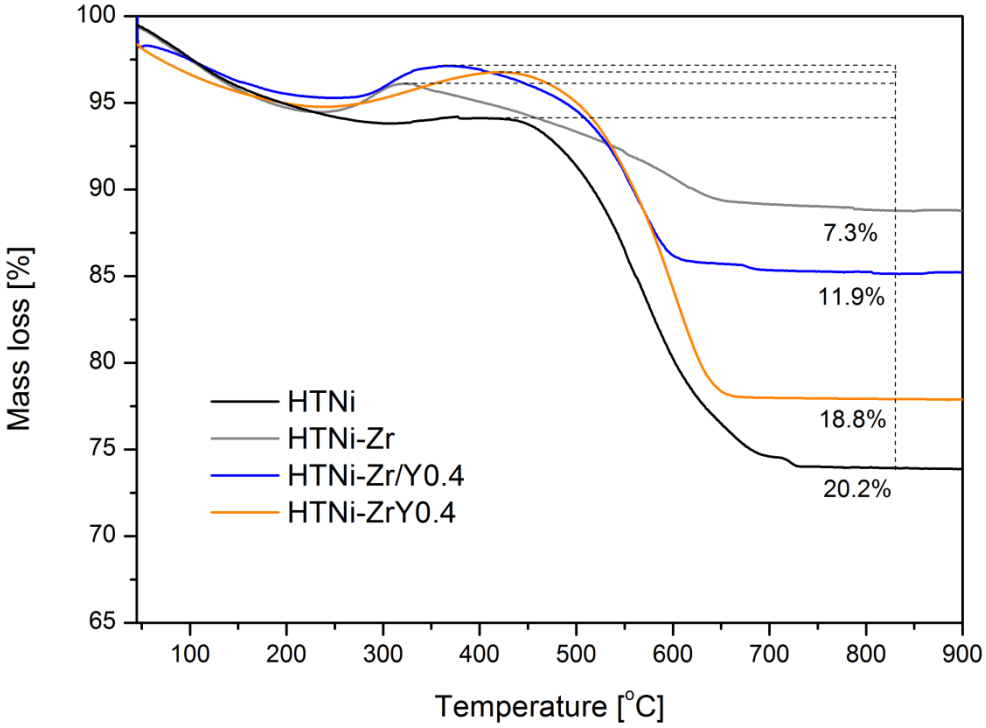

Fig. 4.39 TGA profiles of catalysts modified with Zr and Y using different methods (after isothermal catalytic test) and compared to HTNi. "-" in the name of the sample designates the introduction of promoter/s via co-precipitation with Ni, Mg and Al; "/" designates the introduction via impregnation of Y onto HTNi-Zr.

The type of carbon present on the surface of the spent catalysts was estimated from Raman spectra (Fig. 4.40). Four bands at 1325 cm^{-1} (D band), 1579 cm^{-1} (G band), 1602 cm^{-1} (D' band) and 2679 cm^{-1} (G' band) were recorded for all samples. The origin of the bands was discussed in detail in the previous subchapters. The ratio of intensities of D and G bands (I_D/I_G) is presented in Table 4.20. The I_D/I_G ratios were higher than 2 for both HTNi-Zr and HTNi-Zr/Y0.4 catalysts suggesting that the quantity of amorphous carbon is higher than the proportion of crystalline carbon. At two different places of the HTNi-Zr/Y0.4 sample different I_D/I_G ratios were recorded, i.e., 1.67 and 2.24. Similarly, as described in the **Subchapter 4.2.**, this may have arisen from the heterogeneity of the materials as also observed by Saché et al. [179]. The presence of the amorphous carbon in the Zr/Y samples is in good agreement with TGA results, proving oxidation of carbon species at lower temperature region than for HTNi and HTNi-ZrY0.4.

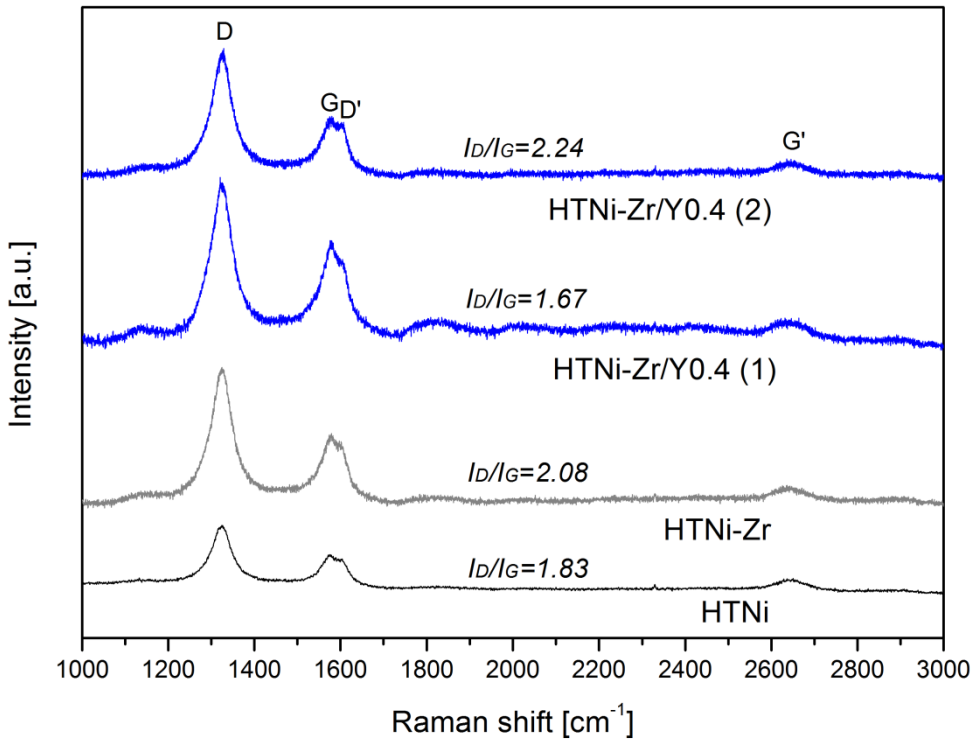

Fig. 4.40 Raman spectra for the spent HTNi-Zr and HTNi-Zr/Y0.4 catalysts compared to HTNi. The I_D/I_G ratio describes the degree of crystallinity of the formed carbon. The numbers in brackets beside the sample designation denote the number of Raman measurement; "-" in the name of the sample designates the introduction of promoter/s via co-precipitation with Ni, Mg and Al; "/" designates the introduction via impregnation of Y onto HTNi-Zr.

4.3.5. *Conclusions*

In this subchapter, Ni-based Mg/Al-hydrotalcites (HT) were co-precipitated with Zr (5 wt.%) and impregnated with Y (0.2, 0.4, 0.6 wt.%), and compared to the catalyst co-precipitated with both Zr (5 wt.%) and Y (0.4 wt.%). The DRM catalytic performance was determined in the TPSR tests (temperature range of 850-600 °C) and in the stability tests at 700 °C for 5 h.

The co-precipitation with Zr resulted in the formation of tetragonal phase of ZrO_2 in all Zr-containing samples, which was partly incorporated within the framework of periclase-like structure, and partly located on the surface of the support. A decrease in reducibility, together with lower H_2 consumption and stronger interactions of nickel with the modified-HT support were observed for the sample

promoted only with zirconia. Additionally, the promotion with Zr decreased basicity. The further impregnation with yttrium led to the percentage share of medium basic sites increasing with the increase of yttrium content. Moreover, considering the promotion with 0.4 wt.% Y, the total number of basic sites was two times higher after having both Zr and Y on the surface (HTNi/ZrY0.4) than only yttrium (HTNi-Zr/Y0.4) (Table 4.18). Then, the incorporation of Zr within the framework of the structure decreased the total basicity, as Zr may strongly interact with Mg and Al. However, when zirconia is incorporated together with yttrium the effect is opposite, resulting in an increased basicity.

No ZrO_2-Y_2O_3 solid solution was evident by XRD characterization method. The yttrium promotion, however, led to bigger Ni crystallites size in contrast to HTNi-Zr. Moreover, the Ni dispersion was decreased due to the decoration of the surface with Y-species, leading to the blockage of available nickel sites.

The TPSR catalytic tests showed the highest catalytic activity for the HTNi-Zr catalyst, whereas the Y impregnation led to the slightly lower CH_4 and CO_2 conversions. All Zr and Y promoted samples were, however, more active than unpromoted HTNi. The H_2/CO molar ratios were below 1.0, pointing to the reverse-water gas shift reaction accompanying DRM.

The co-precipitated Y and Zr catalyst (HTNi-ZrY0.4) presented the highest catalytic activity and a H_2/CO close to 1 after 5 h-isothermal test at 700 °C. The registered ratio slightly above 1.0 may indicate the presence of CH_4 decomposition side reaction, leading to the carbon formation as evidenced by XRD and TGA for this catalyst. On the other hand, the other catalysts only promoted with Zr or impregnated with Y and Zr led to lower activities or lower H_2/CO ratios under the same experimental conditions. The ranking in the catalytic activity is in agreement with the results of metal dispersion. HTNi-ZrY0.4 catalyst presented the dispersion of 10.2% in comparison to 8.6% for HTNi-Zr catalyst, and 6.9% for HTNi-Zr/Y0.4 catalyst. Almost no graphitic carbon was observed for the catalyst which was promoted only by Zr (added during hydrotalcite co-precipitation process). The HTNi-Zr/Y0.4 did not show a structural resistance to the products of the RWGS side reaction, as supported by the presence of

hydrotalcite reflections in the XRD patterns of the spent catalyst. This resistance was however observed in HTNi-ZrY0.4 material.

Taking into account both activity and structural resistance the best results were obtained for the catalyst promoted with Zr and Y via co-precipitation with Ni, Mg and Al. On the other hand, when the type of the carbon deposits formed during DRM is considered the catalyst promoted with Y via impregnation of HTNi-Zr sample showed better results, as this catalyst had both less carbon deposits than HTNi-ZrY0.4 and in the same time a higher proportion of amorphous carbon than the catalyst obtained by co-precipitation of all components (HTNi-ZrY0.4). Possibly the structural stability of the former could be improved by changing calcination temperature.

4.4. Co-precipitation with cerium and impregnation with yttrium of Ni-based double layered-hydroxides

The literature reports that promotion with cerium oxide is beneficial for dry reforming of methane, due to oxygen storage capacity and redox properties of Ce [204,205,317,359,369,370]. According to Daza et al. [371], 3 wt.% of Ce had a positive effect on carbon removal, and it was reported as the optimal content in Ni-based hydrotalcites. Dębek et al. [205] observed less graphitic carbon and amorphous carbon formed on Ce-modified Ni-DLHs. The latter can be more easily gasified during DRM [204]. In another study of Daza et al. [317], the co-precipitation with cerium nitrate (assuming different ratios of Al/Ce: 1.5, 4.0, 9.0 and 24.0) resulted in the best performance at 700 °C for the catalyst with the highest Al/Ce ratio. In the previous chapters, the promotion of Ni-based double-layered hydroxides (DLHs) with Y was described. Particularly the yttrium addition (0.2-0.6 wt.%) to the zirconia co-precipitated DLHs presented interesting findings on material basicity, Ni crystallite size, dispersion, and correlation between reducibility (H_2 uptake) and catalytic activity.

As no recent literature studies dealt with Mg/Al/Ni double-layered hydroxides promoted with Ce and Y in dry reforming of methane, this **Subchapter** is dedicated to their examination. The materials were tested in dry reforming of methane (CH_4/CO_2 = 1/1) for the first time. 3 wt.% of ceria was assumed (theoretical value during preparation) and different concentrations of yttrium (0.2, 0.4 or 0.6 wt.%). The mentioned contents of yttrium were chosen basing on the results described in previous **Subchapters** (**4.2**, **4.3**).

4.4.1. *Physicochemical properties*

XRD diffractograms of freshly synthesized double-layered hydroxides are presented in Fig. 4.41. The XRD patterns show the sharp reflections for (003), (006), (009), (015), (110) and (113) planes at 2θ ca. 11, 23, 35, 39, 60, and 62° arising from $Mg_6Al_2(OH)_{16}CO_3{\cdot}4H_2O$ (ICOD 00-014-0191), respectively. Structural parameters *a* and *c'*, calculated similarly as described in previous Chapters (based on the first three reflections) are summarized in Table 4.21. The parameter *a* remained the same after

promotion with both cerium alone and cerium and yttrium. The c' values suggest the presence of CO_3^{2-} ions (7.65 Å) [204,244]. Apart from hydrotalcite structure, a separate phase of fluorite structure of CeO_2 (ICOD 00-023-1048) is revealed in XRD diffractograms (Fig. 4.41). However, existence of $Ce(OH)_3$ or $CeCO_3OH$ cannot be excluded. The former arises from Ce^{3+}, which oxidizes fast to Ce^{4+} in the presence of H_2O, resulting in CeO_2. On the other hand, $CeCO_3OH$ was considered to be a precursor of cerium oxide upon precipitation in the presence of carbonates. The $CeCO_3OH$ was recorded by Daza et al. [317] only for the sample with higher cerium content (Al/Ce = 1.5). However, the authors concluded that well dispersed cerium carbonate hydroxide could also be formed in the low-loaded cerium materials (with the assumed Al/Ce = 4.0, 9.0, 24.0). The reason for cerium deposition on the surface of the brucite-like layers is its bigger ionic radius (Ce^{3+} = 1.019 Å versus Mg^{3+} = 0.86 Å, Al^{3+} = 0.675 Å) [316]. It is expected that also Y is deposited on the surface of DLHs, since dry impregnation was used to introduce this promoter, but no separate phase of Y_2O_3 was recorded in XRD patterns, probably due to its low content.

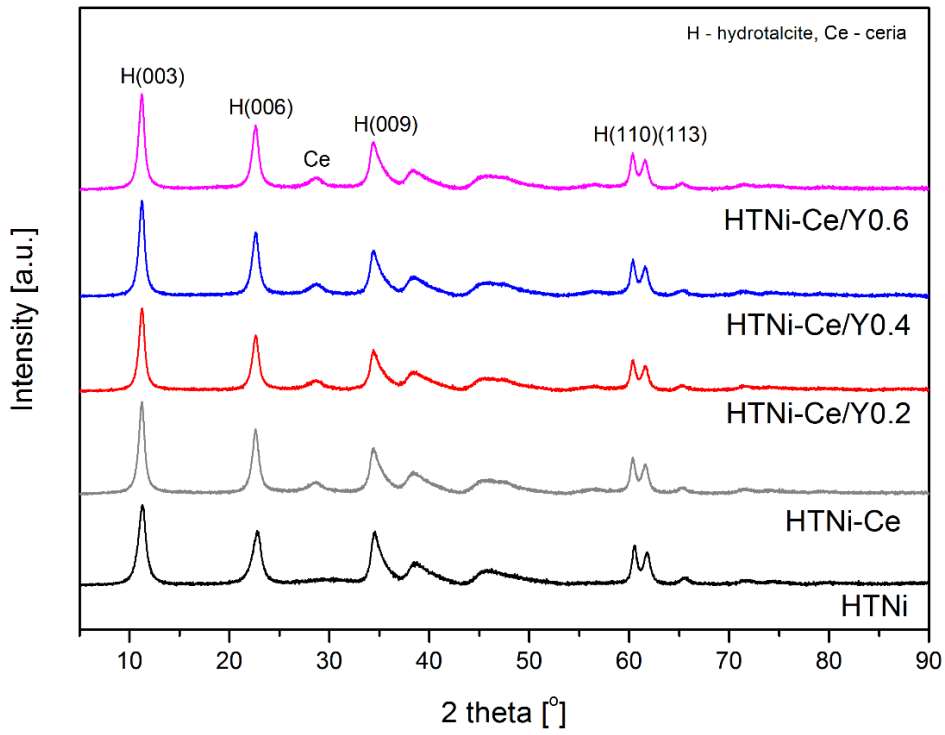

Fig. 4.41 XRD patterns of freshly synthesized Ce- and Y-modified catalysts: HTNi-Ce, HTNi-Ce/Y0.2, HTNi-Ce/Y0.4, HTNi-Ce/Y0.6, compared to HTNi.

Table 4.21 reports the metal contents for the prepared catalysts determined by XRF. The nickel content was found in the range of 20–25 wt.%, and for all Ce-containing catalysts the amount of cerium was close to the one assumed during the synthesis step, i.e., 3 wt.%. The amount of introduced yttrium was also close to the assumed one. Ni^{2+}/Mg^{2+} molar ratio showed values lower than 0.33, especially in Ce- and Y-promoted catalysts. It suggests that Mg^{2+} were only partially substituted by Ni^{2+}, similarly as discussed for Ni/Mg/Al catalysts co-impregnated with Zr and Y. Al/Ce molar ratios calculated for the modified catalysts were in the range of 28-36, and are higher than those in the study of Daza et al. [317].

Table 4.21 Structural parameters, elemental composition, and textural properties of Ce- and Y-promoted catalysts. The numbers in brackets are nominal values.

Catalyst	XRD Freshly Synthesized		XRF After Calcination					N_2 sorption After calcination		
	a [Å][1)]	c' [Å][2)]	Ni [wt.%]	Ce [wt.%]	Y [wt.%]	Al/Ce [-]	Ni^{2+}/Mg^{2+} [-]	S_{BET} [m^2/g][3)]	V_p [cm^3/g][4)]	d_p [nm][5)]
HTNi	3.06	7.82	20	-	-	-	0.29 (0.33)	120	0.6	19
HTNi-Ce	3.07	7.84	25	2.5 (3.0)	-	34	0.21 (0.33)	97	0.5	20
HTNi-Ce/Y0.2	3.07	7.83	23	2.9 (3.0)	0.3 (0.2)	30	0.18 (0.33)	132	0.7	21
HTNi-Ce/Y0.4	3.07	7.84	23	3.2 (3.0)	0.5 (0.4)	28	0.18 (0.33)	133	0.6	19
HTNi-Ce/Y0.6	3.07	7.85	20	2.6 (3.0)	0.7 (0.6)	36	0.15 (0.33)	126	0.6	20

[1)] calculated from d-spacing a = 2d(110) as suggested by Cavani et al. [244]

[2)] c' = c/3, where (c = d(003) + 2d(006) + 3d(009)) [204]

[3)] specific surface area calculated from the BET equation

[4)] pore volumes derived from the BJH desorption calculation method

[5)] pore size distribution obtained from the BJH desorption calculation method

Table 4.21 contains also textural properties for the calcined. The modification with cerium led to a decrease of specific surface area due to a partial blockage of the porous system, as suggested by a decrease of total pore volume from 0.6 for HTNi to 0.5 cm^3/g to HTNi-Ce. Similar observations were reported both for Ni-hydrotalcites promoted with an aqueous solution of $Ce[EDTA]^-$ complexes via ion-

exchange [205], and those obtained by co-precipitation with $Ce(NO_3)_3 \cdot 6H_2O$ [317]. Further modification with yttrium positively affected S_{BET} resulting in an increase of this value, and similarly in some increase in total pore volume. The pore size remained almost unchanged.

4.4.2. *Reducibility, basicity, Ni dispersion and crystallite size*

TPR-H_2 profiles for the calcined Ce-Y-modified catalysts are presented in Fig. 4.42, with the low-to-medium temperature region additionally enlarged in the right-hand side Fig. 4.42. One broad reflection, arising from the reduction of NiO located in the layer of DLHs is observed at ca. 860 °C. Maximum temperature of peaks shifted towards higher values after promotion with Ce (829 for HTNi versus 876 °C for HTNi-Ce). After the addition of 0.6 wt.% of Y the temperature shift is more pronounced (873, 864 and 895 °C for HTNi-Ce/Y0.2, HTNi-Ce/Y0.4, and HTNi-Ce/Y0.6, respectively) (Table 4.22). Lower amounts of Y did not have an observable influence on reduction temperature as compared to HTNi-Ce. Thus, the Ce- or Ce/Y-promotion led to a decrease in reducibility, as confirmed additionally by the uptake of hydrogen (Table 4.22). Apart from the high-temperature maximum also less intense peaks were recorded at moderate temperatures. Nickel oxides weakly-bonded with the surface of hydrotalcite were reduced at 350 °C on the HTNi catalyst. For the samples containing Ce alone or Ce and Y, the peaks registered at temperatures lower than 400 °C arise from the reduction of either NiO weakly interacting with the surface of the catalyst, or from bulk NiO [197,326,327]. For Ce-promoted samples, the peaks arising from the reduction of the promoter may be also expected. Three species of ceria, with increasing reduction temperatures, were reported in literature, the reduction of surface oxygen at 400-420 °C and surface lattice oxygen at 450-600 °C, as well as bulk reduction to Ce_2O_3 up to 880 °C [13]. The former two species, overlapped, can be detected in the right-hand side Fig. 4.42. Temperature of bulk reduction lies in the same region as the main peak for Ni reduction and thus cannot be distinguished.

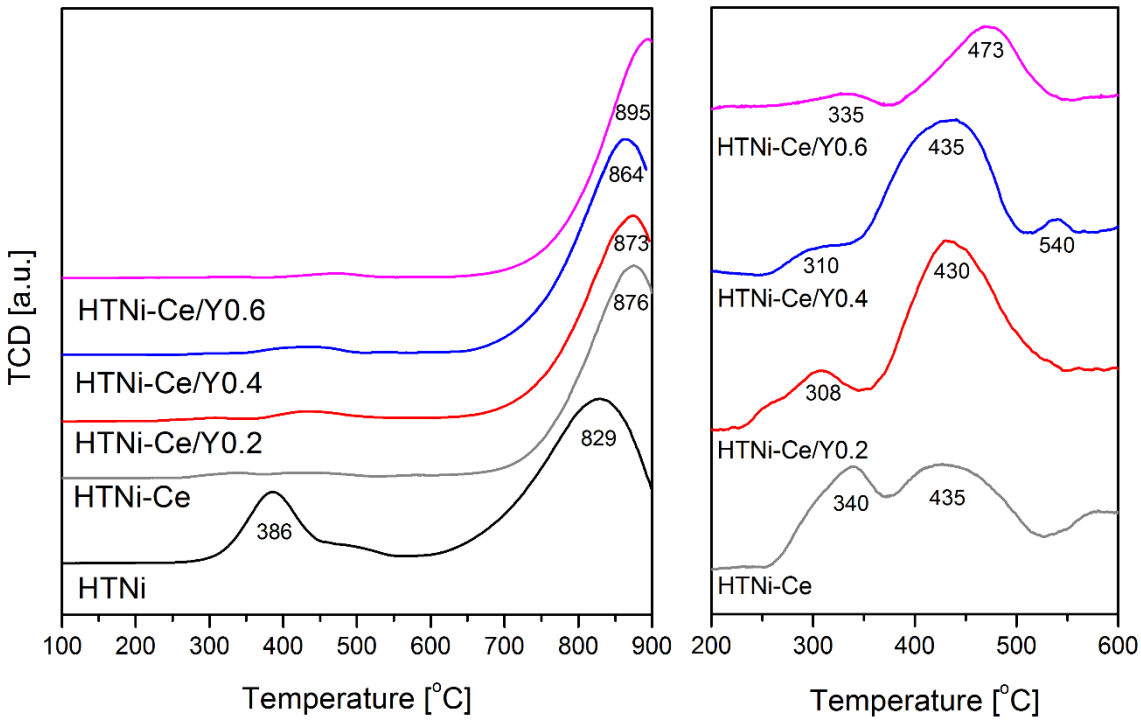

Fig. 4.42 Temperature-programmed reduction (TPR-H_2) profiles recorded for Ce- and Y-modified catalysts. The right-hand picture presents the enlargement of low-to-medium temperature region (200-600 °C) only for the promoted samples.

XRD patterns for the reduced samples are shown in Fig. 4.43. Metallic nickel (ICOD 01-087-0712), fluorite CeO_2 phase (ICOD 00-023-1048) and the periclase mixed-oxides (ICOD 00-045-0946), (the latter typically formed upon calcination [205,317]) may be detected. The Ni crystallite sizes are summarized in Table 4.22. There is no increase of Ni^0 particle size after doping both with cerium and cerium/yttrium. This is in contrast to Daza et al. [317], who observed an increase in Ni particles size and connected it to the fact that the co-precipitation with Ce led to the formation of free nickel oxides.

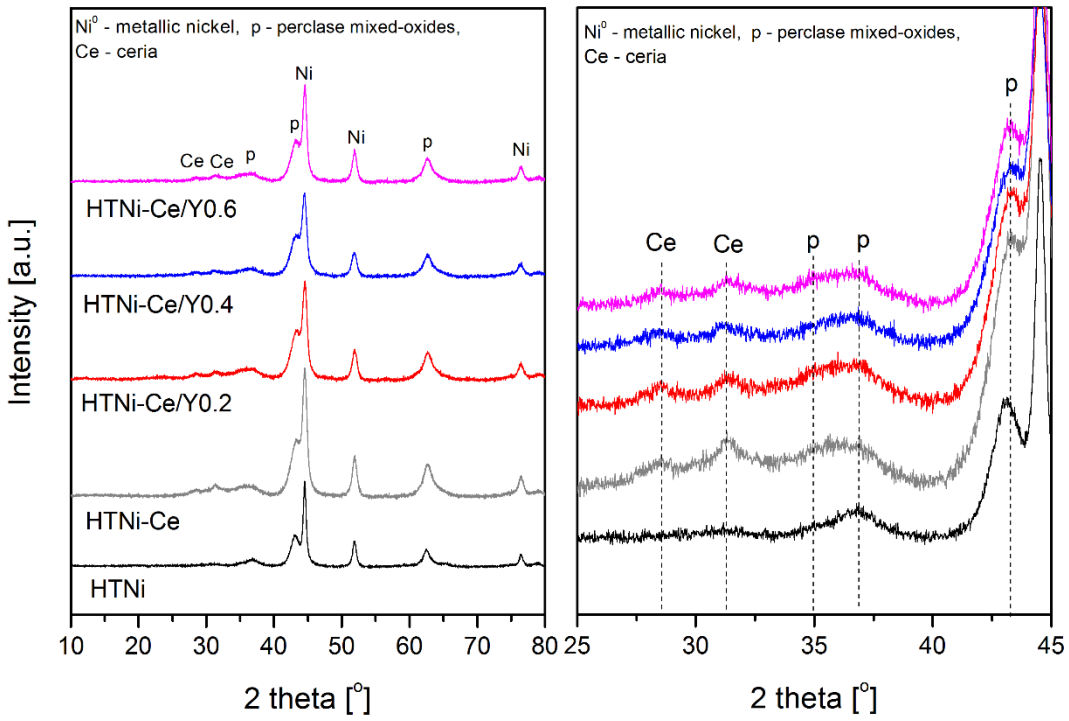

Fig. 4.43 XRD diffractograms of the prepared catalysts after reduction in the mixture 5 vol.% of H_2/Ar.

Textural properties for the studied materials after reduction in a mixture of 5 vol.% of H_2 in Ar are presented in Table 4.22). A significant decrease of S_{BET} can be observed for all samples, as compared to the materials after calcination (cp. Table 4.21). The highest decrease was registered for the sample modified only with ceria, similarly as reported in literature for NiCeAl catalyst [359]. A decrease in the pore volumes and pore diameters was also observed, in contrast to the values obtained for the HTNi sample.

Table 4.22 Texture, reducibility and Ni dispersion and Ni crystallite sizes for the studied materials after reduction in a mixture of 5 vol.% H_2/Ar.

Catalyst	N_2 sorption Reduced materials			TPR-H_2	XRD	H_2 chemisorption	
	S_{BET} [m^2/g] [1)]	V_p [cm^3/g] [2)]	d_p [nm] [3)]	H_2 consumption [mmol H_2/g]	Ni crystallite [nm]	Ni dispersion [%]	Ni crystallite [nm]
HTNi	68	0.4	21	0.209	9	8.9	11
HTNi-Ce	45	0.2	14	0.137	7	11.5	8
HTNi-Ce/Y0.2	99	0.7	28	0.135	7	10.2	10
HTNi-Ce/Y0.4	91	0.6	27	0.134	7	11.6	8
HTNi-Ce/Y0.6	99	0.7	26	0.119	8	11.5	8

[1)] specific surface area calculated from the BET equation

[2)] pore volumes derived from the BJH desorption calculation method

[3)] pore size distribution obtained from the BJH desorption calculation method

Table 4.22 contains also Ni dispersion obtained from chemisorption of H_2. After the modification with Ce and Y a small increase of Ni^0 dispersion is observed, from 8.9 for HTNi to 11.5, 10.2, 11.6, and 11.5% for HTNi-Ce, HTNi-Ce/Y0.2, HTNi-Ce/Y0.4, HTNi-Ce/Y0.6, respectively. The similar increase of dispersion was discussed for Y-promoted catalysts in the previous **Subchapters 4.1.**, **4.2**. The crystallite sizes calculated from H_2 chemisorption (assuming spherical Ni crystallites) are in good agreement with the ones obtained by XRD calculations.

TPD-CO_2 results for the catalysts after TPR-H_2 tests. Both the number and distribution of basic sites were influenced by the promotion are presented in Fig. 4.44 and Table 4.23. The sequence of the total basicity is: 63, 107, 111, 212, 286 μmol/g for HTNi-Ce < HT < HTNi-Ce/Y0.4 < HTNi-Ce/Y0.2 < HTNi-Ce/Y0.6 catalysts, respectively. The decrease in total basicity originating from ceria promotion was previously reported in literature [2,3], and it was similar as was in case of co-precipitation with Zr (**Subchapter 4.3.**). Co-promotion with cerium and yttrium resulted in a higher number of basic sites in comparison to HTNi-Ce. This is in contrast to the catalysts described in **Subchapter 4.1**, where the total

number of sites for Y-promoted samples was lower than for HTNi. It should be reminded, however, that the catalysts described in **Subchapter 4.1.** were promoted by Y via co-precipitation with other components of hydrotalcites, while in the case described in the current **Subchapter**, yttrium was introduced by dry impregnation. Thus, in the latter case it could not be introduced into the brucite layers. This emphasizes the importance of the choice of the method of promoter introduction. However, there is no straight correlation between the increasing Y concentration and the number of basic sites, similarly as for HTNi-Y catalysts described in **Subchapter 4.1.** The increase in total number of sites is especially significant for the samples with 0.2 and 0.6 wt.% Y added, which is in the agreement with the results registered for the HTNi-Zr series (**Subchapter 4.3.).**

Table 4.23 Distribution of basic sites and total basicity for Ce/Y modified catalysts.

Catalyst	**TPD-CO_2** **Reduced materials**			
	Weak [%]	**Medium [%]**	**Strong [%]**	**Total basicity [µmol/g]**
HTNi	15	42	43	107
HTNi-Ce	-	70	30	63
HTNi-Ce/Y0.2	-	52	48	212
HTNi-Ce/Y0.4	-	45	55	111
HTNi-Ce/Y0.6	-	53	47	286

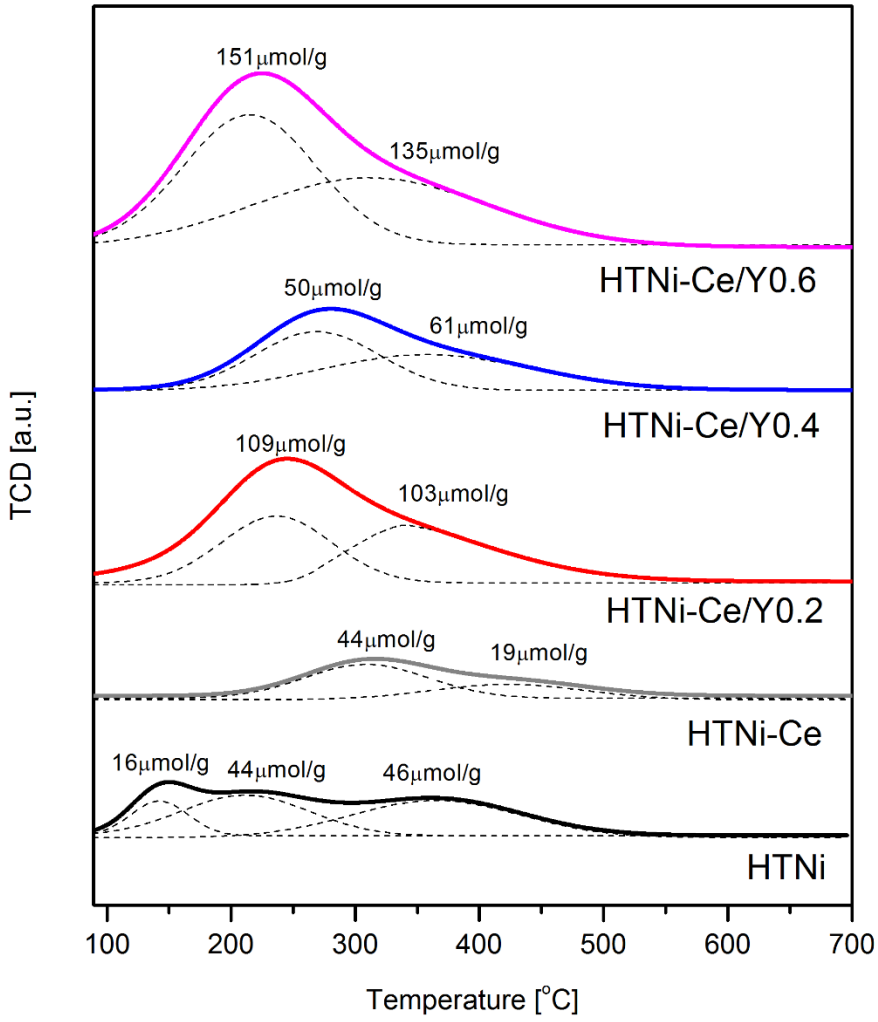

Fig. 4.44 TPD-CO_2 curves for Ce- and Y-modified catalysts. The numbers in brackets are given in μmol/g.The Table illustrates the distribution of sites.

4.4.3. *Catalytic activity and stability in DRM*

CH_4 and CO_2 conversions and H_2/CO molar ratio in dry reforming of methane tests are presented in Fig. 4.45 and Table 4.24. It may be seen that the promotion with cerium resulted in an enhanced conversion for both methane and carbon dioxide at the temperature range of 750-600 °C. The beneficial effect of Ce may be assigned to the increase of Ni^0 dispersion as reported elsewhere [372,373]. On the other hand, in contrast to the observations of Daza et al. [1], in current study the increase in the activity cannot be directly linked with the basicity. This seems to be in line with the observations discussed in **Subchapter 4.1.**, where HTNi-Y catalysts showed higher conversion than

HTNi despite lower basicity. This again proves that for Ni-double-layered hydroxides a proper balance between basic sites and dispersion is important. The former need to reach a certain value, above which their influence is not so pronounced. Ni dispersion slightly higher for HTNi-Ce, and Ce/Y promoted catalysts seems to be more responsible. Both CH_4 and CO_2 conversions were similar for HTNi-Ce and the catalyst promoted with Y 0.4 wt.%. However, a decrease in activity was observed for HTNi-Ce/Y0.6 catalyst, which had the highest basicity. It may be thus speculated that in the latter case, reducibility could have played an additional role, as illustrated by the fact that the sample HTNi-Ce/Y0.6 showed the highest temperature of reduction (cp. Fig. 4.42).

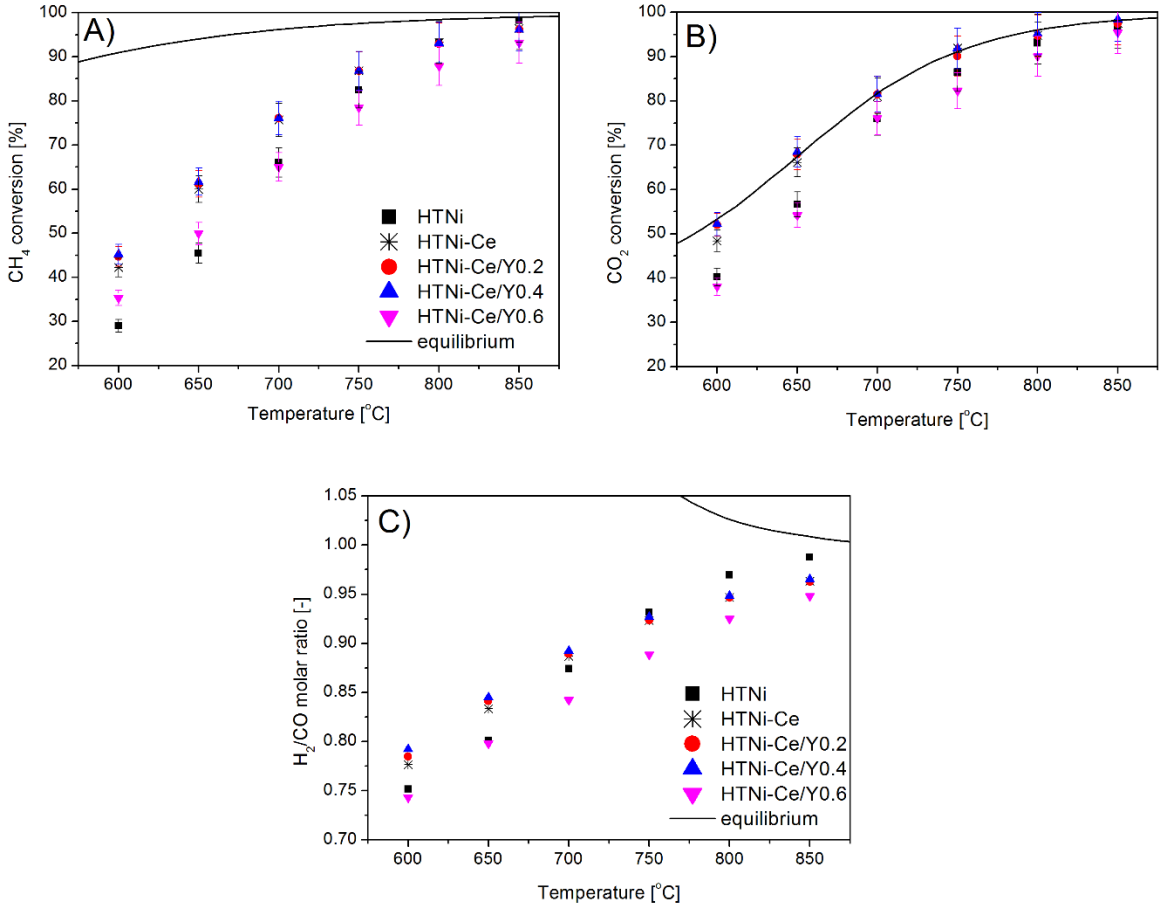

Fig. 4.45 The results of DRM catalytic tests over Ce- and Y-modified catalysts: (a) CH_4 conversion, (b) CO_2 conversion and (c) H_2/CO molar ratio. Reaction conditions: T= 850-600 °C, 30 min at each temperature, GHSV = 20,000 h^{-1}, CH_4/CO_2/Ar = 1/1/8, total flow rate 100 cm^3/min.

Table 4.24 DRM catalytic results over Ce and Ce,Y modified catalysts at different temperatures (from 850 to 600 °C, GHSV = 20,000 h^{-1}, $CH_4/CO_2/Ar$ = 1/1/8, total flow rate 100 cm^3/min).

Temperature [°C]	850	800	750	700	650	600
CH_4 conversion						
HTNi	98.2	93.3	82.5	66.0	45.4	28.9
HTNi-Ce	96.5	93.2	86.9	75.7	60.0	42.2
HTNi-Ce/Y0.2	96.2	92.9	86.8	76.1	61.2	44.7
HTNi-Ce/Y0.4	96.2	93.1	86.8	76.1	61.7	45.2
HTNi-Ce/Y0.6	93.2	87.9	78.4	65.0	49.9	35.3
CO_2 conversion						
HTNi	96.8	93.0	86.5	76.0	56.6	40.2
HTNi-Ce	97.5	94.8	91.9	81.0	66.1	48.4
HTNi-Ce/Y0.2	97.4	94.7	90.1	81.4	67.9	52.0
HTNi-Ce/Y0.4	98.4	95.1	91.8	81.5	68.4	52.2
HTNi-Ce/Y0.6	95.4	90.1	82.3	76.1	54.2	38.0
H_2/CO molar ratio						
HTNi	0.99	0.97	0.93	0.87	0.80	0.75
HTNi-Ce	0.96	0.94	0.92	0.89	0.83	0.78
HTNi-Ce/Y0.2	0.96	0.95	0.92	0.89	0.84	0.78
HTNi-Ce/Y0.4	0.97	0.95	0.93	0.89	0.85	0.79
HTNi-Ce/Y0.6	0.95	0.92	0.89	0.84	0.79	0.74

In order to further examine the influence of Y promotion, isothermal tests were performed at 700 °C for 5 h for the best performing samples from the previous test: HTNi-Ce, HTNi-Ce/Y0.2 and HTNi-Ce/Y0.4, and compared to the unmodified catalyst HTNi. The results are presented in Fig. 4.46. The catalytic activity followed the sequence: HTNi < HTNi-Ce/Y0.4 < HTNi-Ce. For HTNi-Ce/Y0.2 catalyst, a constantly increasing CH_4 and CO_2 conversions were observed, indicating unstable structure during DRM. The lowest values of H_2/CO were obtained for the unmodified catalyst (H_2/CO = 0.90), whereas for both HTNi-Ce/Y0.4 and HTNi-Ce the values were higher, respectively ca. 0.94 and ca. 0.97 after 300 min. Considering that the registered H_2/CO molar ratio is stable from 50 min to 300 min, and

the obtained values are always lower than unity, side reactions such as reverse water-gas shift ($CO_2+H_2=CO+H_2O$) may have occurred. This is to some extent was inhibited in the presence of Y, and was previously observed for the HTNi-Y catalysts discussed in **Subchapter 4.1**., HTNi/ZrY0.4 described in **Subchapter 4.2.**, and HTNi-Zr and HTNi-ZrY0.4 presented in **Subchapter 4.3**.

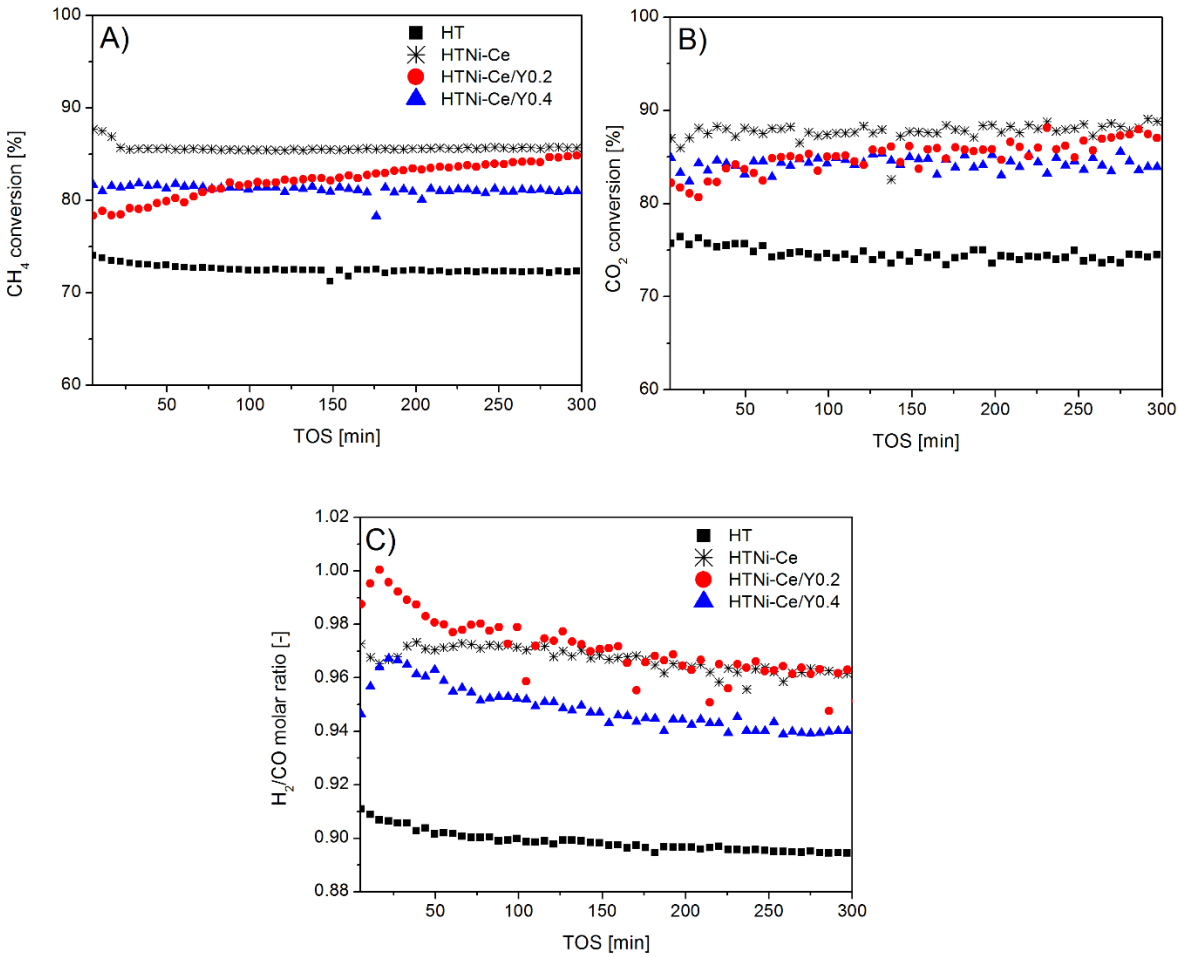

Fig. 4.46 The results of DRM catalytic tests over Ce- and Y-modified catalysts: (A) CH_4 conversion, (B) CO_2 conversion and (C) H_2/CO molar ratio. Reaction conditions: T= 700 °C, 5 hours, GHSV = 20,000 h^{-1}, $CH_4/CO_2/Ar$ = 1/1/8, total flow rate 100 cm^3/min.

The role of cerium may be explained taking into account the DRM mechanism, which, as discussed in **Subchapter 4.1.**, included the decomposition of methane taking place on Ni active site and dissociative adsorption of carbon dioxide on the metal surface and metal-surface interface [154,155]. As a result of the former step (CH_4 decomposition). A catalyst may be deactivated by carbonaceous

deposits. It can, however, be removed in situ via another side reaction (reverse Boudouard reaction, i.e., CO_2+C=2CO) [154,188]. The promoting effect of Ce has been mainly ascribed in literature to its large oxygen storage capacity, which favors the oxidation of the carbon deposits [200,205]. The addition of Ce-species into the hydrotalcite structure was also found to increase the reducibility of the nickel species, as well as the number of basic sites, both strong (low-coordinated surface O^{2-}) and medium-strong (Lewis acid/base pairings), thus increasing the CO_2 adsorption capacity [205]. In this case, the Ce and Y addition does not enhance reducibility, but leads to higher Ni dispersion. The increase in Ni dispersion upon promotion with CeO_2 agrees with the literature reports [374–376]. Akri et al. [374] studied Ce-modified Ni/illite clay-supported catalysts, where enhanced Ni dispersion was observed on the clay surface. Sepehri et al. [375] observed promoting effect of ceria on Ni dispersion in Ni/Al_2O_3 catalysts, as well as a reduction of the bulk NiO on the catalysts surface, pointing the role of the redox properties of Ce. Li et al. [376] also showed that the promotion with CeO_2 of Ni/Al_2O_3-ZrO_2 resulted in the improved dispersion of nickel particles, further enhancing the CO_2 adsorption on the surface. Wang et al. [377] examined series of catalysts of Ni supported on ceria or yttria-doped ceria (YDC). The usage of YDC led to the enhanced catalytic activity and stability in dry reforming of methane, as compared to examined ceria support. The extent of enhancement decreased with increased yttria loading (Ni/5YDC > Ni/10YDC > Ni/20YDC > Ni/40YDC). The beneficial effect of Y^{3+} ions into the ceria lattice is known to arise from the oxygen storage/transport characteristic of yttria-doped ceria phase [377–381]. Thus, the improved stability and increased resistance to carbon deposits formation may arise from the synergic effect of ceria and yttria. The characterization over spent catalysts (HRTEM described further in the text) proved that Ce was always present together with Y, indicating a possible existence of CeO_2-Y_2O_3 phase, which favors Ni^0 dispersion and limits the sintering and the carbon formation.

4.4.4. *Characterization of the spent catalysts after the isothermal tests*

Textural properties for the spent catalysts after methane dry reforming tests at 700 °C for 5 h are shown in Table 4.25. Specific surface areas increased after reaction as compared to the reduced samples, considerably so in case of HTNi and HTNi-Ce and reached the values similar to those for the calcined catalysts (cp. Table 4.21). Total pore volumes were slightly smaller for the spent than for the reduced samples, except HTNi-Ce. The mean pore size decreased after the reaction.

Table 4.25 Textural properties, Ni crystallite size, and Raman of spent catalysts

Catalyst	N_2 sorption			XRD	TGA	Raman
	S_{BET} [m^2/g] [1), 4)]	V_p [cm^3/g] [2)]	d_p [nm] [3)]	Ni crystallite size [nm] [4)]	Mass loss [mg] [5)]	I_D/I_G [-]
HTNi	125 {68}	0.3	10	7 {9}	2.02	1.83
HTNi-Ce	108 {45}	0.4	13	7 {7}	1.97	1.47
HTNi-Ce/Y0.2	139 {99}	0.3	8	7 {7}	2.80	1.63
HTNi-Ce/Y0.4	120 {91}	0.4	12	7 {7}	2.53	1.51

[1)] specific surface area calculated from the BET equation

[2)] pore volumes derived from the BJH desorption calculation method.

[3)] pore size distribution obtained from the BJH desorption calculation method

[4)] the numbers in brackets are for the reduced samples are added for comparison. They are taken from Table 4.21

[5)] resulting from carbon oxidation, calculated assuming the initial mass of the analyzes sample in TGA, i.e., 10.5-10.0 mg

XRD patterns for the spent catalysts after DRM tests are presented Fig. 4.47. The Ni crystallite size, carbon formation and changes in the crystallographic structure were examined and compared to the results obtained for the reduced materials (see Fig. 4.43). For the spent catalysts, typical reflections of metallic nickel (ICOD 01-087-0712) and periclase-like mixed oxides can be found (ICOD 00-045-0946). As presented in Table 4.24, the Ni^0 crystallite sizes did not change after the DRM tests. Thus, sintering of nickel can be excluded, confirming similar observations reported by Dębek et al. [205]. In contrast to the results of Daza et al. [317], no spinel phase was observed. The lack of the spinel phase may be also confirmed by the study of Sepehri et al. [375], where the $NiAl_2O_4$ has been eliminated due to the

addition of 3 and 6 wt.% Ce to Ni/Al_2O_3 materials. The addition of Ce or Ce/Y decreased the intensity of additional hydrotalcite phase reflections in comparison to HTNi, thus proving the beneficial effect of these promoters on structural stability of the catalysts. Similar was observed for the catalysts of HTNi-Y series (**Subchapter 4.1**.). On the other hand, the presence of Zr seems not to have this beneficial effect, as shown in Fig. 4.27 in **Subchapter 4.2** and Fig. 4.38 in **Subchapter 4.3**. Although CH_4 and CO_2 conversions were stable, carbon deposits were formed, as confirmed by the presence of graphite reflections at $2\theta = 26.6°$ (ICOD 01-075-2078).

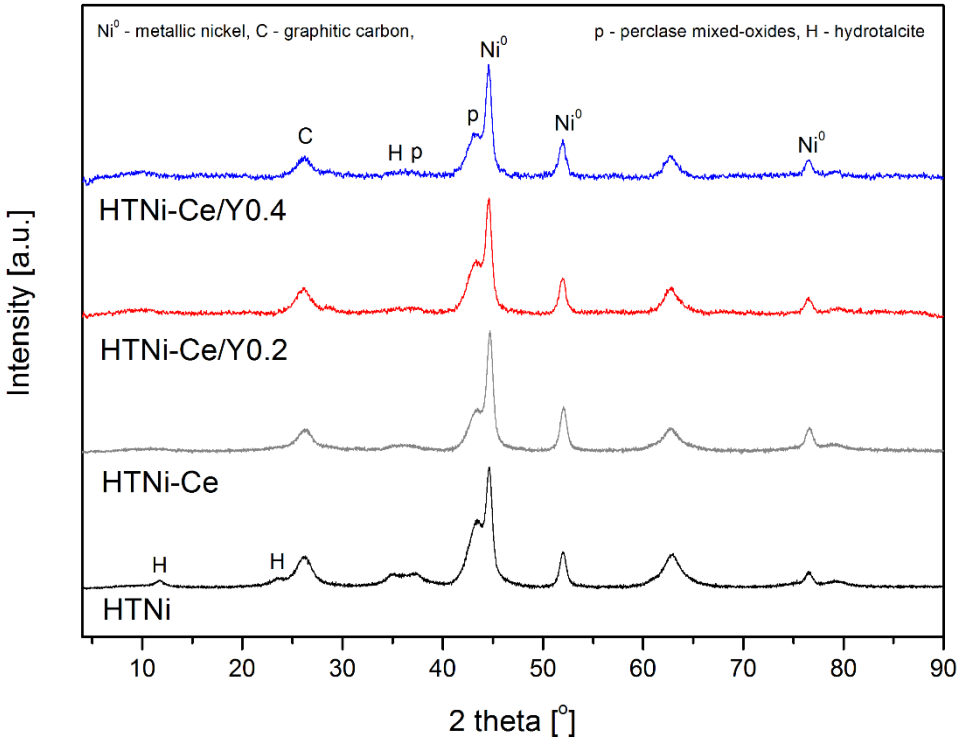

Fig. 4.47. XRD diffractograms recorded for the spent catalysts after isothermal tests at 700 °C for 5 h.

The quantity and the type of carbon formed on the catalysts upon the DRM were examined by TGA (Fig. 4.48) and Raman spectroscopy (Fig. 4.50).

The carbon deposition in TGA was quantified basing on the CO_2 ion current detected during its combustion (Fig. 4.49). During the thermal decomposition of the spent materials, a small decrease of

the mass is registered in the temperature range of 40–300 °C, which is connected with water vapor removal (Fig. 4.49). An increase of the mass observed over 300 °C arises from the oxidation of metallic nickel to nickel oxides [42]. At 400 °C, a significant decrease of the weight due to the combustion of carbon deposits on the surface of the catalysts was registered. This is confirmed by a CO_2 formation presented in Fig. 4.49. The peak centered at 610 °C corresponds to carbon filaments, as shown by TEM results discussed below. The intensities of CO_2 signals agree with the amount of formed carbon obtained from TGA, which were 1.97, 2.02, 2.53 and 2.80 mg respectively for HTNi-Ce, HTNi, HTNi-Ce/Y0.4 and HTNi-Ce/Y0.2 (Table 4.24).

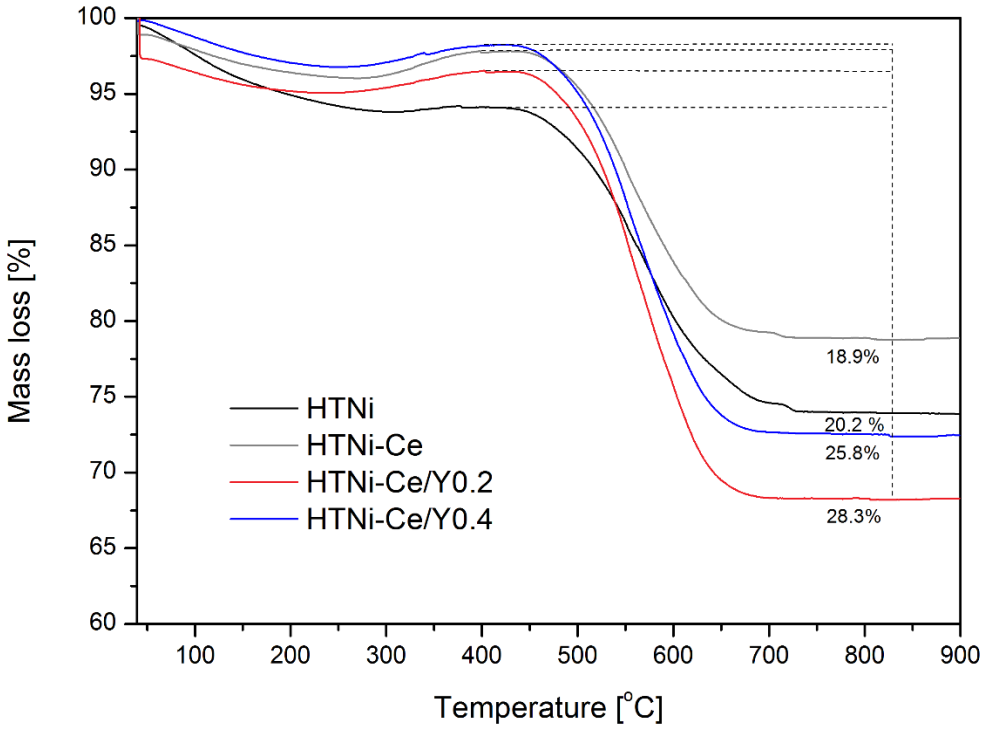

Fig. 4.48 Thermogravimetric analysis (TGA) for the catalysts after isothermal DRM tests.

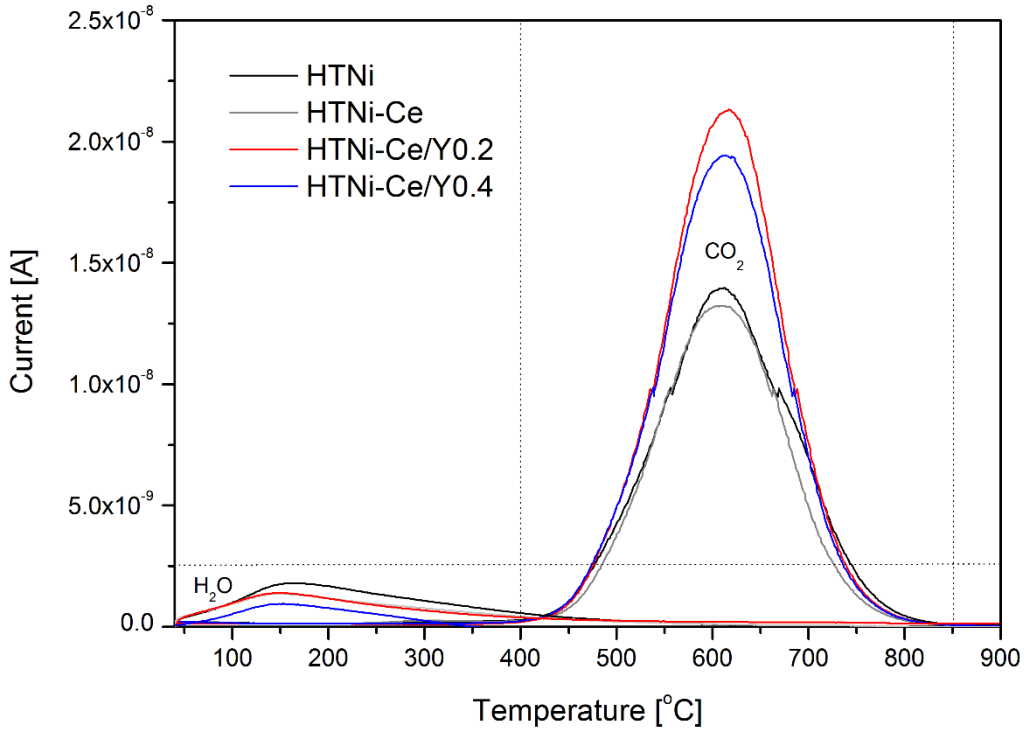

Fig. 4.49 Mass spectrometry (MS) signals of water vapor and carbon dioxide during thermal decomposition of the spent catalysts.

Raman spectroscopy was performed after isothermal tests and the results are presented in Fig. 4.50. Four characteristic peaks located at 1473 cm^{-1} (D band), 1573 cm^{-1} (G band), 1602 cm^{-1} (D' band), and 2644 cm^{-1} (G' band) can be observed for all studied samples, D-bands is related to the disordered structural form of crystalline carbon species and G-bands associated with graphitic carbon, as discussed in more detail in previous subchapters. The degree of the carbon crystallinity (I_D/I_G) is shown in Table 4.23. The highest contribution of the graphitized carbon, related to the lowest I_D/I_G ratio of 1.47, was registered for HTNi-Ce catalyst. For the HTNi-Ce/Y0.2 catalyst less graphitic carbon was observed than for HTNi-Ce, despite the higher mass loss in the TGA analysis (cp. Fig. 4.48). Thus, although the low loadings of yttrium (0.2 wt.%) led to the creation of higher amount of carbon, such deposits should be easier to remove.

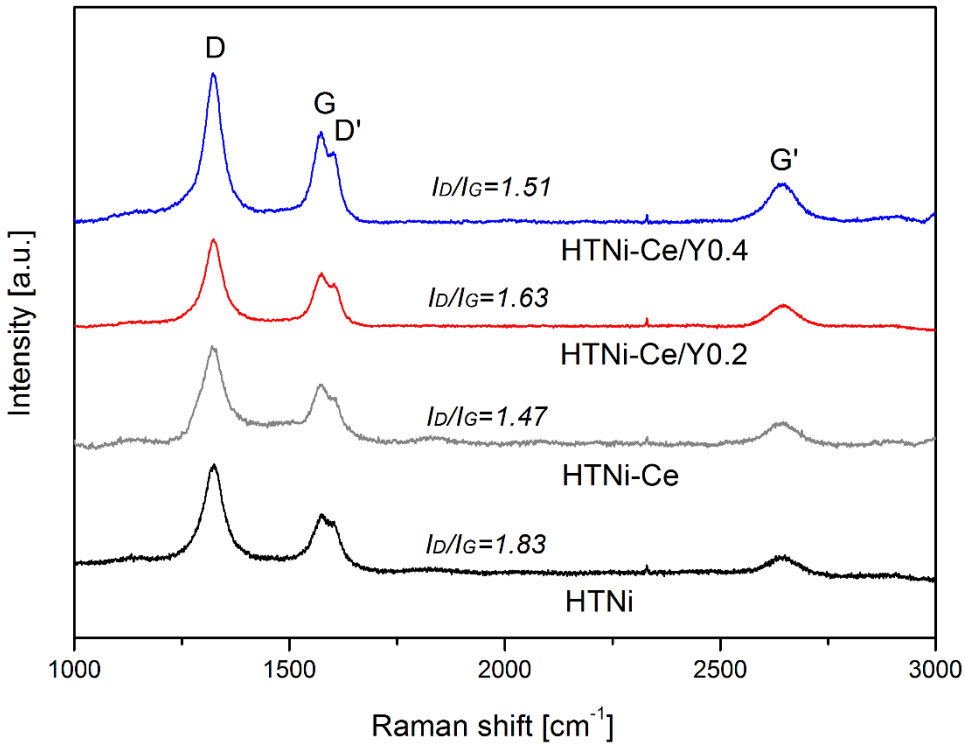

Fig. 4.50 Raman spectra recorded for the spent catalysts.

To gain more information on the structure of carbon deposits, high-resolution transmission electron microscopy analyzes were carried out for the samples after dry reforming of methane tests at 700 °C for 5 h. The micrographs of the spent HTNi-Ce and HTNi-Ce/Y0.4 catalysts are presented in Figs. 4.51 A and B. Helix-shaped carbon nanotubes are observed together with the high number of straight tubes, with well-defined graphite sheets with d-spacing of 3.3 Å for (111) planes. The helix-shaped nanotubes can be formed due to periodic incorporation of pentagon-heptagon pairs into a hexagonal carbon framework, generating curved surfaces [382]. Fig. 4.51 A also shows a high-resolution detail of tightly wound helix-shaped carbon nanotube containing 20–22 graphene sheets. Moreover, well-dispersed cylindrical nickel particles of the mean size of 11–12 nm were registered. However, most of them were encapsulated with the carbon layers of d_{hkl} = 3.35 Å (Figs. 4.51 A and B). In HTNi-Ce catalyst, cerium oxide particles were detected with distance of 3.2 Å (111) and the particle size of 7–13 nm. Such CeO_2 particles formed aggregates in close vicinity to Ni. In case of the Y-modified

sample, the particles of cerium oxide were present separately or together with small particles of yttrium (Fig. 4.51 B). Based on the recorded distance of 3.05 Å, it is hard to distinguish if a solid solution of CeO_2-Y_2O_3 was formed (d_{hkl} = 3.12 Å for cubic) or two particles of cerium oxide and yttrium oxide are just neighboring each other (d_{hkl} = 3.12 Å for cubic CeO_2, d_{hkl} = 3.06 Å for cubic Y_2O_3). As proposed in literature [29], such yttria-doped ceria (YDC) phase could explain the high catalytic activity and better Ni^0 dispersion for the studied catalysts.

Moreover, the mixed oxides have been partially reconstructed, as confirmed by presence of the Mg and Al signals in EDS, and distance of d_{hkl} = 2.52 Å probably arising from (009) plane. Also, the textural properties obtained for the spent samples, as S_{BET} increased and showed similar values to those for the calcined materials (Table 4.25 vs. Table 4.21).

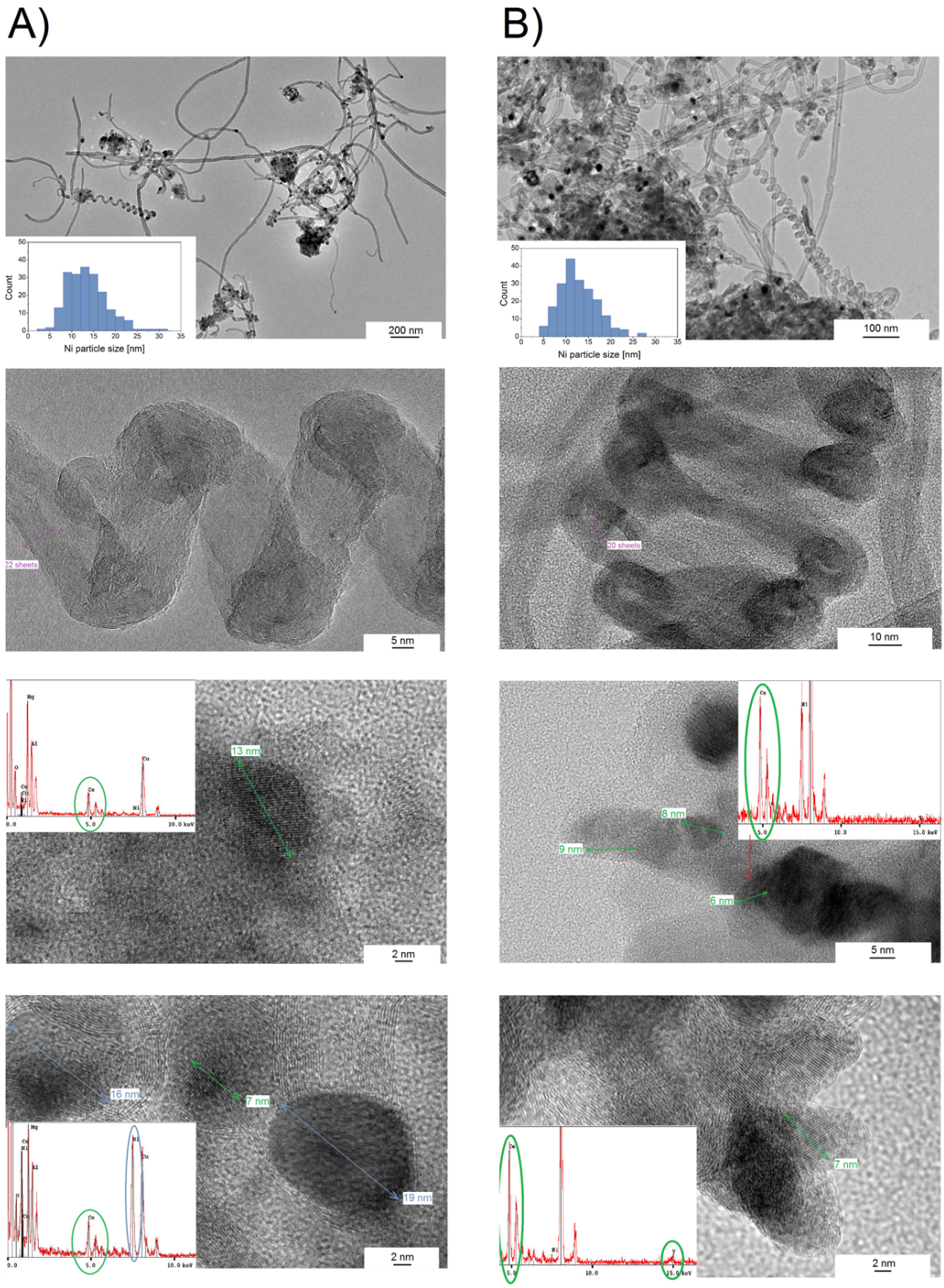

Fig. 4.51 HRTEM micrographs of (A) HTNi-Ce; and (B) HTNi-Ce/Y0.4 catalysts after dry reforming of methane test at 700 ℃ for 5 h.

4.4.5. *Conclusions*

In this subchapter, the dry reforming of methane was presented over the double-layered hydroxides modified with cerium (by co-precipitation method) and with 0.2, 0.4 or 0.6 wt.% yttrium (by the incipient wetness impregnation method).

The co-promotion with Ce and Y led to the decrease of reducibility of Ni, an increase of the basicity, enhanced Ni dispersion and smaller Ni crystallite size as compared to the HTNi catalyst. This can be explained by a possible formation of yttria-doped ceria (YDC) phase. The modification with the smallest loading of yttrium (0.2 wt.%) led to the increase of both CO_2 and CH_4 conversions during isothermal DRM tests for 5 hours. This enhancement of the activity is partly arising from side reactions. No deactivation was reported during the isothermal tests, despite the formation of carbon deposits. The amount of catalytic coke was higher for Y-promoted samples; however, the deposits were less graphitic than for the HTNi-Ce catalyst.

4.5. Overall conclusions on dry reforming of methane

Ni-containing double-layered hydroxides were prepared with a fixed M^{2+}/M^{3+} molar ratio of 3, and Ni^{2+}/Mg^{2+} of 0.33, and tested in dry reforming of methane. The influence of Y, Zr and Ce promotion on the physico-chemical properties of these series of catalysts was analyzed by means of XRD, XRF, low temperature N_2 sorption, TPR-H_2, TPD-CO_2, H_2 chemisorption, transmission electron microscopy, high-resolution microscopy, thermogravimetric analysis coupled with mass spectroscopy and Raman spectroscopy. The promotion with Y, Zr or Ce was carried out by different techniques such as co-precipitation and incipient wetness impregnation. The activity in dry reforming of methane and direct methane decomposition was tested at the temperature range between 850 and 600 °C, and in the isothermal 5-hour tests at 700 °C.

The general conclusion is that the promotion with Y influenced physico-chemical properties (specific surface area, Ni dispersion, basicity and reducibility), to an extent depending on both the amount of introduced yttrium and the method of preparation. This, in turn, influenced the catalytic performance. The presence of two promoters (Y, with Zr or Ce) strongly influenced activity, stability and the selectivity of tested catalysts in DRM. Although all catalysts after DRM showed the presence of carbon deposits, the type of such species and their amount was dependent on the presence of both Y, and Zr or Ce. Regarding activity, the best observed after 5 h was for the catalyst co-precipitated with both Zr (assumed 5 wt.%) and Y (0.4 wt.%). Regarding the amount and type of formed carbonaceous deposits, the best performing catalyst was HTNi-Zr, which showed mostly amorphous carbon.

For the Ni/Mg/Al hydrotalcite-based catalysts, **Y promotion via co-precipitation** of Ni/Mg/Al with Y resulted in increased specific surface area, and Ni dispersion, without creating a separate crystalline phase of this metal. The modification of Ni/Mg/Al hydrotalcite with 0.2-2.0 wt.% Y resulted in incorporation of yttrium into hydrotalcite layers, whereas the promotion with 3 wt.% led to the deposition of this metal on the catalyst's surface. The latter resulted in the stabilization of hydrotalcite structure, and calcination at 550 °C led to only partial transformation to periclase. The presence of yttrium on the surface led to the increased basicity (mainly Lewis pairs), in contrast to the decrease

that was registered when Y was incorporated into the structure (0.2-2.0 wt.%). Yttrium present in the framework of periclase-like structure led additionally to the decreased reducibility, whereas the presence of the metal on the surface increased the H_2 consumption.

The yttrium addition increased catalytic activity in dry reforming of methane. The loading of 0.4 wt.% inhibited important carbon forming reaction – direct methane decomposition. However, three types of carbon were still observed in the spent catalysts, amorphous, filamentous and graphitic-like coke.

The co-impregnation with zirconium and yttrium led to formation of ZrO_2-Y_2O_3 solid solution on the surface of HTNi material, thus resulting in a decrease of S_{BET}. Although the dispersion of metallic Ni increased, the presence of bulk NiO was observed for all Zr,Y-impregnated samples, except the HTNi/ZrY0.4. The formation of the zirconia-yttria phase led to the decreased total basicity. The doping with yttrium clearly influenced the distribution of the basic sites, as percentage of medium-strong basic sites was increasing with yttrium loading. The promotion with 0.4 wt.% was optimal, as confirmed by the enhanced stability. No deactivation was observed in the isothermal DRM catalytic test. Stability improvement was also expressed by the absence of reconstruction to the hydrotalcite structure. However, considerable amounts of amorphous carbon were registered.

The co-precipitation of Ni/Mg/Al with Zr revealed ZrO_2 partly incorporated into the brucite-like layers of catalysts precursors, and partly deposited on the surface. When compared to impregnation, the co-precipitation, led to the formation of smaller ZrO_2 particles and thus better dispersion. **Further impregnation with yttrium** decreased the specific surface area and did not lead to the creation of ZrO_2-Y_2O_3 solid solution. The Ni dispersion decreased for yttrium impregnated samples, due to the partial blockage of these active sites. Also, in this case the percentage of medium-strength basic sites was increasing with yttrium loading. In DRM test, the catalytic activity was the highest for HTNi-Zr and HTNi-Zr/Y0.4, hence these catalysts were tested in isothermal test showing no deactivation in 5-hour on stream. The characterization of the spent catalysts showed, however, that impregnation with Y0.4

led to the significant amount of graphitic-like carbon deposits in contrast to only Zr-containing material for which traces of carbon were detected upon 5 h of DRM reaction at 700 °C.

Co-precipitation of all components (Ni, Mg, Al, Zr and Y) led to a significant decrease of the specific surface area. The Ni dispersion was higher as compared to the HTNi-Zr. The total number of total basic sites increased, and new intermediate strength (Lewis acid-basic pairs) basic sites, and strong (O^{2-}) sites were formed. The isothermal test revealed increasing CH_4 and CO_2 conversions, pointing to the further evolution of Ni-species with TOS. Characterization of the used catalyst did not show sintering of the nickel, as almost the same crystallite size as for the reduced sample was recorded. However, the undesired graphitic carbon was observed.

The co-precipitation of Ni/Mg/Al hydrotalcite with cerium resulted in the formation of the segregated phase of CeO_2. Specific surface area and Ni reducibility were decreased. Further impregnation with yttrium benefited the textural properties, as S_{BET} increased considerably. As shown by HRTEM, most probably yttrium-doped ceria phase (YDC) was formed. The crystallite size of Ni^0 decreased and dispersion of this metal increased. The basicity was influenced by ceria addition, as the percentage share of medium and strong basic sites was enhanced. In contrast to Ni/Mg/Al and Ni/Mg/Al/Zr hydrotalcites promoted with Y, no dependence of the number of basic sites on Y content was registered. The CH_4 and CO_2 conversions were stable for all catalysts, except for HTNi-Ce/Y0.2 for which increasing trend was recorded. All samples showed the unwanted graphitic carbon. Helix-shaped carbon nanotubes were also observed in the jungle of straight nanotubes.

Chapter 5 – Tri-reforming of methane and other reactions on selected catalysts

Chapter 5 – Tri-reforming of methane and other reactions on selected catalysts

In this chapter, an unpromoted catalyst HTNi and a catalyst promoted with 2 wt.% Y (HTNi-Y2.0) were examined in the partial oxidation of methane (POM), assuming ($CH_4/CO_2/O_2/Ar$)=(1/0/0.5/8.5) and CO_2 reforming combined with partial oxidation of methane (CRPOM), i.e., ($CH_4/CO_2/O_2/Ar$)=(1/1/0.5/7.5). These catalysts were chosen as promotion with 2.0 wt.% Y resulted in the improved textural properties and the highest recorded Ni dispersion, i.e., 19.8%. HTNi was tested to determine the influence of yttrium addition on catalytic performance, as compared to the unmodified material. Additionally, these two selected catalysts were examined in tri-reforming of methane assuming two different gas compositions, i.e.,

(i) ($CH_4/CO_2/H_2O/O_2/Ar$) = (1/0.5/0.5/0.1/7.9), similar as proposed in literature [83,85–87,89], and

(ii) ($CH_4/CO_2/H_2O/O_2/Ar$) = (3/1/2/0.3/3.7) simulating the flue gases from natural-gas-fired power plants. This feed gas has been chosen among three others compositions as the one giving the results most favorable according to thermodynamic analysis.

The choice of Ni-hydrotalcites for tri-reforming is based on several literature arguments. The first of them is their good performance in dry reforming of methane, also confirmed in this PhD study.

Ni-based double-layered hydroxides were also reported before as potential catalysts in partial oxidation of methane [231,233–235,383–385]. Shishido et al. [231] reported that the Ni-based double-layered hydroxides can minimize the carbon formation during POM reaction. Zheng et al. [233] observed that nickel-based hydrotalcites with two different loadings (8 wt.% and 15.5 wt.% Ni) had similar catalytic activity in POM.

Mg/Al double-layered hydroxides were also examined by Tsyganok et al. [386] in the process of dry reforming combined with partial oxidation of methane (CRPOM). Ru-promoted Mg/Al double-layered hydroxides under the tested conditions (850 °C; $CH_4/O_2/CO_2/N_2$ = 35.2/16.2/3.18/45.8; vol.%) showed the best catalytic performance towards CRPOM, among three metals tested as promoters (Pt, Rh, Ru).

Thus, the above-mentioned findings suggest good catalytic performance of hydrotalcites in oxidative reactions systems. However, in the existing literature, no studies of tri-reforming of methane over Ni/Mg/Al double-layered hydroxides and the DLHs promoted with yttrium were reported.

5.1. Partial oxidation of methane – one of main reactions in tri-reforming of methane

5.1.1. *TPSR catalytic tests*

Methane conversion during partial oxidation of methane ($CH_4/CO_2/O_2/Ar$=1/0/0.5/8.5, GHSV=20,000 h^{-1}, temperature range of 850-600 °C) is presented in Fig. 5.1. For both studied catalysts methane conversion was over 70% in the considered temperature window. As predicted by thermodynamic calculations, the conversions were the highest for high temperatures (here studied 850 °C). HTNi and HTNi-Y2.0 revealed similar CH_4 conversion results, showing the promoting effect of yttrium only to a small extent, in contrast to the results discussed in **Subchapter 4.1.** for dry reforming of methane ($CH_4/CO_2/Ar$=1/1/8). Nevertheless, the CH_4 conversions were still higher in POM than in DRM, showing the beneficial role of oxygen. In POM, high conversions of CH_4 were observed before in the range of 600-700 °C, suggesting that the combustion of methane was predominant [387]. In the literature, the POM mechanism was described by two pathways leading to either CO_2 or CO as a primary reaction product. The combustion and reforming reaction mechanism (CRR) was first suggested by Prettre et al. [130], and also considered by many other researchers [131,222,388,389]. It assumes that CO_2 and H_2O are produced via combustion reaction of CH_4 and O_2, followed by reforming (steam and dry), resulting in the formation of H_2 and CO. The second pathway is the direct oxidation mechanism (DPO), and was proposed by Hickman and Schmidt [136–138]. This mechanism assumes the formation of CO via methane pyrolysis, followed by the oxidation of carbon-containing species to CO without pre-formation of CO_2.

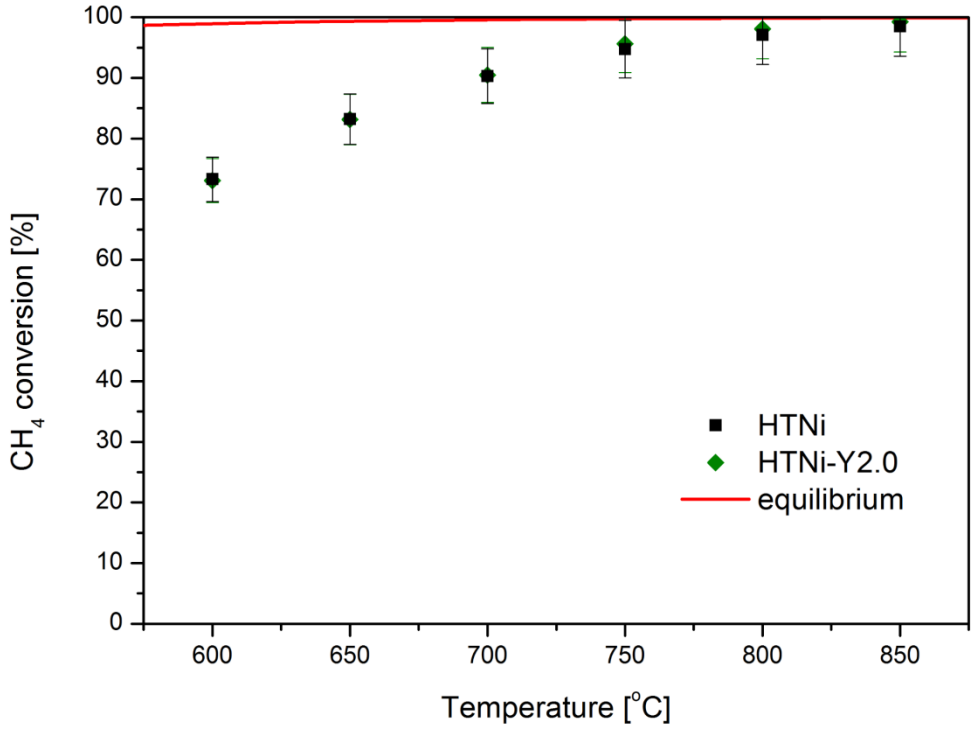

Fig. 5.1 CH_4 conversions registered for HTNi and HTNi-Y2.0 catalysts during POM catalytic test. The reaction conditions ($CH_4/CO_2/O_2/Ar$=1/0/0.5/8.5, GHSV=20,000 h^{-1}, temperature range of 850-600 °C, steady-state at each 50 °C for 30 min).

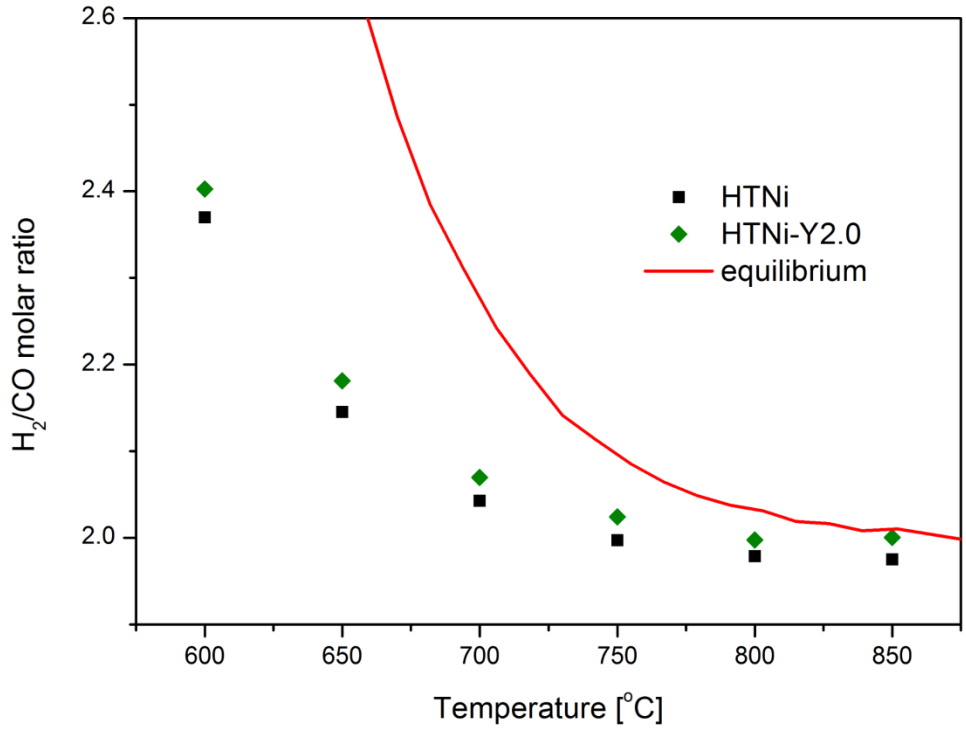

Fig. 5.2 H_2/CO molar ratio for the HTNi and HTNi-Y2.0 catalysts in the POM catalytic test. The reaction conditions ($CH_4/CO_2/O_2/Ar$=1/0/0.5/8.5, GHSV=20,000 h^{-1}, temperature range of 850-600 °C, steady-state at each 50 °C for 30 min).

The H_2/CO molar ratio obtained during POM reaction is presented in Fig. 5.2. The H_2/CO ratio decreased for both catalysts with increasing reaction temperature, from 2.4 at 600 °C to 1.9 at 850 °C. The decreasing trend is in agreement with the equilibrium calculations as well as with literature [132,219]. At higher temperatures H_2 is consumed due to the endothermic nature of the accompanying reforming processes - dry or steam CH_4 reforming, as well as reverse water-gas shift reaction (RWGS) [132,241]. However, it should be mentioned that the ratio value of 2.4 obtained at lower temperature (600 °C) is far from ideal for subsequent liquid fuel synthesis.

In order to illustrate the composition of the mixture after reaction, as well as the changes in concentration during the 30 minutes on line at a given temperature, the TPSR profiles for the partial oxidation of methane (POM) for HTNi and HTNi-Y2.0 are presented in Fig. 5.3 A and B, respectively.

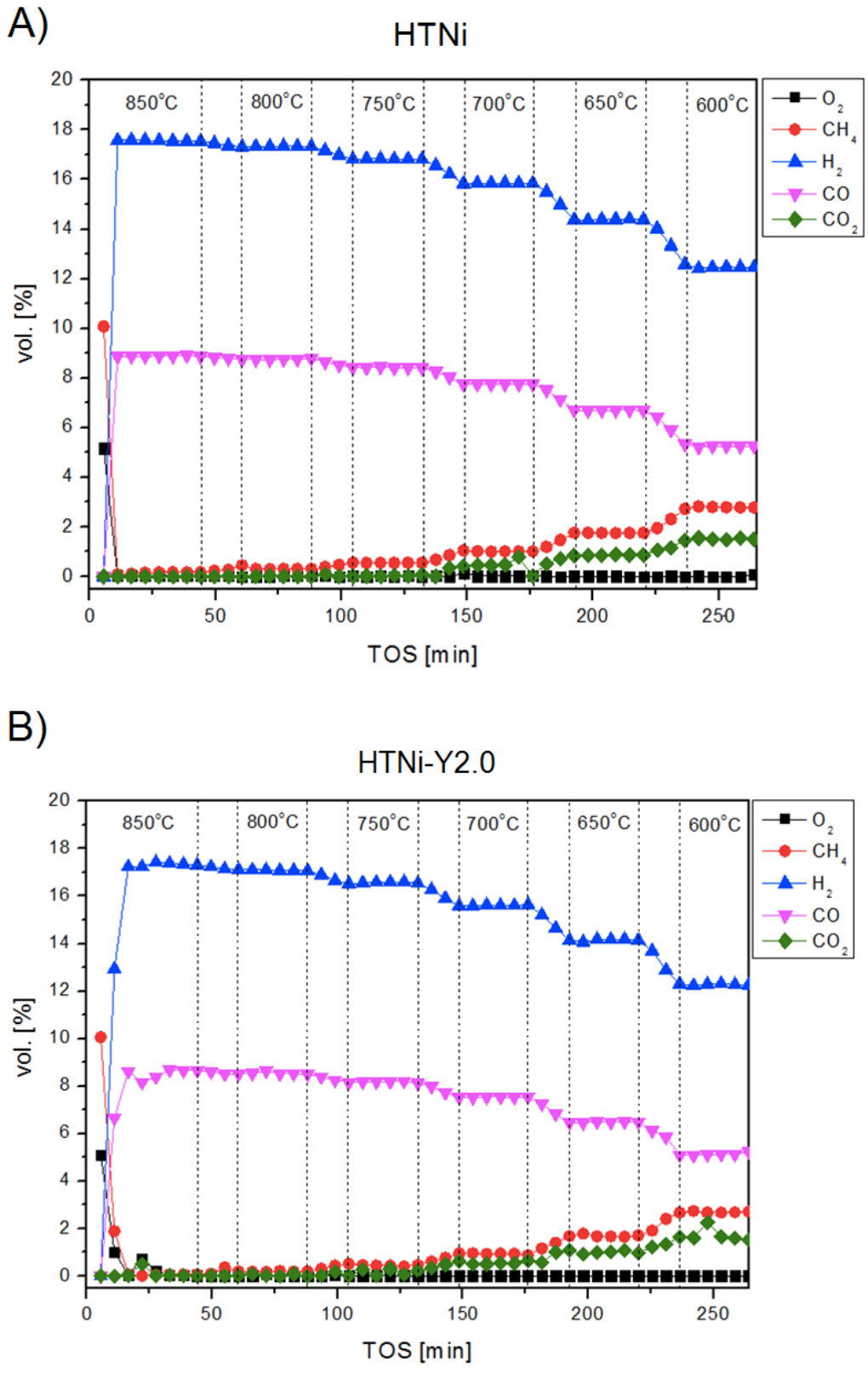

Fig. 5.3 TPSR results for (A) HTNi and (B) HTNi-Y2.0: volumetric percentage of reaction compounds as a function of 30 minutes online at the studied temperatures. The reaction conditions ($CH_4/CO_2/O_2/Ar$=1/0/0.5/8.5, GHSV=20,000 h^{-1}, temperature range of 850-600 °C).

After the first 6 min of the catalytic test, these values decreased as a result of the partial oxidation of methane. It has been clearly shown that the POM reaction took place in the temperature range of 750-850 °C, because only CO was formed and no CO_2 was detected. However, below 750 °C, both CO and CO_2 were formed, confirming the co-existence of partial and total oxidation of methane (TOM) [228]. Modified hydrotalcite-derived catalysts were reported as active in total combustion of methane [390–396]. The TOM resulted also in H_2O formation, but the latter was not quantified during these experiments. Similar results were observed by Chalupka et al. [241] for C-Ni_5AlBEA and C-Ni_5SiBEA catalysts. The TPSR tests revealed the occurrence of TOM in the temperature range of ca. 420-425 to 720-770 °C, whereas POM reaction started above the latter temperature. The presence of CO_2 at lower temperatures and its absence at higher temperatures is in good agreement with thermodynamics (cp. Fig. 3.4, **Chapter 3**) predicting the gradual decrease of carbon dioxide concentration in the products with the increase in temperature. This behavior is in agreement with the mechanism proposed by Prettre et al. [130], in which CO_2 is a primary product of POM, undergoing further the reaction with either CH_4 or H_2O (the product of total methane oxidation) to form CO and H_2. This would explain why CO_2 is registered only at lower studied temperatures where DRM and SRM, due to their highly endothermic nature, have lower conversions than at higher temperatures.

5.1.2. *Isothermal catalytic tests of partial oxidation of methane*

Fig. 5.4 shows the isothermal POM test for HTNi and HTNi-Y2.0 catalysts at 700 °C for 5 h. As it can be seen, both catalysts were stable during this reaction without any decrease in catalytic activity. The HTNi showed 87.5% of converted CH_4, while HTNi-Y2.0 revealed slightly higher value of 93.1%. This is in the agreement with the results obtained previously in the TPSR test (cp. Fig. 5.1).

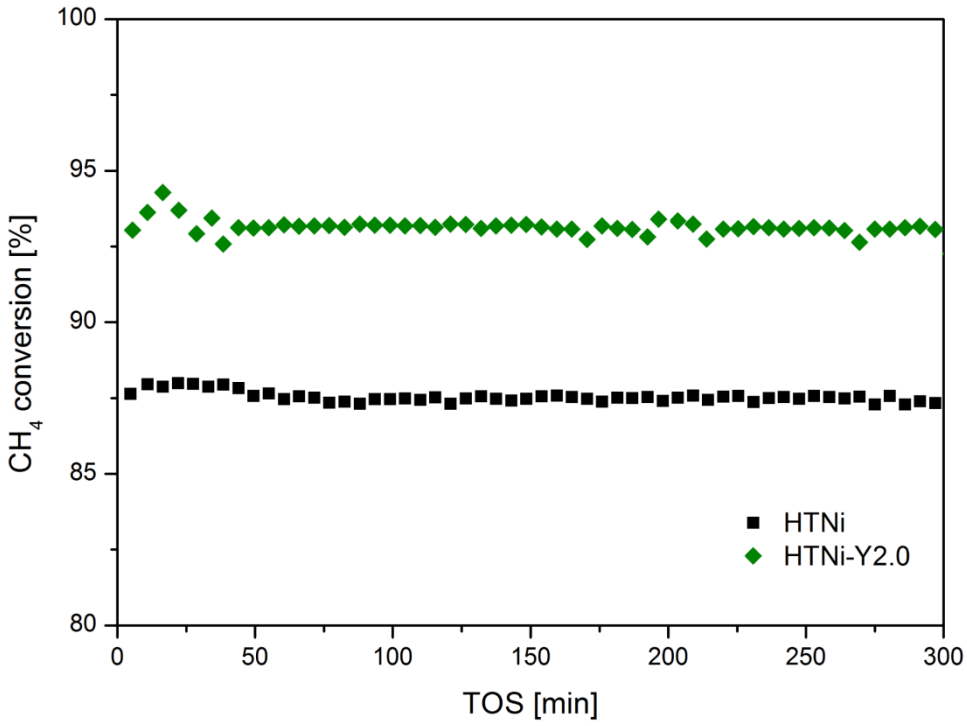

Fig. 5.4 CH_4 conversion in the isothermal POM test at 700 °C for 5 h ($CH_4/CO_2/O_2/Ar$=1/0/0.5/8.5, GHSV=20,000 h^{-1}).

Fig. 5.5 shows the H_2/CO molar ratio recorded during the isothermal test at 700 °C for 5 h. The obtained ratio is around 2.04 for both catalysts. No evident decrease was observed, pointing to a stable behavior under POM conditions of the both catalysts, modified or unmodified by Y.

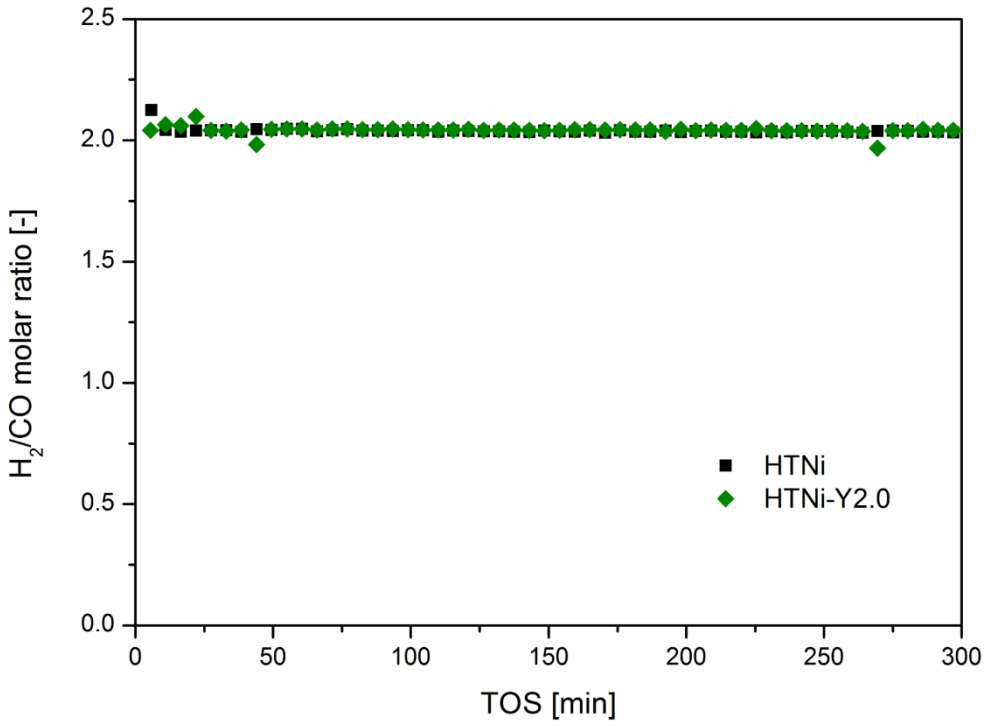

Fig. 5.5 H_2/CO molar ratio recorded for HTNi and NTNi-Y2.0 catalysts during POM test at 700 °C for 5 h ($CH_4/CO_2/O_2$/Ar=1/0/0.5/8.5, GHSV=20,000 h^{-1}).

Apart from CO and H_2 only traces of CO_2 were recorded during the test at 700 °C for 5 h. This could suggest an insignificant role of total oxidation of methane but is also consistent with the mechanism of Prettre et al. [130] discussed above.

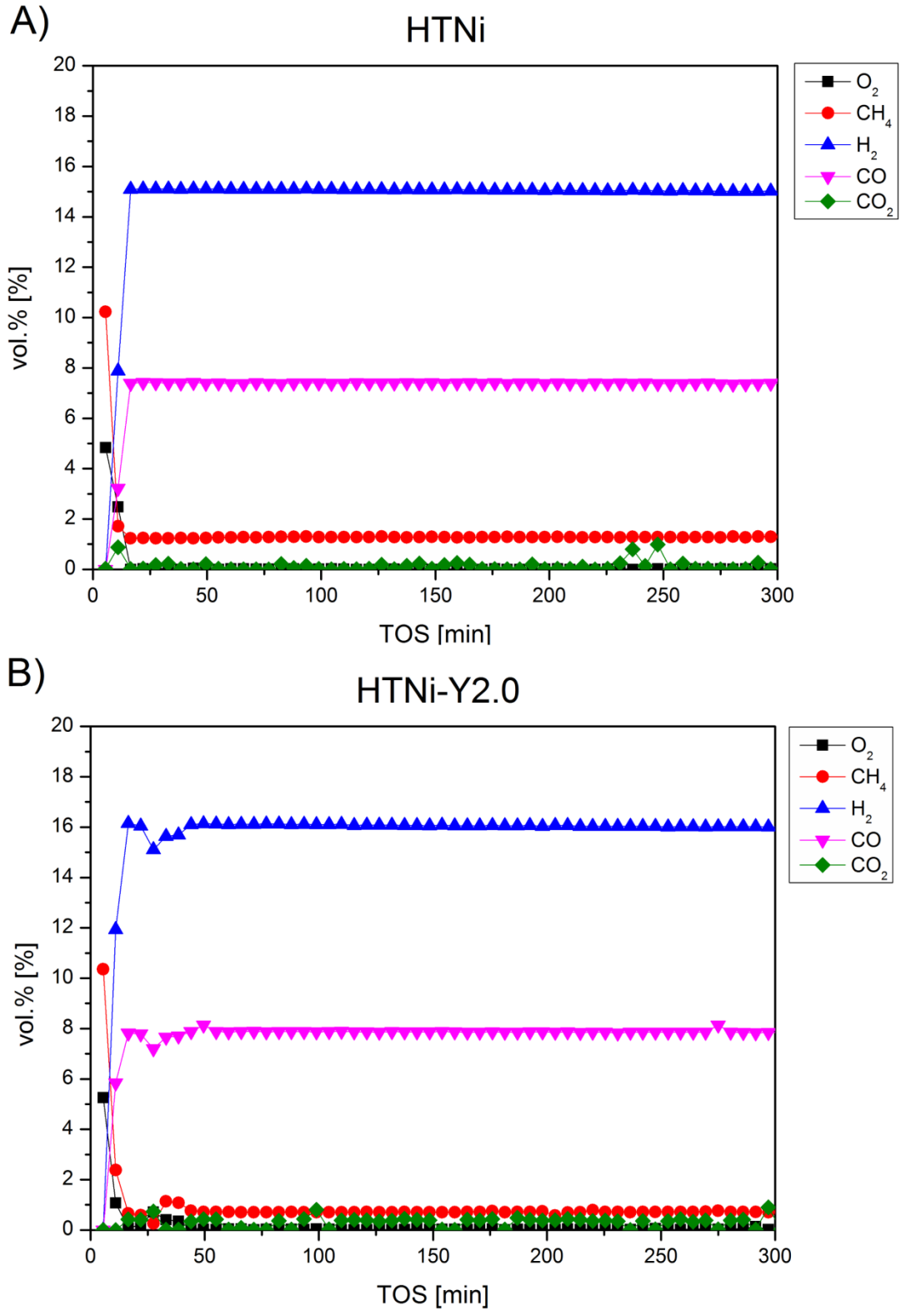

Fig. 5.6 Results of isothermal test of (A) HTNi and (B) HTNi-Y2.0 - the volumetric percentage of reaction compounds as a function of time. The reaction conditions ($CH_4/CO_2/O_2$/Ar=1/0/0.5/8.5, GHSV=20,000 h^{-1}, at 700 °C for 5 h).

5.2. Combined CO_2 reforming and partial oxidation of methane as a part of the process of tri-reforming of methane

Fig. 5.7 presents the CH_4 conversion values in combined CO_2 reforming and partial oxidation of methane ($CH_4/CO_2/O_2/Ar$)=(1/1/0.5/7.5). The addition of 10 vol.% of CO_2 resulted in an increase of CH_4 conversion only for HTNi-Y2.0 catalyst, in comparison to the POM results (cp. Fig. 5.1). Similar observation was reported by Meshkani et al. [224]. The authors investigated the CRPOM process over Ni/MgO prepared by impregnation technique. They reported higher CH_4 conversion for CRPOM than for DRM and POM, as well as amounts of carbon deposits lower for the POM reaction than for DRM, and no carbon deposition in the CRPOM process. This catalytic behavior was ascribed to the presence of oxygen as a substrate and its beneficial role in the removal of C deposits.

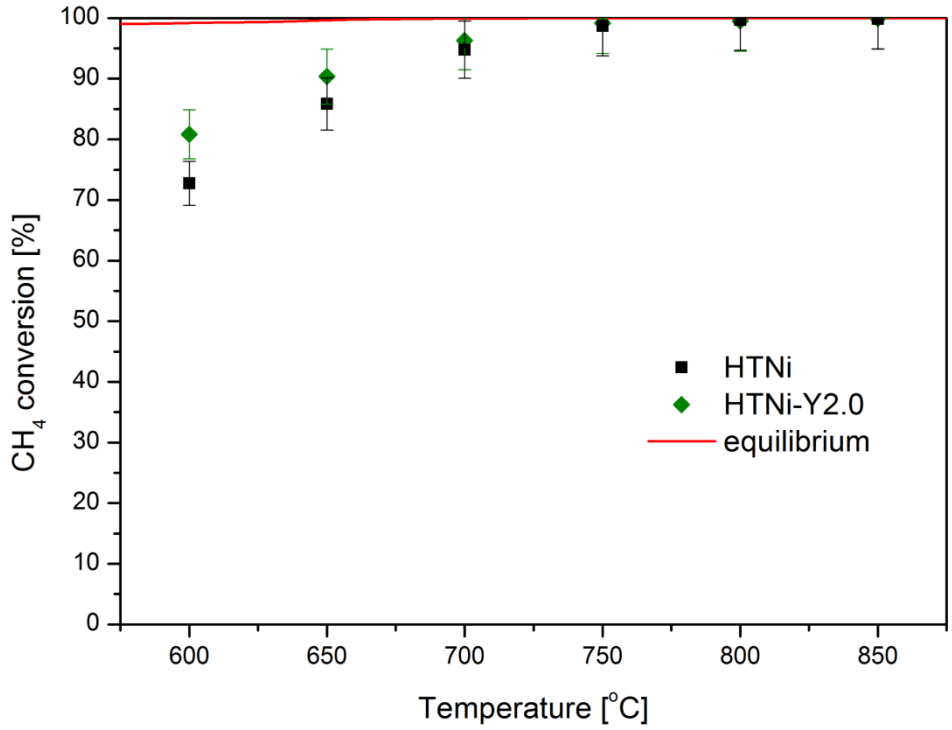

Fig. 5.7 CH_4 conversion as a function of temperature for HTNi and HTNi-Y2.0 catalysts in CRPOM process. The reaction conditions: ($CH_4/CO_2/O_2/Ar$)=(1/1/0.5/7.5), the temperature range of 850-600 °C, steady-state at each 50 °C for 30 min.

The CO_2 conversion as function of temperature is presented in Fig. 5.8. For both catalysts, the carbon dioxide conversions were similar (within experimental error). The values are lower under oxidative CO_2 reforming than in DRM. Additionally, in dry reforming, the CO_2 conversion was higher than the CH_4 conversion due to the reverse water-gas shift reaction. The results presented in Fig. 5.8 are significantly lower due to CO_2-forming side reactions, which are thermodynamically feasible in this temperature window [397].

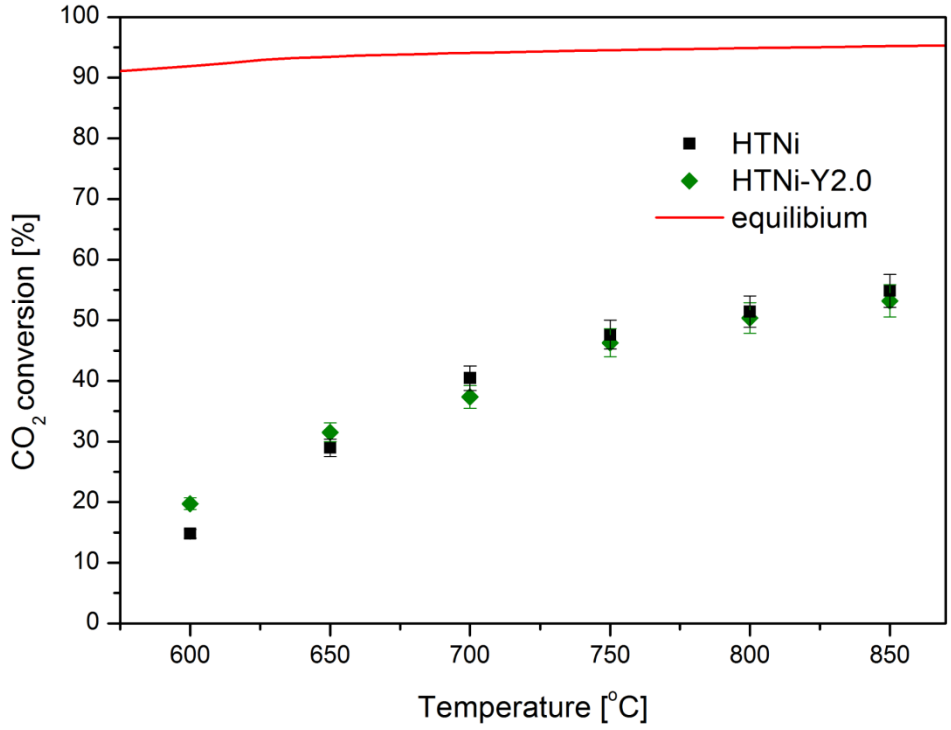

Fig. 5.8 CO_2 conversion as a function of temperature for HTNi and HTNi-Y2.0 catalysts in CRPOM process. The reaction conditions: (CH_4/CO_2/O_2/Ar)=(1/1/0.5/7.5), the temperature range of 850-600 °C, steady-state at each 50 °C for 30 min.

The H_2/CO molar ratio at different temperatures in combined partial oxidation and dry reforming is presented in Fig. 5.9. The obtained values decreased with the temperature, and, apart from the lowest studied temperature (600 °C) coincide with the thermodynamic equilibrium values.

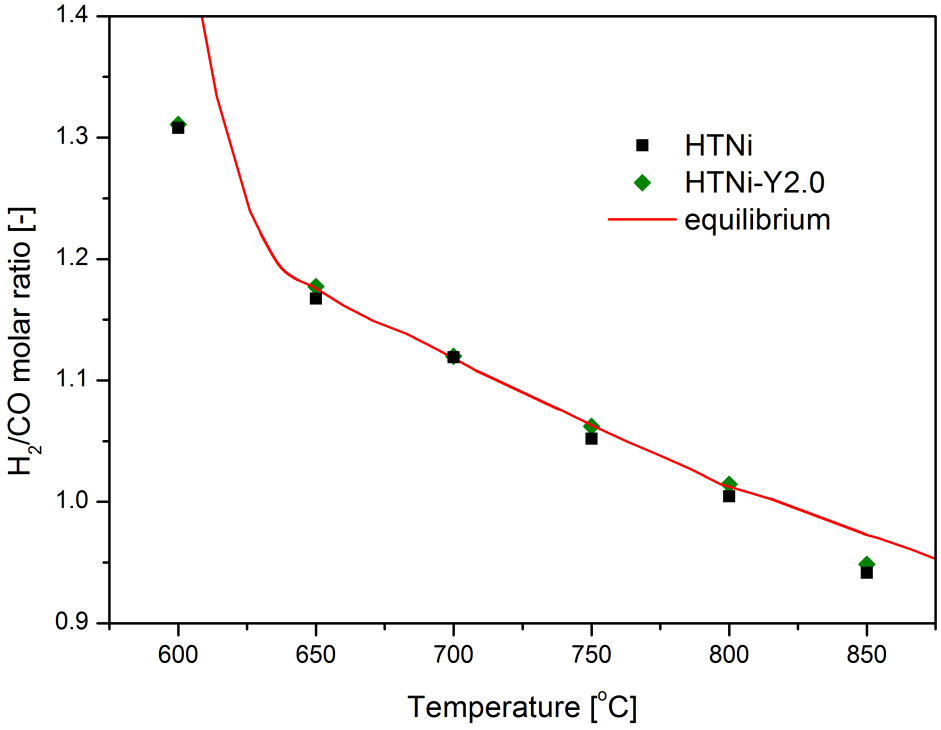

Fig. 5.9 H_2/CO molar ratio as a function of temperature for HTNi and HTNi-Y2.0 catalysts in CRPOM process. The reaction conditions: (CH_4/CO_2/O_2/Ar)=(1/1/0.5/7.5), the temperature range of 850-600 °C, steady-state at each 50 °C for 30 min.

The addition of oxygen to reaction mixture should prevent or decrease catalyst deactivation caused by carbon formation [144,304,398]. However, the controlled amount of oxygen is required, as low O_2 concentrations will not have the desired effect and high O_2 amount results in lower selectivity, hot spots formation and sintering [131,143,144,399]. Moreover, side reactions (direct methane decomposition (DMD) and Boudouard reaction) can occur parallelly during CRPOM and they are the main sources of carbon deposits. Literature studies, however, showed significant inhibition of carbon deposition, as confirmed by the lack of the graphitic carbon reflection in XRD of the spent catalysts of combined CO_2 reforming with partial oxidation (CRPOM) [400,401].

The studied catalysts HTNi and HTNi-Y2.0 were characterized after TPSR tests.

XRD patterns of the spent catalysts are presented in Fig. 5.10. Characteristic XRD reflection of graphitic carbon (2θ ca. 27°) was not observed in either of the spent catalysts. The metallic nickel phase

was detected (ICOD 01-087-0712), together with the periclase structure (ICOD 00-045-0946). Ni^0 crystallite size, calculated from Scherrer equation was 6 and 3 nm for HTNi and HTNi-Y2.0 respectively. Since the carbon formation is favored on large Ni crystallites [402,403], higher resistance of HTNi-Y2.0 catalyst is expected.

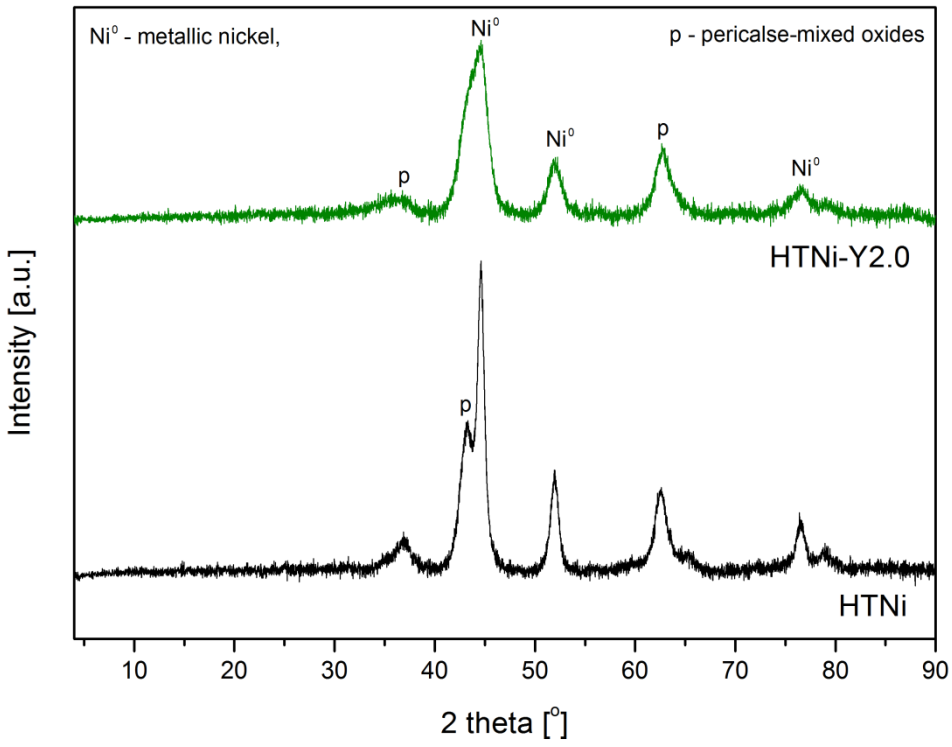

Fig. 5.10 XRD patterns of the spent catalysts after TPSR tests of combined partial oxidation and CO_2 reforming.

5.3. Tri-reforming of methane

5.3.1. *Feed gas composition of ($CH_4/CO_2/H_2O/O_2/Ar=1/0.5/0.5/0.1/7.9$)*

5.3.1.1. *Catalytic tests*

Catalytic activity for tri-reforming of methane in the isothermal 5-hour test at 700 °C is presented in Fig. 5.11. The CH_4 conversion increased in the first 27 minutes, from 85% to 99%, whereas a decrease in the CO_2 conversion from 99% to 55-80% was revealed. The presence of oxygen in the feed promotes the exothermic partial oxidation or total oxidation of a fraction of the CH_4 feed, sustaining the

reforming steps [87]. The methane oxidation reactions result in CO_2 formation which in turn could affect the net CO_2 conversion. The other CO_2-forming reaction is water-gas shift ($CO+H_2O=CO_2+H_2$).

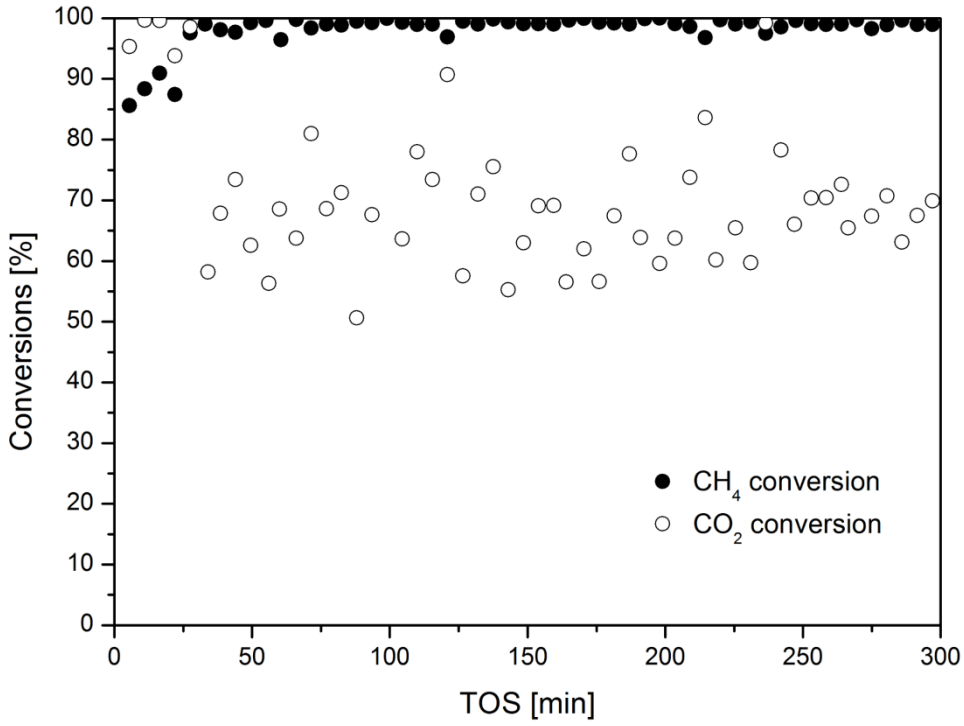

Fig. 5.11 CH_4 and CO_2 conversion for HTNi catalyst recorded in tri-reforming of methane catalytic test. The test conditions: ($CH_4/CO_2/H_2O/O_2$=1/0.5/0.5/0.1/7.9, GHSV=20,000 h^{-1}, 700 °C for 5 h).

On the other hand, CO_2 conversion could also originate from the oxidation of carbon deposit, formed upon dry and/or steam reforming, methane decomposition or Boudouard reaction [85]. The HTNi catalyst showed stable activity during the 5 h of the test under the specified experimental conditions. The experimental data obtained for the CO_2 showed huge variations, and do not provide straight answer about the changes of carbon dioxide conversion. The mean value, however, is ca. 69%.

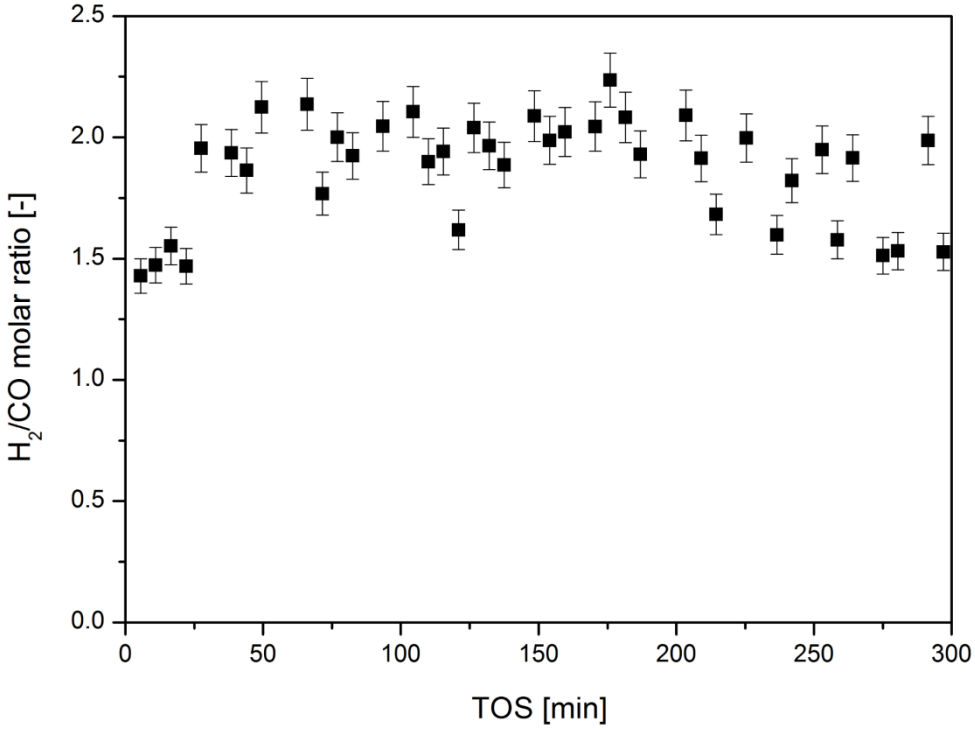

Fig. 5.12 H_2/CO molar ratio for HTNi catalyst recorded in tri-reforming of methane catalytic test. The test conditions: ($CH_4/CO_2/H_2O/O_2$=1/0.5/0.5/0.1/7.9, GHSV=20,000 h^{-1}, 700 °C for 5h).

H_2/CO molar ratio for HTNi material is presented in Fig. 5.12. The obtained values were in the range 1.7-2.2. Because of the unstable CO_2 conversion, the obtained experimental values show fluctuations within time on stream. However, some trends may be recognized. At the beginning of the test the ratio increased. Then, after first 50 min it remained stable within the range of 2.1-1.9, and started to decline after 250 min. The mentioned initial increase may have originated from the formation of additional hydrogen via methane partial oxidation, as suggested before [85]. The final decline in H_2/CO molar ratio may be, on the other hand, ascribed to the production of extra amount of carbon monoxide. The latter could be a final product of reactions directly linked with carbon oxidation, such as $C_{(ads)} + CO_2 = 2CO$, and/or $C_{(ads)} + H_2O = CO + H_2$ [91].

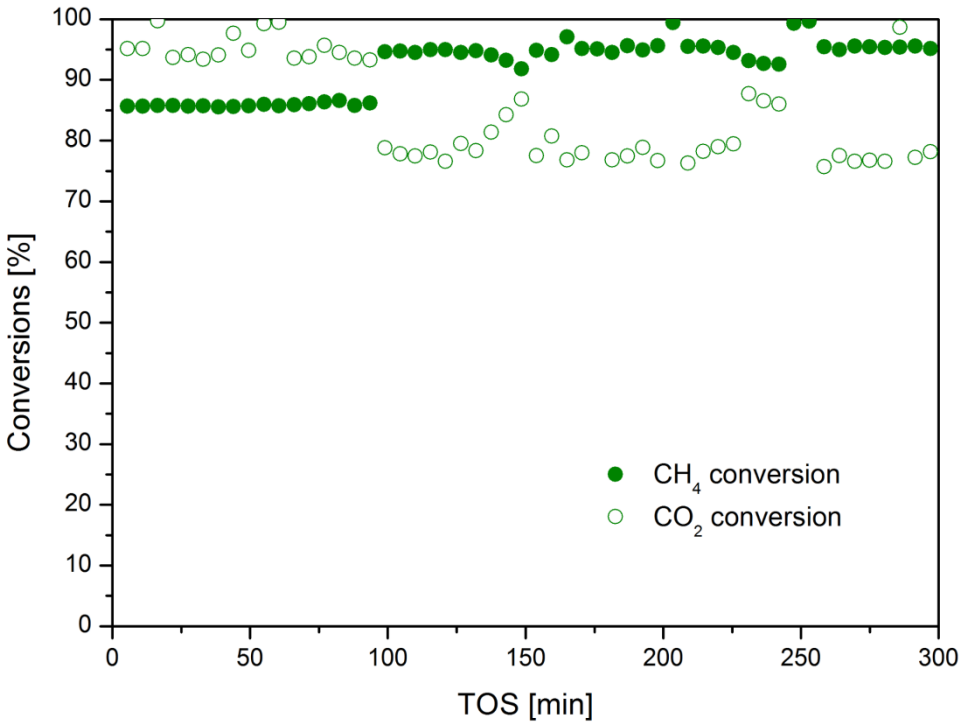

Fig. 5.13 CH_4 and CO_2 conversion for HTNi-Y2.0 catalyst recorded in tri-reforming of methane catalytic test. The test conditions: ($CH_4/CO_2/H_2O/O_2$=1/0.5/0.5/0.1/7.9, GHSV=20,000 h^{-1}, 700 °C for 5 h).

For HTNi-Y2.0, the catalytic performance of tri-reforming of methane is presented in Fig. 5.13. There is an interesting evolution of the side reactions for this material. During the first 90 min of the TRM, the CO_2 conversion was higher than CH_4 conversion, indicating that e.g. reverse water-gas shift reaction could have taken place. The latter is thermodynamically favored at high temperature. Moreover, the reverse water-gas shift reaction would consume a part of the H_2 produced by methane reforming and thus lead to more CO, which may be observed in Fig. 5.14. The totally opposite result was registered after 90 min. CH_4 conversion became higher than CO_2 conversion (Fig. 5.13), indicating the change of the selectivity upon tri-reforming. This can be explained by oxidation of either methane, or carbonaceous deposits. The former seems to be more probable, considering that the CH_4 conversion decreased in the same time as CO_2 conversion increased. Moreover, additional carbon monoxide was produced, and the H_2/CO molar ratio decreased (Fig. 5.14). This shows the possible total oxidation of

methane as the side reaction, in which CO_2 and H_2O are produced. These products seem to influence the subsequent carbon monoxide production.

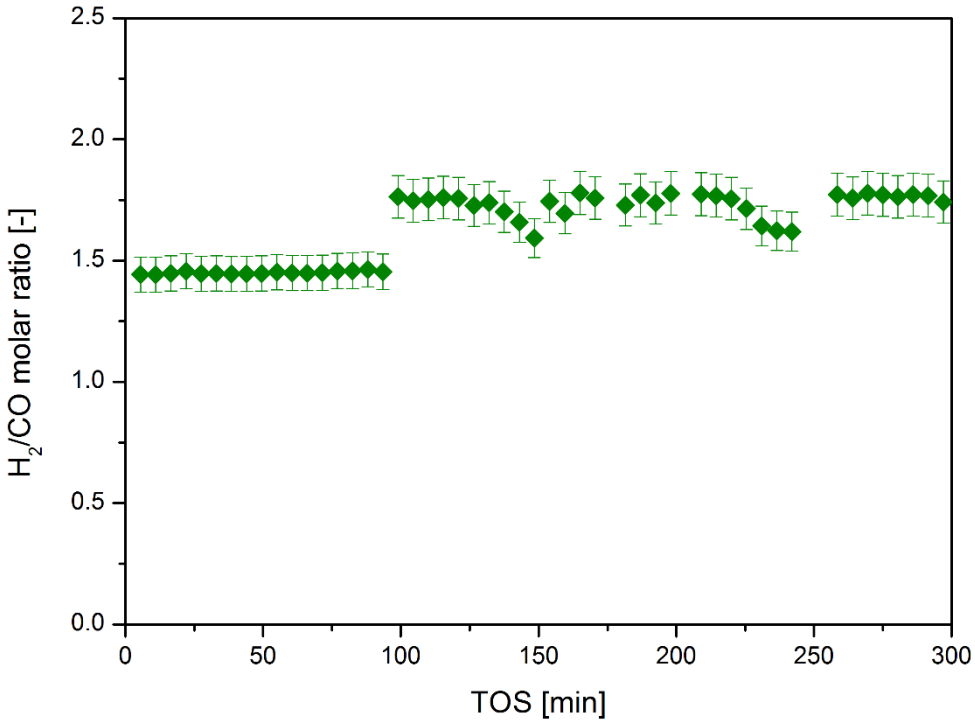

Fig. 5.14 H_2/CO molar ratio for HTNi-Y2.0 catalyst recorded in tri-reforming of methane catalytic test. The test conditions: ($CH_4/CO_2/H_2O/O_2$=1/0.5/0.5/0.1/7.9, GHSV=20,000 h^{-1}, 700 °C for 5 h).

5.3.1.2. *Characterization of the spent catalysts*

The formation of carbon deposits is an important issue in reforming processes. One of the advantages of tri-reforming process is believed to be the inhibition of carbon deposition on catalysts surface. The catalysts after isothermal TRM test (700 °C for 5 h) were characterized by XRD and TGA.

XRD diffractograms of the spent catalysts after tri-reforming ($CH_4/CO_2/H_2O/O_2$=1/0.5/0.5/0.1/7.9) are presented in Fig. 5.15. For both materials, reflections of Ni^0 and periclase-mixed oxides were observed, and no reflection of graphitic carbon was recorded. This shows the beneficial effect of TRM gas composition. For both catalysts, the calculated Ni^0 crystallite size was 5 nm.

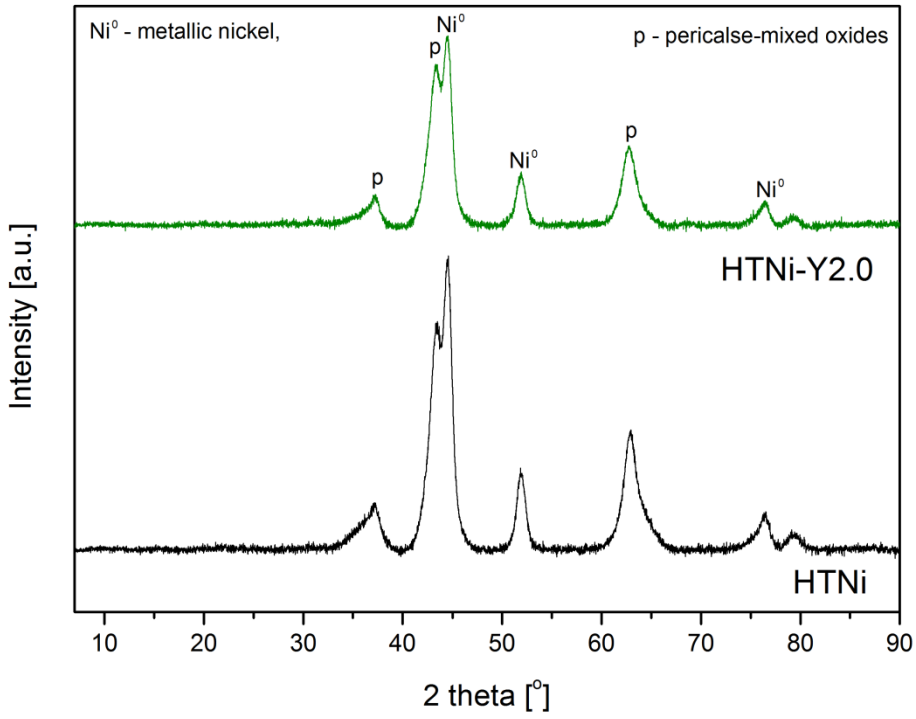

Fig. 5.15 XRD patterns for HTNi and HTNi-Y2.0 spent catalysts after tri-reforming of methane ($CH_4/CO_2/H_2O/O_2$=1/0.5/0.5/0.1/7.9) isothermal tests.

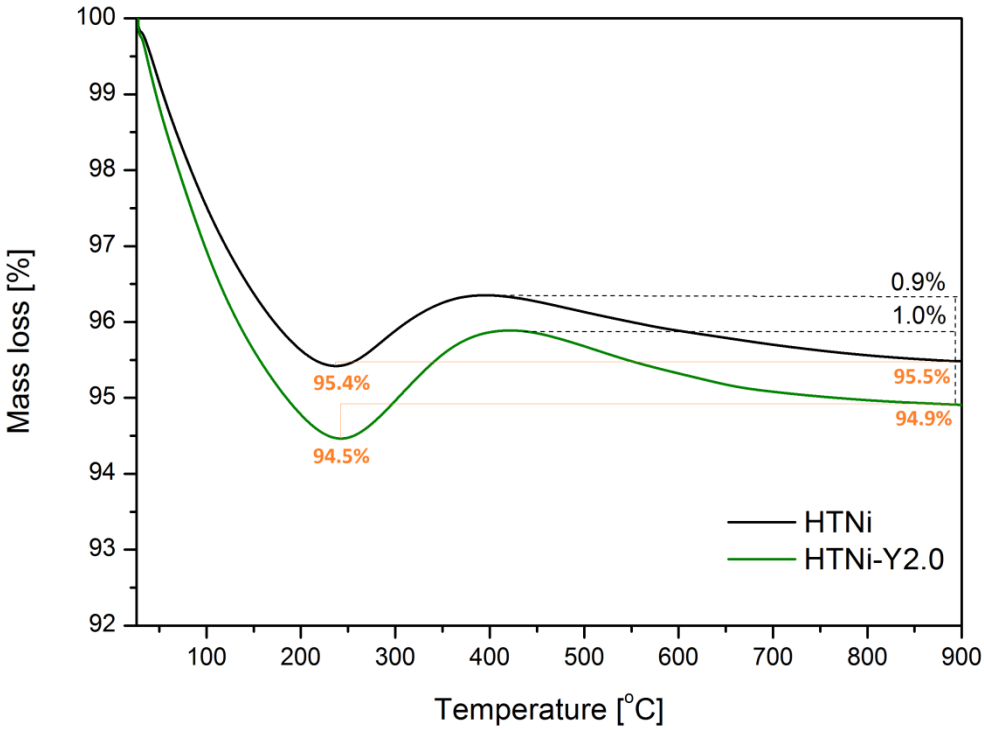

Fig. 5.16 Thermogravimetric analyzes of HTNi and HTNi-Y2.0 spent catalysts after tri-reforming of methane ($CH_4/CO_2/H_2O/O_2$=1/0.5/0.5/0.1/7.9) isothermal tests.

Thermogravimetric analyzes were carried out for HTNi and HTNi-Y2.0 catalysts. Both materials represent a similar trend. First, in the range starting from ambient temperature up to ca. 250 °C the weight decreased to 95.4% and 94.5% of the initial value for, respectively, HTNi and HTNi-Y2.0. As discussed in previous **Subchapters** (**4.1.**, **4.2.**, **4.3.**, **4.4.**), this decline arises from the moisture removal and possibly from the oxidation of amorphous carbon, as suggested by Han et al. [359]. The former is obvious, as steam was a reagent in TRM process. In the next temperature region of 250-450 °C the weight increase was registered, which originates from oxidation of metallic nickel to nickel oxide [191]. Over 450 °C the mass for both catalysts slightly declined, showing mass loss of 0.9% and 1.0% for HTNi and HTNi-Y2.0, respectively. This proves much lower content of carbon deposits than for DRM and, in connection with XRD results, also the presence of non-graphitic type, which would in consequence be easier to remove during regeneration.

5.3.2. *Gas composition of flue gases from natural-gas-fired power station ($CH_4/CO_2/H_2O/O_2/Ar$ = 3/1/2/0.3/3.7)*

5.3.2.1. *Catalytic tests*

CH_4 and CO_2 conversions for HTNi catalyst in an isothermal test at 700 °C are presented in Fig. 5.17. Though some fluctuations are observed, the obtained values of CO_2 conversion remained fairly stable, while a small decrease of CH_4 conversion was registered. CO_2 conversion was always higher than that of CH_4. Possibly one of the reactions resulting in the formation of additional CO_2 was inhibited in the TRM tests over hydrotalcite-derived catalysts. However, further studies are necessary to confirm this hypothesis.

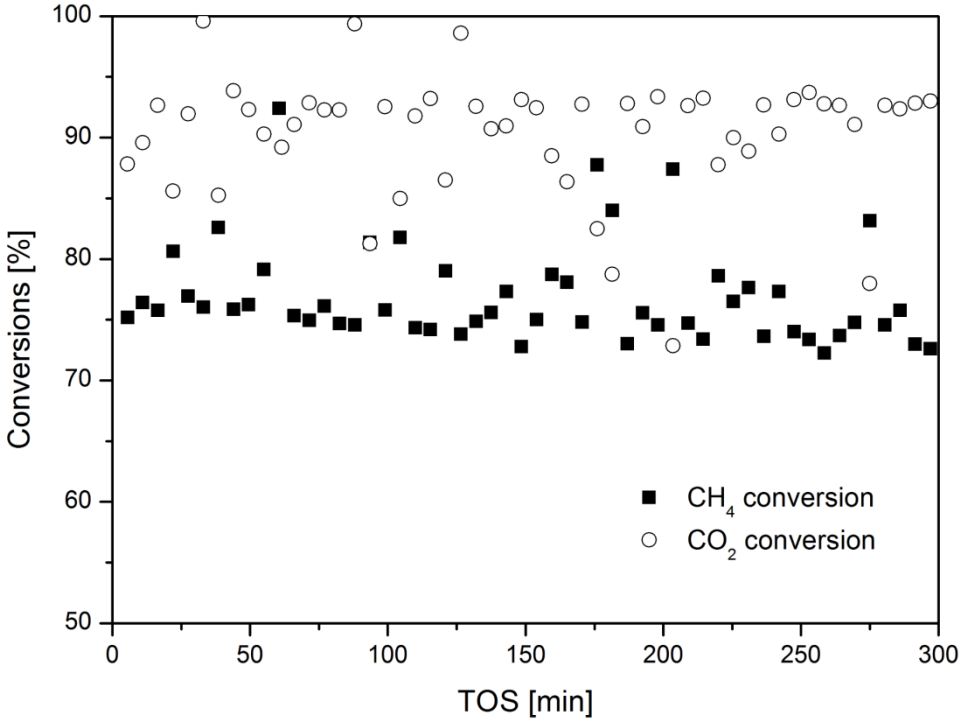

Fig. 5.17 CH_4 and CO_2 conversion for HTNi catalyst recorded in tri-reforming of methane catalytic test. The test conditions: ($CH_4/CO_2/H_2O/O_2$=3/1/2/0.3/3.7, GHSV=20,000 h^{-1}, 700 °C for 5 h).

The H_2/CO molar ratio is shown in Fig. 5.18. The gradually decreasing values were recorded over the time of the measurement, with initial value of 1.7 and 1.5 as the final one after 5 h. This indicates that CO was additionally produced during this TRM test. The enhanced conversion of CO_2 and extra production of CO may also suggest significant increase of reverse-water gas shift ($CO_2+H_2=CO+H_2O$) during TRM. Izquierdo-Colorado et al. [397] observed that, under the catalytic conditions of $CH_4/CO_2/O_2/Ar$ = 2.5/1/0.5/6, the intrinsic properties of the hydrotalcite-derived catalysts favored reverse-water gas shift reaction, leading to the conversion of CO_2 and H_2, the former produced from the complete combustion of methane and the latter arising from methane decomposition, respectively.

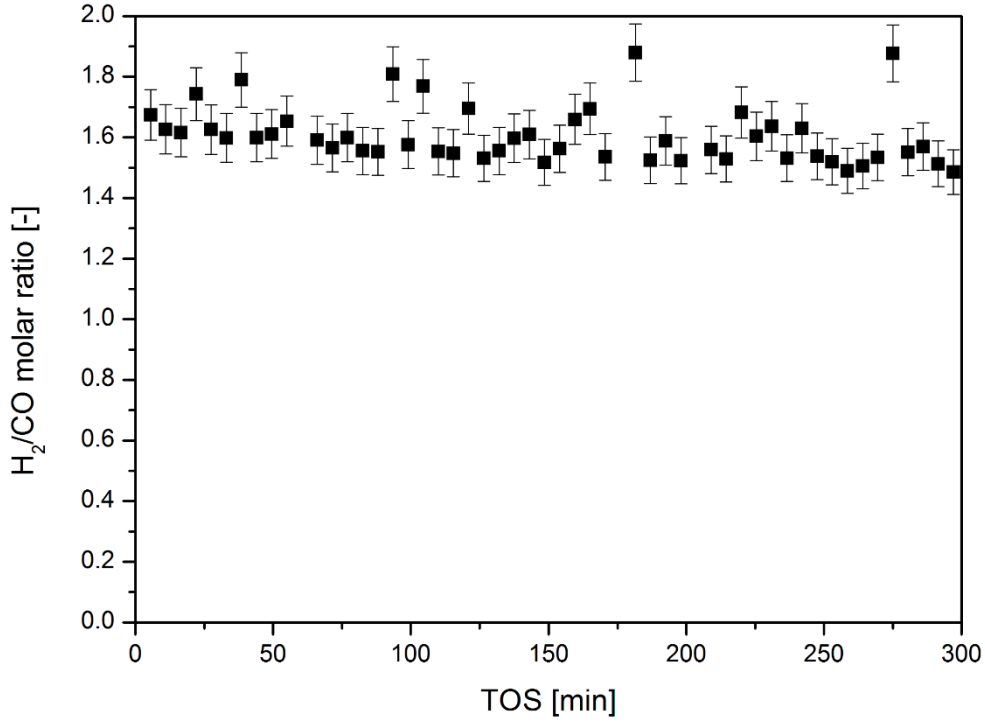

Fig. 5.18 H_2/CO molar ratio for HTNi catalyst recorded in tri-reforming of methane catalytic test. The test conditions: ($CH_4/CO_2/H_2O/O_2$=3/1/2/0.3/3.7, GHSV=20,000 h^{-1}, 700 °C for 5 h).

Catalytic behavior of HTNi-Y2.0 in the tri-reforming of methane is presented in Fig. 5.19. Similarly, as for HTNi catalyst, the CO_2 conversion was higher than that of CH_4. The latter remained more stable than in case of HTNi. The increase in the stability of the Y-containing catalyst may be related to the enhanced Ni^0 dispersion in HTNi-Y2.0 catalyst (as described in **Subchapter 4.1.** it was 19.8% for HTNi-Y2.0 and 8.9% for HTNi). Again, CO_2-converting side reactions had a major contribution to the overall process of TRM. Average values of H_2/CO molar ratio were constant for HTNi-Y2.0 (Fig. 5.20) and presented lower fluctuations, in contrast to those registered for HTNi. The average value of the H_2/CO molar ratio for HTNi-Y2.0 was 1.65.

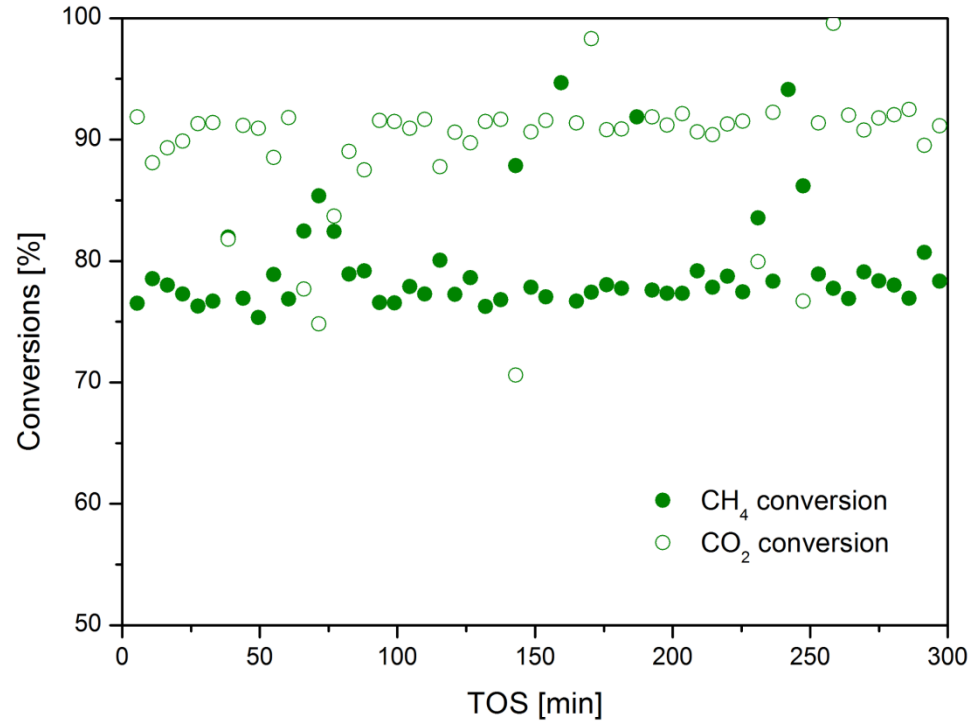

Fig. 5.19 CH_4 and CO_2 conversions for HTNi-Y2.0 catalyst recorded in tri-reforming of methane catalytic test. The test conditions: ($CH_4/CO_2/H_2O/O_2$=3/1/2/0.3/3.7, GHSV=20,000 h^{-1}, 700 °C for 5 h).

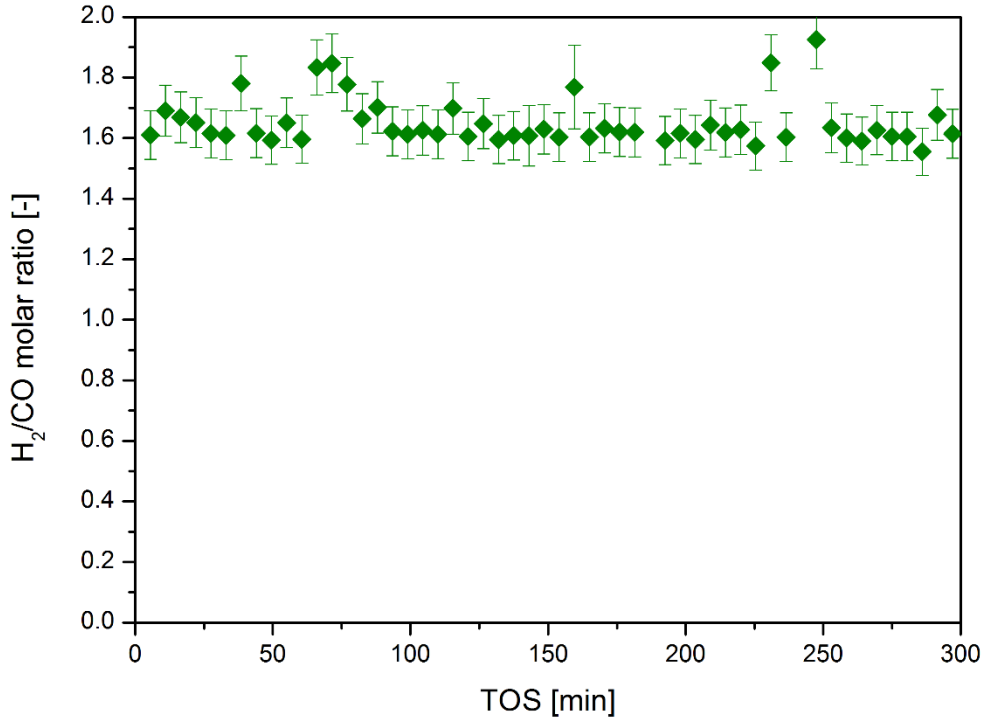

Fig. 5.20 H_2/CO molar ratio for HTNi catalyst recorded in tri-reforming of methane catalytic test. The test conditions: ($CH_4/CO_2/H_2O/O_2$=3/1/2/0.3/3.7, GHSV=20,000 h^{-1}, 700 °C for 5 h).

5.3.2.2. *Characterization of the spent catalysts*

Similarly, as for the TRM process described in **Section 5.3.1.2.,** XRD and TGA were performed for the catalysts after tri-reforming of methane described in this **Subchapter** (under conditions: $CH_4/CO_2/H_2O/O_2$=3/1/2/0.3/3.7).

XRD diffractograms for the materials after TRM catalytic tests are presented in Fig. 5.21. HTNi revealed the presence of metallic Ni, periclase-mixed oxides and graphitic carbon, while HTNi-Y2.0 showed complete transformation of mixed oxides into layered hydrotalcite structure ("H" reflections). Metallic nickel and graphitic coke were also observed after promotion with yttrium. This shows that yttrium led to the reconstruction of the support, as the consequence of the memory effect of double-layered hydroxides, despite a fairly high temperature of the studied process [338]. The metallic Ni did not oxidize to NiO for both HTNi and HTNi-Y2.0, and the Ni^0 crystallite sizes were 8 nm for unmodified material, and 6 nm for the one modified with yttrium.

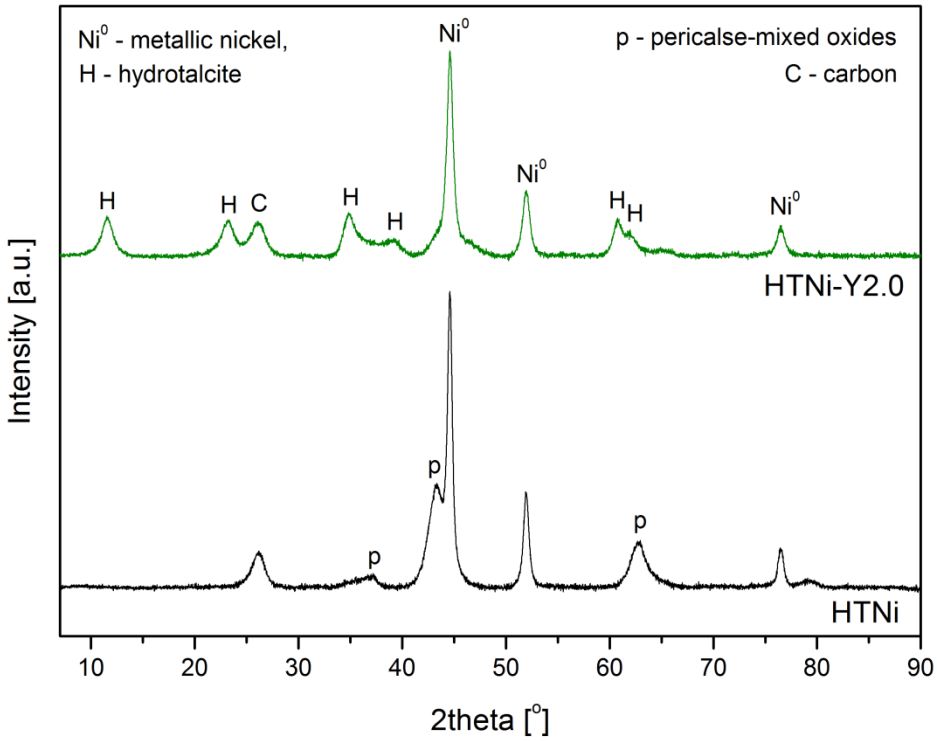

Fig. 5.21 XRD patterns recorded for HTNi and HTNi-Y2.0 spent catalysts after tri-reforming of methane ($CH_4/CO_2/H_2O/O_2$=3/1/2/0.3/3.7) isothermal tests.

TGA results are presented in Fig. 5.22. The profile obtained for HTNi is similar to that recorded for the spent catalyst after dry reforming of methane. The recorded mass loss is, however, lower for the sample after TRM, i.e., 17.3%, than after DRM, i.e., 20.0%.

The HTNi-Y2.0 sample showed thermal decomposition typical of double-layered hydroxides. As described by Tsyganok et al. [190,191], first region of mass decrease arises from the removal of physically sorbed water, whereas desorption of structural water requires higher temperature of ca. 190 °C. The third region of decrease is mostly assigned to the removal of amorphous carbon. The weight decrease observed at temperatures higher than 400 °C arises from oxidation of different form of carbonaceous species.

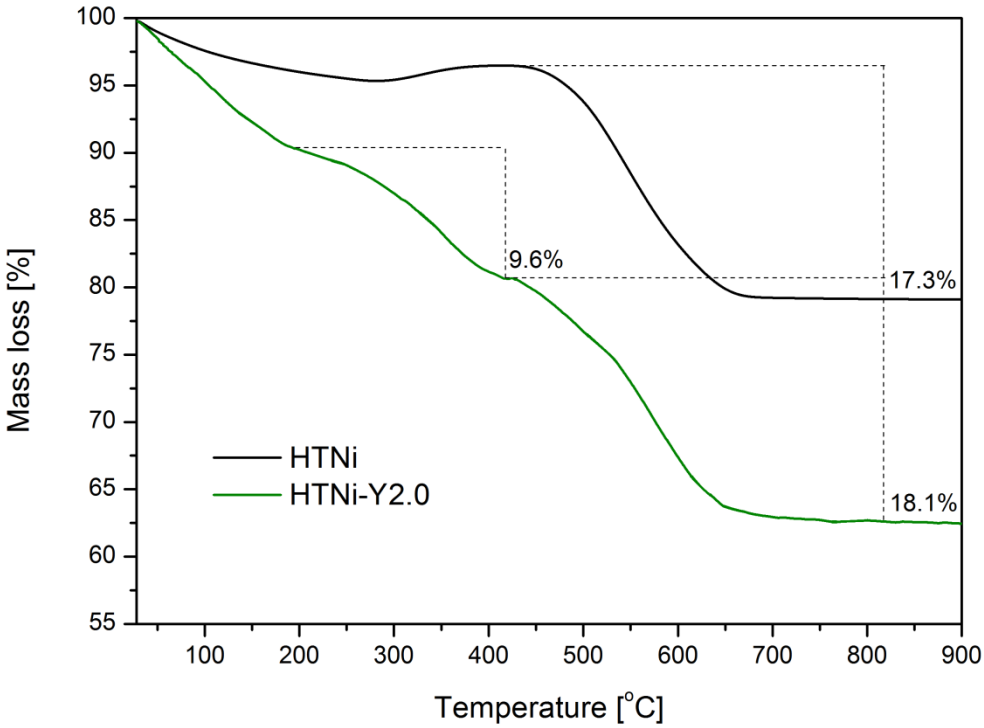

Fig. 5.22 Thermogravimetric analyzes of HTNi and HTNi-Y2.0 spent catalysts after tri-reforming of methane ($CH_4/CO_2/H_2O/O_2$=3/1/2/0.3/3.7) isothermal tests.

5.4. The comparison of HTNi and HTNi-Y2.0 catalysts in DRM, POM, CRPOM and TRM

Table 5.1 summarizes the obtained results, in comparison with the data registered for dry reforming of methane (**Subchapter 4.1.**).

Table 5.1. Average CH_4 and CO_2 conversions and H_2/CO molar ratio for DRM, POM, CRPOM and TRM processes for HTNi and HTNi-Y2.0 catalysts in the isothermal tests at 700 °C, GHSV 20,000 h^{-1}.

Catalyst	Catalytic performance	DRM	POM	CRPOM*	TRM	TRM
		CH_4/CO_2 = 1/1	CH_4/O_2 = 1/0.5	$CH_4/CO_2/O_2$ = 1/1/0.5	$CH_4/CO_2/H_2O/O_2$= 1/0.5/0.5/0.1	$CH_4/CO_2/H_2O/O_2$ = 3/1/2/0.3
HTNi	CH_4 conversion [%]	73.2	87.4	94.8	98.2	75.9
	CO_2 conversion [%]	75.0	-	40.5	69.3	90.8
	H_2/CO molar ratio	0.90	2.0	1.12	1.97	1.59
HTNi-Y2.0	CH_4 conversion [%]	74.2	93.1	96.3	91.9	78.4
	CO_2 conversion [%]	84.8	-	37.3	85.1	89.8
	H_2/CO molar ratio	0.92	2.0	1.12	1.63	1.65

* at 700 °C for 30 min in TPSR test

The tested catalysts were active in partial oxidation of methane (POM) at 700 °C. The obtained molar ratio of H_2/CO was 2.0, which is the stoichiometric value for the POM reaction. The conversion of oxygen was 100%.

The results of the partial oxidation combined with dry reforming of methane (CRPOM) proved that the addition of oxygen to the DRM results in a significant increase of CH_4 conversion, which is higher than either in dry reforming or partial oxidation. This may be ascribed to the presence of two strong oxidants in CRPOM, CO_2 and O_2. The CO_2 conversion, however, is lower than that of CH_4. It is also much lower than CO_2 conversion in dry reforming. Other carbon dioxide forming reactions may have contributed to this effect. For both catalysts, the obtained H_2/CO molar ratio was 1.12. In CRPOM, oxygen was totally converted.

Decreasing the amount of CO_2 and O_2 in the feed, together with the addition of H_2O ($CH_4/CO_2/H_2O/O_2$= 1/0.5/0.5/0.1), resulted in the enhanced CO_2 conversion and H_2/CO molar ratio. The improvement in the CO_2 conversion may be either due to enhanced selectivity of side reactions leading to the extra conversion of CO_2, or the inhibition of CO_2 forming reactions (e.g. total oxidation of methane). In case of gas composition of $CH_4/CO_2/H_2O/O_2$ = 3/1/2/0.3 with increased content of CH_4, H_2O and O_2 in comparison to CO_2, it had a more pronounced effect on CO_2 conversion. The CH_4 conversion decreased, as the added amount of this gas was too high to be totally converted. For both

tested catalysts the reached molar ratio of the TRM products was close to 1.6. Under the conditions of both tests of tri-reforming of methane, oxygen was converted in 100%.

Table 5.2 The comparison of selected data concerning carbon deposits for the spent HTNi and HTNi-Y2.0 catalysts after DRM, CRPOM and TRM in isothermal tests at 700 °C, GHSV 20,000 h^{-1}.

Catalyst	Presence of carbon deposits (based on XRD or TGA)	DRM	CRPOM*	TRM	TRM
		CH_4/CO_2 = 1/1	$CH_4/CO_2/O_2$ = 1/1/0.5	$CH_4/CO_2/H_2O/O_2$= 1/0.5/0.5/0.1	$CH_4/CO_2/H_2O/O_2$ = 3/1/2/0.3
HTNi	**XRD** Presence of graphitic carbon reflection	+	-	-	+
	TGA Amount (%) and temperature range of oxidation	20.0% 400 – 720 °C	n.m.	0.9% 400 – 900 °C	17.3% 450 – 700 °C
	Type of carbon	Graphite-like carbon + filamentous carbon + amorphous carbon	No carbon or traces of amorphous carbon**	No carbon or traces of amorphous carbon	Graphite-like carbon + filamentous carbon + amorphous carbon
HTNi-Y2.0	**XRD** Presence of graphitic carbon reflection	+	-	-	+
	TGA Amount (%) and temperature range of oxidation	16.7% 400 – 650 °C	n.m	1.0% 450 – 900 °C	18.1% 400 – 680 °C
	Type of carbon	Graphite-like carbon + filamentous carbon + amorphous carbon	No carbon or traces of amorphous carbon**	No carbon or traces of amorphous carbon	Graphite-like carbon + filamentous carbon + amorphous carbon

* after TPSR test in the temperature range of 850-600 °C
** only XRD information
n.m. – not measured
"+" indicates presence of graphite reflections, "-" carbon not detected (XRD measurements)

Table 5.2 compares the experimental information on carbon deposits which is important for the discussion of the stability of the tested materials. During dry reforming of methane considerable amount of catalytic coke was formed, as supported by XRD and TGA characterization methods. Graphite-like carbon, filamentous and amorphous carbon were registered. Promotion with yttrium had a beneficial effect, confirmed by lower amount of carbon deposits (16.7% versus 20.0% for HTNi). The combination of dry reforming of methane with partial oxidation (CRPOM) resulted in the improved stability, as no graphitic carbon reflection was found in XRD. This is ascribed to the oxygen presence in the feed. The addition of steam and oxygen, $CH_4/CO_2/H_2O/O_2$= 1/0.5/0.5/0.1, positively influenced the catalytic stability as compared to DRM. Considerably lower amount of carbon deposition observed in spent HTNi and HTNi-Y2.0 catalysts after TRM than after DRM. This indicates, that the carbon formed by side reactions was oxidized with oxidants such as CO_2, O_2 and H_2O. Nevertheless, the gas composition is crucial for determining the stable behavior of the catalysts, as proven by the different amount of carbon deposits for the mixtures with the composition of $CH_4/CO_2/H_2O/O_2$=1/0.5/0.5/0.1 (the ratios CO_2/H_2O=1, O_2/CH_4=0.1 and $(CO_2+H_2O+O_2)/CH_4$=1.1) and that of $CH_4/CO_2/H_2O/O_2$=3/1/2/0.3 (with the ratios CO_2/H_2O=0.5, O_2/CH_4=0.1 and $(CO_2+H_2O+O_2)/CH_4$=1.1). For the latter mixture considerable amount of carbonaceous species were deposited on the surface, as presented in the Table 5.2. For both tested catalysts, amorphous, filamentous and graphitic types of carbons were found. Higher amount of coke (%) was observed for HTNi-Y2.0 (18.1%), however its oxidation took place at lower temperature range (400-680 °C) as compared to the unmodified material (17.3%, 450-700 °C).

5.5. Conclusions

In this chapter, HTNi and HTNi-Y2.0 double-layered hydroxides were examined in partial oxidation of methane, partial oxidation combined with dry reforming of methane, and tri-reforming of methane.

The partial oxidation of methane was feasible on both HTNi and HTNi-Y2.0 catalysts. The obtained CH_4 conversions were high, and the ratio of products was equal 2.0, which is appropriate for Fischer-

Tropsch process with a cobalt based catalyst, requiring synthesis gas ratio (H_2:CO) of 2:1 [104], as well as for methanol synthesis [404]. At lower tested temperatures (650-600 °C), the parallel reactions took place, which resulted in production of additional amounts of CO_2. At higher temperatures (over 700 °C) the amount of CO_2 in the products decreased, possibly due to the consecutive reactions consuming carbon dioxide (dry reforming and/or steam reforming). This is in agreement with the mechanism of POM proposed by Prettre et al. [130].

The test of partial oxidation of methane in the presence of carbon dioxide (CRPOM) showed good catalytic performance of both HTNi and HTNi-Y2.0 catalysts. The methane conversion in combined reforming was higher than that observed in either dry reforming or partial oxidation. However, the CO_2 conversion was lower due to the presence of side reactions. HTNi and HTNi-Y2.0 showed a high potential to produce syngas (H_2-CO) with hydrogen-to-carbon monoxide ratio slightly above unity, i.e., 1.12. The addition of oxygen considerably decreased the catalyst deactivation caused by carbon formation, as evidenced by the absence of graphite reflection in XRD patterns.

Tri-reforming of methane experimental tests ($CH_4/CO_2/H_2O/O_2$=1/0.5/0.5/0.1/7.9) for HTNi and HTNi-Y2.0 showed good catalytic performance under the used conditions. HTNi resulted in H_2/CO ratio of ca. 2.0 which is suitable for F-T process over Co-based catalysts [104], and methanol production [404]. On the other hand, HTNi-Y2.0 showed lower ratio, in the range of 1.45-1.75, and could be used in e.g. DME production. The latter requires H_2/CO=1.2-1.5 [81]. However, considerable fluctuations in CO_2 conversion were observed, especially for HTNi. No sintering of Ni was observed. The enhanced stability was also proved by the inhibition of carbon formation in comparison to the catalytic behavior observed for dry reforming of methane.

The higher content of CH_4, H_2O and O_2 in the feed gas composition of tri-reforming of methane ($CH_4/CO_2/H_2O/O_2$=3/1/2/0.3/3.7) led to the enhanced CO_2 conversion and decreased CH_4 conversion as compared to the results for the first analyzed gas system. The CH_4 could not be completely converted due to low ratio of CO_2/H_2O=0.5. Possibly DRM and SRM processes compete. Carbon formation took place, probably as a consequence of CH_4 decomposition. The presence of graphitic

carbon was confirmed by XRD and TGA analyzes. However, it should be mentioned that structural stability of Y-promoted catalyst was negatively influenced, as evidenced by the transformation of periclase-like structure during reaction into the layered structure of hydrotalcites. The latter was not registered for HTNi sample.

General conclusions

The presented doctoral thesis was focused on the application of double-layered hydroxide catalysts for reforming of methane processes, which belong to the chemical CO_2 utilization methods. The literature review concerning utilization of carbon dioxide was presented in **Chapter 1**, and showed that DRM, CRPOM and TRM may become important industrial processes for synthesis gas production. The commercialization of these processes is, however, limited until a low-cost, active and stable catalyst is offered to industry.

Supported noble metal catalysts (Rh, Ru, Ir, Pt and Pd) show efficient catalytic performance and low sensitivity to carbon deposits, but their high price and low availability prevent their industrial application in contrast to Ni-based catalysts. The latter represent a promising alternative. However, the main drawback of their application is fast deactivation caused by coke formation, sintering of active phase and metal oxidation. The deactivation may be limited by a possible improvement of the physical properties, e.g. the formation of Ni particle size smaller than 10 nm, high dispersion of the metal species as well as proper basicity which will allow to adsorb CO_2. Thus, finding a highly active, selective and stable catalyst remains a serious problem for industrialization of reforming processes, and the design of a novel catalyst is still a challenge. The choice of proper support may contribute to an improvement. Synthetic double-layered hydroxides (DLHs), show good properties as precursors due to their double layered and homogeneous structure with appropriate basic properties and the presence of Mg^{2+} and Al^{3+} introduced by co-precipitation method. These cations may by partly substituted by ions of a promoter, in order to improve properties of the material. The presented studies focused on Ni/Mg/Al double-layered hydroxides into which yttrium, and zirconia or ceria was added.

The prepared catalysts were characterized by XRD (for structural parameters and identification of the crystalline phases), XRF (elemental composition), low temperature N_2 sorption (evaluation of textural properties), TPR-H_2 (reducibility of Ni species), TPD-CO_2 (evaluation of basicity), H_2

chemisorption (dispersion of Ni species), transmission electron microscopy and high-resolution microscopy with EDS (evaluation of the formed carbon and identification of formed phases), thermogravimetric analysis coupled with mass spectroscopy (quantity and type of formed carbon) and Raman spectroscopy (type and graphitization of formed carbon deposits).

The results and discussion concerned the four following topics: (i) co-precipitation of yttrium in Ni-DLHs in DRM, (ii) effect of zirconia and yttrium introduction on Ni-DLHs in DRM, (iii) effect of cerium co-precipitation and yttrium impregnation in Ni-DLHs in DRM, (iv) influence of yttrium promotion on POM, CRPOM and TRM catalytic performance.

Physico-chemical properties of the obtained DRM catalysts promoted with Y, as well as their DRM performance, strongly depended on both the amount of introduced Y, as well as the method of its introduction and the presence of a co-promoter. The catalytic performance was, as a consequence, influenced. In more detail, the following trends were registered.

Yttrium could be introduced into the structure of double-layered Ni/Mg/Al hydroxides when added at the co-precipitation stage and for loadings of yttrium in the range of 0.2-2.0 wt.%. The addition of 3.0 wt.% Y resulted in a partial deposition of this metal on the surface. After modification with 0.2 to 2.0 wt.% yttrium the total basicity decreased, whereas the promotion with 3 wt.% led to a significant increase in the total number of basic sites. Finally, the highest specific surface area and Ni^0 dispersion were found for the sample promoted with 2 wt.% Y.

In DRM, the highest catalytic activity in CH_4 and CO_2 conversion was found for the HTNi-Y3.0 catalyst, with average 85% for CH_4, and 89% for CO_2, which could be attributed to the enhanced number of total basic sites. However, the most stable behavior was observed for HTNi-Y2.0 sample with average 74% for CH_4, and 78% for CO_2 at 700 °C for 5 h.

In the case of both Y and Zr promotion, it was clearly evidenced that the co-impregnation with Zr and Y leads to the formation of yttrium stabilized zirconia (YSZ) phase located on the surface of the double-layered hydroxide. On the contrary, co-precipitation with zirconia and impregnation with yttrium did not result in YSZ phase formation. ZrO_2 was partially introduced within the periclase-like

structure, whereas yttrium was located on the surface leading to its partial blockage. This led to the decreased dispersion of metal active sites and slightly decreased Ni crystallite size.

For both promotion techniques, the percentage of medium basic sites was increasing with the increasing yttrium loading.

These two series were compared to the catalyst co-precipitated together with Zr (assumed 5 wt.%) and Y (0.4 wt.%). The incorporation of these two metals inside the structure led to the extended number of total basic sites, increased Ni dispersion and increased reducibility. This influenced DRM performance in a positive way, since, among all the Zr- and Y-promoted materials, this one showed the highest activity in CH_4 and CO_2. Moreover, the catalyst modified with Zr and Y (0.4 wt.%) presented structural resistance to the products of the RWGS side reaction, as supported by the absence of hydrotalcite reflections in the XRD patterns of the spent catalyst.

Co-promotion with Ce and Y resulted in a decrease of reducibility of Ni, an increase of the basicity, enhanced Ni dispersion and smaller Ni crystallite size as compared to the HTNi catalyst. The highest catalytic performance in DRM was evidenced for HTNi-Ce, where CH_4 conversion was 86%, CO_2 conversion of 88% and H_2/CO molar ratio of ca. 0.97. For Ce and 0.4 wt.% Y-promoted sample the amount of carbon was higher, but less graphitic as compared to the only-Ce-modified material. No deactivation was observed during the isothermal test at 700 °C for 5 hours.

Based on the results in DRM, two catalysts were tested in oxidative reforming reactions.

For the yttrium promoted catalyst (HTNi-Y2.0) a good catalytic performance in partial oxidation of methane, with a high CH_4 conversion of 93% and the desired ratio of H_2/CO of ca. 2.0, were obtained. The combined partial oxidation of methane with dry reforming of methane (CRPOM) led to the increased CH_4 conversion, as compared to the POM, whereas CO_2 conversion decreased significantly due to the other parallelly occurring reactions. The addition of oxygen to the feed of dry reforming of methane, considerably contributed to the removal of carbon deposits, as confirmed by the absence of graphitic carbon reflection in XRD patterns for the spent material.

Two gas feed compositions were used in TRM reaction. The tri-reforming of methane composition of $CH_4/CO_2/H_2O/O_2$=1/0.5/0.5/0.1 led to an improved CO_2 conversion, as compared to CRPOM, and increased H_2/CO molar ratio. The tested material was stable, and only traces of carbon could be observed in TGA analysis. No reflection of graphitic carbon was recorded in XRD.

On the contrary, the composition of $CH_4/CO_2/H_2O/O_2$= 3/1/2/0.3 tri-reforming of methane presented lower CH_4 conversion (in contrast to the first gas composition) but similar H_2/CO molar ratio. The presence of carbon was confirmed by XRD and TGA analyzes, where reflection of graphitic carbon was observed, as well as significant mass loss was registered in TGA. The HTNi-Y2.0 underwent the complete transformation of the periclase-like structure into hydrotalcites.

Some of the future recommendations can be given, considering the promising data on double-layered hydroxides in the dry reforming of methane and oxidative reforming reactions. Firstly, different yttrium introduction methods may be suggested, e.g. wet impregnation with a solution of yttrium nitrate, adsorption from $Y[EDTA]^-$ solution or co-precipitation with $Y[EDTA]^-$. Moreover, some improvements of the preparation conditions should be studied, such as e.g. the influence of different calcination conditions (mainly temperature) on structural stability of hydrotalcites, as well as the size of Ni crystallites. The former is based on the fact that e.g. HTNi-ZrY0.4 catalyst which presented very good catalytic performance in DRM, but it did not show the complete transformation upon the calcination of layered structure into mixed oxides. The latter is of primary importance, as DRM is a structure sensitive reaction and inappropriate Ni crystallite size leads to unrequired methane decomposition resulting in formation of carbon deposits.

The formation of carbon deposit is one of the main problems that may be faced when the process would be introduced on industrial scale. Thus, catalyst regeneration should be studied to prolong the useful life of the catalysts. One of the possibilities, including additional application of carbon dioxide, could be utilizing it for the regeneration step. Then, gasification of carbonaceous deposits via reverse Boudouard reaction could be expected.

Currently, tri-reforming of methane is the most promising process among the studied reforming reactions, considering the net energy used and inhibition of catalyst deactivation. However, as it was shown in this thesis, the proper conditions such as temperature and gas composition are crucial for fulfilling the TRM advantageous aspects. It was clearly shown that when molar ratio of CO_2/H_2O was equal 0.5 in the gas feed, the tested catalysts were suffering from the carbon formation. It would be thus recommended to test other compositions of TRM mixture to reduce the negative effects on the lifetime of the catalysts. Moreover, more catalysts (studied only in dry reforming of methane) should be tested in the oxidative reforming reactions, for example HTNi-Y0.4, HTNi-ZrY0.4, HTNi-Zr/Y0.4, HTNi-Ce/0.2 or HTNi-Ce/Y0.4.

References

[1] G.R. North, Climate and climate change: Greenhouse effect, Second Edi, Elsevier, 2014. doi:10.1016/B978-0-12-382225-3.00470-9.

[2] Intergovernmental Panel on Climate Change, Climate Change 2014 Mitigation of Climate Change, 2014. doi:10.1017/CBO9781107415416.

[3] Eurostat news release, 2018. https://ec.europa.eu/eurostat/documents/2995521/8869789/8-04052018-BP-EN.pdf/e7891594-5ee1-4cb0-a530-c4a631efec19.

[4] Eurostat news release, 2017. http://ec.europa.eu/eurostat/documents/2995521/8010076/8-04052017-BP-EN.pdf/7b7462ca-7c53-44a5-bafb-23cc68580c03.

[5] Eurostat news release, 2016. http://ec.europa.eu/eurostat/documents/2995521/7244707/8-03052016-BP-EN.pdf/88e97313-dab3-4024-a035-93b2ab471cd9.

[6] Eurostat news release, 2015. https://ec.europa.eu/eurostat/documents/2995521/6875491/8-15062015-BP-EN.pdf/8adf74de-e79b-4778-905f-823c42c6e1b1.

[7] Eurostat news release, 2014. https://ec.europa.eu/eurostat/documents/2995521/5176346/8-07052014-AP-EN.PDF/318b117b-2065-4a61-9efb-c382f901a8ea.

[8] Eurostat news release, 2013. https://ec.europa.eu/eurostat/documents/2995521/5166066/8-29052013-AP-EN.PDF/38dda41b-d760-4909-b8bd-77e651c401a3?version=1.0.

[9] BP Statistical Review of World Energy 2018 67th edition Renewable energy, (n.d.). https://www.bp.com/content/dam/bp/en/corporate/pdf/energy-economics/statistical-review/bp-stats-review-2018-full-report.pdf.

[10] S.C. Peter, Reduction of CO_2 to chemicals and fuels: A solution to global warming and energy crisis, ACS Energy Lett. 3 (2018) 1557–1561. doi:10.1021/acsenergylett.8b00878.

[11] Untited Nations, Kyoto Protocol To the United Nations Framework Convention on Climate Change, 1998. doi:10.1111/1467-9388.00150.

[12] T.M.L. Wigley, The Kyoto Protocol: CO_2, CH_4 and climate implications, 25 (1998) 2285–2288.

[13] A. Ghezloun, A. Saidane, H. Merabet, The COP22 new commitments in support of the Paris Agreement, Energy Procedia. 119 (2017) 10–16. doi:10.1016/j.egypro.2017.07.040.

[14] G. Corsi, COP23 : A critical assessment of the Conference's outcomes, (2018). http://climate.org/cop23-a-critical-assessment-of-the-conferences-outcomes/

[15] COP24 in Katowice: Main outcomes, © GKToday. (2018). https://currentaffairs.gktoday.in/cop24-katowice-main-outcomes-12201863429.html.

[16] European Commission, Communication from the commission to the European Parliament, the Council, the European Economic and Social Committee and the Committee of the Regions. A Roadmap for moving to a competitive low carbon economy in 2050, 2011.

[17] T. Pieri, A. Nikitas, A. Castillo-Castillo, A. Angelis-Dimakis, Holistic Assessment of Carbon Capture and Utilization Value Chains, Environments. 5 (2018) 1–17. doi:10.3390/environments5100108.

[18] M. Bui, C.S. Adjiman, E.J. Anthony, A. Boston, S. Brown, P.S. Fennell, S. Fuss, A. Galindo, L.A. Hackett, J.P. Hallett, H.J. Herzog, G. Jackson, J. Kemper, S. Krevor, G.C. Maitland, M. Matuszewski, I.S. Metcalfe, C. Petit, G. Puxty, J. Reimer, D.M. Reiner, E.S. Rubin, S.A. Scott, N. Shah, B. Smit, J.P.M. Trusler, P. Webley, Carbon capture and storage (CCS): the way forward, Energy Environ. Sci. 11 (2018) 1062–1176. doi:10.1039/c7ee02342a.

[19] J. Gibbins, H. Chalmers, Carbon capture and storage, Carbon N. Y. 36 (2006) 4317–4322. doi:10.1016/j.enpol.2008.09.058.

[20] J.C.M. Pires, F.G. Martins, M.C.M. Alvim-Ferraz, M. Simões, Recent developments on carbon capture and storage: An overview, Chem. Eng. Res. Des. 89 (2011) 1446–1460. doi:10.1016/j.cherd.2011.01.028.

[21] H. Yu, Recent developments in aqueous ammonia-based post-combustion CO_2 capture technologies, Chinese J. Chem. Eng. (2018) 1–11. doi:10.1016/j.cjche.2018.05.024.

[22] D. Jansen, M. Gazzani, G. Manzolini, E. Van Dijk, M. Carbo, Pre-combustion CO_2 capture, Int. J. Greenh. Gas Control. 40 (2015) 167–187. doi:10.1016/j.ijggc.2015.05.028.

[23] E. Blomen, C. Hendriks, F. Neele, Capture technologies: Improvements and promising developments, Energy Procedia. 1 (2009) 1505–1512. doi:10.1016/j.egypro.2009.01.197.
[24] G. Scheffknecht, L. Al-Makhadmeh, U. Schnell, J. Maier, Oxy-fuel coal combustion-A review of the current state-of-the-art, Int. J. Greenh. Gas Control. 5 (2011) 16–35. doi:10.1016/j.ijggc.2011.05.020.
[25] K.E. Zanganeh, A. Shafeen, C. Salvador, CO_2 capture and development of an advanced pilot-scale cryogenic separation and compression unit, Energy Procedia. 1 (2009) 247–252. doi:10.1016/j.egypro.2009.01.035.
[26] Global CCS Institue, The Global Status of CCS, 2012.
[27] M.K. Verma, Fundamentals of Carbon Dioxide-Enhanced Oil Recovery (CO_2-EOR)—A Supporting document of the assessment methodology for hydrocarbon recovery using CO_2-EOR associated with carbon sequestration, U.S. Geol. Surv. (2015) 19. doi:https://dx.doi.org/10.3133/ofr20151071.
[28] A. Mathisen, R. Skagestad, Utilization of CO_2 from Emitters in Poland for CO_2-EOR, Energy Procedia. 114 (2017) 6721–6729. doi:10.1016/j.egypro.2017.03.1802.
[29] L.T. Steel, An investigation of CO_2-brine interactions using North Sea oil well data with respect to geological storage of carbon dioxide and enhanced oil recovery, Herriot Watt University, 2017.
[30] IEA GHG, CO_2 Storage in Depleted Gas Fields, (2009) 121. doi:10.1016/s0956-5663(00)00069-5.
[31] D.Y.C. Leung, G. Caramanna, M.M. Maroto-Valer, An overview of current status of carbon dioxide capture and storage technologies, Renew. Sustain. Energy Rev. 39 (2014) 426–443. doi:10.1016/j.rser.2014.07.093.
[32] E.O. Recovery, C. Capture, Carbon capture and utilization for enhanced oil recovery, (2018). https://stillwaterassociates.com/carbon-capture-and-utilization-for-enhanced-oil-recovery/.
[33] S.S. Platform, Carbon Capture and Utilization, 7 (2014) 130–189. doi:10.1039/c3ee42350f.
[34] U.S. Policy, Carbon dioxide enhanced oil recovery : a critical domestic energy, economic, and environmental opportunity, Policy. (2012).
[35] Element Energy, Economic Impacts of CO_2-enhanced oil recovery for Scotland, (2012) 1–111. http://www.scottish-enterprise.com/~/media/SE/Resources/Documents/DEF/Economic Potential of CO2 EOR in Scotland.pdf.
[36] Y. Shi, Y. Jia, W. Pan, L. Huang, J. Yan, R. Zheng, Potential evaluation on CO_2-EGR in tight and low-permeability reservoirs, Nat. Gas Ind. 37 (2017) 62–69. doi:10.3787/j.issn.1000-0976.2017.03.008.
[37] P.S. Ringrose, D.M. Roberts, C.M. Gibson-Poole, C. Bondc, R. Wightman, M. Taylor, S. Raikes, M. Iding, S. Østmo, Characterisation of the Krechba CO_2 storage site: Critical elements controlling injection performance, Energy Procedia. 4 (2011) 4672–4679. doi:10.1016/j.egypro.2011.02.428.
[38] R. Martínez-García, T. García-Martínez, A. Puig-Pujol, J.C. Mauricio, J. Moreno, Changes in sparkling wine aroma during the second fermentation under CO_2 pressure in sealed bottle, Food Chem. 237 (2017) 1030–1040. doi:10.1016/j.foodchem.2017.06.066.
[39] G.J. Butterworth, P.D. Dowling, Electrostatic effects with portable CO_2 fire extinguishers, 11 (1981) 43–55.
[40] G. Centi, S. Perathoner, Opportunities and prospects in the chemical recycling of carbon dioxide to fuels, Catal. Today. 148 (2009) 191–205. doi:10.1016/j.cattod.2009.07.075.
[41] R. Snoeckx, A. Bogaerts, Plasma technology-a novel solution for CO_2 conversion?, Chem. Soc. Rev. 46 (2017) 5805–5863. doi:10.1039/c6cs00066e.
[42] J. Ma, N. Sun, X. Zhang, N. Zhao, F. Xiao, W. Wei, Y. Sun, A short review of catalysis for CO_2 conversion, Catal. Today. 148 (2009) 221–231. doi:10.1016/j.cattod.2009.08.015.
[43] C. Song, Tri-reforming: A new process concept for effective conversion and utilization of CO_2 in flue gas from electric power plants, ACS Div. Fuel Chem. Prepr. 45 (2000) 772–776.
[44] A.A. Olajire, Valorization of greenhouse carbon dioxide emissions into value-added products

by catalytic processes, J. CO2 Util. 3–4 (2013) 74–92. doi:10.1016/j.jcou.2013.10.004.
[45] W. Li, H. Wang, X. Jiang, J. Zhu, Z. Liu, X. Guo, C. Song, A short review of recent advances in CO_2 hydrogenation to hydrocarbons over heterogeneous catalysts, RSC Adv. 8 (2018) 7651–7669. doi:10.1039/C7RA13546G.
[46] J. Wu, Y. Huang, W. Ye, Y. Li, CO_2 Reduction: From the electrochemical to photochemical approach, Adv. Sci. 4 (2017) 1–29. doi:10.1002/advs.201700194.
[47] Q. Lu, F. Jiao, Electrochemical CO_2 reduction: Electrocatalyst, reaction mechanism, and process engineering, Nano Energy. 29 (2016) 439–456. doi:10.1016/j.nanoen.2016.04.009.
[48] L. Brennan, P. Owende, Biofuels from microalgae-A review of technologies for production, processing, and extractions of biofuels and co-products, Renew. Sustain. Energy Rev. 14 (2010) 557–577. doi:10.1016/j.rser.2009.10.009.
[49] H. Puliyalil, D. Lašič Jurković, V.D.B.C. Dasireddy, B. Likozar, A review of plasma-assisted catalytic conversion of gaseous carbon dioxide and methane into value-added platform chemicals and fuels, RSC Adv. 8 (2018) 27481–27508. doi:10.1039/c8ra03146k.
[50] A. Bogaerts, W. Wang, A. Berthelot, W. Wang, A. Berthelot, S. Kolev, C. De Bie, T. Martens, J. Van Dijk, CO_2 conversion by plasma technology: insights from modeling the plasma chemistry and plasma reactor design, (n.d.).
[51] M. Mikhail, B. Wang, R. Jalain, S. Cavadias, M. Tatoulian, S. Ognier, M.E. Gálvez, P. Da Costa, Plasma-catalytic hybrid process for CO_2 methanation: optimization of operation parameters, React. Kinet. Mech. Catal. 8247 (2018). doi:10.1007/s11144-018-1508-8.
[52] A.A. Olajire, A review of mineral carbonation technology in sequestration of CO_2, J. Pet. Sci. Eng. 109 (2013) 364–392. doi:10.1016/j.petrol.2013.03.013.
[53] M. Bodor, R.M. Santos, T. Van Gerven, M. Vlad, Recent developments and perspectives on the treatment of industrial wastes by mineral carbonation - A review, Cent. Eur. J. Eng. 3 (2013) 566–584. doi:10.2478/s13531-013-0115-8.
[54] R.R. Tamilselvi Dananjayan, P. Kandasamy, R. Andimuthu, Direct mineral carbonation of coal fly ash for CO_2 sequestration, J. Clean. Prod. 112 (2016) 4173–4182. doi:10.1016/j.jclepro.2015.05.145.
[55] C. Siriruang, P. Toochinda, P. Julnipitawong, S. Tangtermsirikul, CO_2 capture using fly ash from coal fired power plant and applications of CO_2-captured fly ash as a mineral admixture for concrete, J. Environ. Manage. 170 (2016) 70–78. doi:10.1016/j.jenvman.2016.01.010.
[56] J.H. Wee, A review on carbon dioxide capture and storage technology using coal fly ash, Appl. Energy. 106 (2013) 143–151. doi:10.1016/j.apenergy.2013.01.062.
[57] M. Taniewski, T. Grzybek, J. Cetnar, Viable CO_2 chemical sequestration applications, in: A. Strugała (Ed.), Dev. Coal, Biomass Wastes Gasif. Technol. with Part. Interes. Chem. Sequestration CO2 A Monogr., AKNET, Kraków, 2012: pp. 99–150.
[58] E. Alper, O. Yuksel Orhan, CO_2 utilization: Developments in conversion processes, Petroleum. 3 (2017) 109–126. doi:10.1016/j.petlm.2016.11.003.
[59] E. Koohestanian, J. Sadeghi, D. Mohebbi-Kalhori, F. Shahraki, A. Samimi, A novel process for CO_2 capture from the flue gases to produce urea and ammonia, Energy. 144 (2018) 279–285. doi:10.1016/j.energy.2017.12.034.
[60] Z. Marković, S. Marković, N. Manojlović, J. Predojević-Simović, Mechanism of the Kolbe-Schmitt reaction. structure of the intermediate potassium phenoxide-CO_2 complex, J. Chem. Inf. Model. 47 (2007) 1520–1525. doi:10.1021/ci700068b.
[61] C. Miao, J. Wang, L. He, Catalytic processes for chemical conversion of carbon dioxide into cyclic carbonates and polycarbonates, Open Org. Chemstry J. 2 (2008) 68–82. doi:10.2174/1874095200801020068.
[62] G. Pagani, United States Patent: Process for urea production, 1995. https://patents.google.com/patent/US5403956A/en.
[63] A. Edrisi, Z. Mansoori, B. Dabir, Urea synthesis using chemical looping process - Techno-economic evaluation of a novel plant configuration for a green production, Int. J. Greenh. Gas Control. 44 (2016) 42–51. doi:10.1016/j.ijggc.2015.10.020.

[64] R. Dębek, Novel catalysts for chemical CO_2 utilization, AGH Unverisity of Science and Technology, Université Pierre and Marie Curie. Paris, 2017.
[65] L. Więcław-Solny, G. Łabojko, P. Babiński, Możliwości przemysłowego wykorzystania ditlenku węgla – badania nad zastosowaniem CO_2 w procesie otrzymywania gazu syntezowego, Polityka Energ. (2009).
[66] S.A. Ghoneim, R.A. El-salamony, S.A. El-temtamy, Review on innovative catalytic reforming of natural gas to syngas, Sci. Res. Publ. (2016) 116–139. doi:10.4236/wjet.2016.41011.
[67] J.R. Rostrup-Nielsen, Production of synthesis gas, Catal. Today. 18 (1993) 305–324. doi:10.1016/0920-5861(93)80059-A.
[68] S. Porada, G. Czerski, T. Dziok, P. Grzywacz, Technologie zgazowania węgla i ich przydatność dla potrzeb energetyki i chemii, Przegląd Górniczy. 69 (2013) 200–208.
[69] S. Hernández, M.A. Farkhondehfal, F. Sastre, M. Makkee, G. Saracco, N. Russo, Syngas production from electrochemical reduction of CO_2: Current status and prospective implementation, Green Chem. 19 (2017) 2326–2346. doi:10.1039/c7gc00398f.
[70] M.B. Ross, C.T. Dinh, Y. Li, D. Kim, P. De Luna, E.H. Sargent, P. Yang, Tunable Cu enrichment enables designer syngas electrosynthesis from CO_2, J. Am. Chem. Soc. 139 (2017) 9359–9363. doi:10.1021/jacs.7b04892.
[71] C. De Bie, B. Verheyde, T. Martens, J. Van Dijk, S. Paulussen, A. Bogaerts, Fluid modeling of the conversion of methane into higher hydrocarbons in an atmospheric pressure dielectric barrier discharge, Plasma Process. Polym. 8 (2011) 1033–1058. doi:10.1002/ppap.201100027.
[72] H. Mahmoudi, M. Mahmoudi, O. Doustdar, H. Jahangiri, A. Tsolakis, S. Gu, M. L. Wyszynski, A review of Fischer Tropsch synthesis process, mechanism, surface chemistry and catalyst formulation, Biofuels Eng. 2 (2017) 11–31. doi:10.1515/bfuel-2017-0002.
[73] N.E. Tsakoumis, M. Rønning, Ø. Borg, E. Rytter, A. Holmen, Deactivation of cobalt based Fischer-Tropsch catalysts: A review, Catal. Today. 154 (2010) 162–182. doi:10.1016/j.cattod.2010.02.077.
[74] E. Iglesia, Design, synthesis, and use of cobalt-based Fischer-Tropsch synthesis catalysts, Appl. Catal. A Gen. 161 (1997) 59–78. doi:10.1016/S0926-860X(97)00186-5.
[75] C. Ampelli, S. Perathoner, G. Centi, CO_2 utilization: an enabling element to move to a resource- and energy-efficient chemical and fuel production, Philos. Trans. R. Soc. A Math. Phys. Eng. Sci. 373 (2015). doi:dx.doi.org/10.1098/rsta.2014.0177.
[76] C.R. International, Vulcanol, (n.d.). http://carbonrecycling.is.
[77] N. Thybaud, D. Lebain, Panorama des voies de valorisation du CO_2, Alcimed. (2010) 190. doi:10.1016/0720-048X(94)90364-6.
[78] Chinese Academy of Sciences, A big step achieved in greenhouse gas conversion, 2017. doi:http://english.cas.cn/newsroom/research_news/201708/t20170815_181976.shtml.
[79] Linde, Linde develops a new production process for synthesis gas | Linde Engineering, Linde-Engineering. (2015). https://cen.acs.org/articles/94/i17/Dry-reforming-puts-CO2-work.html.
[80] A. Tullo, Dry reforming puts CO_2 to work, Chem. Eng. News. 94 (2016) 30. http://cen.acs.org/articles/94/i17/Dry-reforming-puts-CO2-work.html.
[81] W. Cho, T. Song, A. Mitsos, J.T. McKinnon, G.H. Ko, J.E. Tolsma, D. Denholm, T. Park, Optimal design and operation of a natural gas tri-reforming reactor for DME synthesis, Catal. Today. 139 (2009) 261–267. doi:10.1016/j.cattod.2008.04.051.
[82] C. Song, W. Pan, Tri-reforming of methane: A novel concept for synthesis of industrially useful synthesis gas with desired H_2/CO ratios using CO_2 in flue gas of power plants without CO_2 separation, ACS Div. Fuel Chem. Prepr. 49 (2004) 128–131.
[83] C. Song, W. Pan, Tri-reforming of methane: A novel concept for catalytic production of industrially useful synthesis gas with desired H_2/CO ratios, Catal. Today. 98 (2004) 463–484. doi:10.1016/j.cattod.2004.09.054.
[84] M. Halmann, A. Steinfeld, Thermoneutral tri-reforming of flue gases from coal- and gas-fired power stations, Catal. Today. 115 (2006) 170–178. doi:10.1016/j.cattod.2006.02.064.
[85] A.J. Majewski, J. Wood, Tri-reforming of methane over Ni@SiO_2 catalyst, Int. J. Hydrogen

Energy. 39 (2014) 12578–12585. doi:10.1016/j.ijhydene.2014.06.071.
[86] J.M. García-Vargas, J.L. Valverde, A. De Lucas-Consuegra, B. Gómez-Monedero, F. Dorado, P. Sánchez, Methane tri-reforming over a Ni/β-SiC-based catalyst: Optimizing the feedstock composition, Int. J. Hydrogen Energy. 38 (2013) 4524–4532. doi:10.1016/j.ijhydene.2013.02.001.
[87] L. Pino, A. Vita, F. Cipitì, M. Laganà, V. Recupero, Hydrogen production by methane tri-reforming process over Ni-ceria catalysts: Effect of La-doping, Appl. Catal. B Environ. 104 (2011) 64–73. doi:10.1016/j.apcatb.2011.02.027.
[88] L. Si, C. Wang, N. Sun, X. Wen, N. Zhao, F. Xiao, W. WEI, Y. SUN, Influence of preparation conditions on the performance of Ni-CaO-ZrO_2 catalysts in the tri-reforming of methane, J. Fuel Chem. Technol. 40 (2012) 210–215. doi:10.1016/S1872-5813(12)60011-5.
[89] L. Sun, Y. Tan, Q. Zhang, H. Xie, Y. Han, Tri-reforming of coal bed methane to syngas over the Ni-Mg-ZrO_2 catalyst, J. Fuel Chem. Technol. 40 (2012) 831–837. doi:10.1016/S1872-5813(12)60032-2.
[90] B. Christian Enger, R. Lødeng, A. Holmen, A review of catalytic partial oxidation of methane to synthesis gas with emphasis on reaction mechanisms over transition metal catalysts, Appl. Catal. A Gen. 346 (2008) 1–27. doi:10.1016/j.apcata.2008.05.018.
[91] D.M. Walker, S.L. Pettit, J.T. Wolan, J.N. Kuhn, Synthesis gas production to desired hydrogen to carbon monoxide ratios by tri-reforming of methane using Ni-MgO-(Ce,Zr)O_2 catalysts, Appl. Catal. A Gen. 445–446 (2012) 61–68. doi:10.1016/j.apcata.2012.08.015.
[92] V.R. Choudhary, K.C. Mondal, T. V. Choudhary, Oxy-methane reforming over high temperature stable NiCoMgCeOx and NiCoMgOx supported on zirconia-haffnia catalysts: Accelerated sulfur deactivation and regeneration, Catal. Commun. 8 (2007) 561–564. doi:10.1016/j.catcom.2006.08.007.
[93] V.R. Choudhary, K.C. Mondal, A.S. Mamman, High-temperature stable and highly active/selective supported NiCoMgCeOx catalyst suitable for autothermal reforming of methane to syngas, J. Catal. 233 (2005) 36–40. doi:10.1016/j.jcat.2005.04.019.
[94] Y. Li, Y. Wang, Z. Zhang, X. Hong, Y. Liu, Oxidative reformings of methane to syngas with steam and CO_2 catalyzed by metallic Ni based monolithic catalysts, Catal. Commun. 9 (2008) 1040–1044. doi:10.1016/j.catcom.2007.10.003.
[95] W. Schakel, G. Oreggioni, B. Singh, A. Strømman, A. Ramírez, Assessing the techno-environmental performance of CO_2 utilization via dry reforming of methane for the production of dimethyl ether, J. CO2 Util. 16 (2016) 138–149. doi:10.1016/j.jcou.2016.06.005.
[96] R. Dębek, M. Motak, T. Grzybek, M. Galvez, P. Da Costa, A short review on the catalytic activity of hydrotalcite-derived materials for dry reforming of methane, Catalysts. 7 (2017) 32–57. doi:10.3390/catal7010032.
[97] W. Donphai, T. Witoon, K. Faungnawakij, M. Chareonpanich, Carbon-structure affecting catalytic carbon dioxide reforming of methane reaction over Ni-carbon composites, J. CO2 Util. 16 (2016) 245–256. doi:10.1016/j.jcou.2016.07.011.
[98] M.M. Nair, S. Kaliaguine, F. Kleitz, Nanocast $LaNiO_3$ perovskites as precursors for the preparation of coke-resistant dry reforming catalysts, ACS Catal. 4 (2014) 3837–3846.
[99] T. Margossian, K. Larmier, S.M. Kim, F. Krumeich, C. Müller, C. Copéret, Supported bimetallic NiFe nanoparticles through colloid synthesis for improved dry reforming performance, ACS Catal. 7 (2017) 6942–6948. doi:10.1021/acscatal.7b02091.
[100] J. Gao, Z. Hou, H. Lou, X. Zheng, Dry (CO_2) reforming, First Edit, Elsevier, 2011. doi:10.1016/B978-0-444-53563-4.10007-0.
[101] J.H. Bitter, K. Seshan, L. J.A., Mono and bifunctional pathways of CO_2/CH_4 reforming over Pt and Rh based catalysts, J. Catal. (1998) 93–101.
[102] J.R. Rostrup-Nielsen, Aspects of CO_2-reforming of methane, Stud. Surf. Sci. Catal. 81 (1994) 25–41. doi:10.1016/S0167-2991(08)63847-1.
[103] M. Hassan Amin, S.K. Bhargava, A mini-review on CO_2 reforming of methane, Prog. Petrochemical Sci. 2 (2018) 1–5. doi:10.31031/PPS.2018.02.000532.

[104] J. Yang, W. Ma, D. Chen, A. Holmen, B.H. Davis, Fischer-Tropsch synthesis: A review of the effect of CO conversion on methane selectivity, Appl. Catal. A Gen. 470 (2014) 250–260. doi:10.1016/j.apcata.2013.10.061.
[105] Z. Zhang, X.E. Verykios, A stable and active nickel-based catalyst for carbon dioxide reforming of methane to synthesis gas, J. Chem. Soc. Chem. Commun. (1995) 71–72. doi:10.1039/C39950000071.
[106] A. Goeppert, M. Czaun, J.P. Jones, G.K. Surya Prakash, G.A. Olah, Recycling of carbon dioxide to methanol and derived products-closing the loop, Chem. Soc. Rev. 43 (2014) 7995–8048. doi:10.1039/c4cs00122b.
[107] S. Wang, G.Q. (Max) Lu, G.J. Millar, Carbon dioxide reforming of methane to produce synthesis gas over metal-supported catalysts: State of the art, Energy & Fuels. 10 (1996) 896–904. doi:10.1021/ef950227t.
[108] A.M. Gadalla, B. Bower, The role of catalyst support on the activity of nickel for reforming methane with CO_2, 43 (1988) 3049–3062. doi:10.1016/0009-2509(88)80058-7.
[109] J. Zhang, H. Wang, A.K. Dalai, Development of stable bimetallic catalysts for carbon dioxide reforming of methane, J. Catal. 249 (2007) 300–310. doi:10.1016/j.jcat.2007.05.004.
[110] C. Papadopoulou, H. Matralis, X. Verykios, Utilization of biogas as a renewable carbon source: dry reforming of methane, in: Catal. Altern. Energy Gener., 2012: pp. 57–127.
[111] N. Jurtz, M. Kraume, G.D. Wehinger, Advances in fixed-bed reactor modeling using particle-resolved computational fluid dynamics (CFD), Rev. Chem. Eng. (2018). doi:10.1515/revce-2017-0059.
[112] M.F. Mark, W.F. Maier, F. Mark, Reaction kinetics of the CO_2 reforming of methane, Chem. Eng. Technol. 20 (1997) 361–370. doi:10.1002/ceat.270200602.
[113] M.S. Fan, A.Z. Abdullah, S. Bhatia, Utilization of greenhouse gases through dry reforming: Screening of nickel-based bimetallic catalysts and kinetic studies, ChemSusChem. 4 (2011) 1643–1653. doi:10.1002/cssc.201100113.
[114] D. Pakhare, J. Spivey, A review of dry (CO_2) reforming of methane over noble metal catalysts, Chem. Soc. Rev. 43 (2014) 7813–7837. doi:10.1039/C3CS60395D.
[115] M.S. Challiwala, M.M. Ghouri, P. Linke, M.M. El-Halwagi, N.O. Elbashir, A combined thermo-kinetic analysis of various methane reforming technologies: Comparison with dry reforming, J. CO2 Util. 17 (2017) 99–111. doi:10.1016/j.jcou.2016.11.008.
[116] J.R. Rostrup-Nielsen, J.-H. Bak Hansen, CO_2 reforming of methane over transition metals, J. Catal. 144 (1993) 38–49. doi:10.1006/jcat.1993.1312.
[117] T.H. Nguyen, A. Łamacz, A. Krztoń, G. Djéga-Mariadassou, Partial oxidation of methane over Ni^0/La_2O_3 bifunctional catalyst IV: Simulation of methane total oxidation, dry reforming and partial oxidation using the Quasi-Steady State Approximation, Appl. Catal. B Environ. 199 (2016) 424–432. doi:10.1016/j.apcatb.2016.06.034.
[118] J. Wei, E. Iglesia, Structural requirements and reaction pathways in methane activation and chemical conversion catalyzed by rhodium, J. Catal. 225 (2004) 116–127. doi:10.1016/j.jcat.2003.09.030.
[119] J.R. Rostrup-Nielsen, Promotion by poisoning, Catal. Deactiv. 68 (1991) 85–101. doi:10.1016/S0167-2991(08)62621-X.
[120] L. Maier, B. Schädel, K.H. Delgado, S. Tischer, O. Deutschmann, Steam reforming of methane over nickel: Development of a multi-step surface reaction mechanism, Top. Catal. 54 (2011) 845–858. doi:10.1007/s11244-011-9702-1.
[121] B. Yousaf, Hydrotalcite based Ni-Co Bi-metallic catalysts for steam reforming of methane, Norwegian University of Science and Technology, 2016.
[122] J.R. Rostrup-Nielsen, Steam reforming of hydrocarbons. A historical perspective, Stud. Surf. Sci. Catal. 147 (2004) 121–126. doi:10.1016/S0167-2991(04)80038-7.
[123] M. Pajak, M. Mozdzierz, M. Chalusiak, S. Kimijima, J.S. Szmyd, G. Brus, A numerical analysis of heat and mass transfer processes in a macro-patterned methane/steam reforming reactor, Int. J. Hydrogen Energy. 43 (2018) 20474–20487. doi:10.1016/j.ijhydene.2018.09.058.

[124] H.S. Bengaard, J.K. Nørskov, J. Sehested, B.S. Clausen, L.P. Nielsen, A.M. Molenbroek, J.R. Rostrup-Nielsen, Steam reforming and graphite formation on Ni catalysts, J. Catal. 209 (2002) 365–384. doi:10.1006/jcat.2002.3579.
[125] J.R. Rostrup-Nielsen, Catalytic steam reforming, Spinger-Verlag, Berlin Heidelberg New York Tokyo, 1984.
[126] J.R. Rostrup-Nielsen, Sulfur passivated nickel catalysts for carbon-free steam reforming of methane, J. Catal. 85 (1984) 31–43. doi:10.1016/0021-9517(84)90107-6.
[127] D.L. Trimm, Coke formation and minimisation during steam reforming reactions, Catal. Today. 37 (1997) 233–238. doi:10.1016/S0920-5861(97)00014-X.
[128] J.R. Rostrup-Nielsen, J. Sehested, J.K. Nørskov, Hydrogen and synthesis gas by steam- and CO_2 reforming, Adv. Catal. 47 (2002) 65–139. doi:10.1016/S0360-0564(02)47006-X.
[129] J. Sehested, J.A.P. Gelten, S. Helveg, Sintering of nickel catalysts: Effects of time, atmosphere, temperature, nickel-carrier interactions, and dopants, Appl. Catal. A Gen. 309 (2006) 237–246. doi:10.1016/j.apcata.2006.05.017.
[130] M. Prettre, C. Eichner, M. Perrin, The catalytic oxidation of methane to carbon monoxide and hydrogen, Trans. Faraday Soc. 42 (1946) 335–339. doi:10.1039/TF946420335b.
[131] Y.H. Hu, E. Ruckenstein, Catalytic conversion of methane to synthesis gas by partial oxidation and CO_2 reforming, Adv. Catal. 48 (2004) 297–345. doi:10.1016/S0360-0564(04)48004-3.
[132] M. Peymani, S.M. Alavi, M. Rezaei, Preparation of highly active and stable nanostructured Ni/CeO_2 catalysts for syngas production by partial oxidation of methane, Int. J. Hydrogen Energy. 41 (2016) 6316–6325. doi:10.1016/j.ijhydene.2016.03.033.
[133] M. Khajenoori, M. Rezaei, B. Nematollahi, Preparation of noble metal nanocatalysts and their applications in catalytic partial oxidation of methane, J. Ind. Eng. Chem. 19 (2013) 981–986. doi:10.1016/j.jiec.2012.11.020.
[134] R. Jin, Y. Chen, W. Li, W. Cui, Y. Ji, C. Yu, Y. Jiang, Mechanism for catalytic partial oxidation of methane to syngas over a Ni/Al_2O_3 catalyst, Appl. Catal. A Gen. 201 (2000) 71–80. doi:10.1016/S0926-860X(00)00424-5.
[135] Gas-To-Liquids, R. Dutch Shell. (2019). https://www.shell.com/energy-and-innovation/natural-gas/gas-to-liquids.html.
[136] D.A. Hickman, E.A. Haupfear, L.D. Schmidt, Synthesis gas formation by direct oxidation of methane over Rh monoliths, Catal. Letters. 17 (1993) 223–237. doi:10.1007/BF00766145.
[137] D. A. Hickman, L. D. Schmidt, Production of syngas by direct catalytic oxidation of methane, Science. 259 (1993) 343–346.
[138] D.A. Hickman, L.D. Schmidt, Steps in CH_4 oxidation on Pt and Rh surfaces: High-temperature reactor simulations, AIChE J. 39 (1993) 1164–1177. doi:10.1002/aic.690390708.
[139] J.R. Rostrup-Nielsen, An industrial perspective on the impact of Haldor Topsøe on research and development in synthesis gas production, J. Catal. 328 (2015) 5–10. doi:10.1016/j.jcat.2015.04.013.
[140] A.T. Ashcroft, A.K. Cheetham, M.L.H. Green, P.D.F. Vernon, Partial oxidation of methane to synthesis gas using carbon dioxide, Nature. 352 (1991) 255–256.
[141] V.R. Choudhary, A.M. Rajput, B. Prabhakar, Energy efficient methane-to-syngas conversion with low H_2/CO ratio by simultaneous catalytic reactions of methane with carbon dioxide and oxygen, Catal. Letters. 32 (1995) 391–396. doi:10.1007/BF00813234.
[142] E. Ruckenstein, Y.H. Hu, Combination of CO_2 reforming and partial oxidation of methane over NiO/MgO solid solution catalysts, 5885 (1998) 1744–1747.
[143] E. Ruckenstein, H.Y. Wang, Combined catalytic partial oxidation and CO_2 reforming of methane over supported cobalt catalysts, Catal. Letters. 73 (2001) 99–105. doi:10.1023/A:1016695830055.
[144] N.A.S. Amin, T.C. Yaw, Thermodynamic equilibrium analysis of combined carbon dioxide reforming with partial oxidation of methane to syngas, Int. J. Hydrogen Energy. 32 (2007) 1789–1798. doi:10.1016/j.ijhydene.2006.12.004.
[145] J.S. Kang, D.H. Kim, S.D. Lee, S.I. Hong, D.J. Moon, Nickel-based tri-reforming catalyst for the

production of synthesis gas, Appl. Catal. A Gen. 332 (2007) 153–158. doi:10.1016/j.apcata.2007.08.017.
[146] M. Schmal, F.S. Toniolo, C.E. Kozonoe, Perspective of catalysts for (Tri) reforming of natural gas and flue gas rich in CO_2, Appl. Catal. A Gen. 568 (2018) 23–42. doi:10.1016/j.apcata.2018.09.017.
[147] S. Kawi, Y. Kathiraser, J. Ni, U. Oemar, Z. Li, E.T. Saw, Progress in synthesis of highly active and stable nickel-based catalysts for carbon dioxide reforming of methane, ChemSusChem. 8 (2015) 3556–3575. doi:10.1002/cssc.201500390.
[148] G. Djéga-Mariadassou, From hydrocarbons "Total oxidation" to syngas: Molecular approach of combustion, reforming, WGS, POM, catalytic looping (CLC,CLR), in: Catal. Environ. Depollution, Renew. Energy Clean Fuels 3th Int. Annu. Meet. 2009, Zakopane, 9-12 Sept. 2009 Proc., Polish Academy of Sciences. Centre of Polymer and Carbon Materials, 2009.
[149] H.A. Nishimoto, K. Nakagawa, N.O. Ikenaga, T. Suzuki, Partial oxidation of methane to synthesis gas over Ru-loaded Y_2O_3 catalyst, Catal. Letters. 82 (2002) 161–167. doi:10.1023/A:1020554309639.
[150] D.J. Moon, J.S. Kang, W.S. Nho, D.H. Kim, S.D. Lee, B.G. Lee, Ni-based catalyst for tri-reforming of methane and its catalysis application for the production of syngas, Patent US 2008/0260628 A1, 2008.
[151] S. Lee, W. Cho, W. Ju, B. Cho, Y. Lee, Y. Baek, Tri-reforming of CH_4 using CO_2 for production of synthesis gas to dimethyl ether, Catal. Today. 87 (2003) 133–137. doi:10.1016/j.cattod.2003.10.005.
[152] R.K. Singha, A. Shukla, A. Yadav, S. Adak, Z. Iqbal, N. Siddiqui, R. Bal, Energy efficient methane tri-reforming for synthesis gas production over highly coke resistant nanocrystalline Ni–ZrO_2 catalyst, Appl. Energy. 178 (2016) 110–125. doi:10.1016/j.apenergy.2016.06.043.
[153] J.M. García-Vargas, J.L. Valverde, J. Díez, P. Sánchez, F. Dorado, Preparation of Ni-Mg/β-SiC catalysts for the methane tri-reforming: Effect of the order of metal impregnation, Appl. Catal. B Environ. 164 (2015) 316–323. doi:10.1016/j.apcatb.2014.09.044.
[154] H. Seo, Recent scientific progress on developing supported Ni catalysts for dry (CO_2) reforming of methane, Catalysts. 8 (2018) 110–128. doi:10.3390/catal8030110.
[155] N.A.K. Aramouni, J.G. Touma, B.A. Tarboush, J. Zeaiter, M.N. Ahmad, Catalyst design for dry reforming of methane: Analysis review, Renew. Sustain. Energy Rev. 82 (2018) 2570–2585. doi:10.1016/j.rser.2017.09.076.
[156] A. Becerra, M. Dimitrijewits, C. Arciprete, A.C. Luna, Stable Ni/Al_2O_3 catalysts for methane dry reforming Effects of pretreatment, Granul. Matter. 3 (2001) 79–81.
[157] M.M. Barroso-Quiroga, A.E. Castro-Luna, Catalytic activity and effect of modifiers on Ni-based catalysts for the dry reforming of methane, Int. J. Hydrogen Energy. 35 (2010) 6052–6056. doi:10.1016/j.ijhydene.2009.12.073.
[158] R. Zanganeh, M. Rezaei, A. Zamaniyan, Dry reforming of methane to synthesis gas on NiO-MgO nanocrystalline solid solution catalysts, Int. J. Hydrogen Energy. 38 (2013) 3012–3018. doi:10.1016/j.ijhydene.2012.12.089.
[159] R. Zanganeh, M. Rezaei, A. Zamaniyan, Preparation of nanocrystalline NiO-MgO solid solution powders as catalyst for methane reforming with carbon dioxide: Effect of preparation conditions, Adv. Powder Technol. 25 (2014) 1111–1117. doi:10.1016/j.apt.2014.02.015.
[160] M. Jafarbegloo, A. Tarlani, A.W. Mesbah, S. Sahebdelfar, One-pot synthesis of NiO–MgO nanocatalysts for CO_2 reforming of methane: The influence of active metal content on catalytic performance, J. Nat. Gas Sci. Eng. 27 (2015) 1165–1173. doi:10.1016/j.jngse.2015.09.065.
[161] R. Zhang, G. Xia, M. Li, Y. Wu, H. Nie, D. Li, Effect of support on the performance of Ni-based catalyst in methane dry reforming, J. Fuel Chem. Technol. 43 (2015) 1359–1365. doi:10.1016/S1872-5813(15)30040-2.
[162] T. Odedairo, J. Chen, Z. Zhu, Metal-support interface of a novel Ni-CeO_2 catalyst for dry reforming of methane, Catal. Commun. 31 (2013) 25–31. doi:10.1016/j.catcom.2012.11.008.

[163] K. Asami, X. Li, K. Fujimoto, Y. Koyama, A. Sakurama, N. Kometani, Y. Yonezawa, CO_2 reforming of CH_4 over ceria-supported metal catalysts, Catal. Today. 84 (2003) 27–31. doi:10.1016/S0920-5861(03)00297-9.

[164] P. Kumar, Y. Sun, R.O. Idem, Nickel-based ceria, zirconia, and ceria-zirconia catalytic systems for low-temperature carbon dioxide reforming of methane, Energy and Fuels. 21 (2007) 3113–3123. doi:10.1021/ef7002409.

[165] F. Huang, R. Wang, C. Yang, H. Driss, W. Chu, H. Zhang, Catalytic performances of Ni/mesoporous SiO2 catalysts for dry reforming of methane to hydrogen, J. Energy Chem. 25 (2016) 709–719. doi:10.1016/j.jechem.2016.03.004.

[166] J.W. Han, C. Kim, J.S. Park, H. Lee, Highly coke-resistant Ni nanoparticle catalysts with minimal sintering in dry reforming of methane, ChemSusChem. 7 (2014) 451–456. doi:10.1002/cssc.201301134.

[167] E. Lovell, J. Scott, R. Amal, Ni-SiO_2 catalysts for the carbon dioxide reforming of methane: varying support properties by flame spray pyrolysis, Molecules. 20 (2015) 4594–4609. doi:10.3390/molecules20034594.

[168] M.E. Gálvez, A. Albarazi, P. Da Costa, Enhanced catalytic stability through non-conventional synthesis of Ni/SBA-15 for methane dry reforming at low temperatures, Appl. Catal. A Gen. 504 (2015) 143–150. doi:10.1016/j.apcata.2014.10.026.

[169] M.N. Kaydouh, N. El Hassan, A. Davidson, S. Casale, H. El Zakhem, P. Massiani, Highly active and stable Ni/SBA-15 catalysts prepared by a “two solvents” method for dry reforming of methane, Microporous Mesoporous Mater. 220 (2016) 99–109. doi:10.1016/j.micromeso.2015.08.034.

[170] Q. Zhang, T. Zhang, Y. Shi, B. Zhao, M. Wang, Q. Liu, J. Wang, K. Long, Y. Duan, P. Ning, A sintering and carbon-resistant Ni-SBA-15 catalyst prepared by solid-state grinding method for dry reforming of methane, J. CO2 Util. 17 (2017) 10–19. doi:10.1016/j.jcou.2016.11.002.

[171] A. Albarazi, P. Beaunier, P. Da Costa, Hydrogen and syngas production by methane dry reforming on SBA-15 supported nickel catalysts: On the effect of promotion by $Ce_{0.75}Zr_{0.25}O_2$ mixed oxide, Int. J. Hydrogen Energy. 38 (2013) 127–139. doi:10.1016/j.ijhydene.2012.10.063.

[172] K. Świrk, M.E. Gálvez, M. Motak, T. Grzybek, M. Rønning, P. Da Costa, Syngas production from dry methane reforming over yttrium-promoted nickel-KIT-6 catalysts, Int. J. Hydrogen Energy. 44 (2019) 44. doi:10.1016/j.ijhydene.2018.02.164.

[173] Z.L. Zhang, X.E. Verykios, Carbon dioxide reforming of methane to synthesis gas over supported Ni catalysts, Catal. Today. 21 (1994) 589–595. doi:10.1016/0920-5861(94)80183-5.

[174] V.M. Shinde, G. Madras, Catalytic performance of highly dispersed Ni/TiO_2 for dry and steam reforming of methane, RSC Adv. 4 (2014) 4817–4826. doi:10.1039/C3RA45961F.

[175] S.S. Kim, H.J. Choi, S.C. Hong, Effect of pretreatment time in dry reforming over Ni/TiO_2 catalyst, J. Chem. Eng. Japan. 45 (2012) 41–45. doi:10.1252/jcej.11we080.

[176] J. Guo, H. Lou, H. Zhao, X. Zheng, Improvement of stability of out-layer $MgAl_2O_4$ spinel for a Ni/$MgAl_2O_4$/Al_2O_3 catalyst in dry reforming of methane, React. Kinet. Catal. Lett. 84 (2005) 93–100. doi:10.1007/s11144-005-0195-4.

[177] Z. Alipour, M. Rezaei, F. Meshkani, Effect of Ni loadings on the activity and coke formation of MgO-modified Ni/Al_2O_3 nanocatalyst in dry reforming of methane, J. Energy Chem. 23 (2014) 633–638. doi:10.1016/S2095-4956(14)60194-7.

[178] E.N. Alvar, M. Rezaei, Mesoporous nanocrystalline $MgAl_2O_4$ spinel and its applications as support for Ni catalyst in dry reforming, Scr. Mater. 61 (2009) 212–215. doi:10.1016/j.scriptamat.2009.03.047.

[179] E. Le Saché, J.L. Santos, T.J. Smith, M.A. Centeno, H. Arellano-Garcia, J.A. Odriozola, T.R. Reina, Multicomponent Ni-CeO_2 nanocatalysts for syngas production from CO_2/CH_4 mixtures, J. CO2 Util. 25 (2018) 68–78. doi:10.1016/j.jcou.2018.03.012.

[180] W. Nimwattanakul, A. Luengnaruemitchai, S. Jitkarnka, Potential of Ni supported on clinoptilolite catalysts for carbon dioxide reforming of methane, 31 (2006) 93–100. doi:10.1016/j.ijhydene.2005.02.005.

[181] A.H. Fakeeha, W.U. Khan, A.S.A.L. Fatesh, A.E. Abasaeed, Stabilities of zeolite - supported Ni catalysts for dry reforming of methane, Chinese J. Catal. 34 (2013) 764–768. doi:10.1016/S1872-2067(12)60554-3.

[182] A. Luengnaruemitchai, A. Kaengsilalai, Activity of different zeolite-supported Ni catalysts for methane reforming with carbon dioxide, 144 (2008) 96–102. doi:10.1016/j.cej.2008.05.023.

[183] H. Drobná, M. Kout, A. Sołtysek, V.M. González-Delacruz, A. Caballero, L. Čapek, Analysis of Ni species formed on zeolites, mesoporous silica and alumina supports and their catalytic behavior in the dry reforming of methane, React. Kinet. Mech. Catal. 121 (2017) 255–274. doi:10.1007/s11144-017-1149-3.

[184] K. Jabbour, N. El, A. Davidson, P. Massiani, S. Casale, Characterizations and performances of Ni/diatomite catalysts for dry reforming of methane, Chem. Eng. J. 264 (2015) 351–358. doi:10.1016/j.cej.2014.11.109.

[185] Y. Liu, Z. He, L. Zhou, Z. Hou, W. Eli, Simultaneous oxidative conversion and CO_2 reforming of methane to syngas over Ni/vermiculite catalysts, Catal. Commun. 42 (2013) 40–44. doi:10.1016/j.catcom.2013.07.034.

[186] S. Barama, C. Dupeyrat-batiot, M. Capron, E. Bordes-richard, O. Bakhti-mohammedi, Catalytic properties of Rh, Ni, Pd and Ce supported on Al-pillared montmorillonites in dry reforming of methane, 141 (2009) 385–392. doi:10.1016/j.cattod.2008.06.025.

[187] A. Bhattacharyya, V.W. Chang, D.J. Schumacher, CO_2 reforming of methane to syngas I: Evaluation of hydrotalcite clay-derived catalysts, Appl. Clay Sci. 13 (1998) 317–328. doi:10.1016/S0169-1317(98)00030-1.

[188] R. Dębek, M.E. Galvez, F. Launay, M. Motak, T. Grzybek, P. Da Costa, Low temperature dry methane reforming over Ce, Zr and CeZr promoted Ni–Mg–Al hydrotalcite-derived catalysts, Int. J. Hydrogen Energy. 41 (2016) 11616–11623. doi:10.1016/j.ijhydene.2016.02.074.

[189] K. Mette, S. Kühl, A. Tarasov, M.G. Willinger, J. Kröhnert, S. Wrabetz, A. Trunschke, M. Scherzer, F. Girgsdies, H. Düdder, K. Kähler, K.F. Ortega, M. Muhler, R. Schlögl, M. Behrens, T. Lunkenbein, High-temperature stable ni nanoparticles for the dry reforming of methane, ACS Catal. 6 (2016) 7238–7248. doi:10.1021/acscatal.6b01683.

[190] A.I. Tsyganok, K. Suzuki, S. Hamakawa, K. Takehira, T. Hayakawa, Mg–Al layered double hydroxide intercalated with $[Ni (EDTA)]^{2-}$ chelate as a precursor for an efficient catalyst of methane reforming with carbon dioxide, Catal. Letters. 77 (2001) 75–86. doi:10.1023/A:1012739112430.

[191] A.I. Tsyganok, T. Tsunoda, S. Hamakawa, K. Suzuki, K. Takehira, T. Hayakawa, Dry reforming of methane over catalysts derived from nickel-containing Mg-Al layered double hydroxides, J. Catal. 213 (2003) 191–203. doi:10.1016/S0021-9517(02)00047-7.

[192] Y. Zhu, S. Zhang, B. Chen, Z. Zhang, C. Shi, Effect of Mg/Al ratio of NiMgAl mixed oxide catalyst derived from hydrotalcite for carbon dioxide reforming of methane, Catal. Today. 264 (2016) 163–170. doi:10.1016/j.cattod.2015.07.037.

[193] H. Liu, P. Da Costa, H.B. Hadj Taief, M. Benzina, M.E. Gálvez, Ceria and zirconia modified natural clay based nickel catalysts for dry reforming of methane, Int. J. Hydrogen Energy. 42 (2017) 23508–23516. doi:10.1016/j.ijhydene.2017.01.075.

[194] H. Liu, P. Da Costa, H. Bel Hadjltaief, M. Benzina, M.E. Galvez, Mg-promotion of Ni natural clay-supported catalysts for dry reforming of methane, RSC Adv. 8 (2018) 19627–19634. doi:10.1039/C8RA02615G.

[195] H. Liu, H. Bel Hadjltaief, M. Benzina, M.E. Galvez, P. Da Costa, Natural clay based nickel catalysts for dry reforming of methane : On the effect of support promotion (La,Al,Mn), Int. J. Hydrogen Energy. (2018). doi:10.1016/j.ijhydene.2018.03.004.

[196] B. Fidalgo, L. Zubizarreta, J.M. Bermúdez, A. Arenillas, J.A. Menéndez, Synthesis of carbon-supported nickel catalysts for the dry reforming of CH_4, Fuel Process. Technol. 91 (2010) 765–769. doi:10.1016/j.fuproc.2010.02.011.

[197] R. Dębek, M. Motak, M.E. Galvez, T. Grzybek, P. Da Costa, Influence of Ce/Zr molar ratio on catalytic performance of hydrotalcite-derived catalysts at low temperature CO_2 methane

reforming, Int. J. Hydrogen Energy. 42 (2017) 1–12. doi:10.1016/j.ijhydene.2016.12.121.
[198] M. Rezaei, S.M. Alavi, S. Sahebdelfar, Z. Yan, Effects of K_2O Promoter on the activity and stability of nickel catalysts supported on mesoporous nanocrystalline zirconia in CH_4 Reforming with CO_2, Energy & Fuels. 22 (2008) 2195–2202. doi:10.1016/S1003-9953(08)60064-X.
[199] T.D. Gould, M.M. Montemore, A.M. Lubers, L.D. Ellis, A.W. Weimer, J.L. Falconer, J.W. Medlin, Enhanced dry reforming of methane on Ni and Ni-Pt catalysts synthesized by atomic layer deposition, Applied Catal. A, Gen. 492 (2015) 107–116. doi:10.1016/j.apcata.2014.11.037.
[200] B. Koubaissy, A. Pietraszek, A.C. Roger, A. Kiennemann, CO_2 reforming of methane over Ce-Zr-Ni-Me mixed catalysts, Catal. Today. 157 (2010) 436–439. doi:10.1016/j.cattod.2010.01.050.
[201] A.F. Lucrédio, J.M. Assaf, E.M. Assaf, Methane conversion reactions on Ni catalysts promoted with Rh: Influence of support, Appl. Catal. A Gen. 400 (2011) 156–165. doi:10.1016/j.apcata.2011.04.035.
[202] B. Erdogan, H. Arbag, N. Yasyerli, SBA-15 supported mesoporous Ni and Co catalysts with high coke resistance for dry reforming of methane, Int. J. Hydrogen Energy. 43 (2018) 1396–1405. doi:10.1016/j.ijhydene.2017.11.127.
[203] R. Dębek, M. Motak, M.E. Galvez, T. Grzybek, P. Da Costa, Promotion effect of zirconia on Mg(Ni,Al)O mixed oxides derived from hydrotalcites in CO_2 methane reforming, Appl. Catal. B Environ. 223 (2018) 36–46. doi:10.1016/j.apcatb.2017.06.024.
[204] R. Dębek, M. Motak, M.E. Galvez, P. Da Costa, T. Grzybek, Catalytic activity of hydrotalcite-derived catalysts in the dry reforming of methane: on the effect of Ce promotion and feed gas composition, React. Kinet. Mech. Catal. 121 (2017) 185–208. doi:10.1007/s11144-017-1167-1.
[205] R. Dębek, M. Radlik, M. Motak, M.E. Galvez, W. Turek, P. Da Costa, T. Grzybek, Ni-containing Ce-promoted hydrotalcite derived materials as catalysts for methane reforming with carbon dioxide at low temperature - On the effect of basicity, Catal. Today. 257 (2015) 59–65. doi:10.1016/j.cattod.2015.03.017.
[206] J. Niu, S.E. Liland, J. Yang, K.R. Rout, J. Ran, D. Chen, Effect of oxide additives on the hydrotalcite derived Ni catalysts for CO_2 reforming of methane, Chem. Eng. J. (2018). doi:10.1016/j.cej.2018.08.149.
[207] H. Liu, D. Wierzbicki, R. Debek, M. Motak, T. Grzybek, P. Da Costa, M.E. Gálvez, La-promoted Ni-hydrotalcite-derived catalysts for dry reforming of methane at low temperatures, Fuel. 182 (2016) 8–16. doi:10.1016/j.fuel.2016.05.073.
[208] B. Li, W. Su, X. Wang, X. Wang, Alumina supported Ni and Co catalysts modified by Y_2O_3 via different impregnation strategies: Comparative analysis on structural properties and catalytic performance in methane reforming with CO_2, Int. J. Hydrogen Energy. 41 (2016) 14732–14746. doi:10.1016/j.ijhydene.2016.06.219.
[209] J.F. Li, C. Xia, C.T. Au, B.S. Liu, Y_2O_3-promoted NiO/SBA-15 catalysts highly active for CO_2/CH_4 reforming, Int. J. Hydrogen Energy. 39 (2014) 10927–10940. doi:10.1016/j.ijhydene.2014.05.021.
[210] T.L. Levalley, A.R. Richard, M. Fan, The progress in water gas shift and steam reforming hydrogen production technologies e A review, Int. J. Hydrogen Energy. 39 (2014) 16983–17000. doi:10.1016/j.ijhydene.2014.08.041.
[211] J. Sehested, Four challenges for nickel steam-reforming catalysts, 111 (2006) 103–110. doi:10.1016/j.cattod.2005.10.002.
[212] M.A. Nieva, M.M. Villaverde, A. Monzón, T.F. Garetto, A.J. Marchi, Steam-methane reforming at low temperature on nickel-based catalysts, 235 (2014) 158–166. doi:10.1016/j.cej.2013.09.030.
[213] D. Hufschmidt, L.F. Bobadilla, F. Romero-sarria, M.A. Centeno, J.A. Odriozola, M. Montes, E. Falabella, Supported nickel catalysts with a controlled molecular architecture for the catalytic reformation of methane, 149 (2010) 394–400. doi:10.1016/j.cattod.2009.06.002.
[214] S.S. Maluf, E.M. Assaf, Ni catalysts with Mo promoter for methane steam reforming, Fuel. 88 (2009) 1547–1553. doi:10.1016/j.fuel.2009.03.025.

[215] J. Xu, L. Chen, K. Fei, A. Borgna, M. Saeys, Effect of boron on the stability of Ni catalysts during steam methane reforming, J. Catal. 261 (2009) 158–165. doi:10.1016/j.jcat.2008.11.007.
[216] T. Takeguchi, H. Watanabe, T. Murayama, H. Takahashi, W. Ueda, Quantitative analysis of coke formation during steam reforming of methane on a nickel–hydrotalcite catalyst under practical operation conditions, Chem. Lett. 42 (2013) 124–126. doi:10.1246/cl.2013.124.
[217] M. Di, M. Dajiang, L. Xuan, G. Maochu, C. Yaoqiang, Partial oxidation of methane to syngas over monolithic Ni/γ-Al_2O_3 catalyst-Effects of rare earths and other basic promoters, J. Rare Earths. 24 (2006) 451–455. doi:10.1016/S1002-0721(06)60142-7.
[218] C. Ding, J. Wang, Y. Jia, G. Ai, S. Liu, P. Liu, K. Zhang, Y. Han, X. Ma, Anti-coking of Yb-promoted Ni/Al_2O_3 catalyst in partial oxidation of methane, Int. J. Hydrogen Energy. 41 (2016) 10707–10718. doi:10.1016/j.ijhydene.2016.04.110.
[219] H. Özdemir, M.A. Faruk Öksüzömer, M. A. Gürkaynak, Preparation and characterization of Ni based catalysts for the catalytic partial oxidation of methane: Effect of support basicity on H_2/CO ratio and carbon deposition, Int. J. Hydrogen Energy. 35 (2010) 12147–12160. doi:10.1016/j.ijhydene.2010.08.091.
[220] S. Xu, R. Zhao, X. Wang, Highly coking resistant and stable Ni/Al_2O_3 catalysts prepared by W/O microemulsion for partial oxidation of methane, Fuel Process. Technol. 86 (2004) 123–133. doi:10.1016/j.fuproc.2003.12.013.
[221] E. Bayrakdar, T. Gürkaynak Altinçekiç, M.A.F. Öksüzömer, Effects of PVP on the preparation of nanosized Al_2O_3 supported Ni catalysts by polyol method for catalytic partial oxidation of methane, Fuel Process. Technol. 110 (2013) 167–175. doi:10.1016/j.fuproc.2012.12.009.
[222] D. Dissanayake, M.P. Rosynek, K.C.C. Kharas, J.H. Lunsford, Partial oxidation of methane to carbon monoxide and hydrogen over a Ni/Al_2O_3 catalyst, J. Catal. 132 (1991) 117–127. doi:10.1016/0021-9517(91)90252-Y.
[223] H. Özdemir, M.A.F. Öksüzömer, M.A. Gürkaynak, Effect of the calcination temperature on Ni/$MgAl_2O_4$ catalyst structure and catalytic properties for partial oxidation of methane, Fuel. 116 (2014) 63–70. doi:10.1016/j.fuel.2013.07.095.
[224] F. Meshkani, M. Rezaei, M. Andache, Investigation of the catalytic performance of Ni/MgO catalysts in partial oxidation, dry reforming and combined reforming of methane, J. Ind. Eng. Chem. 20 (2014) 1251–1260. doi:10.1016/j.jiec.2013.06.052.
[225] C. Ding, X. Gao, Y. Han, X. Ma, J. Wang, S. Liu, K. Zhang, Effects of surface states over core-shell Ni@SiO_2 catalysts on catalytic partial oxidation of methane to synthesis gas, J. Energy Chem. 24 (2015) 45–53. doi:10.1016/S2095-4956(15)60283-2.
[226] A.S. Larimi, S.M. Alavi, A.C. Preparation, Partial oxidation of methane over Ni/$CeZrO_2$ mixed oxide solid solution catalysts, Int. J. Chem. Eng. Appl. 3 (2012) 6–9.
[227] S. Xu, X. Wang, Highly active and coking resistant Ni/CeO_2-ZrO_2 catalyst for partial oxidation of methane, Fuel. 84 (2005) 563–567. doi:10.1016/j.fuel.2004.10.008.
[228] T.H. Nguyen, A. Łamacz, P. Beaunier, S. Czajkowska, M. Domański, A. Krztoń, T. Van Le, G. Djéga-Mariadassou, Partial oxidation of methane over bifunctional catalyst I. In situ formation of Ni^0/La_2O_3 during temperature programmed POM reaction over $LaNiO_3$ perovskite, Appl. Catal. B Environ. 152–153 (2014) 360–369. doi:10.1016/j.apcatb.2014.01.053.
[229] S.J. Lee, H.J. Jun, S.-H. Lee, J.K. Yoon, H.T. Lim, S.-W. Nam, S.-A. Hong, Partial oxidation of methane over nickel-added strontium phosphate, Appl. Catal. A Gen. 230 (2002) 61–71.
[230] T. Wu, Q. Yan, H. Wan, Partial oxidation of methane to hydrogen and carbon monoxide over a Ni/TiO_2 catalyst, J. Mol. Catal. A Chem. 226 (2005) 41–48. doi:10.1016/j.molcata.2004.09.016.
[231] T. Shishido, H. Morioka, K. Takehira, M. Sukenobu, M. Kondo, Y. Wang, K. Takaki, K. Takehira, Partial oxidation of methane over Ni/Mg-Al oxide catalysts prepared by solid phase crystallization method from Mg-Al hydrotalcite-like precursors, Appl. Catal. A Gen. 223 (2002) 35–42. doi:10.1016/S0926-860X(01)00732-3.
[232] F. Basile, G. Fornasari, V. Rosetti, F. Trifirò, A. Vaccari, Effect of the Mg/Al ratio of the hydrotalcite-type precursor on the dispersion and activity of Rh and Ru catalysts for the partial oxidation of methane, Catal. Today. 91–92 (2004) 293–297.

doi:10.1016/j.cattod.2004.03.047.
[233] J. Zheng, S. Jixin, M.O. Jones, S. Huahong, X. Tiancun, P.P. Edwards, Catalytic partial oxidation of methane over Ni-based catalysts derived from Ni-Mg/Al ternary hydrotalcites, Energy and Fuels. 23 (2009) 1634–1639. doi:10.1021/ef800933j.
[234] J. Zhang, N. Zhao, W. Wei, Y. Sun, Partial oxidation of methane over Ni/Mg/Al/La mixed oxides prepared from layered double hydrotalcites, Int. J. Hydrogen Energy. 35 (2010) 11776–11786. doi:10.1016/j.ijhydene.2010.08.025.
[235] F. Basile, G. Fornasari, E. Poluzzi, A. Vaccari, Catalytic partial oxidation and CO_2-reforming on Rh- and Ni-based catalysts obtained from hydrotalcite-type precursors, Appl. Clay Sci. 13 (1998) 329–345. doi:10.1016/S0169-1317(98)00031-3.
[236] R. Shang, Y. Wang, G. Jin, X. Guo, Partial oxidation of methane over nickel catalysts supported on nitrogen-doped SiC, Catal. Commun. 10 (2009) 1502–1505. doi:10.1016/j.catcom.2009.04.001.
[237] H. Liu, H. Wu, D. He, Methane conversion to syngas over Ni/Y_2O_3 catalysts — Effects of calcination temperatures of Y_2O_3 on physicochemical properties and catalytic performance, Fuel Process. Technol. 119 (2014) 81–86. doi:10.1016/j.fuproc.2013.11.001.
[238] H. Liu, D. He, Properties of Ni/Y_2O_3 and its catalytic performance in methane conversion to syngas, Int. J. Hydrogen Energy. 36 (2011) 14447–14454. doi:10.1016/j.ijhydene.2011.08.025.
[239] H. Liu, H. Wu, D. He, Methane conversion to syngas over Ni/Y_2O_3 catalysts - Effects of calcination temperatures of Y_2O_3 on physicochemical properties and catalytic performance, Fuel Process. Technol. 119 (2014) 81–86. doi:10.1016/j.fuproc.2013.11.001.
[240] Y. Kuroda, T. Mori, H. Sugiyama, Y. Uozumi, K. Ikeda, A. Itadani, M. Nagao, On the possibility of AgZSM-5 zeolite being a partial oxidation catalyst for methane, J. Colloid Interface Sci. 333 (2009) 294–299. doi:10.1016/j.jcis.2009.01.015.
[241] K.A. Chalupka, W.K. Jozwiak, J. Rynkowski, W. Maniukiewicz, S. Casale, S. Dzwigaj, Partial oxidation of methane on NixAlBEA and NixSiBEA zeolite catalysts: Remarkable effect of preparation procedure and Ni content, Appl. Catal. B Environ. 146 (2014) 227–236. doi:10.1016/j.apcatb.2013.05.007.
[242] V.R. Choudhary, B. Prabhakar, A. M. Rajput, Beneficial effects of noble metal addition to Ni/Al_2O_3 catalyst for oxidative methane-to-syngas conversion, J. Catal. 157 (1995) 752–754. doi:10.1006/jcat.1995.1342.
[243] S. Liu, G. Xiong, H. Dong, W. Yang, S. Sheng, W. Chu, Z. Yu, Sustainable Ni catalyst for partial oxidation of CH_4 to syngas at high temperature, Stud. Surf. Sci. Catal. 130 (2000) 3567–3572.
[244] F. Cavani, F. Trifirò, A. Vaccari, Hydrotalcite-type anionic clays: Preparation, properties and applications., Catal. Today. 11 (1991) 173–301. doi:10.1016/0920-5861(91)80068-K.
[245] F. Kovanda, D. Koloušek, Z. Cílová, V. Hulínský, Crystallization of synthetic hydrotalcite under hydrothermal conditions, Appl. Clay Sci. 28 (2005) 101–109. doi:10.1016/j.clay.2004.01.009.
[246] O.D. Pavel, D. Tichit, I.C. Marcu, Acido-basic and catalytic properties of transition-metal containing Mg-Al hydrotalcites and their corresponding mixed oxides, Appl. Clay Sci. 61 (2012) 52–58. doi:10.1016/j.clay.2012.03.006.
[247] M. Rosset, O.W. Perez-Lopez, Catalytic properties of Cu–Mg–Al hydrotalcites, their oxides and reduced phases for ethanol dehydrogenation, React. Kinet. Mech. Catal. 123 (2018) 689–705. doi:10.1007/s11144-017-1297-5.
[248] P. Kuśtrowski, L. Chmielarz, E. Bożek, M. Sawalha, F. Roessner, Acidity and basicity of hydrotalcite derived mixed Mg-Al oxides studied by test reaction of MBOH conversion and temperature programmed desorption of NH_3 and CO_2, Mater. Res. Bull. 39 (2004) 263–281. doi:10.1016/j.materresbull.2003.09.032.
[249] Y.F. Lung, Y.S. Sun, C.K. Lin, J.Y. Uan, H.H. Huang, Synthesis of Mg–Fe–Cl hydrotalcite-like nanoplatelets as an oral phosphate binder: Evaluations of phosphorus intercalation activity and cellular cytotoxicity, Sci. Rep. 6 (2016) 2–12. doi:10.1038/srep32458.
[250] J.T. Kloprogge, R.L. Frost, D. Chemistry, Thermogravimetric analysis-mass spectrometry (TGA-MS) of hydrotalcites containing CO_3^{2-}, NO_3^-, Cl^-, SO_4^{2-} or ClO_4^-, in: A Clay Odyssey. Proc. 12th

Int. Clay Conf. Bahai-Blanca, Argentina 2001. doi:10.1016/B978-044450945-1/50147-0.
[251] D. Wierzbicki, R. Dębek, J. Szczurowski, S. Basąg, M. Włodarczyk, M. Motak, R. Baran, Copper, cobalt and manganese: Modified hydrotalcite materials as catalysts for the selective catalytic reduction of NO with ammonia. the influence of manganese concentration, Comptes Rendus Chim. 18 (2015) 1074–1083. doi:10.1016/j.crci.2015.06.009.
[252] W.T. Reichle, Catalytic reactions by thermally activated, synthetic, anionic clay minerals, J. Catal. 94 (1985) 547–557.
[253] L. Chmielarz, P. Kuśtrowski, A. Rafalska-Łasocha, D. Majda, R. Dziembaj, Catalytic activity of Co-Mg-Al, Cu-Mg-Al and Cu-Co-Mg-Al mixed oxides derived from hydrotalcites in SCR of NO with ammonia, Appl. Catal. B Environ. 35 (2002) 195–210. doi:10.1016/S0926-3373(01)00254-5.
[254] M. Gazzanob, P. Kdher, H. Papp, J. Pasel, R. Dziembaj, W. Makowski, T. Lojewski, Characterization and activity of novel copper-containing catalysts for selective catalytic reduction of NO with NH_3, Appl. Catal. B. 13 (1997) 205–217. doi:10.1016/S0926-3373(96)00106-3
[255] E. Lo, J.S. Valente, G. De Produccio, SOx removal by calcined MgAlFe hydrotalcite-like materials : Effect of the chemical composition and the cerium incorporation method, Environ. Sci. Technol. 39 (2005) 9715–9720.
[256] J.N. Armor, T.A. Braymer, T.S. Farris, Y. Li, F.P. Petrocelli, E.L. Weist, S. Kannan, C.S. Swamy, Calcined hydrotalcites for the catalytic decomposition of N_2O in simulated process streams, 7 (1996) 397–406. doi:10.1016/0926-3373(95)00048-8
[257] S. Abate, K. Barbera, E. Giglio, F. Deorsola, S. Perathoner, R. Pirone, G. Centi, Synthesis, characterization and activity pattern of Ni-Al hydrotalcite catalysts in CO_2 methanation, Ind. Eng. Chem. Res. 55 (2016) 8299–8308. doi:10.1021/acs.iecr.6b01581.
[258] D. Wierzbicki, M. Motak, T. Grzybek, M.E. Gálvez, P. Da Costa, The influence of lanthanum incorporation method on the performance of nickel-containing hydrotalcite-derived catalysts in CO_2 methanation reaction, Catal. Today. (2016) 0–1. doi:10.1016/j.cattod.2017.04.020.
[259] D. Wierzbicki, R. Debek, M. Motak, T. Grzybek, M.E. Gálvez, P. Da Costa, Novel Ni-La-hydrotalcite derived catalysts for CO_2 methanation, Catal. Commun. 83 (2016) 5–8. doi:10.1016/j.catcom.2016.04.021.
[260] D. Wierzbicki, R. Baran, R. Dębek, M. Motak, T. Grzybek, M.E. Gálvez, P. Da Costa, The influence of nickel content on the performance of hydrotalcite-derived catalysts in CO_2 methanation reaction, Int. J. Hydrogen Energy. 42 (2017) 23548–23555. doi:10.1016/j.ijhydene.2017.02.148.
[261] S. Basąg, F. Kovanda, Z. Piwowarska, A. Kowalczyk, K. Pamin, L. Chmielarz, Hydrotalcite-derived Co-containing mixed metal oxide catalysts for methanol incineration : Role of cobalt content, Mg/Al ratio and calcination temperature, J. Therm. Anal. Calorim. 129 (2017) 1301–1311. doi:10.1007/s10973-017-6348-7.
[262] A.A. Khassin, T.M. Yurieva, G.N. Kustova, I.S. Itenberg, M.P. Demeshkina, T.A. Krieger, L.M. Plyasova, G.K. Chermashentseva, V.N. Parmon, Cobalt – aluminum co-precipitated catalysts and their performance in the Fischer – Tropsch synthesis, J. Mol. Catal. A Chem. 168 (2001) 193–207.
[263] A. Di Fronzo, C. Pirola, A. Comazzi, F. Galli, C.L. Bianchi, A. Di Michele, R. Vivani, M. Nocchetti, M. Bastianini, D.C. Boffito, Co-based hydrotalcites as new catalysts for the Fischer-Tropsch synthesis process, Fuel. 119 (2014) 62–69. doi:10.1016/j.fuel.2013.11.014.
[264] S. Yu, E. Kim, S. Park, I. Kyu, J. Chul, Isomerization of glucose into fructose over Mg – Al hydrotalcite catalysts, Catal. Commun. 29 (2012) 63–67. doi:10.1016/j.catcom.2012.09.015.
[265] I. Delidovich, R. Palkovits, Structure – performance correlations of Mg–Al hydrotalcite catalysts for the isomerization of glucose into fructose, J. Catal. 327 (2015) 1–9. doi:10.1016/j.jcat.2015.04.012.
[266] O.D. Pavel, B. Cojocaru, E. Angelescu, V.I. Pârvulescu, The activity of yttrium-modified Mg,Al hydrotalcites in the epoxidation of styrene with hydrogen peroxide, Appl. Catal. A Gen. 403

(2011) 83–90. doi:10.1016/j.apcata.2011.06.017.
[267] M. Jia, Y. Zhang, Y. Bao, J. Wang, A. Xu, Green Chemistry Letters and Reviews Recyclable CuMgAl hydrotalcite for oxidative esterification of aldehydes with alkylbenzenes alkylbenzenes, 8253 (2018). doi:10.1080/17518253.2018.1470681.
[268] E. Angelescu, O.D. Pavel, M. Che, R. Bîrjega, G. Constentin, Cyanoethylation of ethanol on Mg-Al hydrotalcites promoted by Y^{3+} and La^{3+}, Catal. Commun. 5 (2004) 647–651. doi:10.1016/j.catcom.2004.07.016.
[269] M.I. Fadlalla, G.E.M. Maguire, H.B. Friedrich, The heterogeneous aminohydroxylation reaction using hydrotalcite-like catalysts containing osmium, Catalysts. 8 (2018) 547–560. doi:10.3390/catal8110547.
[270] Z. Wang, P. Fongarland, G. Lu, N. Essayem, Reconstructed La-, Y-, Ce-modified MgAl-hydrotalcite as a solid base catalyst for aldol condensation: Investigation of water tolerance, J. Catal. 318 (2014) 108–118. doi:10.1016/j.jcat.2014.07.006.
[271] Z. Hou, T. Yashima, Supported Co catalysts for methane reforming with CO_2, React. Kinet. Catal. Lett. 81 (2004) 153–159. doi:10.1023/B:REAC.0000016529.84565.e5.
[272] L.P.R. Profeti, E.A. Ticianelli, E.M. Assaf, Co/Al_2O_3 catalysts promoted with noble metals for production of hydrogen by methane steam reforming, Fuel. 87 (2008) 2076–2081. doi:10.1016/j.fuel.2007.10.015.
[273] K. Ba, A. Oszk, T. Kecsk, A. Erd, Dry reforming of CH_4 on Rh doped Co/Al_2O_3 catalysts, 228 (2014) 123–130. doi:10.1016/j.cattod.2013.11.014.
[274] J. Park, S. Yeo, I. Heo, T. Chang, General Promotional effect of Al addition on the Co/ZrO_2 catalyst for dry reforming, Appl. Catal. A Gen. 562 (2018) 120–131. doi:10.1016/j.apcata.2018.05.036.
[275] M. García-Diéguez, I.S. Pieta, M.C. Herrera, M.A. Larrubia, I. Malpartida, L.J. Alemany, Transient study of the dry reforming of methane over Pt supported, Catal. Today. 149 (2010) 380–387. doi:10.1016/j.cattod.2009.07.099.
[276] R. Dębek, K. Zubek, M. Motak, M.E. Galvez, P. Da Costa, T. Grzybek, Ni-Al hydrotalcite-like material as the catalyst precursors for the dry reforming of methane at low temperature, Comptes Rendus Chim. 18 (2015) 1205–1210. doi:10.1016/j.crci.2015.04.005.
[277] R. Dębek, K. Zubek, M. Motak, P. Da Costa, T. Grzybek, Effect of nickel incorporation into hydrotalcite-based catalyst systems for dry reforming of methane, Res. Chem. Intermed. 41 (2015) 9485–9495. doi:10.1007/s11164-015-1973-x.
[278] J. Guo, H. Lou, H. Zhao, D. Chai, X. Zheng, Dry reforming of methane over nickel catalysts supported on magnesium aluminate spinels, Appl. Catal. A Gen. 273 (2004) 75–82. doi:10.1016/j.apcata.2004.06.014.
[279] T. Shishido, M. Sukenobu, H. Morioka, F. Rie, H. Shirahase, K. Takehira, CO_2 reforming of CH_4 over Ni/Mg–Al oxide catalysts prepared by solid phase crystallization method from Mg–Al hydrotalcite-like precursors, Catal. Letters. 73 (2001) 21–26. doi:10.1023/A:1009066017469.
[280] J.-E. Min, Y.-J. Lee, H.-G. Park, C. Zhang, K.-W. Jun, Carbon dioxide reforming of methane on $Ni–MgO–Al_2O_3$ catalysts prepared by sol–gel method: Effects of Mg/Al ratios, J. Ind. Eng. Chem. 26 (2015) 375–383. doi:http://dx.doi.org/10.1016/j.jiec.2014.12.012.
[281] K. Takehira, T. Shishido, P. Wang, T. Kosaka, K. Takaki, Steam reforming of CH_4 over supported Ni catalysts prepared from a Mg–Al hydrotalcite-like anionic clay, Phys. Chem. Chem. Phys. 5 (2003) 3801–3810. doi:10.1039/b304261h.
[282] F. Basile, L. Basini, M.D. Amore, G. Fornasari, A. Guarinoni, D. Matteuzzi, G. Del Piero, F. Trifir, A. Vaccari, Ni/Mg/Al anionic clay derived catalysts for the catalytic partial oxidation of methane residence time dependence of the reactivity features, J. Catal. 256 (1998) 247–256.
[283] O. Deutschmann, H. Knözinger, K. Kochleoefl, T. Turek, Heterogeneous catalysis and solid catalysts, Ullmann's Encycl. Ind. Chem. (2009). doi:10.1002/14356007.
[284] B. Wiyantoko, P. Kurniawati, T.E. Purbaningtias, I. Fatimah, Synthesis and characterization of hydrotalcite at different Mg/Al molar ratios, Procedia Chem. 17 (2015) 21–26. doi:10.1016/j.proche.2015.12.115.

[285] R. Dębek, M. Motak, D. Duraczyska, F. Launay, M.E. Galvez, T. Grzybek, P. Da Costa, Methane dry reforming over hydrotalcite-derived Ni–Mg–Al mixed oxides: the influence of Ni content on catalytic activity, selectivity and stability, Catal. Sci. Technol. 6 (2016) 6705–6715. doi:10.1039/C6CY00906A.
[286] F. Zaera, Z. Ma, Characterization of heterogeneous catalysts, in: Surf. Nanomolecular Catal., 2006: pp. 1–38. doi:10.1201/9781420015751.ch1.
[287] P. Gallezot, X-ray techniques in catalysis, in: Catal. - Sci. Technol., 1984: pp. 221–273. doi:10.1007/978-3-642-93247-2_4.
[288] M.A. Al-Eshaikh, A. Kadachi, Elemental analysis of steel products using X-ray fluorescence (XRF) technique, J. King Saud Univ. - Eng. Sci. 23 (2011) 75–79. doi:10.1016/j.jksues.2011.03.002.
[289] R. Sitko, B. Zawisza, Quantification in X-ray fluorescence spectrometry, X-Ray Spectrosc. (2012). doi:10.5772/29367.
[290] K. Wirth, M. College, A. Barth, X-ray fluorescence (XRF), Geochemical Instrum. Anal. (2018) 4–7. https://serc.carleton.edu/research_education/geochemsheets/techniques/XRF.html.
[291] A. Maqsood, K. Iqbal, Materials characterization by non-destructive methods, J. Pakistan Mater. Soc. 4 (2010) 31–38.
[292] G. Leofanti, M. Padovan, G. Tozzola, B. Venturelli, Surface area and pore texture of catalysts, Catal. Today. 41 (1998) 207–219. doi:10.1016/S0920-5861(98)00050-9.
[293] E.P. Barrett, L.G. Joyner, P.P. Halenda, The determination of pore volume and area distributions in porous substances. I. Computations from nitrogen isotherms, J. Am. Chem. Soc. 73 (1951) 373–380. doi:10.1021/ja01145a126.
[294] Micromeritics Instrument Corporation, Gas Adsorption Theory, https://www.micromeritics.com/Repository/Files/Gas_Adsorption_Theory_poster.pdf.
[295] G. Leofanti, G. Tozzola, M. Padovan, G. Petrini, S. Bordiga, A. Zecchina, Catalyst characterization: characterization techniques, Catal. Today. 34 (1997) 307–327. doi:10.1016/S0920-5861(96)00056-9.
[296] J. Hagen, Industrial catalysis: A practical approach, Wiley-VCH, Weinheim, Germany, 2006.
[297] L.J.I. Coleman, W. Epling, R.R. Hudgins, E. Croiset, Ni/Mg-Al mixed oxide catalyst for the steam reforming of ethanol, Appl. Catal. A Gen. 363 (2009) 52–63. doi:10.1016/j.apcata.2009.04.032.
[298] D.G. Mustard, C.H. Bartholomew, Determination of metal crystallite supported size and morphology supported nickel catalysts, J. Catal. 67 (1981) 186–206. doi:10.1016/0021-9517(81)90271-2.
[299] S. Bernal, J.J. Calvino, M.A. Cauqui, J.M. Gatica, C. López Cartes, J.A. Pérez Omil, J.M. Pintado, Some contributions of electron microscopy to the characterisation of the strong metal-support interaction effect, Catal. Today. 77 (2003) 385–406. doi:10.1016/S0920-5861(02)00382-6.
[300] B. Sauerer, P.R. Craddock, M.D. AlJohani, K.L. Alsamadony, W. Abdallah, Fast and accurate shale maturity determination by Raman spectroscopy measurement with minimal sample preparation, Int. J. Coal Geol. 173 (2017) 150–157. doi:10.1016/j.coal.2017.02.008.
[301] O. Beyssac, B. Goffé, J.P. Petitet, E. Froigneux, M. Moreau, J.N. Rouzaud, On the characterization of disordered and heterogeneous carbonaceous materials by Raman spectroscopy, Spectrochim. Acta - Part A Mol. Biomol. Spectrosc. 59 (2003) 2267–2276. doi:10.1016/S1386-1425(03)00070-2.
[302] P. Cao, S. Adegbite, H. Zhao, E. Lester, T. Wu, Tuning dry reforming of methane for F-T syntheses: A thermodynamic approach, Appl. Energy. (2017). article in press, doi:10.1016/j.apenergy.2017.08.007.
[303] W.-H. Chen, C.-L. Hsu, S.-W. Du, Thermodynamic analysis of the partial oxidation of coke oven gas for indirect reduction of iron oxides in a blast furnace, Energy. 86 (2015) 758–771. doi:10.1016/j.energy.2015.04.087.
[304] A.C.D. Freitas, R. Guirardello, Thermodynamic analysis of methane reforming with CO_2,

CO_2+H_2O, CO_2+O_2 and CO_2+air for hydrogen and synthesis gas production, J. CO2 Util. 7 (2014) 30–38. doi:10.1016/j.jcou.2014.06.004.

[305] M.K. Nikoo, N.A.S. Amin, Thermodynamic analysis of carbon dioxide reforming of methane in view of solid carbon formation, Fuel Process. Technol. 92 (2011) 678–691. doi:10.1016/j.fuproc.2010.11.027.

[306] A.E. Abasaeed, A.S. Al-Fatesh, M.A. Naeem, A.A. Ibrahim, A.H. Fakeeha, Catalytic performance of CeO_2 and ZrO_2 supported Co catalysts for hydrogen production via dry reforming of methane, Int. J. Hydrogen Energy. 40 (2015) 6818–6826. doi:10.1016/j.ijhydene.2015.03.152.

[307] J.M. Francis, W.H. Whitlow, The effect of yttrium on the high temperature oxidation resistance of some Fe-Cr base alloys in carbon dioxide, Corros. Sci. 5 (1965) 701–710. doi:10.1016/S0010-938X(65)80026-9.

[308] Y. Chen, B. Liaw, C. Kao, J. Kuo, Yttria-stabilized zirconia supported platinum catalysts (Pt/YSZs) for CH_4/CO_2 reforming, Appl. Catal. 217 (2001) 23–31. doi:10.1016/S0926-860X(01)00592-0

[309] J.D.A. Bellido, E.M. Assaf, Effect of the Y_2O_3-ZrO_2 support composition on nickel catalyst evaluated in dry reforming of methane, Appl. Catal. A Gen. 352 (2009) 179–187. doi:10.1016/j.apcata.2008.10.002.

[310] A.S. Al-Fatesh, Promotional effect of Gd over Ni/Y_2O_3 catalyst used in dry reforming of CH_4 for H_2 production, Int. J. Hydrogen Energy. 42 (2017) 18805–18816. doi:10.1016/j.ijhydene.2017.06.165.

[311] B. Li, S. Zhang, Methane reforming with CO_2 using nickel catalysts supported on yttria-doped SBA-15 mesoporous materials via sol-gel process, Int. J. Hydrogen Energy. 38 (2013) 14250–14260. doi:10.1016/j.ijhydene.2013.08.105.

[312] Q. Wu, J. Chen, J. Zhang, Effect of yttrium and praseodymium on properties of $Ce_{0.75}Zr_{0.25}O_2$ solid solution for CH_4-CO_2 reforming, Fuel Process. Technol. 89 (2008) 993–999. doi:10.1016/j.fuproc.2008.03.006.

[313] Z. Taherian, M. Yousefpour, M. Tajally, B. Khoshandam, A comparative study of ZrO_2, Y_2O_3 and Sm_2O_3 promoted Ni/SBA-15 catalysts for evaluation of CO_2/methane reforming performance, Int. J. Hydrogen Energy. 42 (2017) 16408–16420. doi:10.1016/j.ijhydene.2017.05.095.

[314] X. Huang, G. Xue, C. Wang, N. Zhao, N. Sun, W. Wei, Y. Sun, Highly stable mesoporous NiO–Y_2O_3–Al_2O_3 catalysts for CO_2 reforming of methane: effect of Ni embedding and Y_2O_3 promotion, Catal. Sci. Technol. 6 (2016) 449–459. doi:10.1039/C5CY01171J.

[315] J.M. García-García, M.E. Pérez-Bernal, R.J. Ruano-Casero, V. Rives, Chromium and yttrium-doped magnesium aluminum oxides prepared from layered double hydroxides, Solid State Sci. 9 (2007) 1115–1125. doi:10.1016/j.solidstatesciences.2007.07.029.

[316] J.M. Fernández, C. Barriga, M.A. Ulibarri, F.M. Labajos, V. Rives, New hydrotalcite-like compounds containing yttrium, Chem. Mater. 9 (1997) 312–318. doi:10.1021/cm9603720.

[317] C.E. Daza, S. Moreno, R. Molina, Co-precipitated Ni-Mg-Al catalysts containing Ce for CO_2 reforming of methane, Int. J. Hydrogen Energy. 36 (2011) 3886–3894. doi:10.1016/j.ijhydene.2010.12.082.

[318] B.K. Kim, G.H. Gwak, T. Okada, J.M. Oh, Effect of particle size and local disorder on specific surface area of layered double hydroxides upon calcination-reconstruction, J. Solid State Chem. 263 (2018) 60–64. doi:10.1016/j.jssc.2018.03.041.

[319] M. Broda, A.M. Kierzkowska, D. Baudouin, Q. Imtiaz, C. Copéret, C.R. Müller, Sorbent-enhanced methane reforming over a Ni-Ca-based, bifunctional catalyst sorbent, ACS Catal. 2 (2012) 1635–1646. doi:10.1021/cs300247g.

[320] Y.H. Hu, Solid-solution catalysts for CO_2 reforming of methane, Catal. Today. 148 (2009) 206–211. doi:10.1016/j.cattod.2009.07.076.

[321] K.O. Christensen, D. Chen, R. Lødeng, A. Holmen, Effect of supports and Ni crystal size on carbon formation and sintering during steam methane reforming, Appl. Catal. A Gen. 314 (2006) 9–22. doi:10.1016/j.apcata.2006.07.028.

[322] A.F. Lucrédio, J.M. Assaf, E.M. Assaf, Reforming of a model sulfur-free biogas on Ni catalysts

supported on Mg(Al)O derived from hydrotalcite precursors: Effect of La and Rh addition, Biomass and Bioenergy. 60 (2014) 8–17. doi:10.1016/j.biombioe.2013.11.006.

[323] C. García-Sancho, R. Guil-López, A. Sebastián-López, R.M. Navarro, J.L.G. Fierro, Hydrogen production by methane decomposition: A comparative study of supported and bulk ex-hydrotalcite mixed oxide catalysts with Ni, Mg and Al, Int. J. Hydrogen Energy. 43 (2018) 9607–9621. doi:10.1016/j.ijhydene.2018.04.021.

[324] L. He, Q. Lin, Y. Liu, Y. Huang, Unique catalysis of Ni-Al hydrotalcite derived catalyst in CO_2 methanation: Cooperative effect between Ni nanoparticles and a basic support, J. Energy Chem. 23 (2014) 587–592. doi:10.1016/S2095-4956(14)60144-3.

[325] D.Y. Kalai, K. Stangeland, Y. Jin, Z. Yu, Active and stable hydrotalcite derived Ni catalysts for CO_2 reforming of methane: Comparison with catalysts by incipient wetness, J. CO2 Util. 25 (2018) 346–355. doi:10.1016/j.jcou.2017.12.018.

[326] B. Mile, D. Stirling, M.A. Zammitt, A. Lovell, M. Webb, The location of nickel oxide and nickel in silica-supported catalysts: Two forms of "NiO" and the assignment of temperature-programmed reduction profiles, J. Catal. 114 (1988) 217–229. doi:10.1016/0021-9517(88)90026-7.

[327] A. Kadkhodayan, A. Brenner, Temperature-programmed reduction and oxidation of metals supported on γ-alumina, J. Catal. 117 (1989) 311–321. doi:10.1016/0021-9517(89)90342-4.

[328] H. Shang, K. Pan, L. Zhang, B. Zhang, X. Xiang, Enhanced activity of supported Ni catalysts promoted by Pt for rapid reduction of aromatic nitro compounds, Nanomaterials. 6 (2016) 103–117. doi:10.3390/nano6060103.

[329] Y.J.O. Asencios, C.B. Rodella, E.M. Assaf, Oxidative reforming of model biogas over NiO-Y_2O_3-ZrO_2 catalysts, Appl. Catal. B Environ. 132–133 (2013) 1–12. doi:10.1016/j.apcatb.2012.10.032.

[330] A.M. Venezia, L.F. Liotta, G. Pantaleo, V. La Parola, G. Deganello, A. Beck, Z. Koppány, K. Frey, D. Horváth, L. Guczi, Activity of SiO_2 supported gold-palladium catalysts in CO oxidation, Appl. Catal. A Gen. 251 (2003) 359–368. doi:10.1016/S0926-860X(03)00343-0.

[331] A.L. Bonivardi, M.A. Baltanás, Preparation of Pd SiO_2 for methanol synthesis III. Exposed metal fraction and hydrogen solubility, J. Catal. 138 (1992) 500–517. doi:10.1016/0021-9517(92)90302-X.

[332] J.H. Sepúlveda, N.S. Fígoli, The influence of calcination temperature on Pd dispersion and hydrogen solubility in Pd/SiO_2, Appl. Surf. Sci. 68 (1993) 257–264. doi:10.1016/0169-4332(93)90130-4.

[333] X. Xie, T. Otremba, P. Littlewood, R. Schomäcker, A. Thomas, One-pot synthesis of supported, nanocrystalline nickel manganese oxide for dry reforming of methane, ACS Catal. 3 (2013) 224–229. doi:10.1021/cs3003963.

[334] N.D. Charisiou, L. Tzounis, V. Sebastian, S.J. Hinder, M.A. Baker, K. Polychronopoulou, Investigating the correlation between deactivation and the carbon deposited on the surface of Ni/Al_2O_3 and Ni/La_2O_3-Al_2O_3 catalysts during the biogas reforming reaction, Appl. Surf. Sci. (2018) 0–1. doi:10.1016/j.apsusc.2018.05.177.

[335] A. Daneshmand-Jahromi, Sanaz; Reza, Rahimpour Mohammad; Meshksar, Maryam; Hafiz, Hydrogen Production from Cyclic Chemical Looping Steam Methane Reforming over Yttrium Promoted Ni/SBA-16 Oxygen Carrier, Catalysts. 7 (2017) 286. doi:10.3390/catal7100286.

[336] A.A. Lytkina, N. V. Orekhova, M.M. Ermilova, A.B. Yaroslavtsev, The influence of the support composition and structure (MXZr1-XO2-d) of bimetallic catalysts on the activity in methanol steam reforming, Int. J. Hydrogen Energy. 43 (2018) 198–207. doi:10.1016/j.ijhydene.2017.10.182.

[337] A.I. Tsyganok, M. Inaba, T. Tsunoda, S. Hamakawa, K. Suzuki, T. Hayakawa, Dry reforming of methane over supported noble metals: A novel approach to preparing catalysts, Catal. Commun. 4 (2003) 493–498. doi:10.1016/S1566-7367(03)00130-4.

[338] M. Mokhtar, A. Inayat, J. Ofili, W. Schwieger, Thermal decomposition, gas phase hydration and liquid phase reconstruction in the system Mg/Al hydrotalcite/mixed oxide: A comparative

study, Appl. Clay Sci. 50 (2010) 176–181. doi:10.1016/j.clay.2010.07.019.
[339] I. Luisetto, S. Tuti, C. Battocchio, S. Lo Mastro, A. Sodo, Ni/CeO_2-Al_2O_3 catalysts for the dry reforming of methane: The effect of $CeAlO_3$ content and nickel crystallite size on catalytic activity and coke resistance, Appl. Catal. A Gen. 500 (2015) 12–22. doi:10.1016/j.apcata.2015.05.004.
[340] A. Sadezky, H. Muckenhuber, H. Grothe, R. Niessner, U. Pöschl, Raman microspectroscopy of soot and related carbonaceous materials: Spectral analysis and structural information, Carbon N. Y. 43 (2005) 1731–1742. doi:10.1016/j.carbon.2005.02.018.
[341] N.D. Charisiou, G. Siakavelas, K.N. Papageridis, A. Baklavaridis, L. Tzounis, K. Polychronopoulou, M.A. Goula, Hydrogen production via the glycerol steam reforming reaction over nickel supported on alumina and lanthana-alumina catalysts, Int. J. Hydrogen Energy. 42 (2017) 13039–13060. doi:10.1016/j.ijhydene.2017.04.048.
[342] X. Xu, X. Wang, Fine tuning of the sizes and phases of ZrO_2 nanocrystals, Nano Res. 2 (2009) 891–902. doi:10.1007/s12274-009-9092-x.
[343] A. Białas, T. Kondratowicz, M. Drozdek, P. Kuśtrowski, Catalytic combustion of toluene over copper oxide deposited on two types of yttria-stabilized zirconia, Catal. Today. 257 (2015) 144–149. doi:10.1016/j.cattod.2015.01.005.
[344] Y.J.O. Asencios, F.C.F. Marcos, J.M. Assaf, E.M. Assaf, Oxidative-reforming of methane and partial oxidation of methane reactions over NiO/PrO_2/ZrO_2 catalysts: Effect of nickel content, Brazilian J. Chem. Eng. 33 (2016) 627–636.
[345] J.D.A. Bellido, E.Y. Tanabe, E.M. Assaf, Carbon dioxide reforming of ethanol over Ni/Y_2O_3-ZrO_2 catalysts, Appl. Catal. B Environ. 90 (2009) 485–488. doi:10.1016/j.apcatb.2009.04.009.
[346] K. Dong-Hee, L.; Kwang-Seo, C.; Hyo-Sub K.; Chu-Sik, P.; Young-Ho, Syngas and hydrogen production via stepwise methane reforming over Cu-ferrite/YSZ, Int. J. Energy Res. 31 (2007) 1522–1530. doi:10.1002/er.3159.
[347] C. Resini, M. Concepción Herrera Delgado, S. Presto, L.J. Alemany, P. Riani, R. Marazza, G. Ramis, G. Busca, Yttria-stabilized zirconia (YSZ) supported Ni-Co alloys (precursor of SOFC anodes) as catalysts for the steam reforming of ethanol, Int. J. Hydrogen Energy. 33 (2008) 3728–3735. doi:10.1016/j.ijhydene.2008.04.044.
[348] P.A. Dilara, J.M. Vohs, TPD and HREELS investigation of the reaction of formic acid on ZrO_2(100), J. Phys. Chem. 97 (1993) 12919–12923. doi:10.1021/j100151a046.
[349] T. Götsch, W. Wallisch, M. Stöger-Pollach, B. Klötzer, S. Penner, From zirconia to yttria: Sampling the YSZ phase diagram using sputter-deposited thin films, AIP Adv. 6 (2016). doi:10.1063/1.4942818.
[350] M.B. Pomfret, C. Stoltz, B. Varughese, R.A. Walker, Structural and compositional characterization of yttria-stabilized zirconia: Evidence of surface-stabilized, low-valence metal species, Anal. Chem. 77 (2005) 1791–1795. doi:10.1021/ac048600u.
[351] R.P. Ingel, D.L. Iii, Lattice parameters and density for Y_2O_3-stabilized ZrO_2, J. Am. Ceram. Soc. 69 (1986) 325–332. doi:10.1111/j.1151-2916.1986.tb04741.x.
[352] W. Li, Z. Zhao, G. Wang, Modulating morphology and textural properties of ZrO_2 for supported Ni catalysts towards dry reforming of methane, AIChE J. 63 (2017) 2900–2915. doi:10.1002/aic.
[353] A.R. Puigdollers, P. Schlexer, S. Tosoni, G. Pacchioni, Increasing oxide reducibility: The role of metal/oxide interfaces in the formation of oxygen vacancies, ACS Catal. 7 (2017) 6493–6513. doi:10.1021/acscatal.7b01913.
[354] G. Pacchioni, Oxygen vacancy: the invisible agent on oxide surfaces, ChemPhysChem. 4 (2003) 1041–1047. doi:10.1002/cphc.200300835.
[355] W. Wang, S.M. Stagg-Williams, F.B. Noronha, L. V. Mattos, F.B. Passos, Partial oxidation and combined reforming of methane on Ce-promoted catalysts, Catal. Today. 98 (2004) 553–563. doi:10.1016/j.cattod.2004.09.009.
[356] O. V. Kharissova, B.I. Kharisov, Variations of interlayer spacing in carbon nanotubes, RSC Adv. 4 (2014) 30807–30815. doi:10.1039/C4RA04201H.

[357] H. Li, X. He, Z. Kang, H. Huang, Y. Liu, J. Liu, S. Lian, C.H.A. Tsang, X. Yang, S.T. Lee, Water-soluble fluorescent carbon quantum dots and photocatalyst design, Angew. Chemie - Int. Ed. 49 (2010) 4430–4434. doi:10.1002/anie.200906154.

[358] Z. Bao, Y. Lu, J. Han, Y. Li, F. Yu, Highly active and stable Ni-based bimodal pore catalyst for dry reforming of methane, Appl. Catal. A Gen. 491 (2015) 116–126. doi:10.1016/j.apcata.2014.12.005.

[359] J. Han, Y. Zhan, J. Street, F. To, F. Yu, Natural gas reforming of carbon dioxide for syngas over Ni–Ce–Al catalysts, Int. J. Hydrogen Energy. 42 (2017) 18364–18374. doi:10.1016/j.ijhydene.2017.04.131.

[360] M. Khavarian, S.P. Chai, A.R. Mohamed, Direct use of as-synthesized multi-walled carbon nanotubes for carbon dioxide reforming of methane for producing synthesis gas, Chem. Eng. J. 257 (2014) 200–208. doi:10.1016/j.cej.2014.05.079.

[361] B. Rego de Vasconcelos, D. Pham Minh, N. Lyczko, T.S. Phan, P. Sharrock, A. Nzihou, Upgrading greenhouse gases (methane and carbon dioxide) into syngas using nickel-based catalysts, Fuel. 226 (2018) 195–203. doi:10.1016/j.fuel.2018.04.017.

[362] M. García-Diéguez, I.S. Pieta, M.C. Herrera, M.A. Larrubia, L.J. Alemany, Improved Pt-Ni nanocatalysts for dry reforming of methane, Appl. Catal. A Gen. 377 (2010) 191–199. doi:10.1016/j.apcata.2010.01.038.

[363] N.D. Charisiou, G. Siakavelas, L. Tzounis, V. Sebastian, A. Monzon, M.A. Baker, S.J. Hinder, K. Polychronopoulou, An in depth investigation of deactivation through carbon formation during the biogas dry reforming reaction for Ni supported on modified with CeO_2 and La_2O_3 zirconia catalysts, Int. J. Hydrogen Energy. 43 (2018) 18955–18976. doi:10.1016/j.ijhydene.2018.08.074.

[364] S. Velu, D.P. Sabde, N. Shah, S. Sivasanker, New hydrotalcite-like anionic clays containing Zr^{4+} in the layers: Synthesis and physicochemical properties, Chem. Mater. 10 (1998) 3451–3458. doi:10.1016/S0167-2991(98)80262-0.

[365] D. Tichit, N. Das, B. Coq, R. Durand, Preparation of Zr-containing layered double hydroxides and characterization of the acido-basic properties of their mixed oxides, Chem. Mater. 14 (2002) 1530–1538. doi:10.1021/cm011125l.

[366] X. Yu, F. Zhang, W. Chu, Effect of a second metal (Co, Cu, Mn or Zr) on nickel catalysts derived from hydrotalcites for the carbon dioxide reforming of methane, RSC Adv. 6 (2016) 70537–70546. doi:10.1039/c6ra12335j.

[367] D.Y. Kalai, K. Stangeland, Y. Jin, W.M. Tucho, Z. Yu, Biogas dry reforming for syngas production on La promoted hydrotalcite-derived Ni catalysts, Int. J. Hydrogen Energy. 43 (2018) 19438–19450. doi:10.1016/j.ijhydene.2018.08.181.

[368] X. Yu, N. Wang, W. Chu, M. Liu, Carbon dioxide reforming of methane for syngas production over La-promoted NiMgAl catalysts derived from hydrotalcites, Chem. Eng. J. 209 (2012) 623–632. doi:10.1016/j.cej.2012.08.037.

[369] N. Ainirazali, N. Ainun, N. Abghazab, H.D. Setiabudi, C.S. Yee, CO_2 reforming of methane over Ni/Ce-SBA-15: Effects of Ce addition, Indian J. Sci. Technol. 10 (2017) 1–5. doi:10.17485/ijst/2017/v10i17/110380.

[370] K.Y. Koo, H.S. Roh, U.H. Jung, W.L. Yoon, CeO_2 promoted Ni/Al_2O_3 catalyst in combined steam and carbon dioxide reforming of methane for gas to liquid (GTL) process, Catal. Letters. 130 (2009) 217–221. doi:10.1007/s10562-009-9867-4.

[371] C.E. Daza, C.R. Cabrera, S. Moreno, R. Molina, Syngas production from CO_2 reforming of methane using Ce-doped Ni-catalysts obtained from hydrotalcites by reconstruction method, Appl. Catal. A Gen. 378 (2010) 125–133. doi:10.1016/j.apcata.2010.01.037.

[372] S.J.H. Rad, M. Haghighi, A.A. Eslami, F. Rahmani, N. Rahemi, Sol-gel vs. impregnation preparation of MgO and CeO_2 doped Ni/Al_2O_3 nanocatalysts used in dry reforming of methane: Effect of process conditions, synthesis method and support composition, Int. J. Hydrogen Energy. 41 (2016) 5335–5350. doi:10.1016/j.ijhydene.2016.02.002.

[373] P. Mierczynski, A. Mierczynska, R. Ciesielski, M. Mosinska, M. Nowosielska, A. Czylkowska, W.

Maniukiewicz, M. Szynkowska, K. Vasilev, High Active and Selective Ni/CeO_2–Al_2O_3 and Pd–Ni/CeO_2–Al_2O_3 catalysts for oxy-steam reforming of methanol, Catalysts. 8 (2018) 380-400. doi:10.3390/catal8090380.

[374] M. Akri, T. Chafik, P. Granger, P. Ayrault, C. Batiot-Dupeyrat, Novel nickel promoted illite clay based catalyst for autothermal dry reforming of methane, Fuel. 178 (2016) 139–147. doi:10.1016/j.fuel.2016.03.018.

[375] S. Sepehri, M. Rezaei, Ce promoting effect on the activity and coke formation of Ni catalysts supported on mesoporous nanocrystalline γ-Al_2O_3 in autothermal reforming of methane, Int. J. Hydrogen Energy. 42 (2017) 11130–11138. doi:10.1016/j.ijhydene.2017.01.096.

[376] H. Li, H. Xu, J. Wang, Methane reforming with CO_2 to syngas over CeO_2-promoted Ni/Al_2O_3-ZrO_2 catalysts prepared via a direct sol-gel process, J. Nat. Gas Chem. 20 (2011) 1–8. doi:10.1016/S1003-9953(10)60156-9.

[377] J.B. Wang, Y.L. Tai, W.P. Dow, T.J. Huang, Study of ceria-supported nickel catalyst and effect of yttria doping on carbon dioxide reforming of methane, Appl. Catal. A Gen. 218 (2001) 69–79. doi:10.1016/S0926-860X(01)00620-2.

[378] I.S. Metcalfe, S. Sundaresan, Oxygen transfer between metals and oxygen-ion conducting supports, AIChE J. 34 (1988) 195–208. doi:10.1101/gad.9.16.1978.

[379] D. Chen, D. Zhang, D. He, J. Lu, L. Zhong, C. Han, Y. Luo, Relationship between oxygen species and activity/stability in heteroatom (Zr,Y)-doped cerium-based catalysts for catalytic decomposition of CH_3SH, Chinese J. Catal. 39 (2018) 1929–1941. doi:10.1016/S1872.

[380] J.B. Wang, W.H. Shih, T.J. Huang, Study of Sm2O3-doped CeO_2/Al_2O_3-supported copper catalyst for CO oxidation, Appl. Catal. A Gen. 203 (2000) 191–199. doi:10.1016/S0926-860X(00)00484-1.

[381] R.G. Silver, C.J. Hou, J.G. Ekerdt, The role of lattice anion vacancies in the activation of CO and as the catalytic site for methanol synthesis over zirconium dioxide and yttria-doped zirconium dioxide, J. Catal. 118 (1989) 400–416. doi:10.1016/0021-9517(89)90327-8.

[382] S. Amelinckx, X.B. Zhang, D. Bernaerts, X.F. Zhang, V. Ivanov, J.B. Nagy, A formation mechanism for catalytically grown helix-shaped graphite nanotubes, Science. 265 (1994) 635–639. doi:10.1126/science.265.5172.635.

[383] D. V. Cesar, M.A.S. Baldanza, C.A. Henriques, F. Pompeo, G. Santori, J. Múnera, E. Lombardo, M. Schmal, L. Cornaglia, N. Nichio, Stability of Ni and Rh-Ni catalysts derived from hydrotalcite-like precursors for the partial oxidation of methane, Int. J. Hydrogen Energy. 38 (2013) 5616–5626. doi:10.1016/j.ijhydene.2013.02.064.

[384] K.M. Lee, W.Y. Lee, Partial oxidation of methane to syngas over calcined Ni-Mg/Al layered double hydroxides, Catal. Letters. 83 (2002) 65–70. doi:10.1023/A:1020609632354.

[385] A.F. Lucrédio, G. Jerkiewickz, E.M. Assaf, Nickel catalysts promoted with cerium and lanthanum to reduce carbon formation in partial oxidation of methane reactions, Appl. Catal. A Gen. 333 (2007) 90–95. doi:10.1016/j.apcata.2007.09.009.

[386] A.I. Tsyganok, M. Inaba, T. Tsunoda, K. Suzuki, K. Takehira, T. Hayakawa, Combined partial oxidation and dry reforming of methane to synthesis gas over noble metals supported on Mg-Al mixed oxide, Appl. Catal. A Gen. 275 (2004) 149–155. doi:10.1016/j.apcata.2004.07.030.

[387] N. Hadian, M. Rezaei, Combination of dry reforming and partial oxidation of methane over Ni catalysts supported on nanocrystalline $MgAl_2O_4$, Fuel. 113 (2013) 571–579. doi:10.1016/j.fuel.2013.06.013.

[388] F. van Looij, J.C. van Giezen, E.R. Stobbe, J.W. Geus, Mechanism of the partial oxidation of methane to synthesis gas on a silica-supported nickel catalyst, Catal. Today. 21 (1994) 495–503. doi:10.1016/0920-5861(94)80172-X.

[389] K. Heitnes, S. Linderg, O.A. Rokstad, A. Holmen, Catalytic partial oxidation of methane to synthesis gas, Catal. Today. 24 (1995) 211–216. doi:10.1016/0920-5861(94)80169-X.

[390] A. Urdă, I. Popescu, T. Cacciaguerra, N. Tanchoux, D. Tichit, I.C. Marcu, Total oxidation of methane over rare earth cation-containing mixed oxides derived from LDH precursors, Appl. Catal. A Gen. 464–465 (2013) 20–27. doi:10.1016/j.apcata.2013.05.012.

[391] S. Tanasoi, N. Tanchoux, A. Urdă, D. Tichit, I. Săndulescu, F. Fajula, I.C. Marcu, New Cu-based mixed oxides obtained from LDH precursors, catalysts for methane total oxidation, Appl. Catal. A Gen. 363 (2009) 135–142. doi:10.1016/j.apcata.2009.05.007.

[392] A. Urdă, I. Popescu, I.-C. Marcu, G. Carja, N. Apostolescu, I. Sandulescu, Methane and propane total oxidation on catalysts from FeLDH precursors, Rev. Chim. 61 (2010) 267–271.

[393] Z. Jiang, Z. Hao, J. Yu, H. Hou, C. Hu, J. Su, Catalytic combustion of methane on novel catalysts derived from Cu-Mg/Al-hydrotalcites, Catal. Letters. 99 (2005) 157–163. doi:10.1007/s10562-005-2108-6.

[394] Z. Jiang, J. Yu, J. Cheng, T. Xiao, M.O. Jones, Z. Hao, P.P. Edwards, Catalytic combustion of methane over mixed oxides derived from Co-Mg/Al ternary hydrotalcites, Fuel Process. Technol. 91 (2010) 97–102. doi:10.1016/j.fuproc.2009.08.023.

[395] T. Machej, E.M. Serwicka, M. Zimowska, R. Dula, A. Michalik-Zym, B. Napruszewska, W. Rojek, R. Socha, Cu/Mn-based mixed oxides derived from hydrotalcite-like precursors as catalysts for methane combustion, Appl. Catal. A Gen. 474 (2014) 87–94. doi:10.1016/j.apcata.2013.07.048.

[396] K. Jirátová, P. Čuba, F. Kovanda, L. Hilaire, V. Pitchon, Preparation and characterisation of activated Ni(Mn)/Mg/Al hydrotalcites for combustion catalysis, Catal. Today. 76 (2002) 43–53. doi:10.1016/S0920-5861(02)00203-1.

[397] A. Izquierdo-Colorado, R. Dębek, P. Da Costa, M.E. Gálvez, Excess-methane dry and oxidative reforming on Ni-containing hydrotalcite-derived catalysts for biogas upgrading into synthesis gas, Int. J. Hydrogen Energy. (2018) 11981-11989. doi:10.1016/j.ijhydene.2018.04.237.

[398] W.H. Chen, M.R. Lin, J.J. Lu, Y. Chao, T.S. Leu, Thermodynamic analysis of hydrogen production from methane via autothermal reforming and partial oxidation followed by water gas shift reaction, Int. J. Hydrogen Energy. 35 (2010) 11787–11797. doi:10.1016/j.ijhydene.2010.08.126.

[399] S.M. Sajjadi, M. Haghighi, Impregnation vs. sol-gel and sol-gel-plasma dispersion of nickel nanoparticles over Al_2O_3 employed in combined dry reforming and partial oxidation of greenhouse gases to syngas, Int. J. Hydrogen Energy. 43 (2018) 15014–15029. doi:10.1016/j.ijhydene.2018.06.073.

[400] B. Li, X. Xu, S. Zhang, Synthesis gas production in the combined CO_2 reforming with partial oxidation of methane over Ce-promoted Ni/SiO_2 catalysts, Int. J. Hydrogen Energy. 38 (2013) 890–900. doi:10.1016/j.ijhydene.2012.10.103.

[401] S. He, H. Wu, W. Yu, L. Mo, H. Lou, X. Zheng, Combination of CO_2 reforming and partial oxidation of methane to produce syngas over Ni/SiO_2 and Ni-Al_2O_3/SiO_2 catalysts with different precursors, Int. J. Hydrogen Energy. 34 (2009) 839–843. doi:10.1016/j.ijhydene.2008.10.072.

[402] S. He, X. Zheng, L. Mo, W. Yu, H. Wang, Y. Luo, Characterization and catalytic properties of Ni/SiO_2 catalysts prepared with nickel citrate as precursor, Mater. Res. Bull. 49 (2014) 108–113. doi:10.1016/j.materresbull.2013.08.051.

[403] D. Chen, R. Lødeng, A. Anundskås, O. Olsvik, A. Holmen, Deactivation during carbon dioxide reforming of methane over Ni catalyst: Microkinetic analysis, Chem. Eng. Sci. 56 (2001) 1371–1379. doi:10.1016/S0009-2509(00)00360-2.

[404] M. Minutillo, A. Perna, A novel approach for treatment of CO_2 from fossil fired power plants. Part B: The energy suitability of integrated tri-reforming power plants (ITRPPs) for methanol production, Int. J. Hydrogen Energy. 35 (2010) 7012–7020. doi:10.1016/j.ijhydene.2010.04.091.

Summary

The CO_2 atmospheric levels have been continuously increasing in recent years, which mainly originated from fossil fuels combustion, petrochemical, chemical and cement industry. The awareness of the global warming, mainly connected to carbon dioxide emissions, led to the implementation of different CO_2 reduction strategies, with a special emphasis laid on technologies of CCS (Carbon Capture and Storage) and CCU (Carbon Capture and Utilization). The latter approach allows to convert CO_2 into valuable products, chemicals and fuels. Among the technologies that can convert CO_2 into valuable products are processes of reforming of methane - dry reforming of methane (DRM), partial oxidation combined with dry reforming of methane (CRPOM) and tri-reforming of methane (TRM). They all may be considered as an attractive route for syngas production.

The literature reported that the most appropriate active metal for the reforming processes is nickel, due to its low cost, availability and good catalytic performance. Although the noble-metal based catalysts showed higher activity in methane reforming processes, their application is limited due to high price and low availability. However, the industrial application of Ni-based materials may be limited because of sintering of Ni nanoparticles and catalyst deactivation caused by carbon deposits. The catalyst preparation, including the support used and the addition of promoters, significantly influence the catalytic behavior, contributing to both catalytic activity and stability with time on stream.

Double-layered hydroxides (DLHs), also known as hydrotalcites (HTs), show good properties as potential carriers due to their double-layered structure and the presence of NiO, MgO and Al_2O_3 introduced by co-precipitation. Therefore, **the goal of this PhD thesis was to evaluate catalytic performance of different double-layered-hydroxide catalytic systems containing nickel in dry reforming of methane, partial oxidation of methane, partial oxidation combined with dry reforming of methane, and tri-reforming of methane**. A review of the literature revealed that there are several areas of research concerning application of DLHs-derived materials in reforming processes which have not been studied yet, thus this thesis focused on filling these gaps. In order to address these issues a number of different hydrotalcite-based catalysts was synthesized by co-precipitation and incipient

wetness impregnation method. An emphasis was laid on the influence of promoters, especially yttrium which was not studied as an additive to hydrotalcite-based catalysts before. The physico-chemical properties of the prepared materials were evaluated by means of XRD, XRF, low temperature N_2 sorption, TPR-H_2, TPD-CO_2, H_2 chemisorption, transmission electron microscopy, high-resolution microscopy, thermogravimetric analysis coupled with mass spectroscopy and Raman spectroscopy. The obtained catalysts were characterized at various steps of the process – the freshly prepared, calcined, reduced, as well as after reaction. The materials were tested in the set of methane reforming processes, carried out in the temperature range of between 850 and 600 °C, and some of them in isothermal tests at 700 °C.

The thesis covers six main parts:

1. Literature part, reviewing the reduction of CO_2 emissions, solutions and technologies (**Chapter 1**),
2. Experimental part, describing the used preparation techniques, instrumental methods used and types and conditions of catalytic experiments (**Chapter 2**),
3. Thermodynamic calculations (**Chapter 3**),
4. Discussion of catalytic performance in dry reforming of methane of yttrium promoted catalysts, zirconium and yttrium promoted catalysts, and cerium and yttrium promoted catalysts (**Chapter 4**, with **Subchapters 4.1**, **4.2.**, **4.3.**, **4.4.**),
5. Discussion of catalytic behavior in partial oxidation of methane, combined partial oxidation with dry reforming of methane, and tri-reforming of methane (**Chapter 5**), and
6. General conclusions.

The third part (**Chapter 3**) covers thermodynamic equilibrium calculations for CH_4 and CO_2 conversions as well as for H_2/CO molar ratio. The calculations were carried out for dry reforming of methane (DRM), steam reforming of methane (SRM), partial oxidation of methane (POM) and tri-reforming of methane (TRM) processes and showed that they can be efficiently carried out at high

temperatures (over 700 °C). Moreover, the calculations of tri-reforming of methane presented a considerable potential of catalytic CH_4 and CO_2 conversions under the feed gas composition of $CH_4/CO_2/H_2O/O_2$=1/0.5/0.5/0.1 and $CH_4/CO_2/H_2O/O_2$=3/1/2/0.3.

The promoting effect of yttrium loading, discussed in **Subchapter 4.1.**, was evaluated by the comparison of the physico-chemical properties and catalytic activity of double-layered hydroxides containing 0.2, 0.4, 0.6, 2.0 and 3.0 wt.% of yttrium prepared by co-precipitation. It was shown that yttrium in the range of 0.2-2.0 wt.% was introduced into the periclase-like structure, whereas the addition of 3.0 wt.% resulted in partial deposition of this metal on the surface. The best physico-chemical properties, such as extended specific surface area and increased dispersion of Ni, were found for the sample promoted with 2 wt.% Y. After modification with 0.2 to 2.0 wt.% yttrium the total basicity decreased, whereas the promotion with 3 wt.% led to a significant increase in the total number of basic sites. The highest catalytic activity in CH_4 and CO_2 conversion was found for the HTNi-Y3.0 catalysts, with average 85% for CH_4, and 89% for CO_2, which could be attributed to the enhanced number of total basic sites. However, the most stable behavior was observed for HTNi-Y2.0 sample with average 74% for CH_4, and 78% for CO_2 at 700 °C for 5 h.

Subchapter 4.2. and **4.3** cover the evaluation of different ways of promotion of DLHs with Zr (assumed 5 wt.%) and Y (0.2, 0.4 and 0.6 wt.%) and their influence on the catalytic performance in dry reforming of methane. The samples co-impregnated with Zr and Y showed formation of yttrium stabilized zirconia (YSZ) phase located on the surface of the double-layered hydroxide. The hydrotalcite sample modified with Zr and Y (0.4 wt.%) presented structural resistance to the products of the RWGS side reaction, as supported by the absence of hydrotalcite reflections in the XRD patterns of the spent catalyst. The co-precipitation with zirconia and impregnation with yttrium did not result in YSZ phase formation. ZrO_2 was partially introduced within the periclase-like structure, whereas yttrium was located on the surface leading to its partial blockage. This resulted in the decreased dispersion of metal active sites and slightly decreased Ni crystallite size. Irrespectively of the method of Zr and Y introduction, the percentage of medium basic sites was increasing with the increasing yttrium loading.

These two series were compared to the catalyst co-precipitated together with Zr (assumed 5 wt.%) and Y (0.4 wt.%). The incorporation of these two metals inside the structure led to the extended number of total basic sites, increased Ni dispersion and increased reducibility. This influenced DRM performance in a positive way, since, among all the Zr- and Y-promoted materials, this one showed the highest activity in CH_4 and CO_2.

Subchapter 4.4. describes the examination of Ce (introduced by co-precipitation method with assumed 3 wt.%) and Y promoting effect (impregnation with 0.2, 0.4 or 0.6 wt.%) in Ni-based DLHs in dry reforming of methane. Co-promotion with Ce and Y resulted in a decrease of reducibility of Ni, an increase of the basicity, enhanced Ni dispersion and smaller Ni crystallite size as compared to the HTNi catalyst. The highest catalytic performance was registered for HTNi-Ce, where CH_4 conversion was 86%, CO_2 conversion of 88% and H_2/CO molar ratio of ca. 0.97. For Ce and 0.4 wt.% Y-promoted sample the amount of carbon was higher, but less graphitic as compared to the only Ce-modified material. No deactivation was observed during the isothermal test at 700 °C for 5 hours.

All series of the catalysts discussed in **Subchapters 4.1.** to **4.4**. tested in dry reforming of methane resulted in the formation of different types of carbonaceous deposits upon the catalytic test for 5 h at 700 °C - amorphous, filamentous and graphitic-like. However, the amount of each type was dependent on both the preparation method used, the amount of introduced Y and the addition of a second promoter. The lowest amount of carbon deposits was registered for Zr co-precipitated catalyst. The least graphitic deposits were found after reaction for HTNi-Zr and HTNi-Zr/Y0.4.

Chapter 5 discusses the promoting effect of Y in Ni-based DLHs in oxidative reforming reactions, partial oxidation POM, partial oxidation with the addition of carbon dioxide CRPOM and tri-reforming. Two chosen catalysts were examined, unpromoted double-layered hydroxide (HTNi) and double-layered hydroxide promoted with 2 wt.% of Y (HTNi-Y2.0).

In partial oxidation of methane (POM) experiments, the materials showed high CH_4 conversions of ca. 90% and the H_2/CO ratio close to stoichiometric (ca. 2.0). No deactivation was observed within the 5-hour experiment at 700 °C. The partial oxidation of methane combined with CO_2 reforming revealed

that addition of oxygen to DRM considerably improved stability of the catalysts, where carbon removal was concerned, as only traces were detected. The obtained CO_2 conversions were lower than those registered for dry reforming as a consequence of occurrence of parallel reactions.

Catalytic performance of Y-Ni-DLHs in tri-reforming of methane was examined for two gas compositions (i) $CH_4/CO_2/H_2O/O_2$=1/0.5/0.5/0.1 as suggested by the literature, and (ii) $CH_4/CO_2/H_2O/O_2$=3/1/2/0.3 as proposed by the thermodynamic calculations. The application of the former showed very good performance with limited carbon formation for both HTNi and HTNi-Y2.0 catalysts. The materials were catalytically active, both showing conversions of ca. 91-98% for CH_4 and 70-86% for CO_2. The average molar ratio for HTNi was 1.97, which is suitable for methanol synthesis, whereas HTNi-Y2.0 showed lower value (1.63) which may be applied for e.g. dimethyl ether production. The second studied gas composition led to somewhat inferior performance of the tested materials, with the conversion values lower for both tested catalysts - 76-78% for CH_4, and 89-91% for CO_2 conversion, and the average H_2/CO molar ratio for both of ca. 1.62. Additionally, this gas feed composition led to a significant amount of formed carbon on both tested samples, pointing to the important role which the applied reaction conditions.

Résumé

Les niveaux atmosphériques de CO_2 ont constamment augmenté ces dernières années, principalement à cause de la combustion de combustibles fossiles, de la pétrochimie, de la chimie et de l'industrie du ciment. La prise de conscience du réchauffement climatique, principalement liée aux émissions de dioxyde de carbone, a conduit à la mise en œuvre de différentes stratégies de réduction de CO_2, en mettant un accent particulier sur les technologies de captage et de stockage du carbone et de captage et d'utilisation du carbone. Cette dernière approche permet de convertir le CO_2 en produits de forte valeur ajoutés tels que des produits chimiques et des carburants. Parmi les technologies permettant de convertir le CO_2, on peut citer les procédés catalytiques de reformage du méthane - reformage à sec du méthane (DRM), l'oxydation partielle associée au reformage à sec du méthane (CRPOM) et le tri-reformage du méthane (TRM). Malgré le fait que ces procédés ne soient pas encore dans un grand degré de maturité, Ils peuvent tous être considérés comme une voie intéressante pour la production de gaz de synthèse.

Dans la bibliographie, parmi les nombreux catalyseurs utilisés pour ces procédés, il est indiqué que le nickel est le métal actif le plus approprié pour les procédés de reformage, en raison de son faible coût, de sa disponibilité et de ses bonnes performances catalytiques. Bien que les catalyseurs à base de métaux nobles aient montré une activité plus élevée dans les processus de reformage du méthane, leur application est limitée en raison du prix élevé et de la faible disponibilité. Cependant, l'application industrielle de matériaux à base de Ni peut être limitée en raison du frittage de nanoparticules de Ni et de la désactivation du catalyseur provoquée par des dépôts de carbone. Ainsi, la préparation du catalyseur, le support utilisé et l'addition de promoteurs ou de dopants sont des paramètres qui influencent de manière significative le comportement catalytique, contribuant à la fois à l'activité catalytique et à la stabilité dans le temps.

Les **hydroxydes doubles lamellaires** (HDL), également appelés hydrotalcites (HT), présentent de bonnes propriétés en tant que support du fait de leur structure à double couche et de la présence de NiO, MgO et Al_2O_3 introduits majoritairement par co-précipitation. **L'objectif de cette thèse était donc**

d'évaluer les performances catalytiques de différents systèmes catalytiques à base d'hydroxydes doubles lamellaires contenant du nickel dans le reformage à sec du méthane, l'oxydation partielle du méthane, l'oxydation partielle combinée au reformage à sec du méthane et le tri-reformage du méthane. L'étude bibliographique a montrée que les matériaux du type HDL n'ont pas encore été étudiés dans les certains procédés de reformage. Un des objectifs de cette thèse a donc été de combler ces lacunes. Ainsi, un certain nombre de catalyseurs différents à base d'hydrotalcite ont été synthétisés par la méthode de co-précipitation et d'imprégnation à l'humidité naissante. L'accent a également été mis sur l'influence des promoteurs, en particulier de l'yttrium, qui n'avait pas été étudié jusque-là comme promoteur aux catalyseurs à base d'hydrotalcite. Les propriétés physico-chimiques des catalyseurs préparés ont été évaluées par diffraction de rayons X, Fluorescence X, adsorption de N_2 à basse température, chimisorption d'hydrogène, Réduction en température programmée de H_2, TPD-de CO_2, microscopie électronique à transmission, microscopie à haute résolution, analyse thermogravimétrique couplée à la spectroscopie de masse et spectroscopie Raman. Les catalyseurs obtenus ont été caractérisés avant réaction (après calcination et après réduction), mais également après la réaction catalytique. Les matériaux ont été testés en reformage du méthane (DRM, CROM, TRM), dans une plage de température comprise entre 850 et 600 °C, et pour certains d'entre eux en isotherme à 700 °C.

Cette thèse comprend six parties principales :

1. Une partie bibliographique consacrée à la réduction des émissions de CO_2, aux solutions et aux technologies (**chapitre 1**),

2. Une Partie expérimentale décrivant les techniques de préparation utilisées, les méthodes instrumentales utilisées ainsi que les types et les conditions des tests catalytiques (**chapitre 2**),

3. Les calculs thermodynamiques (**chapitre 3**),

4. Une discussion sur les performances catalytiques en reformage à sec du méthane des catalyseurs contenant de l'yttrium, du zirconium et de l'yttrium, et du cérium et de l'yttrium (**chapitre 4, avec les sous-chapitres 4.1, 4.2., 4.3., 4.4.**).

5. Une discussion du comportement catalytique en oxydation partielle du méthane, oxydation partielle combinée avec reformage à sec du méthane et tri-reformage du méthane (**chapitre 5**), et

6. Des conclusions générales.

La troisième partie (**chapitre 3**) traite des calculs d'équilibre thermodynamique pour les conversions de CH_4 et de CO_2 ainsi que pour le rapport molaire H_2/CO. Les calculs ont été effectués pour le reformage à sec du méthane (DRM), le reformage à la vapeur du méthane (SRM), l'oxydation partielle du méthane (POM) et le tri-reformage du méthane (TRM). Ces résultats ont confirmé que les réactions pouvaient être effectués efficacement à haute températures (supérieures à 700 °C). De plus, les calculs de tri-reformage du méthane présentaient un potentiel considérable de conversions catalytiques de CH_4 et de CO_2 avec des compositions de gaz tels que $CH_4/CO_2/H_2O/O_2$ = 1/0,5/0,5/0,1 et $CH_4/CO_2/H_2O/O_2$ = 3/1/2/0,3.

L'effet promoteur de l'yttrium, décrit dans le **sous-chapitre 4.1**., a été évalué en comparant les propriétés physico-chimiques et l'activité catalytique des HDL contenant 0,2, 0,4, 0,6, 2,0 et 3,0% massique d'yttrium préparé par co-précipitation. Il a été montré que de pour des teneurs en yttrium comprises entre 0,2 et 2,0% massiques, l'yttrium était introduit dans la structure même de la périclase, alors que l'ajout de 3,0% massique entraînait un dépôt partiel de ce métal à la surface. Les meilleures propriétés physico-chimiques, telles qu'une plus grande surface spécifique et une plus grande dispersion du Ni^0, ont été mises en évidence pour l'échantillon promu avec 2% massique en Y. Après modification avec 0,2 à 2,0% massique en yttrium, il a été montré que la basicité totale diminue, tandis que la promotion avec 3% massique a entraîné une augmentation significative du nombre total de sites basiques (TPD-CO_2). L'activité catalytique la plus élevée, donnée par la conversion du CH_4 et du CO_2, a été constatée pour les catalyseurs HTNi-Y3.0, avec une moyenne de 85% de conversion de CH_4 et de 89% de conversion de CO_2, ce qui pourrait être attribué au plus grand nombre de sites basiques totaux. Cependant, le comportement le plus stable a été observé pour l'échantillon HTNi-Y2.0 avec une moyenne de 74% de conversion pour le CH4 et 78% de conversion pour le CO_2 à 700 °C pendant 5 h.

Les **sous-chapitre 4.2.** et **4.3** traitent des différentes méthodes de dopage des HDL par le Zirconium (supposée 5% massique) et l'Yttrium (0,2, 0,4 et 0,6% massique) et leurs influences sur les performances catalytiques lors du reformage à sec du méthane. Les échantillons co-imprégnés par Zr et Y ont montré la formation d'une phase de zircone stabilisée à l'yttrium (YSZ) située à la surface de l'hydroxyde double lamellaire. Le catalyseur d'hydrotalcite modifié avec Zr et Y (0,4% massique) présentait une résistance structurelle, comme en témoigne l'absence de pic de diffraction correspondant à l'hydrotalcite en diffraction des rayons X sur le catalyseur après réaction. La co-précipitation avec Zr et l'imprégnation avec Y n'ont pas entraîné la formation de la phase YSZ. Le ZrO_2 a été partiellement introduit dans la structure de la périclase, tandis que l'yttrium était situé à la surface, entraînant ainsi son blocage partiel. Cela a entraîné une diminution de la dispersion des sites actifs (Ni^0) et une légère diminution de la taille des particules de Ni^0. Indépendamment de la méthode d'introduction du Zr et du Y, le pourcentage de sites basiques de moyenne intensité augmentait avec l'augmentation de la masse en yttrium. Ces deux séries ont été comparées au catalyseur co-précipité avec Zr (supposé 5% en poids) et Y (0,4% en poids). L'incorporation de ces deux métaux dans la structure a entraîné une augmentation du nombre de sites basiques totaux, une dispersion accrue du nickel et une réduction de la réductibilité. Cela a donc conduit à une influence positive sur les performances catalytiques en reformage à sec, car parmi tous les catalyseurs promus par le Zr et le Y, celui-ci a montré l'activité la plus élevée.

Le **sous-chapitre 4.4** décrit l'étude de l'introduction de Ce (3% massique) (introduit par la méthode de la co-précipitation) et de l'effet dopant de Y (imprégné avec 0,2, 0,4 ou 0,6% massique) sur des catalyseurs Ni/HDL en reformage à sec du méthane. La co-promotion avec Ce et Y a entraîné une diminution de la réductibilité du nickel, une augmentation de la basicité des matériaux, une dispersion accrue du Ni^0 et une taille de particule de Ni^0 inférieure par rapport au catalyseur de référence HTNi. La performance catalytique la plus élevée a été obtenue pour le catalyseur HTNi-Ce, avec une conversion de CH_4 de 86%, une conversion de CO_2 de 88% et un rapport molaire H_2/CO d'env. 0,97. Pour le catalyseur à base de Ce et de Y (0,4% massique), la quantité de carbone mesurée après réaction

était supérieure, mais le carbone obtenu était moins graphitique que pour le catalyseur dopé uniquement par le cérium. Par ailleurs, aucune désactivation n'a été observée au cours de l'essai en isotherme à 700 °C pendant 5 heures sur ce catalyseur.

Sur toutes les séries des catalyseurs décrites dans les sous-chapitres 4.1 à 4.4, il a été observé, après DRM (test catalytique pendant 5 h à 700 °C), la formation de différents types de dépôts carbonés tels que du carbone amorphe, du carbone filamenteux et enfin du carbone graphitique. Cependant, la quantité de chaque type de carbone dépendait à la fois du procédé de préparation utilisé, de la quantité de Y introduit et, de l'addition d'un second promoteur. La quantité la plus faible en dépôt de carbone a été obtenue pour le catalyseur co-précipité au Zr. Les dépôts les moins graphitiques ont été trouvés après la réaction de DRM en présence de HTNi-Zr et HTNi-Zr/Y0.4.

Le chapitre 5 présente l'effet promoteur de Y dans les HDL à base de nickel dans les réactions de reformage en présence d'oxygène telle que l'oxydation partielle POM, l'oxydation partielle avec addition de dioxyde de carbone CRPOM et le tri-reformage. Deux catalyseurs sélectionnés ont été testés, le catalyseur de référence non dopé (HTNi) et l'HDL dopé avec 2% massique en Y (HTNi-Y2.0).

Dans les expériences d'oxydation partielle du méthane (POM), les matériaux ont montré des conversions élevées de CH_4 d'environ 90% et un rapport H_2/CO proche de la stœchiométrie (environ 2,0). Par ailleurs, aucune désactivation n'a été observée au cours de l'expérience de 5 heures à 700 °C. L'oxydation partielle du méthane associée au reformage du CO_2 a révélé que l'addition d'oxygène au reformage à sec améliorait considérablement la stabilité des catalyseurs, en ce qui concerne l'élimination du carbone, car seules des traces de carbone ont été détectées lors des études de caractérisation après réaction. Les conversions de CO_2 obtenues étaient inférieures à celles obtenues pour le reformage à sec du fait de la présence de nombreuses réactions parallèles.

La performance catalytique des Y-Ni-DLH en tri-reformage du méthane a été étudiée pour deux compositions de gaz (i) $CH_4/CO_2/H_2O/O_2$ = 1/0,5/0,5/0,1 comme suggérée par la bibliographie, et (ii) $CH_4/CO_2/H_2O/O_2$ = 3/1/2/0,3 donnée par les calculs thermodynamiques. En présence de la première composition gazeuse, de très bonnes performances ont été obtenues avec une formation limitée de

carbone pour les catalyseurs HTNi et HTNi-Y2.0 ; les deux catalyseurs présentant des conversions d'environ. 91-98% pour le CH_4 et 70-86% pour le CO_2. Lors de cette réaction un rapport H_2/CO de 1,97 a été obtenu avec le catalyseur HTNi, ce qui convient parfaitement à la synthèse du méthanol. Avec le catalyseur HTNi-Y2.0, le rapport H_2/CO obtenu était de 1,63, ce qui correspond plus à la production de diméthyl-éther, par exemple. La deuxième composition de gaz étudiée a conduit à une performance catalytique quelque peu inférieure. En effet, les conversions obtenues sur les catalyseurs HTNi et HTNi-Y2.0 ont été de 76-78% pour le CH_4 et de 89-91% pour la conversion du CO_2, avec un rapport H_2/CO pour les deux d'environ 1,62. De plus, la réaction de TRM avec cette composition de gaz a conduit à la formation d'une quantité importante de carbone sur les deux catalyseurs, soulignant le rôle important des conditions opératoires dans la conversion de CO_2/CH_4 et dans la stabilité des matériaux de type HDL.

Streszczenie

Na przestrzeni ostatnich kilkudziesięciu lat odnotowujemy stale wzrastające poziomy emisji CO_2. Pochodzą one głównie ze spalania paliw kopalnych, jak również z przemysłu petrochemicznego, chemicznego i cementowego. Świadomość globalnego ocieplenia, związanego przede wszystkim z emisją ditlenku węgla, doprowadziła do zaproponowania różnych technologii poświęconych jego redukcji, ze szczególnym naciskiem na technologie CCS (wychwyt i sekwestracja ditlenku węgla) i CCU (wychwyt i utylizacja ditlenku węgla). Zastosowanie nowoczesnych rozwiązań umożliwia przekształcenie CO_2 w wartościowe produkty takie jak chemikalia i paliwa. Wśród technologii, które mogą przetwarzać CO_2 na produkty, są m.in. procesy reformingu metanu – suchy reforming metanu (DRM), częściowe utlenianie metanu w połączeniu z suchym reformingiem (CRPOM) i tri-reforming metanu (TRM). Procesy te mogą odegrać znaczącą rolę w produkcji gazu syntezowego.

Literatura przedmiotu wskazuje, iż najodpowiedniejszym metalem aktywnym w procesach reformingu metanu jest nikiel, między innymi ze względu na jego niski koszt, dostępność i dobre właściwości katalityczne. Wprawdzie katalizatory na bazie metali szlachetnych wykazują wyższą aktywność w procesach reformowania metanu, lecz ich zastosowanie jest ograniczone ze względu na wysoką cenę i niską dostępność. Przemysłowe zastosowanie materiałów na bazie Ni jest jednak utrudnione ze względu na spiekanie nanocząstek niklowych i deaktywację katalizatora spowodowaną powstawaniem depozytów węglowych. Jednak można zauważyć, iż odpowiednia preparatyka katalizatora, w tym stosowanie odpowiednich nośników oraz dodatek promotorów, znacząco wpływają na jego właściwości, przyczyniając się zarówno do zwiększenia aktywności katalitycznej, jak i stabilności.

Podwójne warstwowe wodorotlenki (DLHs), znane również jako hydrotalkity (HTs), wykazują bardzo dobre właściwości jako potencjalne nośniki ze względu na dwuwarstwową strukturę i obecność NiO, MgO i Al_2O_3 wprowadzanych do struktury na drodze współstrącania. Mając na względzie wyżej opisane aspekty, **niniejsza praca doktorska miała na celu ocenę właściwości katalitycznych różnych**

hydrotalkitowych katalizatorów zawierających nikiel w suchym reformingu metanu, częściowym utlenieniu metanu oraz częściowym utlenianiu w połączeniu z suchym reformingiem metanu i tri-reformingu metanu. Literatura wskazuje, iż istnieje kilka obszarów dotyczących zastosowania materiałów pochodzących z DLHs w procesach reformingu metanu, które nie były jeszcze przedmiotem naukowych badań, a zatem idea pracy koncentrowała się na wypełnianiu tych luk. Mając powyższe na względzie, przygotowano szereg różnych katalizatorów na bazie materiałów hydrotalkitowych metodą współstrącania oraz metodą mokrej impregnacji. Nacisk położono na wpływ promotorów, zwłaszcza itru, który wcześniej nie był badany jako promotor katalizatorów opartych na hydrotalkicie. Właściwości fizyko-chemiczne otrzymanych materiałów oceniano za pomocą XRD, XRF, absorpcji N_2 w niskiej temperaturze, TPR-H_2, TPD-CO_2, chemisorpcji H_2, transmisyjnej mikroskopii elektronowej, mikroskopii HRTEM, analizy termograwimetrycznej, oraz spektroskopii Ramana.

Otrzymane katalizatory scharakteryzowano na różnych etapach procesu - świeżo przygotowany, kalcynowany, zredukowany, a także po reakcji. Materiały badano w procesach reformingu metanu w zakresie temperaturowym od 850 do 600 °C, a wybrane, dodatkowo w testach izotermicznych w temperaturze 700 °C.

Praca obejmuje sześć głównych części:

1. Część literaturową - dotyczącą redukcji emisji CO_2, rozwiązań oraz nowych technologii (**Rozdział 1**).
2. Część eksperymentalną - opisującą stosowane techniki preparatyki, metody instrumentalne oraz rodzaje i warunki testów katalitycznych (**Rozdział 2**).
3. Obliczenia termodynamiczne (**Rozdział 3**).
4. Omówienie budowy katalizatorów oraz ich właściwości katalitycznych w suchym reformingu metanu dla materiałów hydrotalkitowych promowanych itrem, cyrkonem i itrem lub cerem i itrem (**Rozdział 4**, z podrozdziałami 4.1, 4.2., 4.3., 4.4.).

5. Omówienie właściwości katalitycznych wybranych katalizatorów w reakcjach częściowego utleniania metanu, częściowego utleniania metanu połączonego z suchym reformingiem metanu oraz w tri-reformingu metanu (**Rozdział 5**).
6. Wnioski ogólne.

Rozdział trzeci obejmuje obliczenia równowagi termodynamicznej dla stopnia konwersji CH_4 i CO_2, a także dla stosunku molowego H_2/CO. Obliczenia przeprowadzono dla suchego reformingu metanu (DRM), parowego reformingu metanu (SRM), częściowego utleniania metanu (POM) i tri-reformingu metanu (TRM). Wyniki wykazały, iż procesy zachodzą z wysoką wydajnością, w temperaturze ok. 700 °C. Ponadto obliczenia tri-reformingu metanu wykazały wysoki stopień konwersji katalitycznej dla CH_4 i CO_2 przy składzie mieszaniny reakcyjnej $CH_4/CO_2/H_2O/O_2$ = 1/0,5/0,5/0,1 i $CH_4/CO_2/H_2O/O_2$ = 3/1/2/0,3.

Rolę itru jako promotora przedyskutowano w **podrozdziale 4.1**. porównując właściwości fizyko-chemiczne i aktywności katalityczne podwójnych warstwowych wodorotlenków zawierających 0,2, 0,4, 0,6, 2,0 i 3,0 % wagowych itru. Wykazano, że itr w zakresie 0,2-2.0% wag. został wprowadzony do struktury peryklazu, podczas gdy dodanie 3,0% wag. spowodowało częściowe osadzanie tego metalu na powierzchni. Najlepsze właściwości fizyko-chemiczne, takie jak wzrost powierzchni właściwej oraz zwiększony stopień dyspersji Ni, odnotowano dla próbki promowanej 2% wag. Y. Po modyfikacji 0,2 do 2,0% wag. itru całkowita zasadowość zmniejszyła się, podczas gdy promowanie 3,0% wag. doprowadziło do znacznego wzrostu całkowitej liczby grup zasadowych. Najwyższą aktywność katalityczną stwierdzono dla katalizatora HTNi-Y3.0. Średni stopień konwersji CH_4 i CO_2 wynosił odpowiednio 85% i 89%, co można przypisać zwiększonej liczbie centrów zasadowych. Jednak najbardziej stabilny charakter zaobserwowano dla próbki HTNi-Y2.0 ze średnią wartością stopnia konwersji (zarejestrowaną w teście 5-cio godzinnym w 700 °C) równą 74% dla CH_4 i 78% dla CO_2.

Podrozdziały 4.2. i **4.3.** obejmują ocenę różnych metod promowania podwójnych warstwowych wodorotlenków za pomocą Zr (zakładano 5% wag.) i Y (0,2, 0,4 i 0,6% wag.) i ich wpływu na pracę

katalizatorów w suchym reformingu metanu. Próbki ko-impregnowane Zr i Y wykazały tworzenie fazy ditlenku cyrkonu stabilizowanego tlenkiem itru (YSZ) zlokalizowanej na powierzchni podwójnego warstwowego wodorotlenku. Próbka hydrotalkitu modyfikowana za pomocą Zr i Y (0,4% wag.) wykazywała odporność strukturalną na produkty reakcji ubocznej (RWGS odwrotna reakcja z gazem wodnym), na co wskazuje brak refleksów hydrotalkitowych w dyfraktogramach katalizatora po reakcji DRM. Współstrącanie hydrotalkitu z dodatkiem cyrkonu i impregnacja itrem w kolejnym kroku nie spowodowały utworzenia fazy YSZ. ZrO_2 został częściowo wprowadzony do struktury peryklazu, podczas gdy itr znajdował się na powierzchni częściowo ją blokując. Spowodowało to zmniejszenie stopnia dyspersji metalicznego niklu i nieznaczne zmniejszenie wielkości jego krystalitów. Niezależnie od metody wprowadzania Zr i Y, procentowa zawartość centrów zasadowych wzrastała wraz ze wzrostem zawartości itru. Obie omówione serie katalizatorów porównano do katalizatora otrzymanego przez współstrącanie z Zr (założono 5,0% wag.) i Y (0,4% wag.). Włączenie tych dwóch metali do struktury doprowadziło do zwiększenia całkowitej ilości grup zasadowych, zwiększonego stopnia dyspersji Ni i zwiększonej redukowalności. Wpłynęło to w pozytywny sposób na właściwości katalityczne w procesie suchego reformingu, ponieważ wśród wszystkich materiałów promowanych przez Zr i Y, ten wykazał najwyższą aktywność w CH_4 i CO_2.

Podrozdział 4.4. opisuje badania ko-promowania DLHs z Ce (wprowadzonego metodą współstrącania z założeniem 3,0% wag.) i Y (impregnacja 0,2, 0,4 lub 0,6% wag.) i testy suchego reformingu metanu. Ko-promowanie z Ce i Y doprowadziło do zmniejszenia redukowalności Ni, wzrostu zasadowości, zwiększenia stopnia dyspersji Ni i zmniejszenia wielkości krystalitów Ni w porównaniu z niepromowanym katalizatorem HTNi. Najwyższą aktywność katalityczną odnotowano dla HTNi-Ce, dla którego stopień konwersji CH_4 był równy 86%, stopień konwersji CO_2 był na poziomie 88%, a stosunek molowy H_2/CO wynosił ok. 0,97. Dla katalizatora promowanego Ce i 0,4% wag. Y ilość depozytu węglowego była wprawdzie wyższa niż dla HTNi-Ce, ale odznaczał się on mniejszym stopniem grafityzacji niż dla materiału modyfikowanego tylko cerem. Nie zaobserwowano deaktywacji podczas testu izotermicznego w temperaturze 700 °C przez 5 godzin.

Dla wszystkich serii katalizatorów, omówionych w **podrozdziałach 4.1.** do **4.4.** zarejestrowano, po teście suchego reformingu metanu przez okres 5 h w temperaturze 700 °C, różne rodzaje depozytów węglowych. Ilość każdego typu była jednak zależna zarówno od zastosowanej metody preparatyki, ilości wprowadzonego Y i dodania drugiego promotora. Najmniejszą ilość depozytów węglowych zarejestrowano po reakcji dla katalizatora współstrąconego z Zr, a najmniejszy stopień grafityzacji dla HTNi-Zr i HTNi-Zr/Y0.4.

Rozdział 5 omawia badania niklowych podwójnych warstwowych wodorotlenków w reakcjach reformingu z dodatkiem tlenu lub tlenu i wody, tj. w częściowym utlenianiu metanu (POM), w częściowym utlenieniu metanu połączonym z suchym reformingiem metanu (CRPOM) i w tri-reformingu metanu (TRM). Przebadano dwa wybrane katalizatory, niepromowany podwójny warstwowy wodorotlenek (HTNi) i podwójny warstwowy wodorotlenek zawierający Ni i promowany 2,0% wag. itru (HTNi-Y2.0).

W eksperymentach częściowego utleniania metanu (POM) oba katalizatory wykazywały wysokie stopnie konwersji CH_4 na poziomie ok. 90%, a odnotowany stosunek molowy H_2/CO był zbliżony do stechiometrycznego (około 2,0). Nie zaobserwowano deaktywacji w ciągu 5-godzinnego testu katalitycznego w temperaturze 700 °C. Częściowe utlenianie metanu w połączeniu z suchym reformingiem wykazało, iż dodanie tlenu do DRM znacznie poprawia stabilność katalizatorów. Na powierzchni zaobserwowano jedynie śladowe ilości depozytu węglowego. Uzyskane stopnie konwersji CO_2 były niższe niż te zarejestrowane dla suchego reformingu metanu na skutek wystąpienia reakcji ubocznych.

Aktywność katalityczną Y-Ni-DLH w tri-reformingu metanu badano dla mieszanin reakcyjnych o dwóch składach (i) $CH_4/CO_2/H_2O/O_2$=1/0,5/0,5/0,1, sugerowanej przez literaturę, i (ii) $CH_4/CO_2/H_2O/O_2$ = 3/1/2/0,3 wybrane na podstawie obliczeń termodynamicznych. Przy zastosowaniu tej pierwszej, odnotowano bardzo dobrą pracę obu katalizatorów HTNi i HTNi-Y2,0 przy ograniczonym tworzeniu depozytu węglowego. Materiały były aktywne katalitycznie, oba wykazywały średni stopień konwersji ok. 91-98% dla CH_4 i 70-86% dla CO_2. Średni stosunek molowy H_2/CO dla HTNi wynosił 1,97, który jest

odpowiedni dla syntezy metanolu, podczas gdy HTNi-Y2.0 wykazał niższą wartość (1,63), którą można stosować np. do produkcji eteru dimetylowego. Druga badana mieszanina reakcyjna dała nieco gorsze wyniki, z niższymi wartościami stopnia konwersji dla obu badanych katalizatorów - 76-78% dla CH_4 i 89-91% dla konwersji CO_2, i średnim stosunkiem molowym H_2/CO ok. 1,62 w obu przypadkach. Dodatkowo, w przypadku mieszaniny o tym składzie zarejestrowano tworzenie znacznej ilości depozytu węglowego na obu badanych próbkach, co wskazuje na ważną rolę stosowanych warunków reakcji w stabilności materiałów typu DLH.

Academic achievements of the author

Publications concerning Doctoral thesis:

The results presented in this thesis were partially published in the following international journals *with Impact Factor (values for 2017):*

1. **K. Świrk**, M.E. Gálvez, M. Motak, T. Grzybek, M. Rønning, P. Da Costa, Yttrium promoted Ni-based double-layered hydroxides for dry methane reforming, J. CO2 Util. 27 (2018) 247–258. doi:10.1016/j.jcou.2018.08.004. **IF: 5.503, MNiSW (40)**
2. **K. Świrk**, M. Motak, T. Grzybek, M. Rønning, P. Da Costa, Effect of low loading of yttrium on Ni-based layered double hydroxides in CO_2 reforming of CH_4, React. Kinet. Mech. Catal. (2018) article in press. doi:10.1007/s11144-018-1515-9. **IF: 1.515, MNiSW (15)**
3. **K. Świrk**, M.E. Gálvez, M. Motak, T. Grzybek, M. Rønning, P. Da Costa, Dry reforming of methane over Zr- and Y-modified Ni/Mg/Al double-layered hydroxides, Catal. Commun. 117 (2018) 26–32. doi:doi.org/10.1016/j.catcom.2018.08.024. **IF: 3.463, MNiSW (30)**
4. **K. Świrk**, M. Rønning, M. Motak, P. Beaunier, P. Da Costa, T. Grzybek, Ce- and Y-modified double-layered hydroxides as catalysts for dry reforming of methane: On the effect of yttrium promotion, Catalysts. 9 (2019) 56–74. doi:10.3390/catal9010056. **IF: 3.465, MNiSW (30)**

Without Impact factor:

1. **K. Świrk**, T. Grzybek, M. Motak, Tri-reforming as a process of CO_2 utilization and a novel concept of energy storage in chemical products, E3S Web Conf., vol. 14, art. no. 02038 (2017). doi:10.1051/e3sconf/20171402038. **MNiSW (15)**
2. **K. Świrk**, M. E. Gálvez, A. Izquierdo, M. Motak, P. Da Costa, T. Grzybek, Thermodynamic equilibrium analysis of methane reforming as a prospective process for synthesis gas production, Contemporary Problems of Power Engineering and Environmental Protection, Gliwice (2016) 169–177, ISBN 978-83-93-02-32-2-6, **MNiSW (5)**

Other publications in international journals:

With Impact Factor:

1. **K. Świrk**, M.E. Gálvez, M. Motak, T. Grzybek, M. Rønning, P. Da Costa, Syngas production from dry methane reforming over yttrium-promoted nickel-KIT-6 catalysts, Int. J. Hydrogen Energy. 44 (2019) 274–286. doi:10.1016/j.ijhydene.2018.02.164. **IF: 4.229**, **MNiSW (35)**
2. H. Liu, **K. Świrk**, M.E. Gálvez, P. Da Costa, Nickel supported modified ceria zirconia lanthanum/ praseodymium/yttrium oxides catalysts for syngas production through dry methane reforming, Mater. Sci. Forum. 941 (2018) 2214–2219. doi:10.4028/www.scientific.net/MSF.941.2214. **IF: 0.30**

Without Impact Factor:

1. **K. Świrk**, M. Rønning, B. Samojeden, Influence of the amount of urea modification of activated carbon on DeNOx catalyst efficiency, Współczesne Problemy Energetyki, Gliwice (2015) 151-162, ISBN 978-83-942601-2-5, **MNiSW (5)**
2. **K. Świrk**, M. Motak, T. Grzybek, C. Czosnek, P. Kniaź, The influence of the modification of acidic montmorillonites with polyacrylamide and copper deposition on SCR-NH_3 catalytic performance, E3S Web Conf., vol. 14, art. no. 02037 (2017). doi:10.1051/e3sconf/20171402037. **MNiSW (15)**

Oral presentations at the conferences:

1. 3rd Edition of the Conference „Ochrona Środowiska i Energetyka", 11 December 2015 in Gliwice, Poland

   K. Świrk, M. Rønning, B. Samojeden, Title: „Influence of the amount of urea modification of activated carbon on DeNOx catalyst efficiency"

2. 4th Edition of the Conference „Ochrona Środowiska i Energetyka", 9 December 2016 in Gliwice, Poland

   K. Świrk, M. E. Gálvez, A. Izquierdo, M. Motak, P. Da Costa, T. Grzybek, Title: „Thermodynamic equilibrium analysis of methane reforming as a prospective process for synthesis gas production"

3. North American Catalysis Meeting 25, 4 - 9 June 2017 in Denver, Colorado, USA

   K. Świrk, M. E. Gálvez, M. Motak, P. Da Costa, T. Grzybek, Title: „Yttrium modified Ni-Zr-Ce hydrotalcite-derived catalysts for dry reforming of methane"

4. AIChE 2017, 25 October - 3 November 2017 in Minneapolis, Minnesota, USA

   K. Świrk, M. E. Gálvez, M. Motak, T. Grzybek, M. Rønning, P. Da Costa, Title: "Dry reforming of methane over Zr,Y-modified Ni/Mg/Al hydrotalcite-derived catalysts for hydrogen and carbon monoxide production".

   This communication was awarded as a "Best Presentation" at the session: *Advances in Catalysis for Hydrogen Production*

5. Reaction Kinetics, Mechanism and Catalysis Conference, 6-9 June 2018 in Budapest, Hungary

K. Świrk, M. Motak, M. E. Galvez, T. Grzybek, M. Rønning, P. Da Costa, Title: "Effect of yttrium doping on Ni-based layered double hydroxides in dry reforming of methane for syngas production"

6. INASCON2018, 7-10 July 2018 in Trondheim, Norway

K. Świrk, M. Motak, M. E. Gálvez, T. Grzybek, M. Rønning, P. Da Costa, Title: "Ce,Y-modified double-layered hydroxides as catalysts for dry methane reforming: The effect of yttrium promotion".

Poster presentations:

1. 58th Meeting of the Polish Chemical Society, 21-25 September 2015, Gdańsk, Poland

- B. Samojeden, **K. Świrk,** Title: „The influence of urea modification on catalytic activity of activated carbon" Materiały 58, page 275, Warszawa 2015, ISBN: 978-83-60988-20-6.

2. XLVIII Polish Annual Conference on Catalysis: 16-18 March 2016, Cracow, Poland

- M. Motak, B. Samojeden, D. Wierzbicki, **K. Świrk**, T. Grzybek**,** Title: „The modified layered materials as catalysts for the SCR reaction", page 340, Kraków 2016, ISBN: 978-83-60514-24-5.
- M. Motak, D. Duraczyńska, R. Dębek, D. Wierzbicki, **K. Świrk**, B. Samojeden, Title: „The SEM characterization of hydrotalcite-like catalysts in DRM process", page 339, Kraków 2016, ISBN: 978-83-60514-24-5.

3. 13th Pannonian International Symposium on Catalysis: 19-23 September 2016 Siófok, Hungary

- **K. Świrk**, M. Motak, B. Samojeden, C. Czosnek, K. Kucharczyk, P. Kniaź, Tytuł: „Montmorillonite modified with polyacrylamide and copper deposition as a catalyst in catalytic reduction of NO with ammonia", page 131, Siófok 2016, ISBN: 978-963-9970-56-4.
- **K. Świrk**, D. Wierzbicki, R. Baran, M. Krawczyk, R. Dębek, M. Motak, T. Grzybek, Title: "Selective catalytic reduction of nitrogen oxides by NH_3 over iron-promoted vermiculites", page 131, Siófok 2016, ISBN: 978-963-9970-56-4.
- D. Wierzbicki, R. Baran, **K. Świrk**, M. Krawczyk, R. Dębek, M. Motak, T. Grzybek, Title: "Al-pillared, copper-containing vermiculites as prospective catalysts for NH_3-SCR", page 147, Siófok 2016, ISBN: 978-963-9970-56-4.

4. 9th international conference on Advanced Nano Materials, 19-21 July 2017, Aveiro, Portugal

- **K. Świrk**, M. E. Gálvez, M. Motak, T. Grzybek, P. Da Costa, Title: „Hydrogen production from dry methane reforming over KIT-6 modified with Ni and Y", Aveiro 2017, *electronic version of the abstract https://goo.gl/M4c6VS [2017-07-28]*